Universidade de Aveiro Departamento de Física
2018

Dhananjay Kumar Sharma

Crescimento e caracterização de Grafeno de grande área e de Dissulfureto de Molibdénio por Deposição Química em fase de Vapor (CVD)

Growth and characterization of large area Graphene and Molybdenum disulfide by Chemical Vapor Deposition (CVD)

Universidade de Aveiro Departamento de Física
2018

Dhananjay Kumar Sharma

Crescimento e caracterização de Grafeno de grande área e de Dissulfureto de Molibdénio por Deposição Química em fase de Vapor (CVD)

Growth and characterization of Large Area Graphene and Molybdenum disulfide by Chemical Vapor Deposition (CVD)

Tese apresentada à Universidade de Aveiro para cumprimento dos requisitos necessários à obtenção do grau de Doutor em nanociências e nanotecnologia, realizada sob a orientação científica do Dr. Andrei Leonidovitch Kholkine, Investigador Coordenador do Departamento de Fisica e do CICECO da Universidade de Aveiro.

Dissertation submitted to the University of Aveiro, as the fulfilment of necessary requirements for obtaining the Ph.D. degree in Nanoscience and Nanotechnology was carried out under the supervision of Dr. Andrei Leonidovitch Kholkine, Research Coordinator of the Department of Physics and CICECO of the University of Aveiro.

Apoio financeiro através de uma bolsa Svāgata Erasmus Mundus

Financial support from Svāgata Erasmus Mundus Fellowship

Dedicated to my father, someone who is very special in my life!

The Board of Examiners

Presidente	**Prof. Doutor Nuno Miguel Gonçalves Borges De Carvalho** Professor Catedrático e Reitor da Universidade de Aveiro
Vogais	**Prof. Doutor José Ramiro Afonso Ferandes** Professor Auxiliar da Universidade de Trás-os-Montes e Alto Douro
	Prof. Doutor Vitor Brás Sequeira Amaral Professor Catedrático da Universidade de Aveiro
	Doutor Andrei Leonidovitch Kholkine Investigador Coordenador da Universidade de Aveiro
	Prof. Doutor Senentxu Lanceros-Méndez Professor Associado da Universidade do Minho
	Prof. Doutora Maria do Carmo Henriques Lança Professora Auxiliar da Universidade NOVA de Lisboa

"*I hear and I forget. I see and I remember. I do and I understand*"

- *Confucius*

Acknowledgements

Firstly, I would like to express my sincere and deepest gratitude to my supervisor Professor Dr Andrei Leonidovitch Kholkine for his invaluable guidance, support and encouragement throughout the thesis. I thank him for critical supervision, powerful advisement and patient listening of my thoughts. His guidance helped me in all the time of research and writing of this thesis. I could not have imagined having a better advisor and mentor for my Ph.D. study.

My sincere thanks also go to Professor Seema Sharma (A N College, Bihar, India) for encouraging me, who supported me during my masters and shared the knowledge about Svāgata (Erasmus Mundus Fellowship) and encourage me to apply this. Without her precious support, I would not be here to complete my Ph.D.

I am thankful to Dr Gonzalo Otero-Irurueta and Dr María J. Hortigüela for providing and sharing XPS technical expertise required for my studies. Besides this, I am thankful to Professor Antonio Bastos, Dr Paula Marques, Dr Duncan Paul Fagg and Dr Igor Bdikin for allowing and providing me the access to the department for conducting my experiments.

I would like to thank all members of the Department of Materials and Ceramic Engineering of the University of Aveiro, who shared scientific knowledge and created a friendly atmosphere during my stay. Special thanks to Marta Ferro and Dr. Ana Violeta Girão for my TEM measurements.

I would like to thanks to Professor Naheed Ahmad (Patna Science College, Bihar, India), Dr. Naser Aziz Anjum, Dr. Srikanth Koigoora, Dr. Suresh Kumar Jakka (University of Aveiro), Dr. Kazi Saidul Huq (Instituto de Telecomunicações, University of Aveiro), Dr. Imran Khan (Sultan Qaboos University, Oman) and Professor Sangeeta Sinha (A N College) for their blessings, motivations during my Ph.D.

I would like to convey my thanks to all my close friends out of the group in Portugal, who made this period enjoyable, unforgettable and supported me during difficult times; they are immense in number so I avoid to mention their names. Special thanks to Dr Amit Mahajan and Dr Eskilla Venkata Ramana for sharing me their expertise knowledge in material science.

I would also like acknowledge Niall Power (University of Aveiro), Karel Vercamst (India Platform, Ghent) and Anne Cardinael (India Platform, Ghent) for organizing Svāgata which is now converted to India Platform.

Gratitude to all my colleagues who was sitting in the room 29.3.24 at CICECO for creating friendly atmosphere required for thesis writing. Thanks to Patrícia Neves, Sofia Bruno and Márcia Neves for final touch up of the thesis.

I am also thanks to my friends Wioleta Borzęcka, Konrad Białecki, Natália Braz Barroca, Ruchi Singh, Nawnit Kumar, Anand Ranjan, Arpana Singh and Shweta Thakur for supporting and boosting me during my Ph.D.

Special thanks to God and my family for their blessings which help me to overcome the obstacles during my work.

Finally, I would like to thank the financially support from Svāgata Erasmus Mundus Fellowship for providing me the fellowship for my Ph.D.

Palavras-Chave

Grafeno, Dissulfeto de Molibdénio, Deposição Química na fase de Vapor Espectroscopia de fotoeletrões de alta resolução (HR-XPS), Raman, Defeitos, Dopagem com azoto, Metais de Transição Dicalcogénios, Injeção / relaxamento de carga, Fotoeletrões Potencial de superfície, Microscópio Eletrónico, Microscopia de Força Atómica e Piezo.

Sumário

O presente trabalho, tem com objetivo promover a descrição da parte experimental da síntese de grafeno e de estruturas bidimensionais (2D). Foram usadas as técnicas já existentes, que aplicam deposição química na fase de vapor (CVD), para a síntese de grafeno e estruturas bidimensionais com aplicações multidisciplinares, como indústrias de nano-eletrónicos e de semi-condutores. Todos os problemas, sugestões e questões importantes relacionados com o crescimento e parametrização da condição ótima para formação de estritamente monocamadas a pequenas camadas foram brevemente discutidas.

Isto pode trazer benefícios duplos como a produção de dispositivos eletrónicos 2D com altas motilidades de transporte e o entendimento do comportamento dos materiais 2D sujeitos a intercalação iónica.

Os grafenos sintetizados no substrato cobre (Cu) apresentaram um espectro ideal de Raman com uma concentração de defeitos menor. A presença de pequenos picos D confirmou a elevada qualidade dos cristais de grafeno com estritamente monocamadas a pequenas cadeias.

Além disso, a espectroscopia de Raios-X de alta resolução (HR-XPS) mostrou o grafeno de elevada qualidade com C 1s em configuração sp^2 (com energia de ligação a ~284.8 eV). A ausência de outros componentes reforça a pureza e a qualidade do grafeno sintetizado. As imagens de mapping Raman demonstraram a cobertura total do grafeno de elevada área no substrato cobre. Adicionalmente, os resultados de microscopia de transmissão eletrónica de alta resolução (HRTEM) confirmaram a elevada natureza cristalina com dois tipos de planos rotacionais que podem ser atribuídos à presença de rugas durante a transferência de folhas de grafeno nas grelhas de TEM.

Esta tese dedica-se também à dopagem heteroatómica do grafeno com o objetivo de alterar as suas propriedades eletrónicas. A amónia (NH_3) foi usada como fonte de azoto (N) como átomo externo para a dopagem do grafeno puro. Mais uma vez, foram feitos esforços para discutir todos os problemas, sugestões e outras questões importantes relacionadas com o crescimento e parametrização das condições ótimas para a dopagem in-situ de amónia do grafeno no cobre. O papel do substrato (espessura do filme) na criação de defeitos foi também discutida. Os resultados de Raman mostram o aumento dos picos D e *D'*, o que confirma a dopagem do grafeno por NH_3.

Os dados de HRXPS mostraram o pico C 1s centrado a uma energia de ligação (BE) de 284.5 eV, atribuído ao C sp^2 que pode ser correlacionado com a boa qualidade do C. Então, de acordo com o XPS, o grafeno que cresceu no substrato Cu 20 µm apresentou uma melhor intercalação do azoto nas folhas de grafeno sob as mesmas condições de crescimento. As duas componentes (substitucional a BE de 401.7 eV e piridínica de 398.5 eV) foram claramente distinguidas no respetivo pico N 1s.

A dopagem com o tipo de configuração substitucional envolve três eletrões de valência do nitrogénio formando três ligações σ, um eletrão a preencher os estados π e o quinto eletrão no estado π* da banda de condução que conduzem, no total, a um forte efeito de doping.

O presente trabalho também reporta um método in-situ para a caraterização quantitativa das propriedades eletrostáticas na escala nano das folhas de grafeno multicamada (MLG) crescidas no níquel (Ni) por combinação de dados de microscopia de força atómica (AFM) e microscopia de força atómica Kelvin (KPFM). Folhas MLG de larga área epitaxial cresceram no Ni usando a técnica CVD. A elevada natureza cristalina das folhas MLG no níquel foi confirmada por espectroscopia Raman com valor de FWHM tão baixo como ~20 cm^{-1} para o pico G. Foi feita a injeção de carga (e subsequente difusão de carga com o tempo) no recém sintetizado grafeno no Ni. Os resultados revelaram que : (i) a superfície MLG pode ser carregada quer positivamente quer negativamente pelo processo de injeção usando sondas de Si revestidas de Pt; (ii) as cargas podem ser acumuladas e eventualmente atingir concentrações de saturação de (+4.45±0.1) μC/m^2 e (−1.3±0.1) μC/m^2, respetivamente; e (iii) os coeficientes de difusão de carga na superfície medidos foram de (1.50±0.05) × 10^{-16} m^2/s e (0.64±0.05) × 10^{-16} m^2/s para as cargas positivas e negativas, respetivamente.

As experiências relacionadas com a descoberta de injeção de carga no MLG podem conduzir a uma maneira de desenhar uma nova classe de dispositivos de recolha de energia. Além disso, este estudo também demonstra uma técnica para nano-modelação/litografia de carga das superfícies de carga por eletrificação do contacto, que pode vir a ser uma aplicação promissora para criar nanoestruturas carregadas para a próxima geração de dispositivos nano-eletrónicos baseados em grafeno.

Uma breve descrição da qualidade dos substratos transferidos foi também explorada. Foram usados vários substratos, como SiO_2/Si e Au. Uma comparação qualitativa da qualidade entre a transferência do grafeno antes e depois foi criticamente descrita. Os resultados de HRXPS mostram a interação da camada de ferro com o grafeno.

Por fim, esta pesquisa também mostrou as principais etapas de parametrização e síntese, e o fluxo de trabalho para materiais de elevada qualidade TMDs (como MoS_2), por modificação do actual aparelho de CVD. Uma revisão completa das propriedades fundamentais, assim como do método de síntese, propriedades e problemas relacionados com o crescimento de materiais 2D foram também salientados. O efeito da pressão e outras condições para o crescimento de elevada qualidade foram completamente descritos. Este estudo indica que a pressão ótima para o crescimento de uma larga área MoS2 com uma bandgap direta de 1.6 eV é de 50 mbar. Os resultados de micro-Raman mostram claramente a distinção de picos E^1_{2g} e A^1_g picos e os dados de HR-XPS reconfirmam a sua elevada qualidade através de diferentes picos de nível interno de Mo and S.
Além disso, através do uso da técnica microscopia eletrónica de varrimento (SEM) com feixe de iões focalizados (FIB), foram preparados elétrodos de platina necessários para medidas elétricas. O resultado mostrou: (i) o comportamento óhmico e semi-condutor dos cristais; (ii) a importância das monocamadas de elevada qualidade (SL) MoS_2 nas indústrias de semi-condutores e (iii) o potencial das SL MoS_2 de elevada qualidade para substituir o grafeno num futuro próximo.

Keywords

Graphene, Molybdenum disulfide, chemical vapor deposition (CVD), High Resolution -X-ray Photoelectron Spectroscopy (HR-XPS), Raman, Defects, Nitrogen-doping, transition metal dichalcogenides (TMDs), Charge injection/relaxation, Surface potential, Atomic and Piezo Force Microscopy.

Abstract

The present work is aimed to provide description of experimental part of graphene and two-dimensional structures. State-of-the-art techniques employing chemical vapor deposition (CVD) were used to deposit graphene and two-dimensional structures for their multidisciplinary applications including nano-electronics and semi-conducting industries. All the problems, suggestions and other important issues related to the growth and parameterizing the optimum condition for strictly monolayer to few layers have been briefly discussed. This may give double benefits such as realizing 2D electronic devices with high carrier motilities and understanding the behaviour of these 2D materials upon small ion intercalation. The as synthesized graphene grown on copper (Cu) substrate showed the ideal Raman spectrum with least defect concentration. The presence of very small D peaks confirmed the high quality of graphene crystals with strictly monolayer to few layers. Moreover, High Resolution X-rays Spectroscopy (HR-XPS) analysis showed the high quality graphene with C 1s in sp^2 configuration (with binding energy at ~284.8 eV). The absence of other components resembled the purity of graphene and again reconfirmed the good quality of synthesized graphene. The Raman image mapping, demonstrated the full coverage of large area graphene on copper substrate. Additionally, the High Resolution Transmission Electron Microscopy (HRTEM) results reconfirmed that the high crystalline nature with two-type of rotational planes, which may attributed to the presence of wrinkles formed during the transfer of graphene sheet on TEM grids.

This thesis is also devoted to the heteroatom doping in order to tune the electronic properties of graphene. Ammonia (NH_3) was used herein to provide nitrogen (N) as a source for foreign atom for the doping of pure graphene. Here again, efforts were made to discuss all the problems, suggestions and other important issues related to growth and parameterizing the optimum conditions for in-situ ammonia doping of graphene on Cu. The substrate (thickness of films) playing role in the defect creations was also discussed. Raman results showed the enhanced D and *D'* peaks, which confirmed the doping of graphene by NH_3. HRXPS showed the C 1s core level centred at a BE of 284.5 eV, ascribed to C sp^2 can be co-related with the good quality of C. Thus, in context with the XPS, the graphene grown on 20 µm Cu substrate showed the better nitrogen intercalation in the graphene sheets under the same growing conditions. Two components (substitutional at BE of 401.7 eV and pyridinic at BE of 398.5 eV) were clearly distinguished in the respective N 1s core level. The doping with substitutional type of configuration, involves three nitrogen valence electron forming three σ– bonds, one electron filling the π–states, and the fifth electron entering the π*–states of the conduction band, and altogether provide a strong doping effect.

The presented work also reported a study demonstrating an in-situ method for the quantitative characterization of nanoscale electrostatic properties of as-grown multilayer-graphene (MLG) sheets on nickel (Ni) by combining atomic force microscopy (AFM) and Kelvin probe force microscopy (KPFM). Large area epitaxial MLG sheets were grown on Ni by using CVD technique. The high crystalline nature of MLG sheets on Ni was confirmed by Raman spectroscopy with the FWHM value as low as ~20 cm^{-1} for G peak. We performed the charge injection (and subsequent charge diffusion over time) on the as synthesized graphene on Ni. The results unveiled that: (i) MLG surface can be either positively or negatively charged through injection process using Pt coated Si-based AFM probes; (ii) the charges can be accumulated and eventually reached to saturated concentrations of (+4.45±0.1) $\mu C/m^2$ and (−1.3±0.1) $\mu C/m^2$, respectively; and (iii) the charge diffusion coefficients on graphene surface were measured to be (1.50±0.05) × 10^{-16} m^2/s and (0.64±0.05) × 10^{-16} m^2/s for the positive and the negative charges, respectively. The concerned experiment related to the discovery of charge injection in MLG may pave the way for designing a new class of energy harvesting devices. In addition to this, study also demonstrated a technique for nano-patterning/charge lithography of surface charges by contact electrification, which could be a promising application to create charged nanostructures for next generation graphene based nano-electronic devices.

A brief description on the quality of transferred substrate has also been noted. Various substrates such as SiO_2/Si and Au substrate have been used. A relative quality comparison between before and after transfer of graphene has been critically described. Results from HRXPS show the iron monolayer interaction with graphene.

Lastly, this research also showed the major parameterizing and synthesizing steps, and the work flow for the high quality TMDs materials (such as MoS_2) by modifying the current CVD equipment. A thorough review of the fundamental properties as well as methods of synthesis, properties and problems related to the growth of 2D materials was also highlighted. The effect of pressure and other conditions for the growth of high quality were fully described. This study found 50mbar as an optimum pressure for the growth of large area MoS_2 having a direct bandgap of 1.6eV. Micro-Raman results clearly showed distinguish E^1_{2g} and A^1_g peaks and HRXPS re-confirmed its high quality by the different Mo and S core-level peaks. Additionally, employing Focused ion beam equipped with SEM (scanning electron microscopy) technique (FIB), the present study prepared platinum (Pt) electrodes required for the electrical measurements. The result showed: (i) the ohmic and semi-conducting behavior of the crystals; (ii) the importance of high-quality single-layer (SL) MoS_2 in the semi-conducting industries; and (iii) the potential of high quality SL MoS_2 for replacing graphene in near future.

Contents

Thesis outline

The present thesis comprises eight chapters dedicated to the specific objectives including the introduction, six experimental chapters and conclusions. *Chapter 1* presents the scientific motivation and rationale, which states the author's interest and dedication, and also shows the encouragement and enthusiasm for the PhD work. The major focus of the *Chapter 2* is to critically review the literature available on graphene and other two-dimensional materials and to summarize the *state-of-the-art* on the topic. This chapter also highlights the basic electronic properties and importance of graphene, as well as defects in graphene (and their intentional introduction). Efforts were also made to overview the *state-of-the-art* literature on molybdenum disulfide (MoS_2) and its importance. *Chapter 3* reveals the fundamentals of the advanced methods applied for the characterization of samples, graphene, nitrogen-doped graphene and MoS_2. *Chapter 4* mainly deals with the experimental growth methods, where a brief summary of experimental conditions used for the deposition of pure graphene on copper substrates and its characterization using Raman, High-Resolution X-Ray Photoelectron Spectroscopy (HR-XPS) and High-Resolution Transmission Electron Microscopy (HR-TEM) are presented. In *Chapter 5*, the experimental growth conditions are detailed for the deposition of *in situ* ammonia doped graphene on copper substrates and its characterization using Raman, HR-XPS and HR-TEM. A brief summary of the substrate thickness dependence and calculations of created defects (upon doping by nitrogen atoms) is also noted.

Details of the experimental conditions required for the growth of pure graphene on nickel substrates and its characterization using Raman and HR-XPS are discussed in *Chapter 6.* This chapter also studies the charge injection phenomena in multi-layer graphene (MLG) on nickel via Kelvin Probe Force Microscopy. *Chapter 7* is focused on the transfer of pure and nitrogen doped graphene samples on the arbitrary substrate. Additionally, in this chapter, the major details are also summarized on the wet transfer techniques employed to transfer graphene on silicon dioxide (SiO_2/Si) and auric. Experimental details on the upgrade of Chemical Vapor Deposition (CVD) equipment for the growth of MoS_2 are discussed in *Chapter 8*. This chapter also presents the results obtained through the advanced characterization of MoS_2. Final *Chapter 9* summarizes the major outcomes of the present PhD thesis work and also enlightens mastering of the synthesis and understanding of the properties of graphene and other 2D materials. Additionally, it describes the prospects for the graphene and 2D materials in the field of electronic and optical applications.

List of figures

List of tables

List of abbreviations

AFM	Atomic Force Microscopy
APCVD	Atmospheric Pressure Chemical Vapor Deposition
CNT	Carbon Nanotubes
CMOS	Complementary Metal-Oxide-Semiconductor
CVD	Chemical Vapor Deposition
dc	Direct Current
ac	Alternating Current
DI	De-ionized
E_a	Activation Energy
EBSD	Electron Backscattering Diffractometry
EDS	Energy Dispersive X-Ray Spectroscopy
FIB	Focused Ion Beam
FE	Ferroelectric
FET	Field Effect Transistor
FLG	Few Layer Graphene
FM	Ferromagnetic
FeRAMs	Ferroelectric Random-Access Memories
HOPG	Highly Oriented Pyrolytic Graphite
HR-TEM	High Resolution Transmission Electron Microscope
I	Light Intensity of a Raman spectrum
IC	Integrated Circuit
LEED	Low Energy Electron Diffraction
LEEM	Low Energy Electron Microscopy
LPCVD	Low Pressure Chemical Vapor Deposition

MLG	Multi-Layer Graphene
NTs	Nanotubes
PFM	Piezoresponse Force Microscopy
PMMA	(Poly methyl) methacrylate
PVD	Physical Vapor Deposition
SEM	Scanning Electron Microscopy
SPM	Scanning Probe Microscopy
STM	Scanning Tunneling Microscopy
TEM	Transmission Electron Microscopy
UHV	Ultra High Vacuum
XRD	X-Ray Diffraction
0D	Zero Dimensional
1D	One Dimensional
2D	Two Dimensional
3D	Three Dimensional

Chapter 1

Scientific motivation and rationale

1. Scientific motivation and rationale

It is more than a decade since the Nobel Prize winners Andre Geim and Konstantin Novoselov published the first series of their seminal papers, which triggered a sharp enhancement of the graphene research worldwide. Graphene has been the subject of many studies in the field of surface science due to its atomically flat carbon atoms with honeycomb lattice holding a wide range of promising applications. This is also due to its unique band structure and excellent electronic, optical, mechanical and thermal properties. For this research, the ultimate goal is to achieve the highest quality of graphene at the large scale with low cost having a precise control of layer thickness, stacking order and crystallinity. In order to achieve this goal, it is quite necessary to understand and to effectively control the growth procedure and other conditions required during the processing. Also, the cost-effective fabrication of graphene with high quality is undoubtedly crucial. It was reported in 2008, four years after its re-discovery, that the price of a microsized piece of graphene exceeds that of the same size of silicon wafer (Si wafer). The list of methods for the cost-effective production of graphene includes the graphitization of silicon carbide, chemical reduction of graphite oxide, liquid exfoliation etc. However, all these methods are not capable to solve the critical issues for graphene synthesis with controlled thickness, grain size, defects and doping. In fact, a synthesis route using Chemical Vapor Deposition (CVD) can provide a solution of this complex problem. Using CVD-based method it can be possible to synthesize graphene with controlled thickness, grain size, defects and doping. A typical CVD process mainly consists of four elementary steps, namely: (i) adsorption and catalytic decomposition of precursor gas, (ii) diffusion and dissolution of decomposed carbon species into the bulk, (iii) segregation of dissolved carbon atoms onto the metal surface, and, finally, (iv) surface nucleation and growth of graphene.

Back to the late 1960s, it was a breakthrough revealing that certain metals if treated at high temperature with hydrocarbon could produce ultrathin graphitic films on the surface. The list of various metals which can be used as catalysts in CVD for graphene growth includes nickel (Ni) [1-4], cobalt (Co) [4-6], copper (Cu) [7-10], ruthenium (Ru) [11, 12], iridium (Ir) [13], and palladium (Pd) [14]. Hitherto, the use of Ni and Co as catalytic substrates did not yield uniform monolayer graphene mainly due to the variation in their thickness (ranging from single to multilayers) and the difficulty in the control of carbon dissolved in Ni and Co films. The latter is due to high solubility of carbon and enhanced precipitation at the grain boundaries (0.6 wt% for

Ni and 0.9 wt% for Co at ~1300°C) [1-3]. On the contrary, Cu is an excellent candidate, which enabled researchers to grow single-layer high quality graphene with uniform thickness (95%), because of the low carbon solubility (0.001 - 0.008 wt% at 1080°C) [7-10].

Taking the above concept in mind, the present thesis aims at obtaining high quality graphene at large scale and low cost using Cu and Ni as catalytic substrates. We study the growth process using alumina based Hot Thermal CVD (HTCVD) and controlling the flow of precursor gases such as methane (CH_4) and hydrogen (H_2) in the tubular furnace at adequate vacuum. This method is expected to yield single-layer defect free graphene that may be subsequently used for various industrial applications.

It is quite important to tune the electronic properties of the pristine graphene, so that to use it in semiconductor applications, especially for the field effect transistors (FET). This tuning can be done in CVD process by molecular doping without degrading the transparency and electrical properties of graphene. The tuning leads to the alteration of graphene's Fermi level, which is important factor for the successful operation of the electronic devices such as diodes, field effect transistors, light emitting diodes, solar cells etc. From the experimental point of view, doping of graphene with nitrogen (*n*-doped graphene) can be made possible by controlling the adequate flow of precursor gases including ammonia (NH_3) during the deposition of graphene in alumina based HTCVD [15].

Although graphene demonstrates outstanding electrical properties, there are still limits in its direct application for low-power electronic devices such as transistors. To overcome this problem the research started refocusing on other graphene-like 2D materials, aiming to conquer the shortages of graphene and to broaden its range of applications. The desired materials should stand on the expectation of the researchers such as higher melting temperature (~1000 °C) and they should be both chemically inert and stable at room temperature. Graphite, hBN (hexagonal boron nitride) and molybdenum disulfide (MoS_2) are the best candidates in this competition. Due to its wide availability in nature as molybdenite, MoS_2 has been one of the most studied layered transition metal dichalcogenides (TMDCs). Monolayer MoS_2 is a semiconductor with a direct electronic bandgap of ~1.8 eV [16]. This outstanding property of MoS_2 is inspiring, probably overcoming the weakness of gapless graphene and thus making it possible to use 2D materials for the next generation of switching and optoelectronic devices.

For the synthesis of MoS_2 two vapor methods are currently used, namely, physical vapor deposition (PVD) and chemical method (CVD). Different versions of PVD, namely, thermal evaporation, molecular beam epitaxy (MBE), Van der Waals epitaxy (VDWE), pulsed laser deposition (PLD), electron beam evaporation (EBE), radio frequency sputtering (RFS) and direct current sputtering (DCS) are currently used for the growth of MoS_2. However, these techniques are relatively expensive, hence restricting their use. Also, it has been reported that by using PLD, EBE and RFS one can easily get other morphological structures (such as nano particles, nano rods, and nano tubes etc.) instead of desired layered structure [62-65]. In fact, CVD-based method has been the most common and desired technique for the synthesis of MoS_2, because herein regulating the temperature and the carrier gas flow can control the deposition parameters.

Given the above, this PhD work is focused on the MoS_2 growth in the quartz tube furnace, by using sulfur and MoO_3 powders as precursors in the upstream position relative to the gas flow direction under the pressure of 50 mbar. Notably, the stabilization of the furnace temperature and the flow rate of Ar gas can help in obtaining highly crystalline MoS_2 films. Thus, we show the CVD grown MoS_2 can be a promising material in the field of micro- and optoelectronics. In particular, applications of MoS_2 films are foreseen in such diverse areas as transistors [17], photodetectors [18], solar cells [19], etc.

The aim of this PhD work was to assemble, to parameterize and to use the CVD method for the synthesis and characterization of graphene and other 2D materials (MoS_2). This may help in realizing 2D electronic devices with high carrier mobilities and also to understand the behavior of these 2D materials upon small ion intercalation. In order to tune the electronic properties of graphene, this work was focused on assembling the CVD setup for the growth of high quality graphene and on *in-situ* heteroatom doping by ammonia (NH_3). In addition to this, the effect of the substrate thickness on defect creation was investigated. Furthermore, this research aimed at the synthesis of high quality TMDs materials (MoS_2) by modifying the current CVD equipment and parameterizing the growth conditions. By using Ultraviolet Photoemission Spectroscopy, we determined the structure of the valence band and work function (4.67 eV) of MoS_2 on SiO_2/Si substrates. *In-situ* electrical measurements confirmed the expected semiconducting behavior. A thorough review of the fundamental properties as well as the synthesis methods of 2D materials was one of the objectives of this PhD work.

Overall, the scientific results obtained in this work are supposed to contribute significantly to the mastering of the synthesis process and to understanding of the properties of graphene and

other 2D materials. This work may be also useful for the future applications of graphene in electronic and optical devices thus creating new perspectives for their further development.

Chapter 2

Fundamentals, Literature review and the *State-of-the-art*

Abstract

The purpose of this chapter is to provide the background of the PhD work. This chapter presents a thorough review on the *state-of-the-art* of graphene and other two-dimensional materials, especially molybdenum disulfide. It starts from the description of the electronic properties of graphene and its importance for both fundamental science and industrialization/commercialization. It also overviews major technical approaches employed for achieving graphene and overall qualities comparisons. Furthermore, this chapter also enlightens the role of defects (and problems associated with them), as well as intentional doping of graphene, including the methods of thereof. It also briefly introduces the two-dimensional materials other than graphene. Additionally, a short review on the *state-of-the-art* of molybdenum disulfide is given and its properties are compared with graphene in view of the increasing demands of such materials in nano-electronic world.

2. Introduction – fundamentals and *state-of-the-art*[*]

2.1. Why graphene and its benefits

Carbon is one the most important building block elements in the universe. It is an element that holds the fundamental role in the life on our planet. It is also the primitive block of virtually all organic chemistry having the highest sublimation temperatures among all elements ~ 3500 ^{o}C. A number of extraordinary properties makes it suitable material for a wide range of technological applications [20-23]. Therefore, the field of research on graphene as a single atomic layer of graphitic carbon, and on other two-dimensional materials has been enjoying extraordinary growth during the past decade. Carbon has four valence electrons, which can hybridize in many ways. This hybridization may be *sp*, sp^2 or sp^3 allowing carbon to form linear chains, planar sheets and tetrahedral structures (**Figure 2-1)**. As a result, carbon has intrigued and inspired physicists, chemists, biologists and, recently, medical scientists in their research. Its excellent charge-carrier mobility quickly grabbed the attention of the scientific community bringing a hope that one day it will compete with silicon to be a material of choice for the next generations for certain applications in the electronic industries. Furthermore, many extraordinary properties, such as its 2.3% optical absorption of the white light spectrum, high surface area, high Young's modulus, and excellent thermal conductivity, have all been reported. Because of these remarkable properties, applications using graphene in a wide range of areas, including high-speed electronic and optical devices, energy generation and storage, hybrid materials, chemical sensors, and even DNA sequencing, have all been explored. Beyond this, very recently, graphene based field-effect transistors (GFETs) were implemented showing exciting and bright prospects for sensing applications due to their much higher sensitivity and stronger selectivity [24-26]. GFETs play a role for the preparation of ultra-sensitive nanoelectronic biosensors because of their perfect characteristics, including high carrier mobility, strong and flexible structure, and so on. Seon Joo Park and co- workers [27] have been able to make an ultrasensitive and flexible FET olfactory system named "Bioelectronic nose". There are numerous examples in which graphene was used for biological applications, for example, as detectors of living cells and bacteria [28], as GFETs functionalized with Escherichia coli antibodies [29], and as FETs for the detection of malaria-infected red blood cells [30].

[*] The part of introduction has been submitted as Chapter in "Chemical Vapor Deposition (CVD): Technology and Applications", Editor – Kwang-Leong Choy, Publisher - CRC Press & Taylor & Francis Inc.

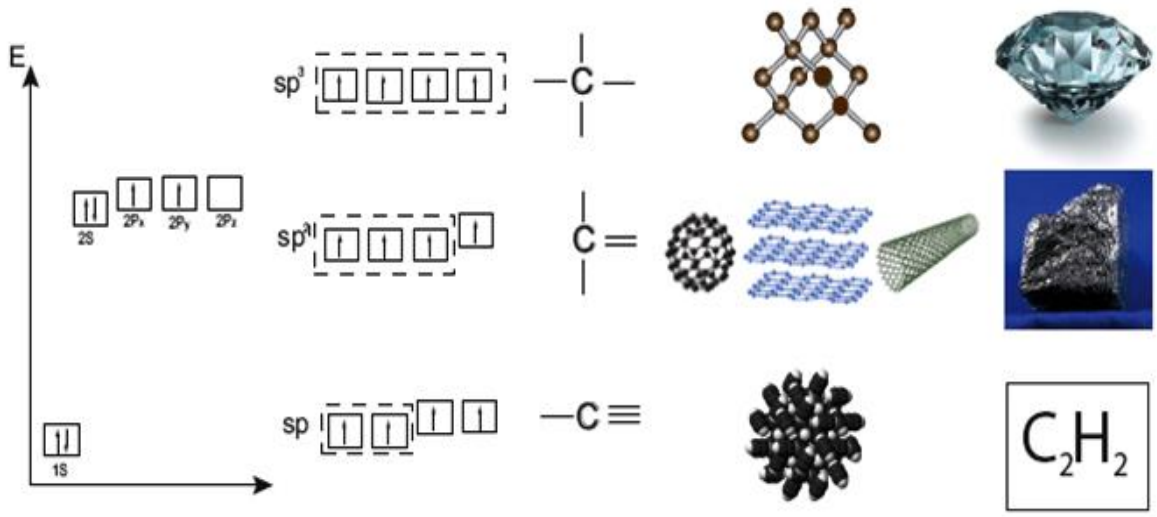

Figure 2-1: Examples: Possible carbon-carbon hybridization. The top shows the *sp³* hybridization with its atomic structure (diamond); the middle one presents the *sp²* hybridization and its atomic structures (C60, graphite, and carbon nanotube; the bottom one describes the *sp* hybridization and its atomic structure (acetylene-C_2H_2), respectively. Adapted from [31].

A variety of proof-of-concept devices has also been demonstrated. Materials science had a major scientific breakthrough in 2004, when Konstantin Novoselov and Andre Geim isolated the first single layer of two-dimensional (2D) material, graphene, through the Scotch tape exfoliation of graphite [32], and received Nobel Prize in 2010. However, the obtained samples were suitable only for the fundamental studies. Moreover, pristine graphene itself is unlikely to be used for the fabrication of logical circuits operated at room temperature with low standby power dissipation because graphene has no band gap. This results in a small current on/off ratio in graphene field-effect transistors. The prerequisite for such applications is the mass production of graphene in a controlled manner because the number of graphene layers as well as the defects in these significantly influence the resulting transport properties. In this direction, some other 2D materials like transition metal dichalcogenides (TMDCs) have also been tried to overcome these problems. Very recently such 2D lattices, such as silicene, and germanene (sp^2-hybridized equivalent of graphene) offered better compatibility with silicon processing and may provide solutions for some of the problems of graphene associated with the lack of an energy gap. Methods such as mechanical exfoliation, liquid-phase exfoliation, chemical vapor deposition, and

molecular beam epitaxy have been developed in order to fabricate single- and few layers of 2D lattices. Despite these efforts, the fine control of the number and structure of graphene and other 2D lattices over entire substrate remains a major challenge. More realistic samples from an industry point of view were obtained by CVD and related techniques on metallic substrates.

The story of graphene is quite old, in fact we were using it from long time when Petroski in 1564 invented pencil using graphite (which comprises stacked graphene) but we were not aware that we are making graphene in a simple way (by pressing pencil against a sheet of paper) [33]. Moreover, theoretically graphene has been studied sixty years ago, and was widely used for describing properties of various carbon-based nanostructured materials. After forty years, it was accidently re-discovered by Andre Geim and his colleague Konstantin Novoselov from HOPG (Highly Oriented Pyrolytic Graphite) with simple Scotch tape method by mechanical exfoliation [32]. For this achievement, the group was awarded with the Noble Prize in 2010. Up to now, the best quality graphene, in terms of structural integrity, has been obtained by this method, consequently only small graphene sheets (several micrometers in size) can be produced, and the number of exfoliated layers is not easily controlled. However, large area high-quality graphene with low number of structural defects is needed for the practical applications such as microelectronics (field effect transistors), optoelectronics (solar cells, touch screens, liquid crystal displays), biosensors, nanofluidics, graphene based batteries, super-capacitors, for various energy applications, etc. In this context, "bottom-up" synthesis route using chemical vapor deposition (CVD) holds promise for the large area graphene deposition.

2.2. Electronic structure of single layer graphene

Graphene is made out of carbon atoms arranged in hexagonal structure, as represented in **Figure 2-2**. The structure can be viewed as a triangular lattice with a basis of two atoms per unit cell. The lattice vectors can be written as

$$\boldsymbol{a_1} = \frac{a}{2}\left(\mathbf{3}, \sqrt{\mathbf{3}}\right), \boldsymbol{a_2} = \frac{a}{2}\left(\mathbf{3}, -\sqrt{\mathbf{3}}\right), \qquad \text{(Eq. 2-1)}$$

where a ≈ 1.42 Å is the carbon-carbon distance. The reciprocal-lattice vectors are given by:

$$\mathbf{b_1} = \frac{\mathbf{2\pi}}{\mathbf{3a}}\left(\mathbf{1}, \sqrt{\mathbf{3}}\right), \mathbf{b_2} = \frac{\mathbf{2\pi}}{\mathbf{3a}}\left(\mathbf{1}, -\sqrt{\mathbf{3}}\right) \qquad \text{(Eq. 2-2)}$$

In the physics of graphene, the two points K and *K´* at the corners of the graphene Brillouin zone (BZ) represented as Dirac points. Their positions in momentum space are given below:

$$\mathbf{K} = \left(\frac{2\pi}{3a}, \frac{2\pi}{3\sqrt{3}a}\right), \mathbf{K}' = \left(\frac{2\pi}{3a}, -\frac{2\pi}{3\sqrt{3}a}\right). \quad \text{(Eq. 2-3)}$$

The three nearest-neighbor vectors in real space are given by

$$\boldsymbol{\delta_1} = \frac{a}{2}(1, \sqrt{3})\ \boldsymbol{\delta_2} = \frac{a}{2}(1, -\sqrt{3})\ \boldsymbol{\delta_3} = -\boldsymbol{a}(1, 0), \quad \text{(Eq. 2-4)}$$

while the six second-nearest neighbors are located at $\delta'_1 = \pm a_1, \delta'_2 = \pm a_2, \delta'_3 = \pm(a_2 - a_1)$.

The tight-binding Hamiltonian for electrons in graphene considering that electrons can hop to both nearest and next nearest neighbor atom, has the form (we use units such that $\hbar$ = 1)

$$\boldsymbol{H} = -\boldsymbol{t}\sum_{(i,j),\sigma}\left(\boldsymbol{a}^{\dagger}_{\sigma,i}\boldsymbol{b}_{\sigma,j} + \mathbf{H}.\boldsymbol{c}\right) - \boldsymbol{t}'\sum_{\ll i,j\gg,\sigma}\left(\boldsymbol{a}^{\dagger}_{\sigma,i}\boldsymbol{a}_{\sigma,j} + \boldsymbol{b}^{\dagger}_{\sigma,i}\boldsymbol{b}_{\sigma,j} + \mathbf{H}.\boldsymbol{c}.\right), \quad \text{(Eq. 2-5)}$$

where $a_{i,\sigma}(a^{\dagger}_{i,\sigma})$ annihilates (creates) an electron with spin σ ($\sigma = \uparrow, \downarrow$) on site R_i on sublattice A (an equivalent definition is used for sublattice B), $t(\approx 2.8\text{eV})$ is the nearest-neighbor hopping energy difference between different sub lattices), and t' is the next nearest-neighbor hopping energy (hopping in the same lattice). The energy bands derived from this Hamiltonian have the form [34].

$$\boldsymbol{E}_{\pm}(\mathbf{k}) = \pm\boldsymbol{t}\sqrt{\mathbf{3} + \boldsymbol{f}(\mathbf{k})} - \boldsymbol{t}'\boldsymbol{f}(\mathbf{k}),$$

$$\boldsymbol{f}(\boldsymbol{k}) = \mathbf{2}\,\boldsymbol{cos}\left(\sqrt{3}\,\boldsymbol{k_y a}\right) + \mathbf{4}\,\boldsymbol{cos}\left(\frac{\sqrt{3}}{2}\boldsymbol{k_y a}\right)\boldsymbol{cos}\left(\frac{3}{2}\boldsymbol{k_x a}\right), \quad \text{(Eq. 2-6)}$$

where the plus sign applies to the upper (π^*) and the minus sign - to the lower (π) band. It is clear from Eq. 2-6 that the spectrum is symmetric around zero energy if $t' = 0$. For finite values of t', the electron-hole symmetry is broken and the π and π^* band become asymmetric.

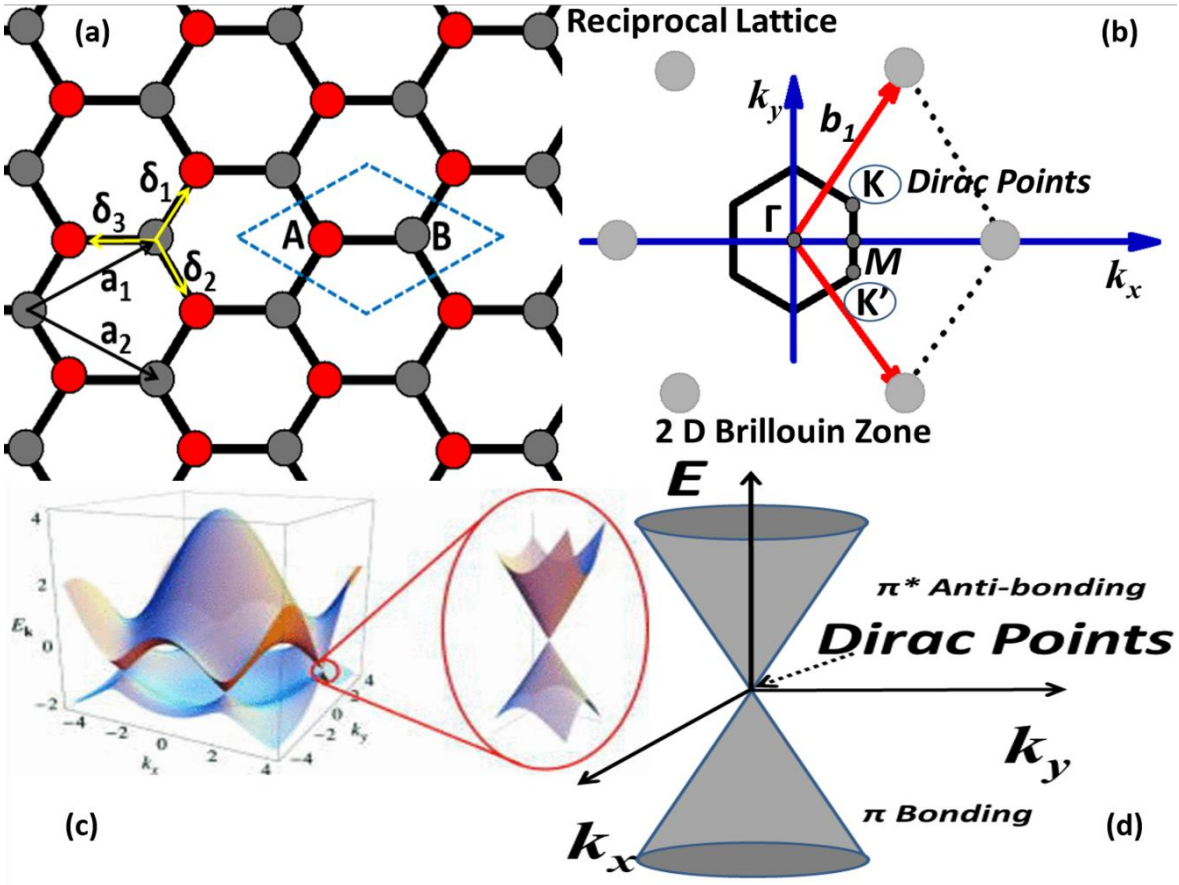

Figure 2-2: (a) Lattice structure of graphene honeycomb lattice, (b) its Brillouin zone, electronic dispersion in the honeycomb lattice, (c) energy spectrum (in units of t) for finite values of t and t' for t = 2.7 eV and t'= −0.2t with zoomed energy bands close to one of the Dirac points. Modified from [34]

Figure 2-2 shows the full band structure of graphene with both t and t'. This figure (**b**) also shows the zoom in of the band structure close to one of the Dirac points (at the K or K' point in the BZ) (**Figure 2-2**). This dispersion can be obtained by expanding the full band structure (Eq. 2-6) close to the K (or K') vector, Eq. 2-3 as k = K+q, with |q| ≪ |K| [34].

$$\boldsymbol{E_{\pm}(\mathbf{q}) \approx v_F|\mathbf{q}| + O[(q/K)^2],} \qquad \text{(Eq. 2-7)}$$

where q is the momentum measured relatively to the Dirac points and v_F is the Fermi velocity, given by $v_F = 3ta/2$, with a value $v_F \cong 1 \times 10^6$ m/s. This result was first obtained by P.R. Wallace [34].

2.3. Graphene synthesis and properties

Graphene exhibits remarkable electronic, mechanical, optical, and thermal properties as compared to those obtained in any other material justifying its nickname of a "miracle material". Many graphene characteristics measured in experiments have reached theoretically predicted limits such as: i) room-temperature electron mobility of 2.5 x 10^5 cm^2V^{-1} s^{-1} [35] (theoretical limit ~2 x 10^5 $cm^2V^{-1}s^{-1}$) [36]; Young's modulus of 1 TPa and intrinsic strength of 130 GPa [37] (very close to that predicted by theory [38]); very high thermal conductivity (above 3,000 W mK^{-1}; [39]); optical absorption of exactly $\pi\alpha \approx$ < 2.3% (in the infrared limit, where α is the fine structure constant) [40]; complete impermeability to any gases [41], ability to sustain extremely high densities of electric current (a million times higher than the copper) [42]. In addition, graphene can be readily chemically functionalized by various heteroatoms, and functional molecules for many "exotic" applications in the field of nanotechnology [43].

The above described superior properties have been achieved only with the highest quality samples (mechanically exfoliated graphene [44]) and for graphene deposited on special substrates like hexagonal boron nitride substrates. However, equivalent characteristics have not been yet achieved on graphene prepared by other techniques. There is a lot of research undergoing to master the conditions for the high-quality mass production of graphene for real state-of-the-art device applications at the industry level.

Currently, there are many methods used and developed to prepare graphene of various dimensions, shapes, and qualities. The list of those methods includes:

(i) Liquid phase exfoliation,
(ii) Synthesis on SiC,
(iii) Chemical vapor deposition

The above-mentioned production methods can be used for scalable production. However, graphene can also be grown under UHV conditions [45]. Literature also reveals the synthesis of graphene on different metallic single crystals like Pt(111), Ir(111) or Ru(0001).

Figure 2-3 shows Scanning Tunneling Microscopy (STM) images (a and b) and a LEED pattern (**Figure 2-3 (c)**) obtained after growing single layer graphene on Pt(111) under Ultra High Vacuum (UHV) conditions. STM reveals a rich variety of Moiré-like superstructures covering the whole surface while characteristic LEED pattern shows bright spots (red arrow in **Figure 2-3 (b)**) related

to the Pt(111) surface together with a low intensity ring that can be related to the graphene sheet. High resolution STM image of one of these Moiré like superstructures (**Figure 2-3 (b)**) shows the honey-comb pattern of the carbon atoms in the background while the aspect of the STM image is modulated by the Moiré. The red arrows indicate the vectors of the unit cell, which in the example presented here, are around 1.5 nm in length.

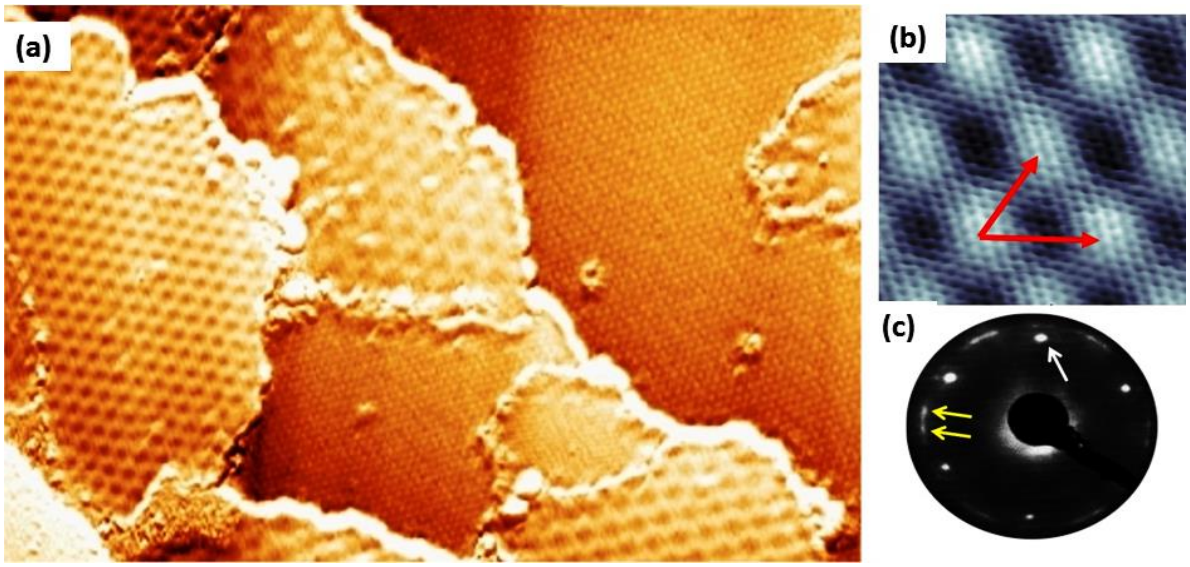

Figure 2-3: STM images (a, b) and LEED (c) pattern obtained after growing single layer graphene on Pt(111) under UHV conditions.

The analysis of the STM images combined with the one obtained by LEED indicates that the graphene sheet on Pt(111) is formed by small domains that follow different angular orientations with respect to the main crystallographic directions of the metallic surface. Thus, when the molecular precursors are introduced in the experimental facility, graphene starts growing in several points that are spatially separated. Then, as the coverage increases, the islands slowly grow covering the surface until the borders of neighbor domains get in contact. Interestingly, the intensity of the graphene ring detected by LEED is modulated as a function of the angle (see yellow arrows in **Figure 2-3 (c)**) rather than uniform. This modulated intensity indicates that the structural angular orientation of the graphene domains follows specifics angles with respect to the Pt(111) main crystallographic directions. A phenomenological model based on the strain of the graphene domains following different on-surface angular orientation, predicts up to 22 different possibilities [46].

Similar Moiré-like superstructures have been observed on other metallic substrates like Ru(0001) [47], Rh(111) [48] and Ir(111) [49]. Interestingly, the observed Moiré patterns depend strongly (in particular their orientation, corrugation and periodicity) on the particular substrate underneath. That indicates a non-negligible correlation between the metallic atoms of the last layer of the substrate and the graphene sheet. The XPS characterization of graphene shows that both the shapes of the carbon spectra and their binding energies strongly depend on the particular metallic substrate. The reference sample, HOPG, presents a sharp peak that can be fitted by only one peak centered at a binding energy of 284.23 eV and 0.35 of *FWHM*. Also, the spectra corresponding to graphene on Pt(111) and Ir(111) are very sharp and can be fitted by only one component. The BE and *FWHM* obtained for the first case are 283.97 eV and 0.34, while for the second case they are 284.16 eV and 0.4, respectively. On the other hand, the Rh(111) and Ru(0001) cases present several differences. The XPS spectra show that at least two components are necessary for fitting the peaks. The BEs obtained for Rh(111) case are 284.94 eV and 284.41 eV, while their respective *FWHM* are 0.56 and 0.46. In the Ru(0001) case values of 285.12 and 284.52 eV are obtained for the BEs and 0.61 and 0.48 for the *FWHM*, respectively. This splitting of the C 1s core level peak with respect to the HOPG sample indicates that the carbon atoms of the graphene sheets are under different chemical environments. Thus, in the last two cases, the modulation of the Moiré structures observed in the topographic STM images have a counterpart in the XPS, indicating an alternating sequence of high and low interaction between carbon atoms and the metallic substrate.

2.3.1. Graphene by liquid phase exfoliation

In order to develop the commercial applications from laboratory, it is quite necessary to have industrially scalable methods for the large area production of graphene. In this respect, liquid exfoliation technique is a promising method [50]. The basic principle is to make colloidal dispersions of graphite or graphite oxide powder in different solvents followed by sonication. There can be various categories depending upon the starting precursor and process involved such as the liquid-phase exfoliation from **graphite oxide**, **pristine graphite and expanded graphite (EG),** and **sonication-free liquid-phase exfoliation**.

2.3.1.1. *Graphene from liquid-phase exfoliation from graphite oxide via Hummers method*

Using graphite as a precursor, graphene oxide (GO) can be easily grown by exfoliation method with the help of sonication. This method is known as the Hummers method [51]. The GO contains carbon having sp^2 bonded structured with hydroxyl or carboxyl groups. These hydroxyl and carboxyl groups can make significant advantages for GO [52-54]. But, due to the oxidation process, GO gets defects which degrade its anticipated properties. In 2007 Stankovich *et al.* [53] used hydrazine as reducing agent at 100 °C for 24 h to obtain GO. Later, a few more reducing agents were introduced such as hydroquinone [55] and sodium borohydride ($NaBH_4$) [56]. It was Wang *et al.* who used hydrazine along with N, N-dimethlyformamide (DMF) at 180 °C as a reducing agent. This was quite effective as they were using solvothermal reduction process [57].

Later, it was reported that Fe (iron) can also be used as reducing agent for the formation of graphene oxide [58]. There can be numerous methods for obtaining graphene from graphite oxide but none of these can yield perfectly structured graphene. Also the oxygen-containing groups in GO are highly sustainable and it is very difficult to remove them [58].

2.3.1.2. *Graphene from liquid-phase exfoliation from pristine graphite oxide via sonication*

It was well known about the demerits of presence of oxides in graphene prepared from graphene oxide. So keeping this in mind in 2008 Hernandez *et al.* used a gentle method to produce high-quality graphene through dispersion and exfoliation of pristine graphite in certain organic solvents such as *N*-methyl-pyrrolidone (NMP), DMF, γ – butyrolactone (GBL), 1,3 – dimethyl-2-imidazolidinone followed by sonication for 30 min and centrifugation (500 rpm, 90 min) [59]. This result can yield the concentration of graphene dispersion in the solution for up to 0.01 mg mL^{-1}, and a few monolayers were also found. Among all the organic solvents NMP provides the best thermodynamic stabilization due to best matching of surface energy to that of graphite. This energy balance is expressed as the enthalpy of mixing per unit volume and is given by

$$\frac{\Delta H_{mix}}{V_{mix}} = \frac{2}{T_{flake}} (\delta_G - \delta_{sol})^2 \phi \quad , \qquad \text{(Eq. 2-8)}$$

where δ is the square root of the surface energy of graphite or solvents (the surface energy of graphite is defined as the energy per unit area minimum required to overcome the Van der Waals forces when peeling two sheets apart). T_{flakes} is the thickness of a graphene flake and ϕ is the volume fraction of the graphene. This matching is quite important criterion for successful exfoliation. The closer the graphene and solvent surface energies are, the smaller the enthalpy of mixing is, and the higher degree of exfoliation will be. Later Lotya *et al.* [60] used water and sodium dodecyl benzene sulfonate to exfoliate graphite with the help of sonication process. It is quite important to mention that the experiment resulted in more than 40% of the flakes thinner than 5 layers. The results from HR-TEM and Raman spectra confirm that 3% of flakes have defect free monolayer.

2.3.1.3. *Graphene from liquid-phase exfoliation from expanded graphite*

In this method, high temperature or microwave treatments have been employed to expand graphite for better liquid-phase exfoliation [61-63]. The heat treatment at high temperature followed by sonication makes liquid phase exfoliation easier with solutions.

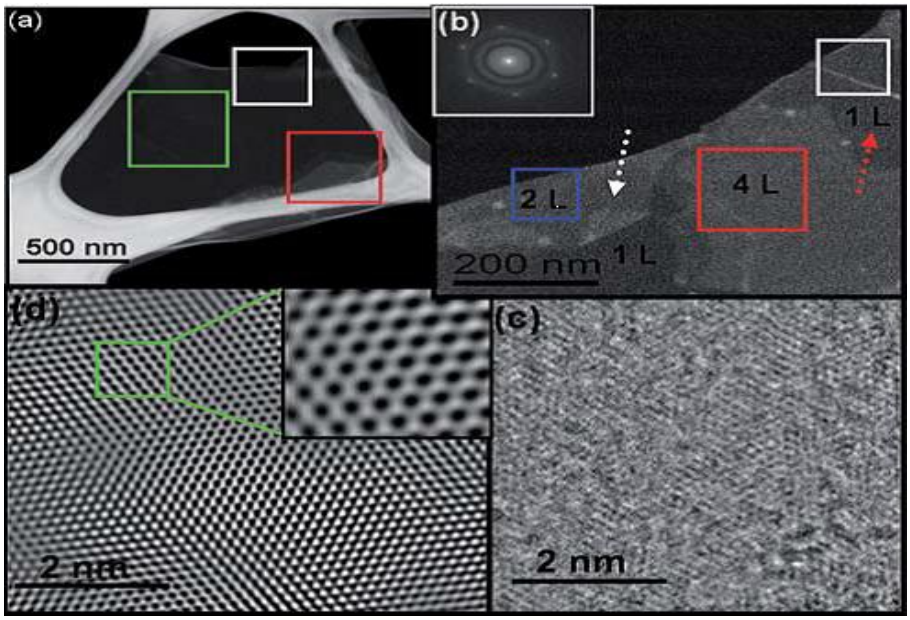

Figure 2-4: HR-TEM images of a freely suspended graphene membrane. (a) Bright-field TEM image of a suspended graphene membrane. (b) Magnified view of the region denoted by a green box in (a); the inset shows 2D FFT performed in the region indicated with a white box. (c) HR-TEM image of single-layer graphene acquired from the region indicated with a red dotted arrow in (b). (d) Reconstructed image after filtering in the frequency domain to remove unwanted noise, for clarity. The inset shows the hexagonal graphene network. Adapted from [64].

Using these technique Singh *et al*. [64] reported fabrication of single or FLG (few layer graphene, 2-6 layers) dispersed in DMF solution. Although the percentage of single-layer graphene was lower as compared to FLG, they were able to explain the rotational stacking faults with various rotation angles in 2, 3 and 6 layer graphene sheets (**Figure 2-4**).

In another work, Qian *et al.* [61] used expanded graphite as starting material and were able to achieve monolayer and bilayer graphene nanosheets (GNS) around 10 wt%. They produced them by a solvothermal-assisted exfoliation process in acetonitrile (ACN) (**Figure 2-5**).

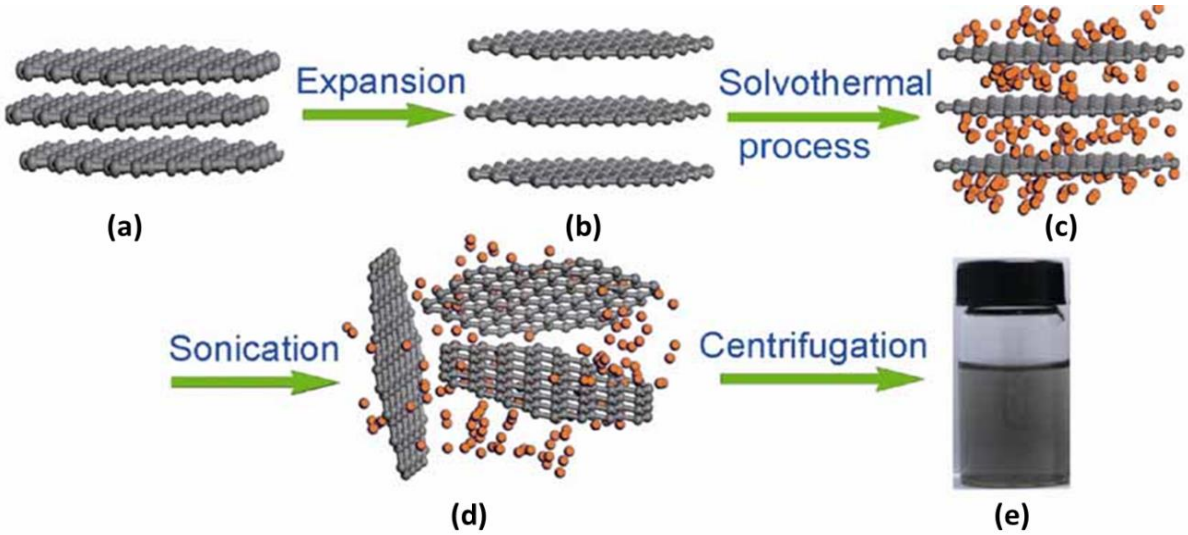

Figure 2-5: Schematic diagram of the solvothermal-assisted exfoliation and dispersion of graphene sheets in acetonitrile (ACN): (a) pristine expandable graphite; (b) Expanded Graphite (EG); (c) insertion of ACN molecules into the interlayers of EG; (d) exfoliated graphene sheets dispersed in ACN; (e) Optical images of samples obtained. Adapted from [61].

The authors made homogenous colloidal suspension of single or FLG sheets up to 0.15 mg mL^{-1} in N,N-dimethylformamide (DMF) solution. Their method included high temperature heat treatment (~2000 ^{o}C) of commercially available pyrolytic graphite powders in a vacuum (1.3 x 10^{-5} mbar) for 3h followed by probe-tip sonication for 2h of as obtained heat-treated graphite in DMF solution. The pyrolytic graphite has weakly bonded graphene layers by interlayer interaction forces along the c-axis, which can easily slide against each other and can also be peeled off. They gave quite informative knowledge about the introduction of Moiré pattern along with rotation stacking faults in AB Bernal stacked graphene bilayers, which changes the dispersion relationship close to the k-point from parabolic (AB) to linear band behavior (rotation disorder) and leads to some monolayer graphene properties being observed in two-layer and FLG films.

Another factor affecting the liquid-phase exfoliation is insolubility of graphite. To overcome this problem, chemical modification of graphite has been explored for facilitating their solubility and subsequent exfoliation. Keeping this in the mind, in 2010 Sun *et al.* [65] used *in-situ* diazonium reactions to bond 4-bromom-phenyl onto the surface of expanded graphite and followed by mild sonication in DMF. The method used higher solubility of exfoliated graphene as compared to pristine graphene, and also increased the chance of obtaining more than 70% of the soluble flakes with less than five layers.

2.3.1.4. *Graphene from sonication-free liquid-phase exfoliation*

In this technique of exfoliation, the powdered pure graphite is immersed in the atmosphere of super-critical CO_2 (carbon dioxide) for about 30 min and is immediately depressurized the supercritical fluid to expand and exfoliate graphite. Avoiding restacking, the graphene sheets were collected by discharging the expanding CO_2 gas directly into a solution with sodium dodecyl sulfate (SDS). This technique (see **Figure 2-6**) was demonstrated by Nen-Wen *et al.* in 2009 [66]. The authors used commercially powdered natural graphite (particle size of ~ 70 μm) with a purity of 99.99995% and a density of 2.25 g/cm^3.

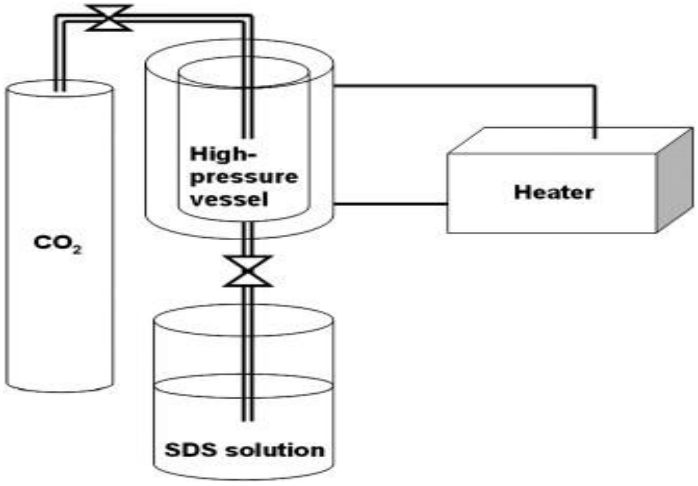

Figure 2-6: Schematic diagram of the supercritical CO_2 processing system used for exfoliation of powdered graphite. Adapted from [66].

Approximately, 1.0 g of graphite was placed in a high-pressure vessel with a heater and a temperature controller. CO_2 was then added into the vessel until the pressure reached 7.5 x 10^4

Torr. After that, heat was applied to the vessel so that the temperature of the vessel should maintain at 45 °C. The graphite was then immersed in the solution of sodium dodecyl sulfate (SDS) for 30 min. During the 30-min immersion in the supercritical fluid (SDS), the supercritical CO_2 diffused in between the layers of graphite due to its low viscosity, high diffusivity, and small molecule size. The described above technique was suitable for large-quantity production of graphene and the purity of the produced graphene was much better because this technique did not involve any steps that convert graphene into graphite oxide or introduce any functional groups, impurities, or coating agents. The yield of pure graphene sheets in this technique is as high as ~ 30 to 40 wt.% [66].

Graphene can also be self-exfoliated by induced strong repulsions between its interlayers. To this end, Behabtu *et al.* observed that graphite could be spontaneously exfoliated in single layer graphene if treated in chlorosulfonic acid and dissolved at isotropic concentrations (2.0 mg mL^{-1}) [67].

Although the liquid exfoliation can yield the mass production graphene using various techniques but, due to poor electrical properties (**Table 2-1**), it could not get more attention for industrial applications. The graphene oxide (GO) is mainly synthesized by the Brodie, Staudenmaier, or Hummers methods or by modification of these methods. Major steps in the methods are to be performed very carefully. This is because reactions such as potassium chlorate ($KClO_3$) with nitric acid (HNO_3) are quite dangerous. Notably, the methods used by Brodie and Staudenmaier, also the Hummer method, the treatment of potassium permanganate ($KMnO_4$) and sulfuric acids (H_2SO_4) is risky and health hazardous.

Table 2-1: Comparison of sheet resistances and optical transmittance between graphene and graphene oxide.

Graphene obtained	Resistance/Conductance	Transmittance Wavelength	Reference
Spin coating of reduced graphene oxide –SiO_2 composite	0.45 Ω/cm^{-2} (28nm thick)	95% (550 nm)	[68]
Spin coating of reduced graphene oxide	$10^2 – 10^3$ Ω/cm^{-2}	80% (550 nm)	[69]
Dip-coating of graphene oxide followed by reduction	550 Ω/cm^{-2} (10nm thick)	70.7% (1000 nm)	[70]
Spray coating of chemically modified graphene oxide suspension at pH 10	2×10^7 Ω/cm^{-2}	96% (600–1000 nm)	[71]
Vacuum filtration of graphene platelets made by sonication of graphite in n-methyl-2-pyrrolidone (NMP)	3×10^3 Ω/cm^{-2}	75% (550 nm)	[72]
Spray deposition of graphene platelets made by sonicating graphite in dimethylformammide (DMF)	5×10^3 Ω/cm^{-2}	90%	[73]
Spin assisted self-assembly of reduced graphene oxide	1.1×10^4 Ω/cm^{-2}	87% (550 nm)	[74]
Liquid-liquid assembly of graphene platelets	100 Ω/cm^{-2}	70% (500 nm)	[75]

2.3.2. Graphene by synthesis on silicon carbide (SiC)

Silicon carbide (SiC) is a semiconductor, which has high thermal conductivity and chemical stability, and is also able to operate at high temperature and in a high radiation environment. It is composed of silicon and carbon in an equal stoichiometric ratio, which has a wide bandgap (2.3-3.3 eV). Naturally developed SiC is very rarely found, either in some inclusions in minerals and diamond or in meteorites. SiC is very interesting material, which has wide spread applications, especially in high power devices, high temperature controllers and sensors, high voltage switching, and microwave components.

In 1975 Bommel *et al.* using UHV conditions ($<10^{-10}$ Torr) sublimed silicon atoms from silicon carbide (SiC (0001)) to form thin sheets of graphene [76]. This process allows to have low-defect

density graphene films deposited directly on the semi-conducting substrates [77-83]. In the year 1970, the basic principles of a modified seeded sublimation growth process, which was required for the growth of 6H-SiC were established by Tairov and Tzvetkov [84, 85]. This was the breakthrough in the growth of SiC and it was also known as Lely process. Later, using LEED and Auger electron spectroscopy, van Bommel *et al.* [86] were able to obtain monolayer flakes of carbon consistent with the structure of graphene. In fact, the first SiC was synthesized in 1824 by the Swedish scientist Jöns Jocab Berzelius. However, the process of SiC powder production was introduced in 1892 by E.G. Acheson [87] and the first SiC production on an industrial scale was started by Acheson in 1893 [88] which included the electrochemical reaction of sand and carbon at high temperatures (up to 2550 ^{o}C). SiC is a semiconductor material of group IV-IV with mainly covalent Si-C bonds (88% covalent and 12% ionic). The distance between the two neighboring silicon or carbon atoms is about 3.08 Å, while very strong sp^3 bond between carbon and silicon atoms is because of the very short distance between them, approximately 1.89 Å [89].

The growth of graphene (graphitization process) on SiC surfaces can be made in different growth arrangements such as vertical RF-heated furnace consisting of a quartz tube, porous graphite insulation and graphite crucible shown in **Figure 2-7 (a)**. In a standard procedure for obtaining high quality graphene on SiC substrate, the samples need to be heated at ~1680 ^{o}C in a controlled atmosphere [83]. The preparation method includes a first step of H-etching of the surface followed by an annealing at ~1680 ^{o}C in an atmosphere of 900 mbar of argon. The samples prepared by following this method normally exhibit very high quality single layer graphene terraces.

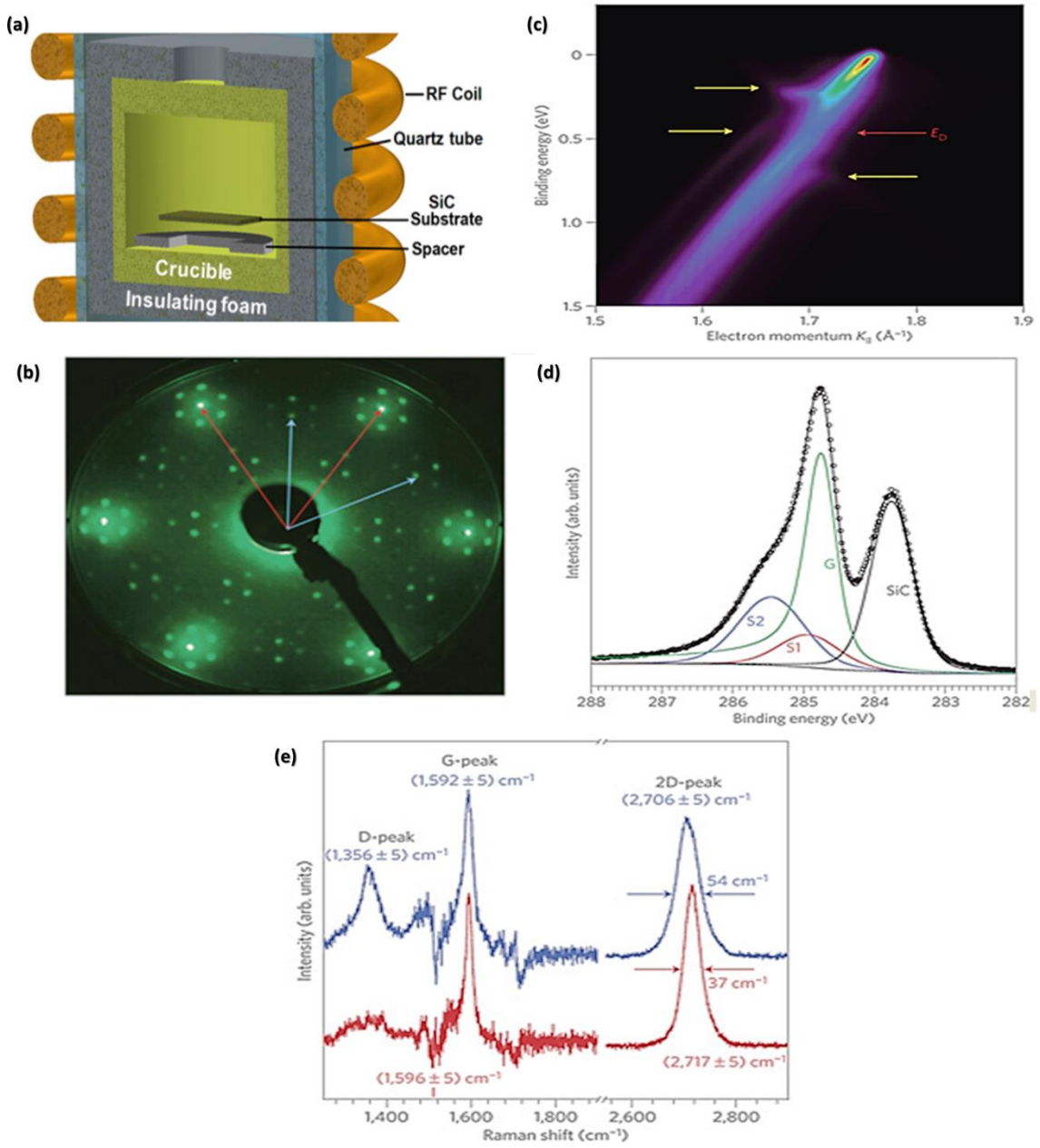

Figure 2-7: (a) Typical vertical RF-heated furnace in cross-section for graphitization of SiC [89], (b) LEED pattern at 74 eV having diffraction spots due to SiC(0001) substrate and graphene lattice, (c) XPS peak of C1s core-level spectrum measured at a photon energy of 700 eV (d) ARPES image of π bands in the vicinity of the K-point of the hexagonal Brillouin zone measured along the Γ K-direction, and (e) comparison of Raman spectra of Ar-grown (red) and UHV-grown (blue) epitaxial graphene on 6H–SiC(0001). Adapted from [83].

Figure 2-7 (b) shows a diffraction pattern performed by low-energy electron diffraction (LEED) technique. The diffraction patterns consisting of sharp spots show a high level of order in the graphene samples and also their orientation (blue arrows) with respect to the substrate main

crystallographic direction (red arrows). Thus, the basal plane unit vectors of graphene are rotated at 30° with respect to the SiC(0001) surface. In **Figure 2-7 (d)** the C 1s core level peak obtained by XPS shows a rich variety of components related to carbon atoms under different chemical environments. At lower binding energies, there is a component related to the carbon atoms of the SiC substrate (indicated as SiC in the **Figure 2-7**). Then, a main sharp peak dominates the spectrum and is related to the carbon atoms of the graphene sheet (indicated as G). And, finally, two components, indicated as **S1** and **S2** coming from the (6√3×6√3) R30° interface layer (buffer layer) of the sample. Interestingly, the electronic properties of the graphene sheet can be probed by angle resolved photoelectron spectra near the K point **(Figure 2-7 (c))**. It shows the characteristic band structure that corresponds to high quality single layer graphene sample [90]. The position of the Dirac energy (red arrow in **Figure 2-7 (c)**) at 0.45eV below the Fermi level indicates an electronic doping of the graphene sheet from the substrate. Finally, Raman spectra presented in **Figure 2-7 (e)** compare the quality of the graphene samples obtained by this methodology (red spectra) with respect to other techniques (blue). The characteristic *G* and *2D* lines are clearly observed. The narrowest width of the *2D* line of the red spectra together with the low intensity of the *D* peak indicate that the quality of the sample obtained by the above preparation procedure is better than that for other techniques. Importantly, the blue-shift (38 cm^{-1}) detected in the *2D* peak with respect to exfoliated graphene [91] is due to a compressive strain of graphene produced by the substrate underneath.

2.3.3. Graphene by chemical vapor deposition

The first report on CVD synthesis of graphene was published in 2006 by Somani *et al*. [92]. The growth and development of high quality and large area graphene on the catalytic metal substrates have been undertaken in the following years [11, 13, 93].

Produced so far large-scale graphene films were polycrystalline, and the research efforts were more focused to control the domain size, the number of graphene layers, the density of grain boundaries, the defects etc. Using CVD technique, one can easily produce graphene on polycrystalline metals with up to micrometer- to millimeter-size size domains. However, the graphene films grown on Ni foils do not yield uniform monolayer graphene; in most cases, it resembles a mixture of monolayer and a few layer graphene (polygraphene). On the other hand, it was experimentally proved that Cu is an excellent candidate for making large-area of single-

layer graphene with uniform thickness (95%). This could be due to the low solubility of C in the Cu. Previous results showed that graphene growth on Cu is somehow surface-mediated and self-limiting [7]. It is worth mentioning here that Cu-catalyzed CVD graphene growth, and the hexagonal lattice of Cu(111) favored the high quality of the as-grown graphene. Furthermore, during growth by CVD on Cu(111), the orientation of graphene nuclei became well controlled by the domain boundaries of Cu.

The Hummers' method – based production of graphene by graphite oxide (the most popular wet chemical method) involves the exfoliation mechanism of the oxidative intercalation and production of oxygen-containing functional groups on the graphene layers which disperse and stabilize GO sheet in the water [94]. The story of Hummers' method started in the 1859, when Brodie oxidized graphite in the presence of potassium chlorate and fuming nitric acid and beyond that it slowly evolved to the widely used Hummers' method that involves the combination of sodium nitrate, potassium permanganate and sulfuric acid [95]. Since then, efforts have been made to improve further the Hummers method by eliminating the use of sodium nitrate (which produces toxic nitrous gas) [96]. The production of GO is lagging behind due to GO's chemical inhomogeneity, batch-to-batch irreproducibility and inevitable creation of irreparable hole defects on the graphene sheets during the oxidation, which effects the conductivity of GO. However, Eigler *et al.* recently showed the production of GO with larger region of pristine network at low temperature oxidation [97].

The use of SiC and involvement of thermal decompositions can make the large-scale production of graphene possible. When SiC substrates are annealed at high temperatures, Si atoms selectively desorb from the surface and C atoms left behind naturally form FLG. Because SiC is a wide-band-gap semiconductor, FLG on SiC can serve as a graphene substrate for electronics applications. However, two fundamental problems must be solved before the thermal decomposition method can be used at a wide scale. Firstly, the FLG obtained does not meet the uniform thickness requirement, because the electronic properties of FLG strongly depend on its thickness. Secondly, the mechanism behind the factors affecting the physical properties of FLG's are not fully understood.

Notably, the industrialization of graphene production mainly depends on a number of factors including the production cost, scalability, reproducibility, processability and the performance of the graphene products. No doubts, available promising methods of production using CVD, GO, and SiC, each have their own advantages and limitations. In the case of GO (using Hummers'

method), graphene (or GO) can be obtained with the advantage of high yield and high dispersibility. However, this method has a major drawback of using potentially explosive process and structural inhomogeneity. The SiC method could be a good candidate for commercialization at wide scale for future applications; however, it may lose its importance due to the problem discussed above. Finally, graphene grown by CVD technique is acquiring the potential interest of the research community and significant R&D efforts are focusing on this field due to the low-cost production and easy processability in this method. Additionally, the CVD graphene performance is very good and the technique can be easily scaled up by semiconductor industry.

2.4. Defects in graphene

Doping of graphene-related systems has attracted a lot of research activity during the past few years. In fact, the concept of the doping of carbon materials is not new. The first reported doping of carbon-based materials was done in carbon nanotubes using poly(ethyleneimine) (PEI) – an electron-donating polymer. Similar concept was adopted to dope graphene, which results in n-type behavior [98, 99]. It was observed that the concentration of holes and electrons was imbalanced, which enhanced the electron conduction and the reduced the hole conduction. Similar phenomena were observed when graphene is used as electrode beneath the metal electrodes like the diazonium salts.

Doping of graphene can be done in two distinct ways: (i) electrically, by changing gate voltage (known as surface transfer doping) and (ii) chemically, by introducing the dopants (known as substitutional doping) in a honeycomb structure, which shift the Dirac point relative to the Fermi level. The involvement of foreign atoms such as nitrogen, boron etc. would disturb the sp2 hybridization of carbon atoms, and can, in turn, cause both *n*- or *p*-type doping.

P-type doping drives the Dirac points of graphene above the Fermi level, and *n*-type doping drives the Dirac points below the Fermi level. By adding atoms with fewer valence electrons than carbon like boron etc. one can achieve *p*-type doping while *n*-type doping is generally obtained by adding atoms with more valence electrons than carbon, e.g. nitrogen. Normally, the Dirac point of the pristine undoped graphene is at the zero; whereas, it becomes *n* type if the same shifts up. However, if it goes down, it is converted to *p* type. As a result, if the band gap opens, graphene-based transistors will have higher on/off ratio [100].

There are various methods that can be successfully applied to dope graphene in both *n* and *p* types. Literature shows that ammonia is the most suitable for incorporating free electrons, which turns graphene into the *n* type [101, 102]; whereas, boron is responsible for *p* type doping [103]. Given above, researchers are more interested to dope graphene for *n* type behavior as compared to *p* type.

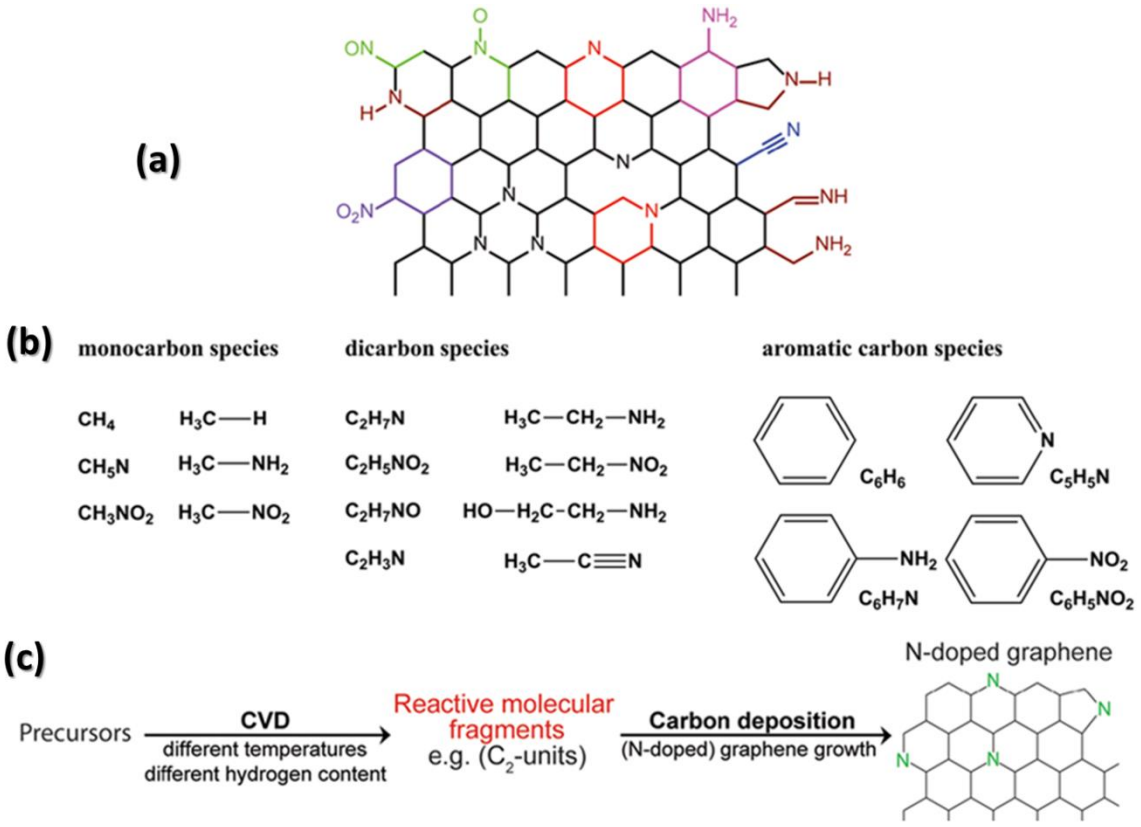

Figure 2-8: (a) Possible nitrogen (N) configuration in *n*-doped graphene. (b) CVD precursors with different functional groups as used in by Ito *et al.* (namely methane, methylamine, ethylamine, ethanol amine, nitromethane, nitroethane, acetonitrile, pyridine, aniline, nitrobenzene, (c) Schematic formation of nitrogen-containing graphene by CVD, Adapted from [104].

It is interesting to mention that Arun *et al*. used p-toluenesulfonic acid (PTSA) for converting pristine graphene into *n* type graphene [65]. These authors first deposited CVD manufactured graphene on Si/SiO_2 using PMMA coating for reducing the breakage and creation of defects. Afterwards they soaked the as transferred graphene into PTSA solution (0.1 M) for the certain period of time. Upon drying, the graphene changed its behavior and they were successfully able to convert it into *n* type. In another work, Ito *et al.* [104] explained the role of precursors and the gas phase in carbon films, especially in graphene. Using numerous precursors, namely, methane,

methylamine, nitro-methane, ethylamine, ethanolamine, nitro-ethane, acetonitrile, benzene, pyride, aniline and nitrobenzene, the authors studied the effect of doping and observed interesting results by Raman spectroscopy (*D*, *G*, *D'*, *2D*, I_D/I_G, $I_{D'}/I_G$ and $I_{2D}/I_{D'}$).

Figure 2-8 shows the schematic overview of the possible nitrogen functional present in *n* doped graphene. It also shows the study of different aliphatic nitrogen compounds, namely, methylamine, ethylamine, ethanol amine, nitromethane, nitroethane, acetonitrile, pyridine, aniline, nitrobenzene, and benzene [104].

As mentioned also above, graphene is a two-dimensional material with large surface area and ultra-high conductivity, which changes rapidly when external molecules (gas/other chemicals) adsorb on the surface. Hence, graphene has become an excellent candidate for sensors with high sensitivity that can detect even individual molecules [105]. Literature shows that, , graphene as a sensor can be used to detect bacteria [28], glucose [106], pH and proteins [107, 108]. Furthermore, GO can be also be used for the detection for DNA [109, 110] and for DNA sequencing [111-116].

2.5. Beyond graphene, other two-dimensional (2D) materials

During recent years researchers started looking for other materials, which can show unusual physical phenomena that occur when charge and heat transport is confined to a plane. Many novel materials that were initially only considered to exist theoretically are now being synthesized. Extensive research is now focused on elements from the groups IV and II-VI of periodic table. Semiconductor analogues of graphene/graphane (the sp^2/H-terminated sp^3 derivatives) such as silicone [117-120] and germanane [121] are now attracting researchers. These materials are quite similar to graphene and, hence, typically show different properties as single layer as compared to the bulk. Besides this, there are over 30 different layered metal chalcogenides (LMDCs), which are now being investigated for their interesting properties [122-124]. Other than this, some Van der Waals solids that have been exfoliated into single layers are intensively studied. These include hexagonal boron nitride [125], vanadium oxide derivatives, and other chalcogenides such as Bi_2Te_3, Sb_2Te_3, and *β*-FeSe [126, 127].

The transition metal chalcogenides have become the subject of extensive studies over the years. For example, in the late fifties McTaggart *et al.* conducted a thorough review on the synthesis, structure and properties of the group IV chalcogenides [128-130]; whereas, Wilson *et al.* have investigated dichalcogenides across the *d*-block metals [131, 132]. Intensive research done in the sixties and seventies covered much of the initial structural aspects [133, 134]. In fact, the outcomes of these works helped to lay the set of the foundations for many future investigations.

Structurally, the transition metal dichalcogenides can be divided into two categories, namely:

1. Layered type structures and,
2. Non-layered type structures

Layered type structures: Layered type structures are exemplified by the dichalcogenides of the early transition metals (typically groups IV-VI) and consist of covalently bonded (X-MX) sheets. These sheets propagate along the c-axis and are weakly bound to each other by Van der Waals interactions. The metals can have either trigonal prismatic or octahedral coordination depending on the system, i.e. MoS_2 or NbS_2 contain T-S trigonal prisms, whereas HfS_2 and ZrS_2 contain octahedral species.

Non-layered structures: Examples of non-layered MX_2 compounds emerge from the group VII and onwards. They can be categorized into four different sub-groups: pyrites, marcasites, $IrSe_2$, and PdS_2 type structures [131]. Their structures differ from the layered structures, since they are essentially 3D in nature (with no Van der Waals gaps) and contain complex anions which show strong chalcogen to chalcogen bonds (X_2^{2-} pairs) [135]. Non-layered structures crystallize in a similar fashion as fcc lattice of NaCl rock salt, the structure where the positions of Na^+ and Cl^- are substituted by the transition metal and X_2^{2-} pairs (**Figure 2-9)** [136]. These non-layered type structured materials are of particular interest for their range of semiconducting and metallic behavior coupled with a variety of magnetic properties [137]. For example, iron disulfide, which has a narrow band gap of 0.95 eV, is extensively used in photochemical and photovoltaic solar cells and as a cathode material for lithium batteries [138]. Another example is cobalt disulfide, which has a higher electronic conductivity and thermal stability when compared to other metal sulfides (such as FeS_2) and has been investigated for its application in secondary lithium-ion batteries [139].

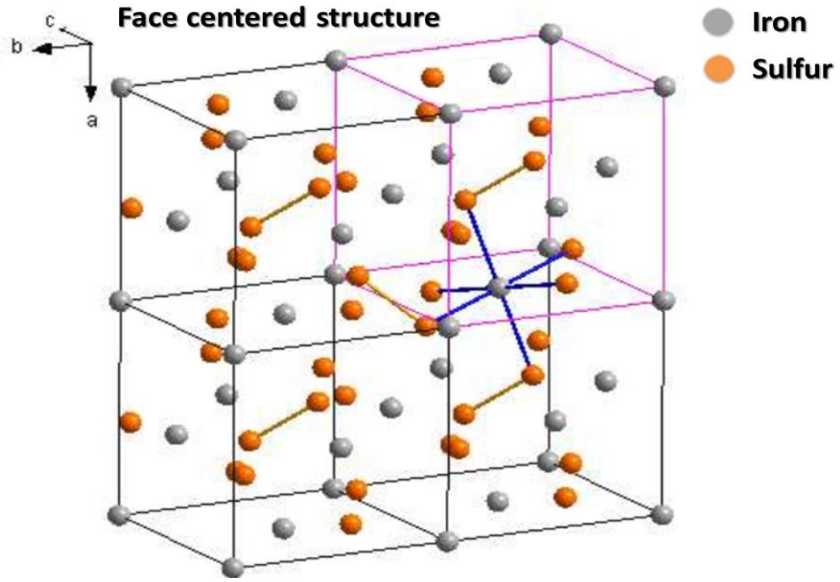

Figure 2-9: Face centered structure showing cubic pyrite structure; example of rock salt showing the metal atoms in a distorted octahedral coordination to X_2^{2-}, share common corners. In figure, iron atoms are shown in grey spheres, sulfur in orange spheres. Sulfur to sulfur bonds are represented in gold and iron to sulfur bonds in blue, Adapted from [140].

For the purposes of this research only layered structured especially MoS_2 will be discussed in the following section.

2.5.1. MoS_2: an introduction

As mentioned also earlier, transition metal dichalcogenides (MX_2, M = transition metal, X = chalcogenide) can be characterized by two basic structural categories, namely: layered and non-layered. Numerous possible atomic arrangements can be possible as a result of the covalent character of the M-X bond and the polarizability of the anionic chalcogen. In standard single layer of MoS_2, Mo ($^{+4}$) and S ($^{-2}$) are arranged as a sandwich by covalent bonds in the sequence of S-Mo-S, in such a way that Mo and S occupy alternate positions in the hexagonal corners to give a honey comb-like structure (**Figure 2-10**). Six neighboring S atoms surround each Mo in trigonal prismatic arrangement. Each S atom forms a pyramidal center since it has three neighboring Mo atoms. Additionally, the bulk MoS_2 unit cell consist of two MoS_2 layers, which are displaced in such an arrangement that each Mo atom in one layer is on the top of the S atom from the two adjacent layers.

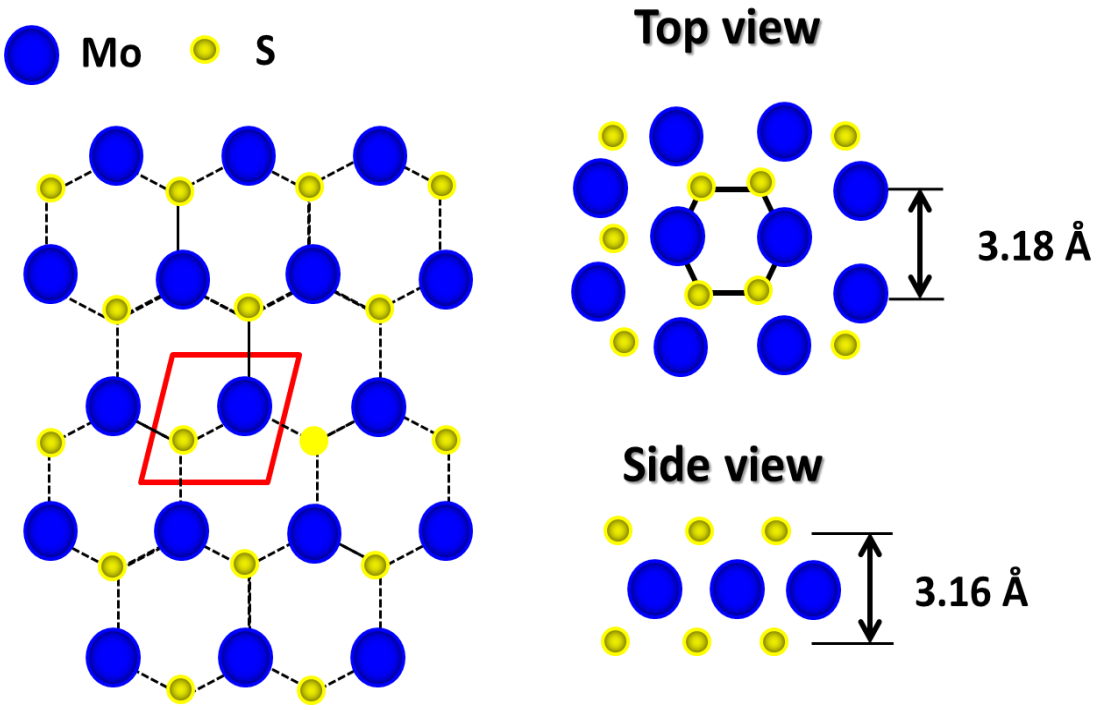

Figure 2-10: Honeycomb like lattice structure of MoS_2 showing the top and side view. The blue spheres present Mo and yellow spheres show sulfur (S). The distance between Mo-Mo and S-S is 3.18 Å and 3.16 Å, respectively.

The electronic structure of Mo and S atoms are [Kr]$4d^5$, $5s^1$ and [Ne]$3s^2$, $3p^4$, respectively; with *d* state mainly responsible for its unique properties. It is worthy to mention here that Density

Function Theory (DFT) calculations show that the band structure tends to change with a decrease in the number of MoS_2 layers [141] because of the hybridization between *p* states of *s* and *d* states of Mo along with quantum confinement. For better comparison, the properties of MoS_2 compound are listed below in **Table 2-2**.

Table 2-2: Major critical and fundamental properties of MoS_2.

Physical Properties		References
Lattice constants (Å)	*a = ~ 3.160*	[142]
	c = ~ 6.147	
	c/a = ~ 1.945	
Interlayer height (Å)	*M – S = ~ 4 3.19*	
van der Waals gaps (Å)	*S – S = ~ 3.47*	
Band gap energy (eV)	*Bulk = ~ 1.29*	[143]
	Monolayer = ~ 1.89	
Raman active modes	A_{1g} *= ~ 409* cm^{-1}	[142, 144]
	E^1_{2g} *= ~ 383* cm^{-1}	
	E_{1g} *= ~ 287* cm^{-1}	
Monolayer relaxed ion piezoelectric coefficient (pmV^{-1})	d_{11} *= ~ 3.73*	
Thermal conductivity ($Wm^{-1}K^{-1}$)	*k = ~ 18.06*	

MoS_2 has become an emerging and exciting material system for future nanoelectronics due to its unique electronic properties and atomically thin configuration [17, 122, 145-150]. In the past, graphene was explored for ultrahigh-speed transistors with the intrinsic cut-off frequency exceeding 400 GHz [151]. However, it was not successful because of its insufficient current on–off ratio and little voltage gain due to its zero-band gap. On the other hand, MoS_2 is attracting more interest and attention, since these disadvantages of graphene can be overcome by MoS_2 and it

has been possible to fabricate atomically thin transistors with high on–off ratio and intrinsic voltage gain [152-159]. It also possesses high mechanical flexibility and partial optical transparency [17, 145]. Moreover, as applied for 2D electronics based on single- or few-layer materials, MoS_2 represents the ultimate limit of thickness for pushing the limits of the Moore's law. Since it has a larger band gap comparable to silicon and being atomically flat, MoS_2 is also advantageous for suppressing the source-to-drain tunneling current in ultrashort transistors at the scaling limit and offers superior immunity to short-channel effects [160].

The most common methods applied for obtaining single- and few-layer-thick 2D materials are mechanical exfoliation of large crystals using "Scotch tape" and chemical exfoliation by dispersing in a solvent of appropriate surface tension and molecule/atom intercalation in order to exfoliate these layers. Since 1960s, these mechanical and chemical exfoliation processes were used to prepare and study the properties of a few layer Van der Waals materials, such as MoS_2 and $NbSe_2$ [161-163]. Because of their less destructive than the other methods nature the technique has been successfully used to create large (up to 10 μm single-layer flakes) on a variety of substrates. Peeling out of individual and a few layers using mechanical exfoliation remains the most powerful approach for studying their properties. However, in order to have much larger samples, chemical vapor deposition techniques are preferred and are now being implemented worldwide.

Chapter 3:

Experimental Section

Abstract

This chapter describes the experimental strategy followed to fulfil the defined objectives of this thesis. A brief introduction of all the techniques followed by the characterization of the samples is given. The description on the Raman spectroscopy, and HR-XPS is followed by the details on HR-TEM, Scanning Electron Microscopy (SEM), Atomic Force Microscopy (AFM), Piezo Force Microscope (PFM) and X-Ray diffraction. Additionally, this chapter includes the description of the synthesis equipment (Chemical Vapor Deposition, CVD), used for the growth of graphene and molybdenum disulfide in this study. Major components and layout diagrams for the assembling and parameterizing of CVD are detailed.

3. Experimental details

3.1. Characterization techniques used

3.1.1. Raman spectroscopy and micro Raman mapping

Raman spectroscopy was discovered by Indian scientist C.V Raman who was awarded the Nobel Prize in physics in 1930. Raman spectroscopy, known also as vibrational spectroscopy, is used to study various modes such as vibration, rotation etc. in the system by means of inelastic light scattering. Laser light is used as a source for Raman spectroscopy in visible, infrared and near ultraviolet ranges. Laser light interacts with the phonons from the sample and results in the shift of energy. These shifts in energy give the useful information about the electronic environment of the molecules [164].

The working principle of Raman spectroscopy is based on the inelastic scattering of light when it interacts with the molecules. When a monochromatic light from the source interacts with the molecules or bonds inside the sample it gives rise to different scattering phenomena, namely Rayleigh, Stokes Raman and anti-Stokes Raman scattering. During this interaction, the photon excites the molecules from the ground state to the virtual energy states **(Figure 3-1)**, where they stay for some time and return to the ground state in different or same vibration levels after emitting the photon. The molecule, if excited from first vibrational level, returns back to the same vibrational level then it is known as Rayleigh scattering or elastic scattering (no change in frequency of photons) (Figure 3-6). If the molecule returns to different vibrational level, the difference between the original state and the new state leads to a shift in the emitted photon's frequency, away from the excitation wavelength. When the photon frequency is shifted towards lower wavelength then it is known as Stokes scattering, otherwise it is known as anti-Stokes scattering. Energy of scattered phonons is discrete for every bounding and electronic environment; therefore, it shows typical frequency for all Raman active molecules [165].

Raman spectroscopy gives very valuable information, which is useful for chemical identification, characterization of molecular structures, effects of bonding, environment and stress on a sample. Due to the highlighted features, Raman spectroscopy is widely used for carbon-based materials, polymers, oxide films, ceramics, semiconductors, etc.

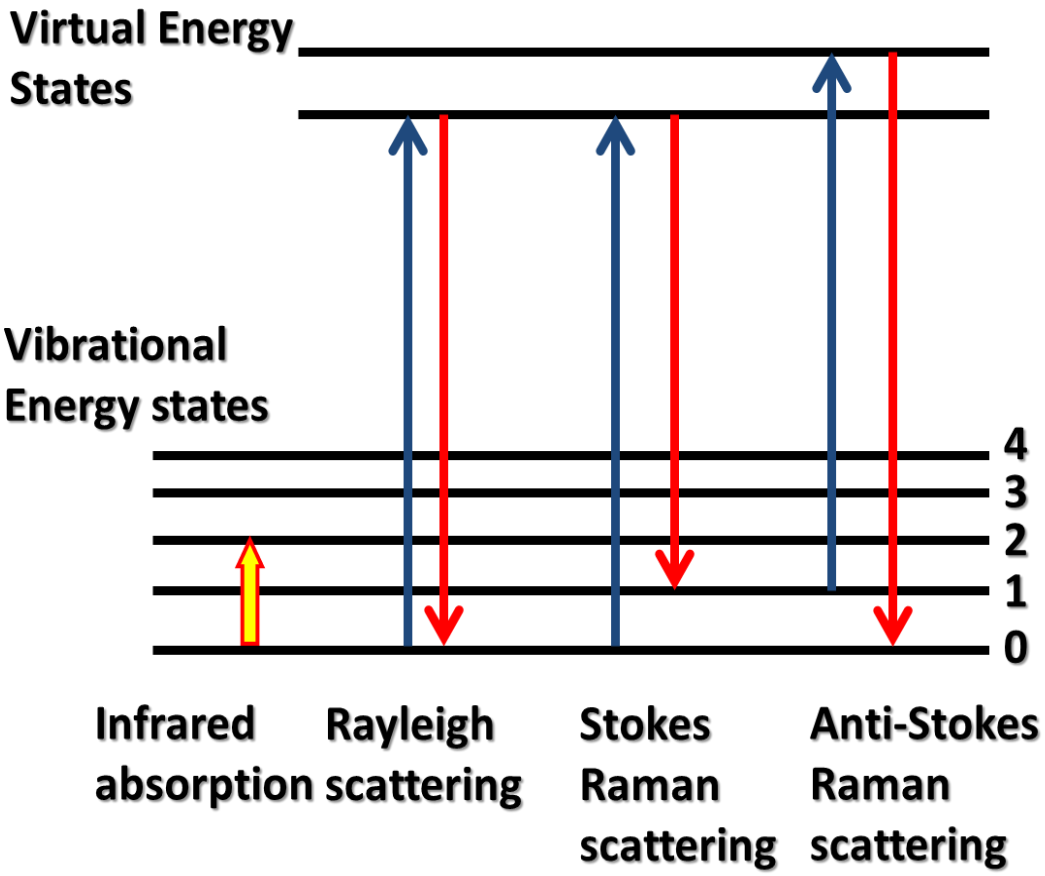

Figure 3-1: Schematic representation of the energy transfer model in Rayleigh scattering, Stokes Raman and Anti-Stokes Raman scattering, Adapted from [164].

Raman spectroscopy is the most important and best fingerprint technique extensively used for the property analysis of carbon related materials including graphene [166]. This technique allows distinguishing among single layer, a few layers graphene and graphite. It is also sensitive to defects, excess charge, strain and atomic arrangement of the edges. The spectra consist of 2 main peaks, namely *G* and *2D*, at around 1580 and 2680 cm^{-1}, respectively, when taken at an excitation energy of 2.4 eV (514 nm) [91]. *G* and *2D* peaks always satisfy the Raman selection rule and this makes Raman spectroscopy one the most important tools for probing the structural defects. *G* peak relates to E_{2g} phonon at the Brillouin zone center (Γ point) [166]. On the other hand *2D* peak is an overtone peak which is associated with the breathing modes of the six-atom rings [91]. Also it comes from the TO phonons in the vicinity of the K point and it is activated by a resonant intervalley scattering process [167, 168]. Besides these two peaks, we are able to find two more peaks at around 1350 and 1620 cm^{-1} named as *D* and *D'* and they are due to single phonon

intervalley and intravalley scattering events, respectively. Sometimes, *D* peak is also known as a defect peak and provides the missing momentum in order to satisfy the momentum conservation rule during Raman scattering process [167-169]. However, in some spectra we are able to find small defect-activated (weak) peak at around 3000 cm^{-1} which corresponds to the combination mode of the *D* and *D'* peaks, and is sometime referred as *D+D'* peak.

Raman mapping or Raman spectral mapping is a method for generating detailed chemical images based on a sample's Raman spectrum. A complete spectrum is acquired at each and every pixel of the image, and then interrogated to generate false color images based on material composition and structure. In this method, the laser is point – focused, and the sample is translated relative to the laser focus, or the focus is raster scanned across the object. Motor-driven x–y stages (by piezoelectric translators) are the most commonly used devices for translating the object. Stages available for Raman microscopes can be positioned with an accuracy better than ±1 μm and can be stepped in 0.1μm increments. Therefore, Raman spectral imaging is an invaluable technique for scientists in various fields, since it allows chemical distribution to be viewed which is invisible by standard optical microscopy.

Raman spectroscopy measurements were performed with a combined Raman-AFM-SNOM confocal microscope WITec alpha300 RAS+. A He:Ne laser operating at 633 nm and a Nd:YAG laser operating at 532 nm were used as excitation sources. The objective used was from 10x to 100x for better laser spot area $\sim$ 350 nm. The power of laser was changed variably from 0.5 to 5 mW so that not to damage/heat the sample. The spectral resolution was $\simeq$ 3 nm^{-1} along with the piezoelectric stage that allowed Raman mapping of the area $\sim$ 200 x 200 μm^2. Raman imaging experiments involved raster-scanning the laser beam over the samples and accumulating the full Raman spectra at each pixel. Raman images were constructed by integrating over specific Raman bands using WITec software for data evaluation and processing. **Figure 3-2** shows the confocal microscope WITec alpha300 RAS+ used for Raman-AFM-SNOM [170].

Figure 3-2: Confocal Microscope WITec alpha300 RAS+ for Raman-AFM-SNOM, Adapted from [170].

3.1.2. X-Ray Photoemission Spectroscopy

The photoemission spectroscopy is based on the photoelectric effect in which a free electron is extracted from an atom after absorbing a photon. Heinrich Hertz first observed this effect in the year 1887. Later, Albert Einstein provided full details on the photoelectric effect in 1905, and was awarded the Nobel Prize in Physics [171].

The effect can be described as follows: one bound electron absorbs a high – energy photon, normally X-ray or ultraviolet, turning into a free electron of kinetic energy (E_K) (**Figure 3-3)**. The binding energy (E_B), the photon energy ($h\nu$) and the work function (∅) obey the relation:

$$\boldsymbol{E_K = h\nu - E_B - \emptyset} \quad . \qquad \text{(Eq. 3-1)}$$

Knowing the energy of the impinging photon and measuring the kinetic energy of the resulting free electron, we can extract the energy of the former bound electron. For measuring the kinetic energy of the free electrons, we normally use an experimental set up consisting of a cylindrical electron analyzer for energy filtering and an electron multiplier like a channeltron or a

channelplate as a collector. The laboratory standard X-Ray guns normally have a double anode of Mg $(K_\alpha, hv = 1253.6\, eV)$ and Al $(K_\alpha, hv = 1486.6\, eV)$ and the usual UV illumination is a He lamp whose principal lines and He I $hv = 21.2\, eV$ and He II $hv = 40.8\, eV$. Synchrotron radiation can also be used as an illumination source; its main advantages are higher photon flux and better monochromacy, which both increase the energy resolution up to a tenth of meV for XPS and a few meV for UPS. Another big advantage is that we can tune the energy of the arriving photons in a continuous range and thus set photon energy that maximizes the photoexcited electrons of the element under analysis.

Depending on the energy of the illuminating photon, we can excite different bound electrons giving rise to different photoemission spectroscopies. Thus, if we use X-rays, the electrons that are mainly excited due to the core level electrons (XPS) while if we use ultraviolet electrons we will excite the valence band electrons (UPS) [172].

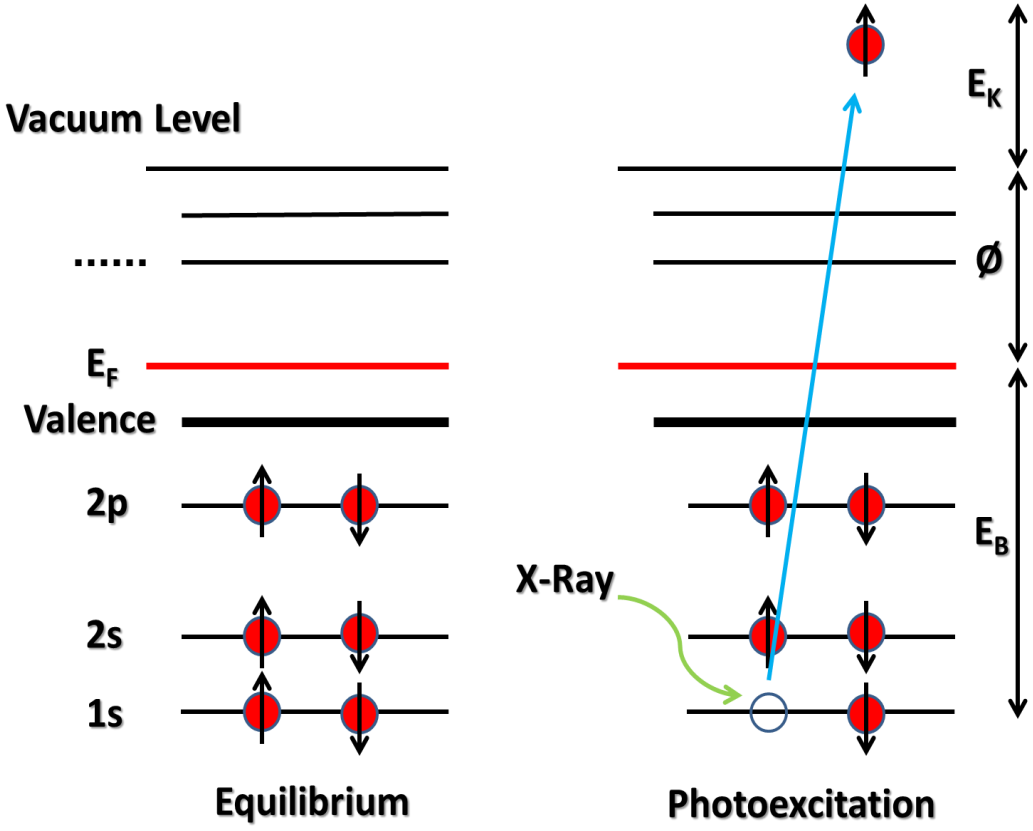

Figure 3-3: Schematic representation of the photoelectric effect. Sketch shows the working principles of XPS. A photon excites a core-level electron above the vacuum level. The kinetic energy of the outgoing electron is recorded and the binding energy can be calculated.

XPS is a powerful technique for the characterization of the chemical species present on a surface. The characteristic energy values of the levels in every chemical element has been tabulated since the technique was developed, and complete inventories of the resonances appearing under standard X-Ray illumination are present in many handbooks [172] or web applications. XPS is not only sensitive to the chemical element but it is also sensitive to the electronic and chemical environment of the particular element. Small energy shifts (surface core level shifts or SCLS) from the nominal value of a particular state are normally attributed to different chemical bonding configurations and thus to the electronic environments of this elements (**Figure 3-4**). If we have, for example, a carbon (C) atom bonded in sp^2 configuration with C atoms the C1s peak will have its maximum at energy around 284.8 eV [173]. Whereas, if we have C bonded to Si in the form of carbide (SiC), the C1s peak will appear shifted to lower energies, around 283 eV. The XPS spectra were analyzed using the Casa XPS program developed by Casa Software Ltd. This program allows a fit of the peaks by convoluting Lorentzian and Gaussian contribution to the width of a specific core level.

UPS spectrum is a measure of the valence band of a particular material. If this substance is conductive we will find electron-populating levels around the Fermi level. Because of the Fermi-Dirac distribution we will find a small quantity of electrons above it, as the thermal excitation makes these electron to spill over the Fermi level. On the other hand, if the material is insulating, we will find that no electrons are populating the Fermi level and we can very easily calculate the band gap as the energy difference between the last occupied electronic band and the Fermi level. However, one must take care of charge effects that might occur and make the band gap distorted.

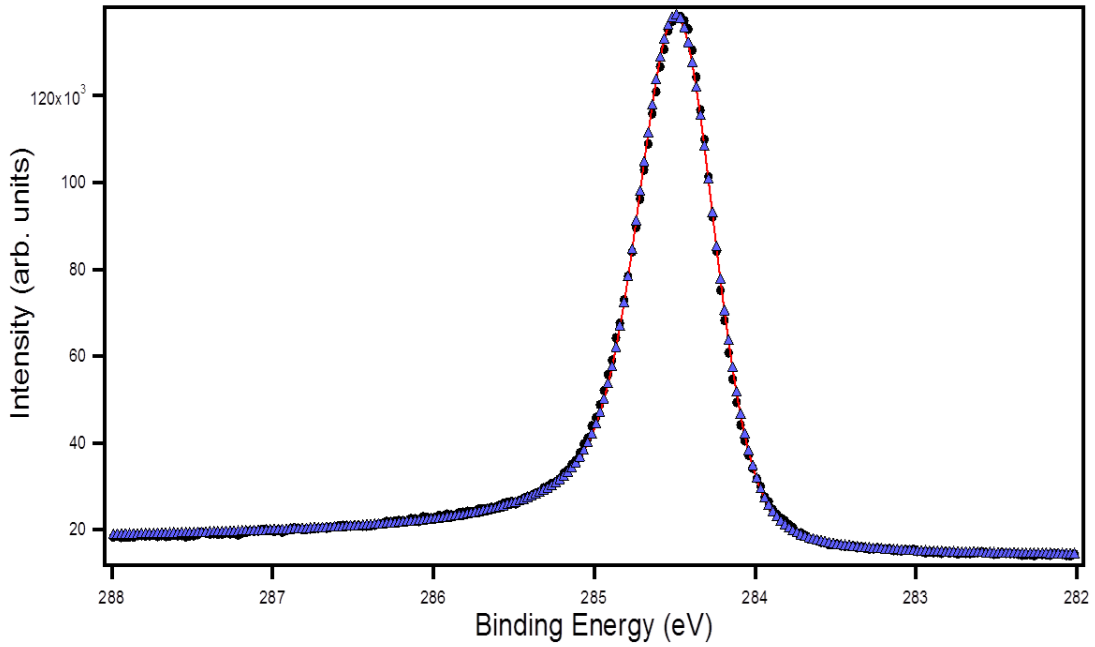

Figure 3-4: XPS spectra deconvolution of graphene. The black dots are the experimental results, blue dots are fits performed with the help of CasaXPS and the red line is the overall fitting result. The peak centered at 284.8eV corresponds to C in sp^2 configuration.

High-resolution X-ray Photoelectron Spectroscopy was performed with an Ultra High Vacuum (UHV) system using a base pressure of $2x10^{-10}$ mbar. The system was equipped with a hemi-spherical electron energy analyzer (SPECS Phoibos 150), a delay-line detector and a monochromatic AlKα (1486.74 eV) X-ray source. High-resolution spectra were recorded at normal emission take-off angle and with a pass-energy of 20 eV, which provides an overall instrumental peak broadening of about 0.5 eV.

The XPS experiment as discussed above was carried out in ultra-high vacuum (UHV) pressure. UHV chambers are necessary in order to prevent the sample from getting contaminated from the residual gases present in the atmosphere within seconds. In order to ensure the cleanliness of the sample for periods in the order of 1 hour, an estimation of the minimal time we will need for performing our experiments, we will need to lower down the pressure to the range of 10^{-10} mbar. According to kinetic theory of gas, the number of particles striking a surface per square cm per second can be given by:

$$n_s = N_g \sqrt{\frac{RT}{2\pi M}} \approx 2.7 \times 10^{22} \frac{p}{\sqrt{MT}} \left(cm^{-2}\, s^{-1}\right), \qquad \text{(Eq. 3-2)}$$

where p is the pressure in mbar, M is the molecular weight of the dominant species of the residual gas, and T is the temperature in K (Kelvin). Assuming M = 28 and T = 300, we have $n_s \approx 10^6\, p$, so we need at least a pressure lower than 10^{-6} mbar in order to keep the surface clean for a second. However, there is some other important factor that needs to be taken into account when calculating the deposition rates - sticking factor of the adsorbate. In the following sections, XPS components are discussed in order to have better understanding on the instrument performance.

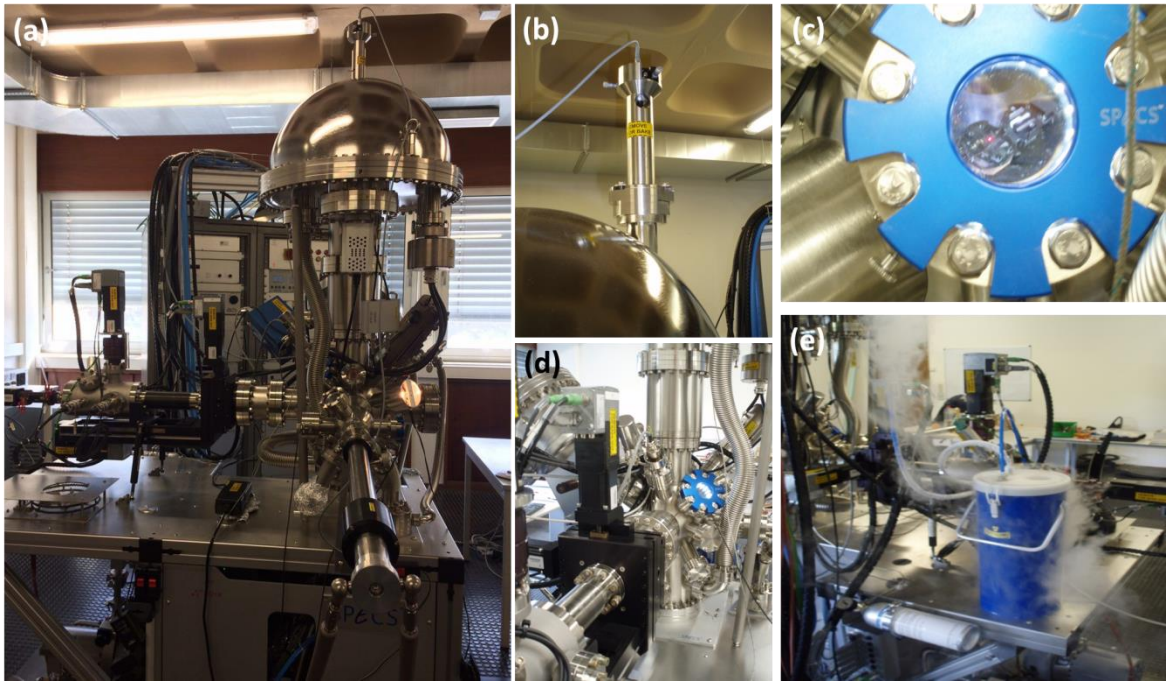

Figure 3-5: Representative images of the XPS equipment and major components. (a) High-Resolution PHOIBOS 150 1D-DLD, (b) Laser pointer fixed on top of Phoibos for better mark during measurement, (c) Laser pointer on the standard sample placed on master stage, (d) 5-axes motorized manipulator (for X, Y, Z, azimuthal and Polar angle), (e) Liquid nitrogen used to low temperature measurements.

Figure 3-5 shows the XPS equipment with the major component installed, **(a)** indicating PHOIBOS 150 with 1D-DLD detectors installed at the end of the Phoibos. Due to the energy dispersion of photoelectrons traversing the hemispherical analyzer, a spectrum can be acquired using the energy channels of the DLD without scanning the input lens or analyzer. The result is a spectrum acquired within seconds. The hemispherical electron energy analyzer – which is a fully electrostatic instrument (no magnetic fields) and the dual-anode (Mg and Al) x-ray source. **(b)** Showing the laser pointer installed at the top of the semi-hemispherical Phoibos for indicating the

area on the sample for better understanding while performing the measurements. **(c)** Shows the laser point at the sample kept on the master stage. The laser spot is actually focused/set to meet the center of the analyzer acceptance area (centrically position related Iris aperture and aperture 6 of the wheel). **(d)** Shows the 5-axes motorized manipulator for controlling the sample movements very precisely (for more details see **Figure 3-6**). **(f)** Shows the liquid nitrogen test for low temperature measurements.

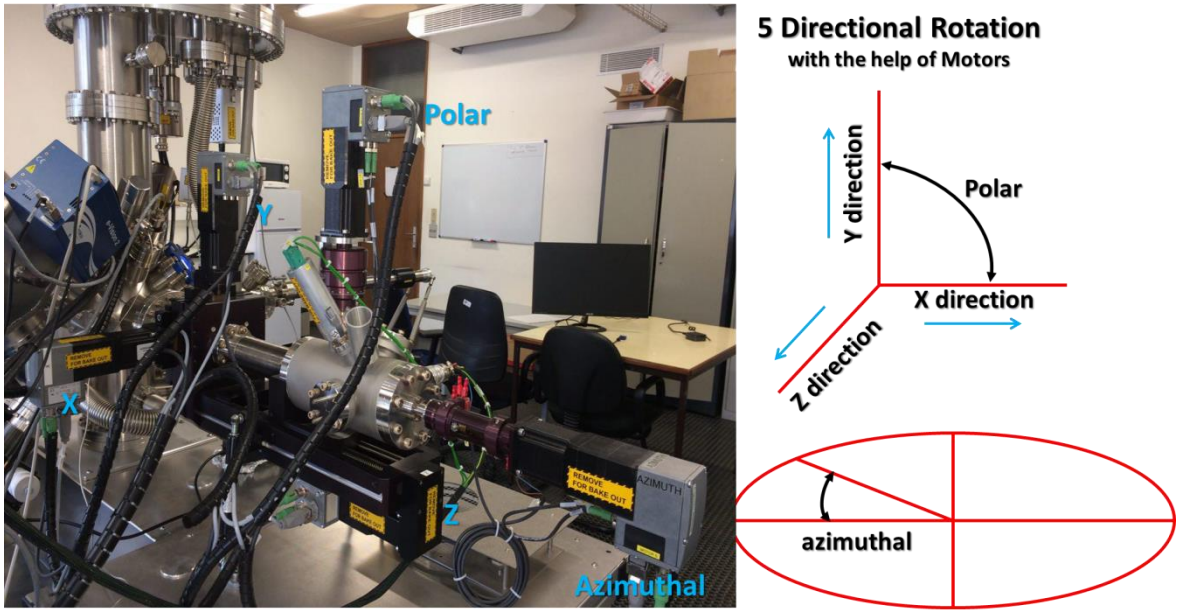

Figure 3-6: 5-axes motorized manipulator and the direction of movement when using it.

Figure 3-6 shows the advanced 5-axes motorized manipulator used for the movements of the sample kept at master stage. The master can be moved in X, Y, Z directions including polar (+ and -) and azimuthal (angle movements along right-left). This manipulator can be moved in X-Y: ±12.5 mm stroke, Z: appropriate size, Azimuthal: ± 180 degree and Polar: -10 degree to +90 degree.

Figure 3-7 (below) **(a)** shows the load-lock chamber, which is manufactured from the 316 non-magnetic stainless steel with all flanges (except the gate for inserting the sample) sealed with CF copper gaskets. This is place where the samples are inserted and initially the vacuum is achieved by using fast turbo molecular pump. This is the fast-entry vacuum load-lock, which pump out till 10^{-9} mbar, upon which the gate valve of main chamber is open for letting the sample into main chamber. The load lock is pumped by a turbo pump, which is backed by an oil-lubed forvacuum

pump. The load lock is separated from the turbo by a pneumatic angle valve and separated from the main chamber by a manual gate valve. There is a cold-cathode vacuum gauge (MKS instruments), which reads the load-lock vacuum as well as the pressure of the foreline using a Pirani gauge.

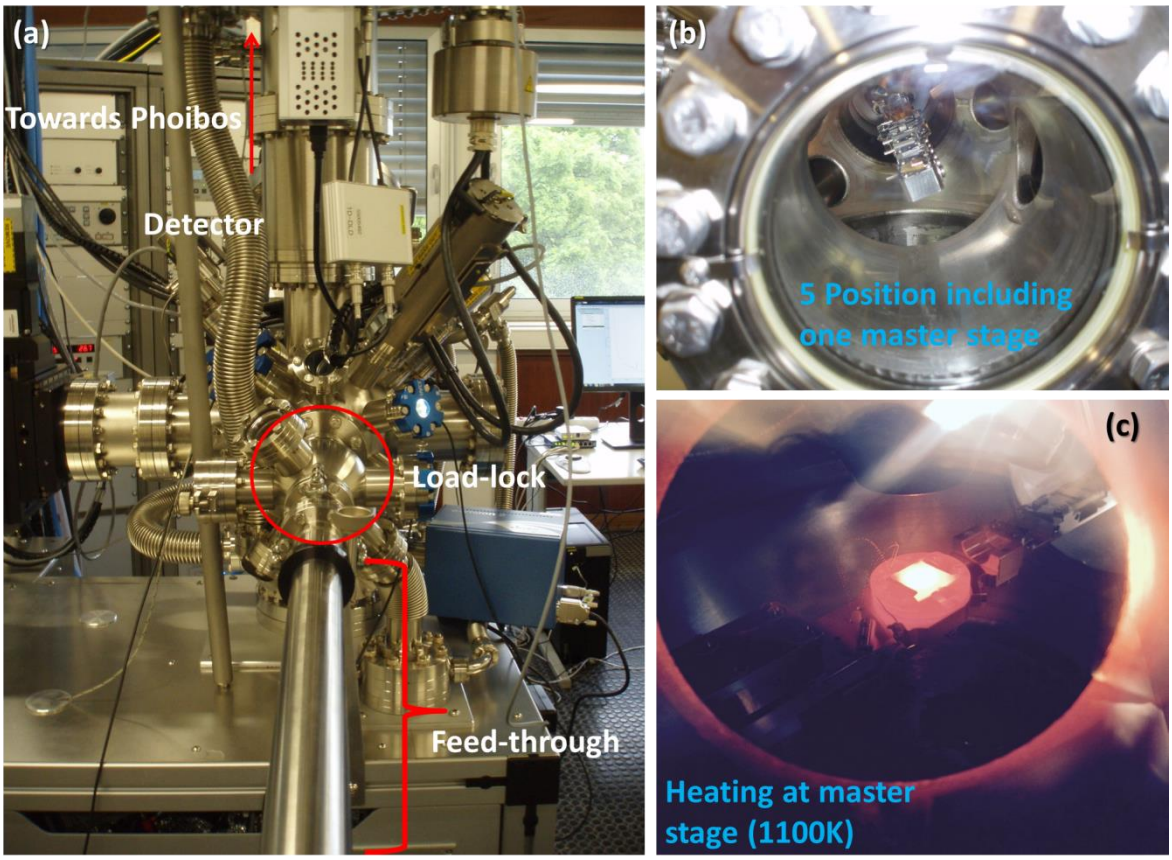

Figure 3-7: (a) Load-lock chamber with feed-through, (b) different parking positions for additional samples, (c) Annealing performed at master stage with as the red-glowing platelet is the sample holder irradiating visible light. The temperature is about 1100K.

Figure 3-7 (b) shows different parking positions when feed-through is at the main chamber. There are total 5 parking lots including one main stage. **(c)** Shows the master stage with the annealing at about 1100 K. This annealing is needed in order to obtain a clean surface well suitable for XPS measurements. Also, this will help to remove water and other contaminations present (if any) on the surface before performing the XPS measurements. In addition, in order to have XPS at low temperature, liquid nitrogen can be used **(see Figure 3-8).** Using liquid nitrogen provides us low temperature, which is especially required for biological samples.

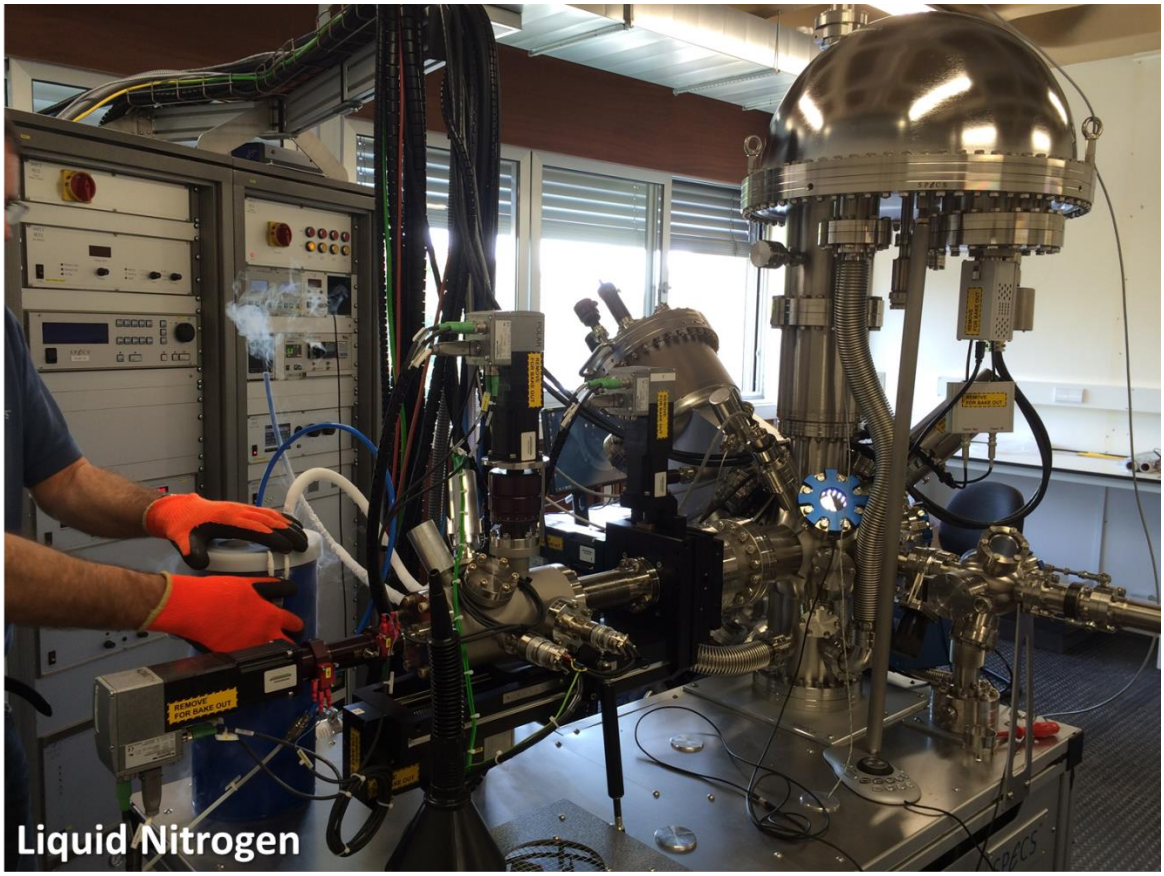

Figure 3-8: Using liquid nitrogen for the measurements in temperature range.

Figure 3-9: shows different pumps used in XPS for achieving ultra-high vacuum condition, which is the primary requirement for running the equipment. These pumps are connected to both load-lock chamber and main chamber. A turbo molecular pump backed by an oil-free rotary pump is attached to load-lock chamber. The main analysis chamber is pumped by a means of a getter (ion) pump equipped with an additional titanium sublimation pump (TSP). The ion pump is fitted with a cryobaffle, which may be filled with liquid nitrogen to increase the efficiency of the pump. A wide range cold cathode gauge also measures the pressure in the main chamber. The load lock is isolated from the main chamber by an electrically operated flap valve allowing the load lock to be vented by dry gas in order to introduce sample bars to the vacuum system.

Figure 3-9: Base pressure (Ultra High Vacuum) achieved by using different pumps used. (b) Dry (oil free) rotary pumps, (c) Ion pump and titanium sublimation pump (TSP).

3.1.3. Transmission Electron Microscopy

The Transmission Electron Microscope (TEM) operates on the same basic principles as light microscope but instead of light it uses electrons. The use of electrons as the light source is related to its lower wavelength, which gives high resolution, thousands of times better than the light microscope. TEM works under high vacuum created by different pumps such as ionic, diffusion and rotary pumps.

TEM is divided into three main parts: the first one is the electron source, the second one is the column consisting of electromagnetic lenses, sample holder and aperture and the third one is the detector, where one will have the final image (fluorescent screen) which is now replaced by CCD camera **(Figure 3-10).**

The electrons are generated by three known mechanisms, field emission, thermoionic emission and Schottky emission. To guide these electrons through the column the electromagnetic lenses are used that focuse the electrons into a very narrow beam. The electron beam then travels through the specimen to the detector, where it gives the final image [174].

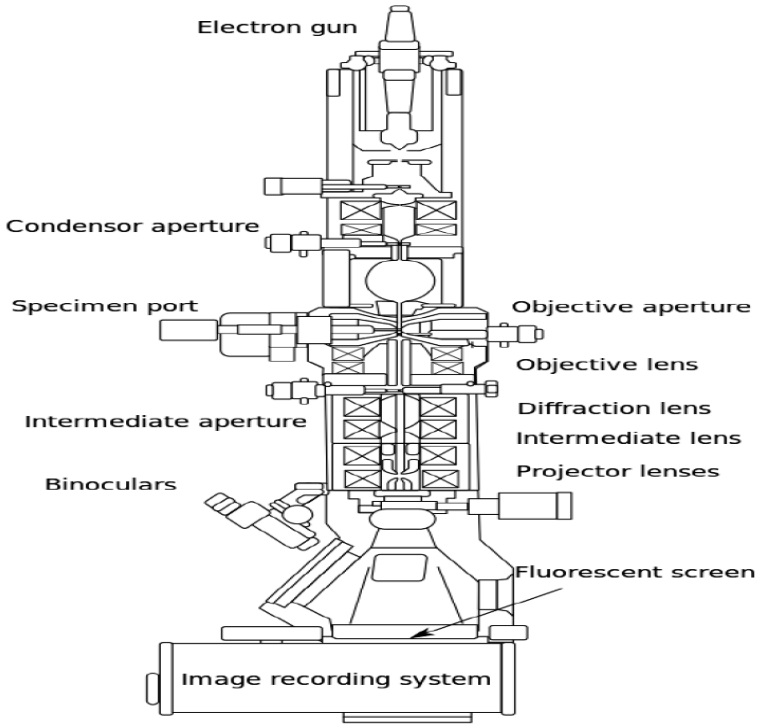

Figure 3-10: Layout of a Transmission Electron Microscope. Adapter from [175]

There are different image modes in which the TEM can work. The most common mode is bright field and in which TEM generally starts. In this mode, contrast is formed directly by the blockage and absorption of electrons in the sample. Thicker regions of the sample or regions with a higher atomic number appear dark, whereas regions with no sample in the beam path appear bright, hence the term bright field.

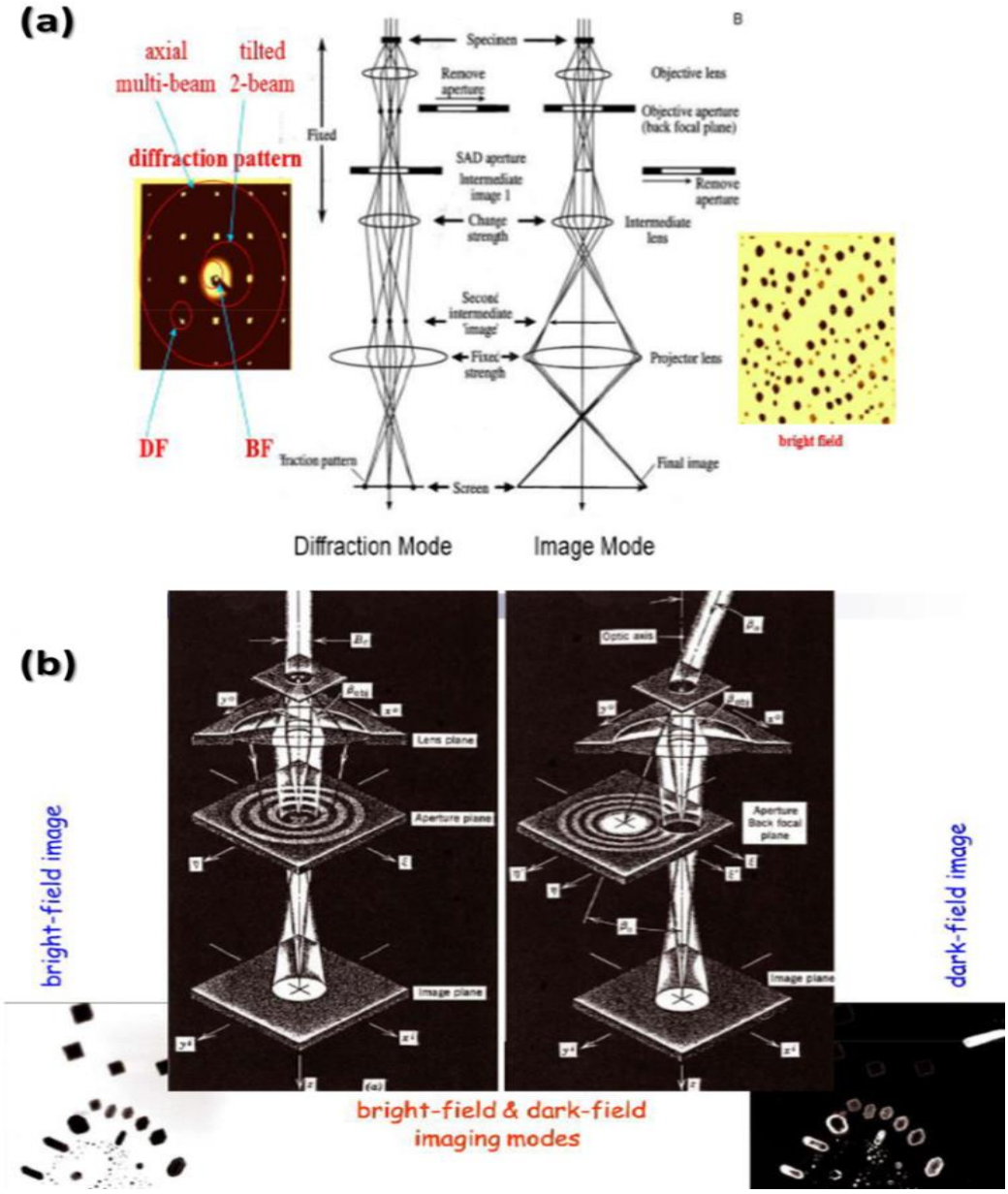

Figure 3-11: Structural layout of the (a) diffraction and image modes, and the (b) bright field and dark field modes. Adapted from [176].

In dark field mode, the objective aperture (a metallic plate with different sizes of holes) is placed in back focal plane that blocks the direct beam from the interacted electrons and allow only scattered electrons to produce an image, due to which the image appears to be dark. In this mode, it is possible to identify if the particles are crystalline or amorphous. The crystalline particles appear dark in this mode.

The diffraction mode, also known as selected area electron diffraction (SAED), is obtained by adjusting the magnetic lenses such that the image comes from back focal plane of the lens rather than the image plane. Here, the spots are observed for single crystal and rings in case of polycrystalline material.

The major application of TEM is to study the morphology of materials, and to obtain crystallographic and compositional information, if so equipped. TEM can also give information about structural aspects, phases, impurities, elemental analyses and dislocations. SAED is also required to calculate the lattice parameter and to observe the crystallinity of the composites.

The resolution of the TEM is limited primarily by the spherical aberration. By the reduction of the spherical aberration (by aberration correctors), an increase of the mechanical stability and the use of high voltages has led to the development of HR-TEM which allows the production of images with sufficient resolution to show carbon atoms in diamond separated by only 0.89 Å and atoms in silicon at 0.78 Å [177]. The ability to determine the positions of atoms within materials has made HR-TEM an important tool for nanotechnology and materials development.

In this work, the microstructures were analyzed by HR-TEM with Jeol 2200FS Field Emission Electron Microscope, with the resolution of 0.19 nm (Ultrahigh), 0.23 nm (High), 0.25 nm (High Specimen Tilt). The electron gun was made up of ZrO/W (100) with Schottky emitter. The base pressure was 7.5×10^{-8} Torr. During measurements, we used accelerating voltage in the range 160-200 kV. The condenser lens used were at 3-stage (1^{st} Cl, 2nd CL, condenser minilens CM). The sample was inserted using specimen stage of side-entry eucentric with Z-axis fine control and common specimen holder.

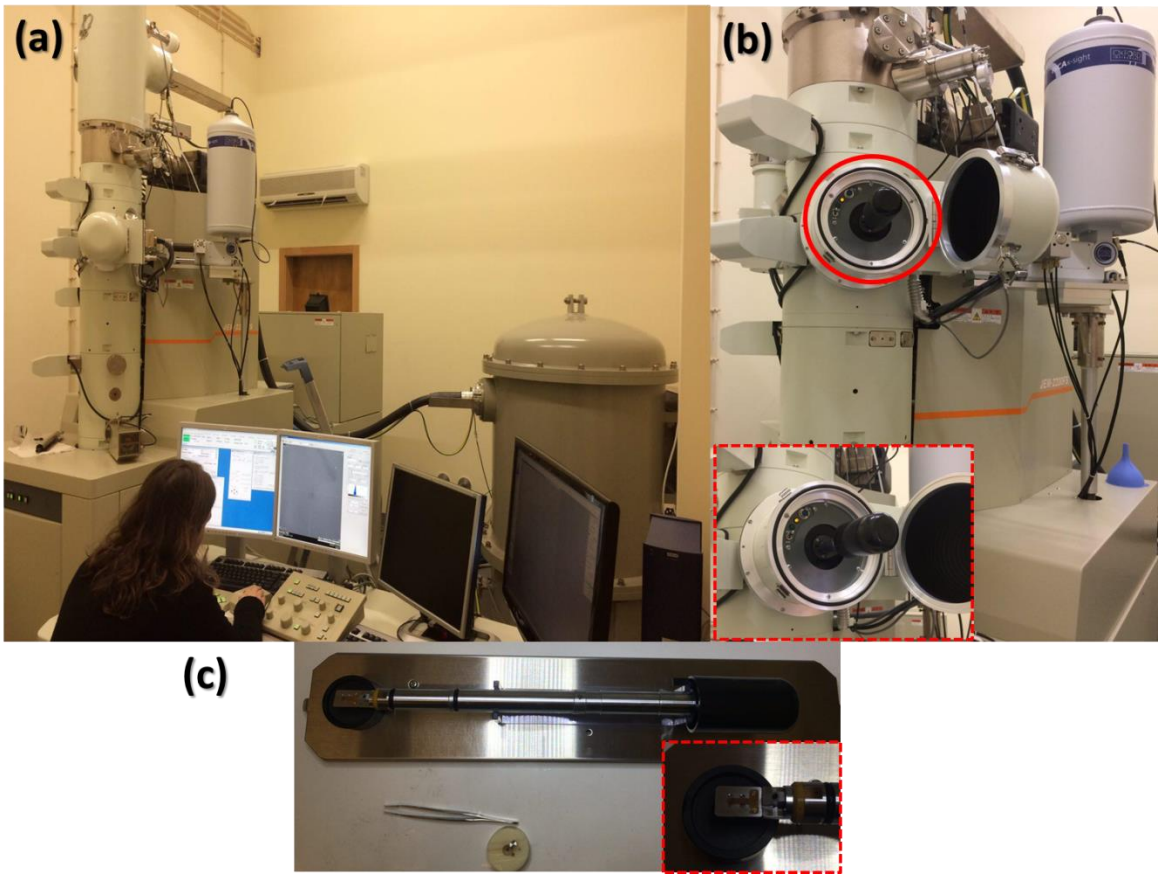

Figure 3-12: (a) Showing the HR-TEM equipment used for the characterization of the samples, (b) Position for inserting the sample holder, inset showing the sample holder inside the holder, (c) double tilt sample holder for better view, inset showing the fixed TEM grid with screws for measurements.

HR-TEM sample preparation involved the deposition of graphene on Cu foil (Good Fellow, thickness ~ 0.10 mm). The copper foil was then etched away by strong etchant iron chloride, which led to Graphene floating on the surface, and finally, it was collected and deposited on a copper grid of 400 mesh (Agar Scientific, G6210).

3.1.4. Scanning Electron Microscope

Most of the electronic systems of Scanning Electron Microscope (SEM) are similar to the ones of TEM. However, herein, the sample image is formed from the secondary electrons, which reflect from the sample rather than transmitted and detected by the detector **(Figure 3-13)**.

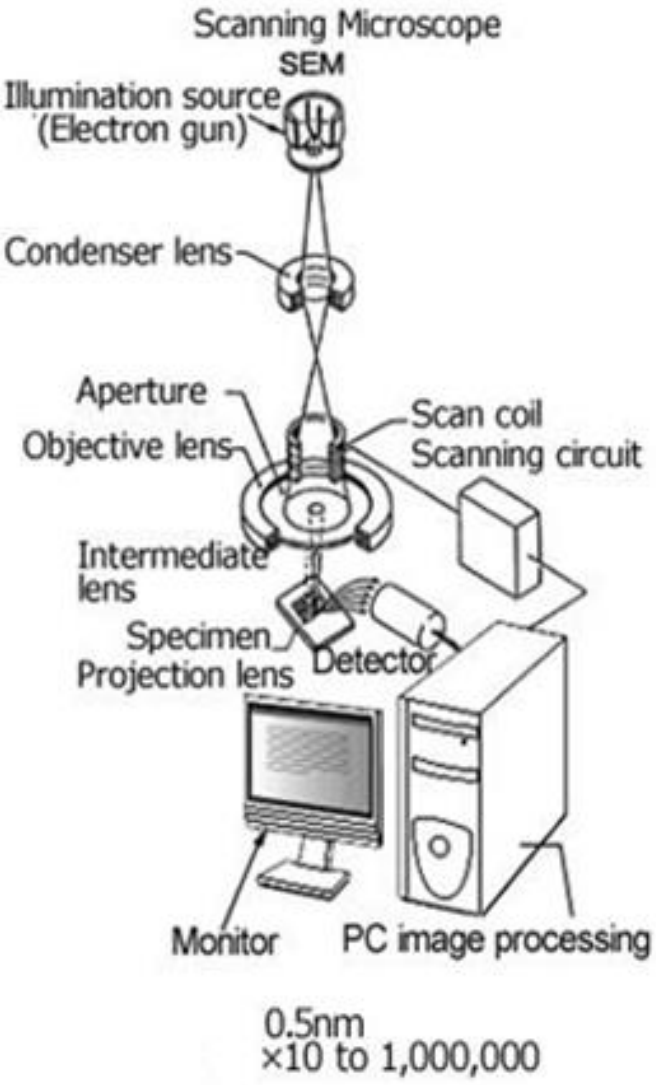

Figure 3-13: Schematics representation of the Scanning Electron Microscope and its important parts. Adapted from [178].

SEM (in transmission mode detection) was performed before analyzing graphene by TEM. SEM was performed using a Hitachi Su-70 instrument on graphene on copper grids. **Figure 3-14** shows the deposition of graphene at x30 in secondary electron and transmitted electron image mode.

The figure also shows the uneven distribution of graphene and we can observe that it was not covering the whole grid.

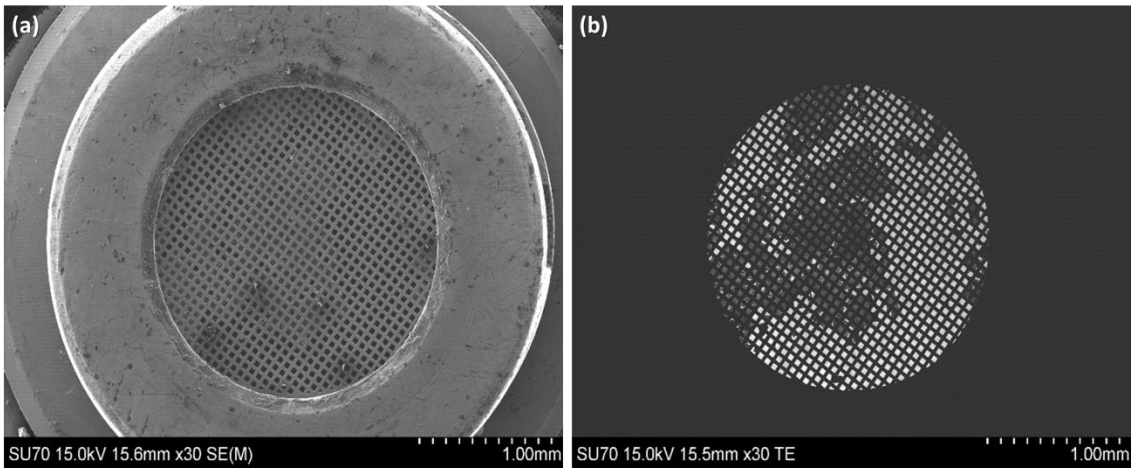

Figure 3-14: Graphene on copper grid in (a) Secondary Electron imaging mode, and (b) Transmitted Electron imaging mode.

To be sure regarding the graphene on upper or lower part of grid, we acquired SEM images from the detector placed on upper and a lower secondary electrons detector, also a mix detection using both, which confirm that the graphene was on the upper part of grid. **Figure 3-15** shows the images of graphene from upper, lower and mix contribution of the secondary electron detector at x300.

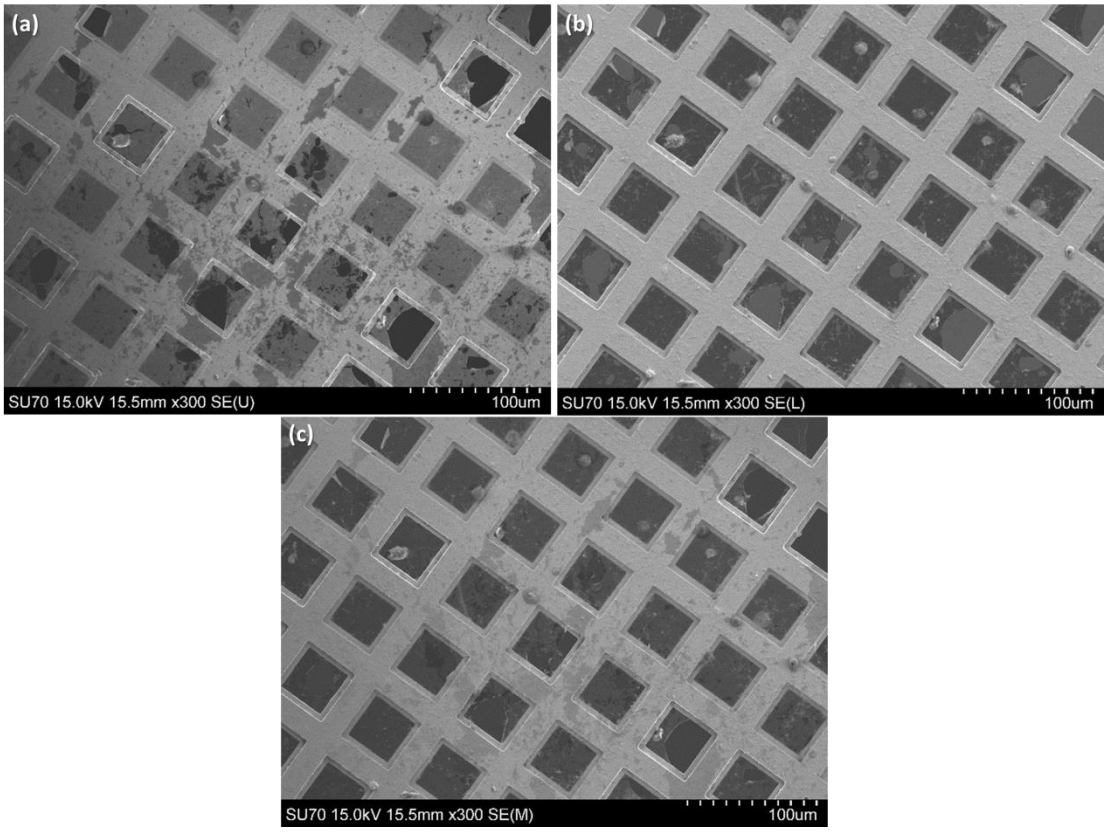

Figure 3-15: Representative images of graphene from: (a) upper, and (b) lower secondary electrons detectors, and (c) mix contribution of both detector.

3.1.5. Atomic Force and Piezoresponse Force Microscopies

After the invention of the Scanning Tunneling Microscope (STM), it quickly became obvious that other physical processes could be used to map surfaces, not just a tunneling current. Indeed, physical forces (Van der Waals forces, electrostatic forces and so on) between the sample and the tip were proven to be used for imaging surfaces, and this technique was termed Atomic Force Microscopy (AFM) [179].

AFM works in two basic modes: contact mode and non-contact mode. In contact mode AFM, the tip (scanning probe) mounted on the cantilever is brought in contact with the sample and scanned using piezoelectric actuators. The deflection of the cantilever is accurately monitored by laser spot reflected from the cantilever to the mirror and photo diode **(Figure 3-17 (a))**. These signals are passed to the feedback system, which allows mapping of the sample surface [180]. During the interaction between the tip and the sample surface, the tip experiences rapidly changing forces. As the function of the magnitude of these interaction forces the deflection of the cantilever changes and used as a feedback to get topography profile of the samples.

The other mode of AFM operation is non-contact or tapping mode (TAFM). In this mode, the cantilever is placed at some particular Z distance from the sample (knows as set point), where the tip oscillates close to its resonance frequency (with free amplitude). When the tip comes in contact with the sample, the amplitude of the tip vibration reduces or increases. This change in amplitude is monitored by the photo diode similar to contact mode to acquire the topography of the sample. The major advantages of the tapping over the contact one is better resolution due to the negligible lateral forces and less wear of the tip.

AFM images are not a true representation of the sample topography due to the complex dynamics of the vibration of tip and surface system. Therefore, there are limitations in achieving atomic resolution. This limitation can be overcome using tips with very small (1-2 nm) tip diameter and having high aspect ratio. However, the standard tips used for AFM imaging are not ideally sharp and have low aspect ratio as shown in **Figure 3-16 (a** and **b)**. Therefore, an AFM image does not reflect the true sample topography, but rather represents the interaction of the probe with the sample surface. This is called tip convolution. Nevertheless, the tip convolution does not affect the height of the feature only affects the lateral resolution.

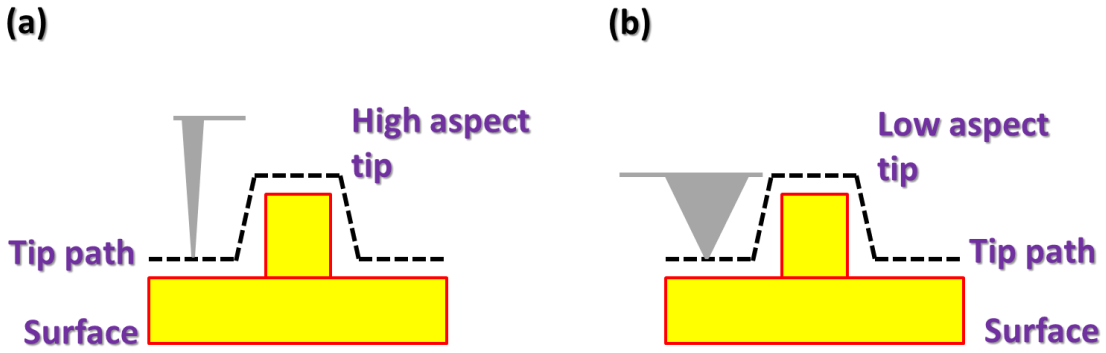

Figure 3-16: Schemes illustrating the topography acquired from: (a) high aspect ratio and (b) low aspect ratio tip. A high aspect ratio tip is the ideal probe (tip) to acquire best resolution; whereas, low aspect ratio results in the convolution. This does not often influence the height of a feature but the lateral resolution. Adapted from [181].

In the present work, AFM was used to study the RMS roughness in a semicontact mode using Ntegra Prima, NT-MDT in tapping mode with the cantilevers of resonance frequency of 50 kHz.and force constant 3 Nm^{-1}

3.1.5.1. *Piezoresponse Force Microscopy (PFM)*

Piezoresponse Force Microscopy (PFM) is used to study the local piezoelectric properties of different ferroelectric substrates (PMN-PT of different compositions). Schematic of experimental setup for PFM is shown in **Figure 3-17 (a)** [179, 182]. In general, PFM is carried out in contact mode using a conductive tip, used as a moveable nanoelectrode. The PFM response image is created from the deformation of piezoelectric surface due to the applied external field. This deformation can be in the form of contraction, elongation or shear depending upon the polarization vector and direction of the applied field. The PFM works based on the converse piezoelectric effect, where electric field-induce strain (S) is expressed as follows:

$$\mathbf{S_j} = \mathbf{d_{ij}E_i}\,, \qquad \text{(Eq. 3-3)}$$

where $\mathbf{E_i}$ is the applied field and $\mathbf{d_{ij}}$ is the piezoelectric tensor. For a single-domain ferroelectric the piezoelectric coefficient is related to the spontaneous polarization P_s via the following expression:

$$\mathbf{d_{ij}} = \boldsymbol{\varepsilon_{im} Q_{jmk} P_s},$$ (Eq. 3-4)

where ε_{im} is the dielectric constant, Q_{jmk} is the electrostriction coefficient and $\mathbf{d_{ij}}$ is the piezoelectric tensor.

The above equation states a linear coupling between piezoelectric and polarization parameters and can be used to determine the domain polarity from the sign of field induced strain. The electric field along the polarization direction results in the elongation of the domain. The contraction of the domains is observed, when the direction of the polarization is opposite to the applied field direction. The relation between induced strain (S) and changes in thickness (ΔZ) is given by following equation:

$$\mathbf{S} = \frac{\Delta \mathbf{Z}}{\mathbf{Z}} = \pm \boldsymbol{d_{33}} \mathbf{E},$$ (Eq. 3-5)

where, ΔZ is the sample deformation, Z is the thickness of the sample, d_{33} is the effective piezoelectric constant. The above equation can be further rewritten as follows:

$$\Delta \mathbf{Z} = \pm \boldsymbol{d_{33}} \mathbf{V},$$ (Eq. 3-6)

where V is the applied voltage. The contribution related to the electrostriction is typically much smaller than the piezoelectric response in a polarized state and vanishes if no DC field is applied to the sample. In the dynamic piezoelectric imaging method, an AC voltage is applied and the surface displacement is measured by the change in the vertical vibration of the cantilever, this response is known as vertical piezoresponse (VPFM), and amplitude is given by **Equation 3-6**.

When domain polarization direction is parallel to the surface, the imaging of that domain is represented by detecting the torsional vibration of the cantilever **Figure 3-17 (b)** known as lateral PFM (LPFM). This surface vibration translates via friction forces to the torsional movement of the cantilever. The amplitude of the in-plane oscillation is given by:

$$\Delta \mathbf{X_o} = \mathbf{d_{15}} \mathbf{V_o},$$ (Eq. 3-7)

where $\mathbf{\Delta X_o}$ is the change in the deflection along the X-axis and $\mathbf{V_o}$ is the applied voltage and $\mathbf{d_{15}}$ is the shear piezoelectric coefficient. The local ferroelectric hysteresis of the materials can be

measured at the single point by the method known as switching spectroscopy (SS) PFM. In this method, the switching response of the domain is measured as the function of applied dc bias from positive to negative cycle. The typical local PFM hysteresis from the ferroelectric material is shown in **Figure 3-17 (c)**.

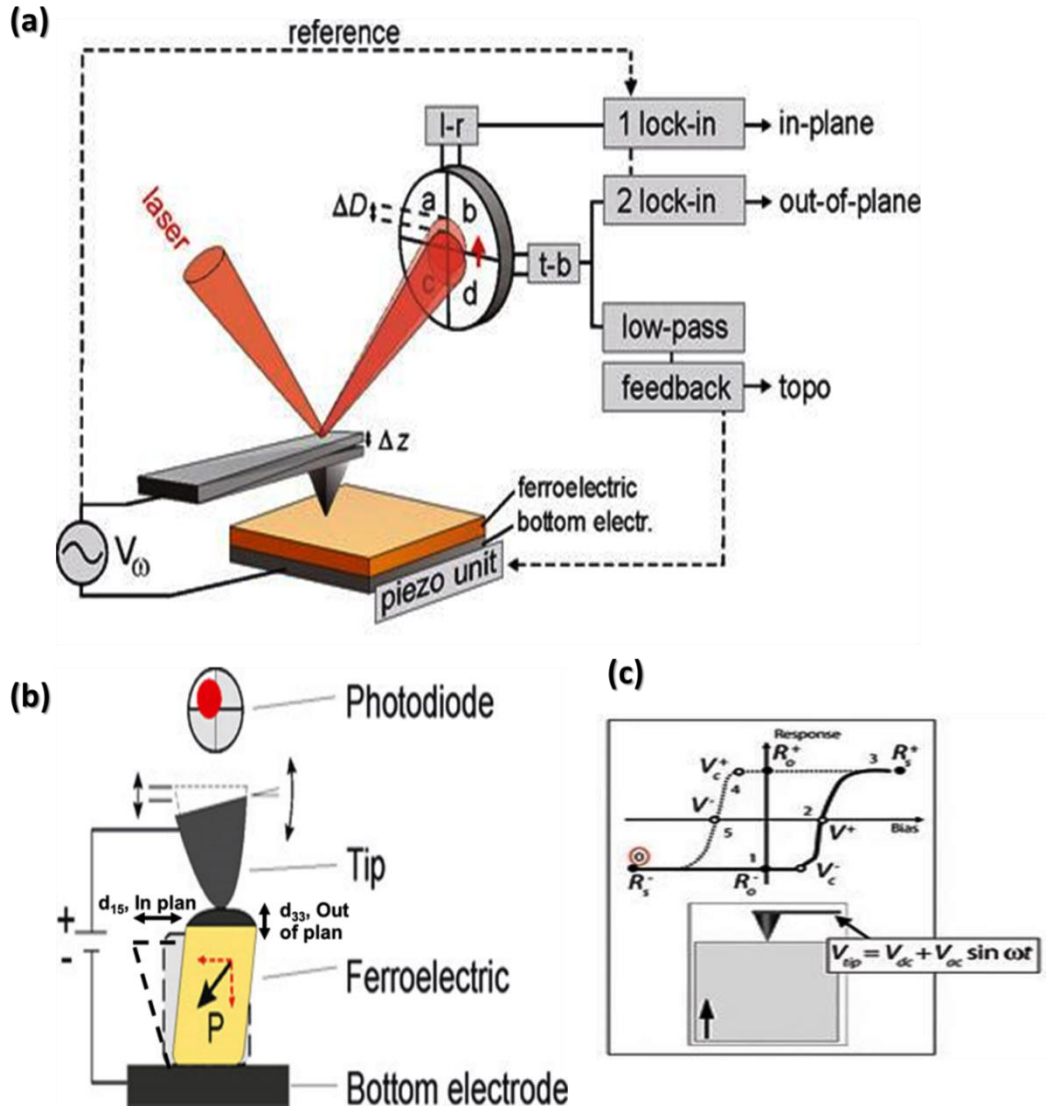

Figure 3-17: (a) Schematic representation of the PFM setup to simultaneously acquire the topography and the in- and out-of-plane component of the polarization. A function generator is used to apply an alternating voltage Vω between the tip and the bottom electrode of the material. (b) Schematic illustration explaining how PFM signals are acquired by the deformation under the applied field; the voltage induced cantilever deflection is detected by a reflected laser beam on a four-sector photodiode. (c) Scheme highlighting a hysteresis loop acquired by switching spectroscopy (SS-PFM). Adapted from [183].

3.1.5.2. *Kelvin Probe Force Microscopy*

Kelvin Probe Force Microscope (KPFM) or Kelvin Force Microscope (KFM) is a based on the contact potential measurement method introduced by Lord Kelvin in 1898 [184] and further improved by Zisman in 1932 [185]. Therein, the determination of the work function is based on the measurement of the electrostatic forces between the small AFM tip and the sample. With KPFM the work function of surfaces can be observed at atomic or molecular scales. In this experiment, two conductive plates are arranged in parallel forming small capacitor. When a vibrating cantilever (with frequency ω) is brought near the surface of the plates (which behaves as the capacitance) it shows the changes due to the electrostatic differences. This results in the current, which could be measured directly. However, the charges might be influenced by some other factors also and with an adjustable dc voltage source V and a null-current detector are inserted in series in the circuit. The current in the circuit can be given as:

$$\boldsymbol{i(t) = \left(V - V_{cpd}\right) \frac{dC}{dt}} \text{ ,} \qquad \text{(Eq. 3-8)}$$

where $\frac{dC}{dt}$ is the change of the capacitance in the interval of time dt. The voltage V is changed until the sensitive current amplifier detects null-current condition. This compensating voltage is recorded as the contact potential difference between the two plates of the capacitor. It is known that different surface potentials generate different electrostatic force between the surfaces [186]. Hence, the electrostatic force between the tip and the sample is given by:

$$\boldsymbol{F_{es} = \frac{1}{2} \frac{dC}{dz} \left(V_{cpd}\right)^2} \text{ ,} \qquad \text{(Eq. 3-9)}$$

where, *C* is the capacitance between the tip and the sample surface and z is the distance between the tip and the sample.

In the KPFM method, direct detection of the amplitude of the vibration of the tip, which was assumed to be proportional to the force acting on the tip, depends on several ill controlled factors, in particular $\boldsymbol{\frac{dC}{dz}}$. Keeping this in mind so called null force method was used where an external voltage (modulated ac voltage - $V_{ac}sin\omega t$ and dc voltage - ϕ_{dc}) is applied between the tip and the sample. This results the total potential written as:

$$\boldsymbol{V = V_{dc} - V_{ac} \sin \omega t}\ , \qquad \text{(Eq. 3-10)}$$

where V_{dc} is the total dc voltage ($V_{dc} = V_{cpd} - \phi_{dc}$; V_{cpd} is the surface potential, ϕ_{dc} is the feedback voltage supplied to the sample surface). Hence the electrostatic force can be written as:

$$\boldsymbol{F_{es} = \frac{1}{2}\left(\frac{dC}{dz}\right)\left(\left(V_{dc}^2 + \frac{V_{ac}^2}{2}\right) - 2V_{dc}V_{ac}sin\omega t - \frac{V_{ac}^2}{2}cos\omega t\right)} \qquad \text{(Eq. 3-11)}$$

In order to measure the surface potential, the dc voltage is changed until there is no detectable oscillation. If the voltage can be maintained at $\boldsymbol{V_{cpd} = \phi_{dc}}$, the surface potential $\boldsymbol{V_{cpd}}$ can be obtained directly by measuring the external voltage $\boldsymbol{\phi_{dc}}$.

In the present work, we did KPFM by using the two-pass technique for imaging of the contact potential difference between the sample and the AFM tip. During the first pass, a topographic image is acquired in tapping mode. In the second pass, the tip follows the topographic profile at a preset lift height. During the second pass, the cantilever is electrically excited by the sum of a variable dc voltage V_{tip} dc, and an ac voltage, V_{tip} ac, with a frequency close to the cantilever resonance. V_{tip} dc is adjusted to nullify the force component at the frequency of V_{tip} ac. The value of V_{tip} dc is then equal to the surface potential. The tip was lifted by just a few nanometers in order to ensure that the tip–sample capacitance was dominant over the cantilever – sample capacitance. In our setup, we grounded the nickel substrate and applied a bias voltage to the tip.

3.1.6. X-Ray Diffraction

X-Ray Diffraction (XRD) technique is not only quite relevant to the analysis of graphene but also can be used for visualizing/characterizing the graphene planes on Cu (substrate). It was also important to check the impurities present (if any) available on Cu besides graphene (carbon). X-ray Diffraction is one of the most important and used characterization tools to study the crystalline structure of materials.

The working principle of XRD is based on the diffraction of X-rays from Bragg plane. When a beam of X-ray interacts with the atom and electrons in the crystal, they will oscillate under the X-ray impact and emit a large number of electromagnetic waves in particular directions. The direction

of the emissions will be in phase in certain directions, which depends on the incident X-ray (**Figure 3-18**), on the wavelength and on the spacing between atoms in the crystals. The relation between all of these parameters is given by Bragg relation:

$$\boldsymbol{n\lambda = 2d.sin\theta}\text{ ,} \qquad \text{(Eq. 3-12)}$$

where, n is an integer and λ is the wavelength of the x-ray used, d is the inter planar spacing, and θ is the angle made by the incident ray with the crystal plane.

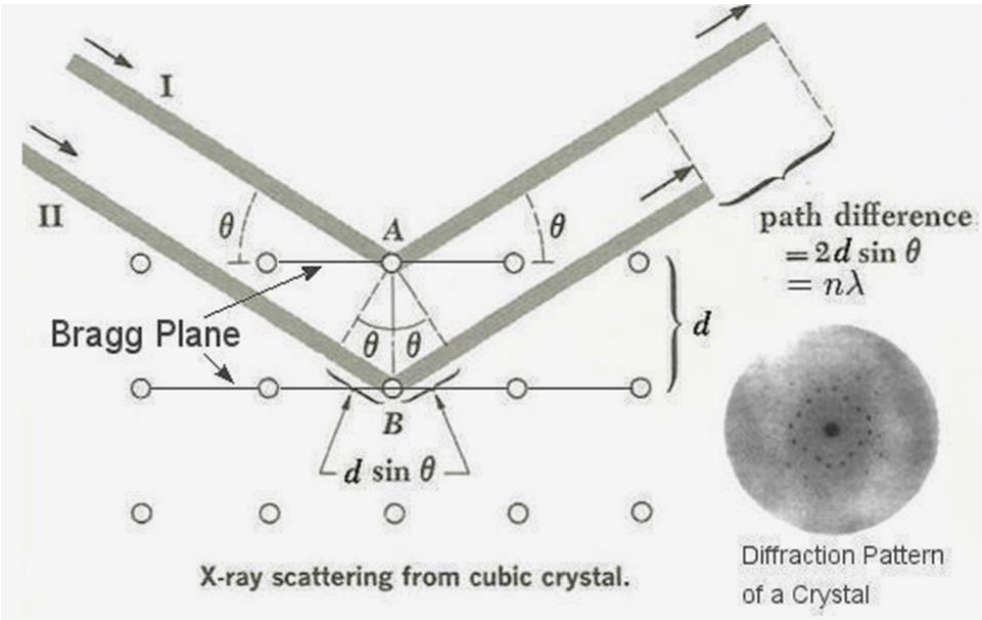

Figure 3-18: X-ray diffraction from the Bragg plane of cubic crystal with path difference equal to 2d sinθ, diffraction pattern is shown on the bottom right of the figure. Adapted from [187].

Diffracted rays are detected by a diffractometer and the obtained diffraction patterns are then compared with the reference standards for identification. Each solid has its unique crystallographic characteristics and X-ray powder patterns can be used as a "fingerprint" for crystal identification. Once the material has been identified, XRD may be used to determine its crystalline or microcrystalline structure, i.e. the relative orientation of atoms in the crystal or crystallite and interatomic distances. Furthermore, it is possible to determine the size of the crystallites using the Scherrer equation [188].

In the present work, we used room temperature Rigaku diffractometer with Cu-Kα (=1.5418 Å) radiation. The diffraction patterns were acquired at a wide range of Bragg angles *2Θ* (5º < *2Θ* < 80º) with a step length of 0.04º.

3.1.7. UV- Visible Absorption Spectroscopy

Energy absorbed in the UV or visible region causes a change in the electronic excitation of the molecule, and hence results in corresponding change in its ability to absorb light in the UV-visible region of the electromagnetic radiation. This leads to color transition. The relationship between energy absorbed in an electronic transition and the frequency (υ), wavelength (λ) and wave number (ṽ) of radiation producing the transition is given as:

$$\Delta \boldsymbol{E} = \boldsymbol{h\nu} = \boldsymbol{h}\frac{\boldsymbol{c}}{\boldsymbol{\lambda}} = \boldsymbol{h\tilde{\nu}c}\,, \qquad \text{(Eq. 3-13)}$$

where h is the Planck's constant, c is the velocity of light and ΔE is the Energy absorbed in an electronic transition in a molecule from ground state (lower energy) to excited state (higher state).

In the present work, we used at room temperature spectrophotometer (UV–vis/near IR, Perkin Elmer, Lambda 950). For the reference, virgin SiO_2/Si was used in case of MoS_2 measurement.

3.2. Sample preparation

3.2.1. Chemical Vapor Deposition: assembling and parameterizing

Restriction to have a large area uniform layer of graphene does not allow using exfoliation method. Therefore, CVD method emerged as a potential pathway for graphene commercialization [1, 7]. CVD is a complex process in which chemical components react in the vapor phase close to or on a hot substrate that is usually heated by external heating, radiation or plasma. This deposition consists of either homogenous gas phase reactions or heterogeneous chemical reactions, which occur on/near the hot surface of substrate. One can get materials with different properties by changing the substrate temperature, composition of the gas mixture, total pressure,

gases flow and experimental conditions, etc. [189, 190]. These reactive processes distinguishes CVD from Physical Vapor Deposition (PVD) processes such as physical evaporation, sputtering and sublimation methods [191].

Typical CVD process includes volatilization of a solid or liquid precursors that produce gaseous compound which is deposited on the substrate. Carrier gases (usually argon (Ar) or nitrogen (N_2)) are used to transport gaseous materials to a hot substrate (in a chamber). Hydrogen (H_2) is used as reducing agent in chemical reduction and also to clean the substrates (for another use) and reaction chambers. It must be kept in mind that all parts (chamber) of the system are at least as hot as the vapor supply otherwise condensation of vapors will occur on their contact with any comparatively cold surface. The reactive part (the place where reaction should be expected) of the system is usually much hotter than the vapor. However, the temperature should be kept less than melting point of the deposit. Importantly, the mentioned below two main points should be considered despite of volatility:

(i) For proper elimination of the unnecessary materials from the deposition system, they must be in gaseous form, and

(ii) The deposit must have vapor pressure low enough to prevent its own volatilization.

The deposition reaction occurs either via thermal decomposition or via chemical reduction. CVD is valuable for the production of a very thin deposit. One of the most important applications of CVD is the preparation of coatings and the manufacturing of materials to finished size for those substances, which are not conveniently fabricated via more conventional ways. Such materials cannot be suitably fabricated either by PVD or by electrodeposition. High melting elements such as tantalum or tungsten cannot be deposited by PVD. Similarly, electrodeposition techniques cannot be used for some commercially significant elements such as silicon and tungsten [192]. CVD has an additional benefit of depositing many alloys and some other compounds like carbides, oxides and nitrides.

In a CVD process, the deposition depends upon the thermal energy of the substrate. However, sometimes it is desirable to minimize the temperature of the substrate in order to protect the materials that have already been formed. A number of methods have been developed to perform CVD at lower temperature, allowing the coatings to be grown at thermally sensitive substrates and, therefore, improving the quality and purity of these coatings. These include the use of plasmas, ion beams, reactive carrier gases, lasers, synchrotron radiation, etc. Plasma

Enhanced Chemical Vapor Deposition (PECVD) is employed to accomplish high quality coatings at a reduced temperature. In this process, electron energy (plasma) is used as an excitation method in order to perform coating at a low temperature and at a moderate rate. In PECVD, a radio frequency field activates the injected gases. This results in the generation of a plasma zone containing free electrons, ionized gas molecules, free radicals and normal neutral gas molecules. In PECVD, additional energy is provided, which then causes thin films to be produced at a lower temperature. However, this process involves additional cost related to purchasing plasma producing equipment. Furthermore, PECVD is carried out in vacuum, therefore, more sophisticated reactor needs to be purchased. Similarly, the use of high ion energy plasma (more than 20 eV) could cause serious damage to a few fragile substrates [193-195]. Due to the above drawbacks of the PECVD, the use of catalysts is preferred to deposit thin films on thermally sensitive substrate.

In certain CVD processes, catalytically active metals deposited first act as autocatalysts. Seeding a surface with such active metals can lead to selective CVD on the seeded zones especially if a reactive carrier gas like oxygen or hydrogen is used, too. It is believed that the adsorption and dissociation of the CVD precursor occur at the surface of the catalytically active metals since they act as reactive sites for these precursors. In the presence of a reactive carrier gas such as hydrogen or oxygen, a catalytically active metal serves for the elimination of the ligand fragments from the surface by catalytic oxidation or reduction, respectively. Consequently, a clean surface is reproduced for additional precursor adsorption and decomposition. Therefore, it can be concluded that co-deposition of catalytically active material causes catalysis of the CVD of a non-catalytic material. Such a phenomenon can be termed as Catalyst-Enhanced Chemical Vapor Deposition (CECVD). In this process, small quantity of a catalyst precursor is introduced in the reactor along with the major CVD precursor [196]. Catalytic Chemical Vapor Deposition (CCVD) or Hot Filament Chemical Vapor Deposition (HFCVD) is another simple and economic process, which uses a hot filament for the chemical decomposition of the precursor at the surface of already prepared catalyst particles precursor supported on a surface. CCVD or HFCVD are performed at comparatively low temperature (500-1500 ^{o}C) and ambient pressure (low vacuum). Therefore, CCVD or HFCVD are particularly useful for the synthesis of carbon-based materials such as carbon nanotubes (CNTs) and graphene. The process can be performed using various carbon sources in any physical state. Furthermore, it allows using different substrates and ensures carbon synthesis in a variety of forms like films and powders [197, 198].

During this PhD work, assembling and parameterizing the Catalytic Chemical Vapor Deposition (CCVD) or HFCVD were done for the growth of graphene and molybdenum disulfide. A more detailed description of the CCVD (HFTCVD) follows. In this type of CVD, an appropriate precursor species are fed into a reaction chamber. The reactions take place and lead to the production of solid materials on the substrate kept at high temperatures. In case of graphene growth, a hydrocarbon gas such as methane (CH_4) was used as a precursor to yield graphitic material on a suitable catalytic material.

The main steps of the CVD assisted growth of graphene include:

(i) The decomposition of hydrocarbon into carbon, and

(ii) The formation of the graphitic structure, i.e., graphene on the catalytic surface.

Therefore, the most important roles of a catalyst in graphene growth are to lower the energy barrier of reactions involving hydrocarbon pyrolysis and effective formation of graphene layers. This condition is mostly satisfied by the transition metals like Ni, Cu, Pt, Pd, Rh, Fe, and Co. The catalytic activity of these metal is argued to arise from partially filled d orbitals [10]. **Figure 3-19** shows the assembled CVD for graphene growth.

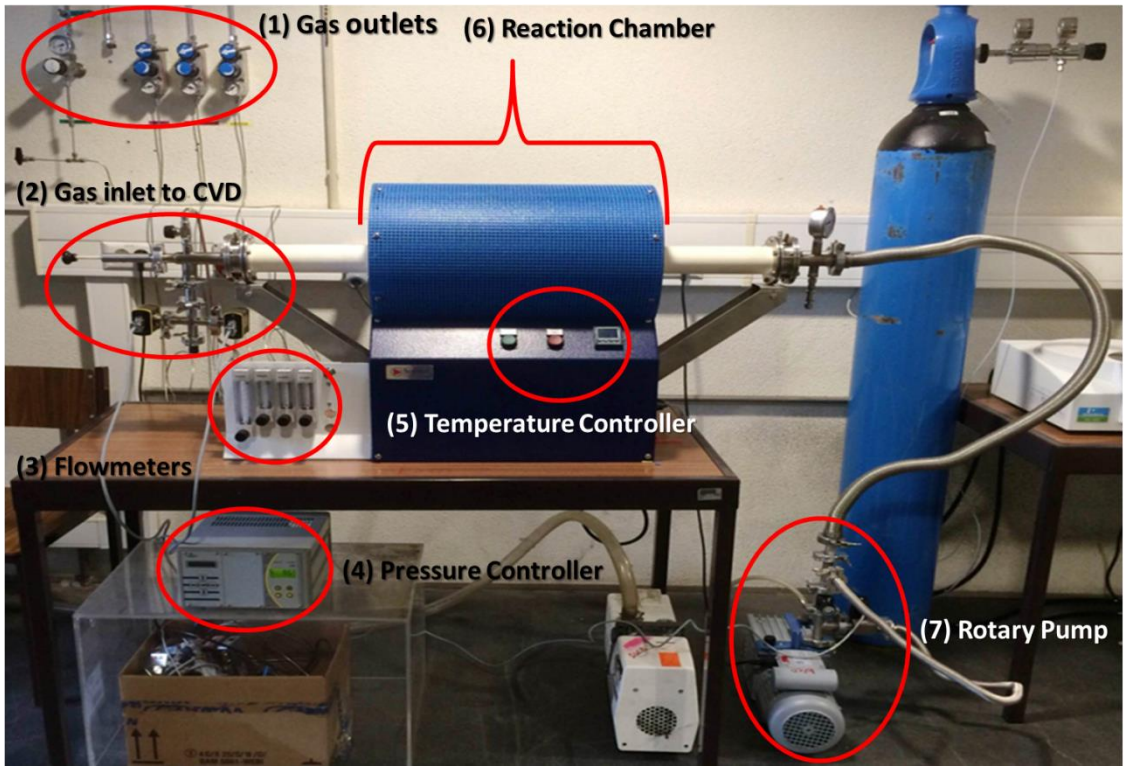

Figure 3-19: Assembled chemical vapor deposition (CVD) setup with different components. (1) Gas outlets, (2) Gas inlets for inserting different gases, (3) Flowmeters, (4) Pressure controller, (5) Temperature controller of CVD, (6) Reaction chamber, (7) Rotary pump.

The main components shown in the figure are:

(i) Gas outlets,

(ii) Gas inlets for inserting different gases,

(iii) Flowmeters,

(iv) Pressure controller,

(v) Temperature controller of CVD

(vi) Reaction chamber,

(vii) Rotary pump.

These components are the basic elements for CVD to be functional. Forthcoming section provides brief description of the major CVD components.

(i) Gas outlets: These are outlets extension for gas, which is being used during CVD depositions. The typical gases outlets consist of gas regulators with pressure gauge indicates and shut-off valve **(Figure 3-20).** Shut-off valves are required to maintain the right pressure, which is provided in gas lines. It may contain another shut-off valves, which are applied to over the high pressures (accidently created) by bye-passing it.

Figure 3-20: Gas regulator for gas pipeline connections. Pressure gauge indicates the gas pressure before it is supplied to pipeline. Adapted from [199].

(ii) Gas inlets: These are the starting point for inserting the gases in CVD. **Figure 3-21 (a),** shows the gas inlets, leak valve, and Pirani, which is further connected with pressure controller. The connection of flange (KF16), leak valve and pipeline is shown in schematic diagram in **Figure 3-21 (b)**. The schematic diagram presents additional connection of test-tube with butterfly valve, which is useful for other type of reaction like hBN and other volatile chemical reactions.

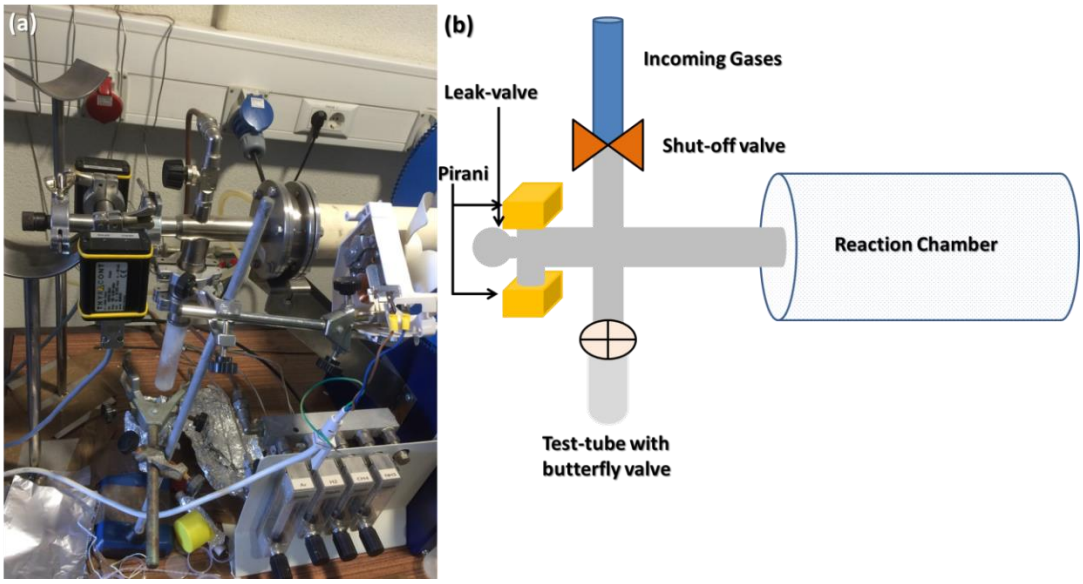

Figure 3-21: (a) Gas inlets for different gases. It also shows the different flanges, leak valve, and Pirani, (b) Schematic diagram for the connections.

(iii) Flow meter: The flow meters are used to monitor and control the gas flow inside the chamber. In our experiments, argon (Ar), hydrogen (H_2), methane (CH_4) and ammonia (NH_3) were used. The flow meters were purchased from Swagelok, and 1 flowmeter indicator (q/l) equaled to 17 sccm. These flowmeter were well calibrated from the company and were specific for different gases.

(iv) Pressure controller: It is used to monitor and control the pressure of CVD reaction chamber. This pressure controller has two electronic components (Pirani and Piezoelectric transducer connector), which are further connected with chamber to monitor CVD pressure. Notably, one electronic component (bye-pass) is connected to rotary pump to reduce/cut the high pressure, if occurred. VD9, obtained from THYRACONT GmbH was used in all the experiments performed in the present work **(Figure 3-22)**.

Figure 3-22: Pressure controller (VD9) for controlling the CVD reaction chamber's pressure. Adapted from [200].

(v) Temperature controller of CVD: As the name suggests, it was used to control the CVD reaction temperature. These PID (proportional integral derivative) temperature controllers are program based which store different programs. In our CVD, the PID controller was from EUROTHERM 3216 with 8 step heating programs see **Figure 3-23**.

Figure 3-23: PID (Proportional integral derivative) from EUROTHERM. Adapted from [201].

The program steps used were as follow:

TSP 1 (Target Set Point): 1050°C
RMP 1 (Ramp): 7.0
DWEL 1 (DWELL): 1:00
TSP 2 (Target Set Point): 1080°C
RMP 2 (Ramp): 0.5
DWEL 1 (DWELL): 0:10
TSP 3 (Target Set Point): 300°C
RMP 3 (Ramp): OFF

DWEL 3 (DWELL): OFF

The above codes were used for the deposition of pure graphene on Cu substrate at 1080^{o}C. The heating rate used was 7^{o}C/min till 1050^{o}C before annealing. After annealing Cu substrate at 1050 ^{o}C (1h), the temperature increases slowly with the rate of 0.5^{o} C until it reached 1080 ^{o}C and then it dwells for 10 mins. Afterwards it goes cooling slowly until 300 ^{o}C. Point to be noted here is that for cooling, no rate was used as during this period, the furnace was shut down because no cooling fans were used for a rapid cooling.

(vi) Reaction chamber: The most important part of CVD is the reaction chamber, which is typically of alumina or quartz. Normally, for a high temperature CVD, alumina is preferred. Though quartz can also sustain high temperature it is always recommended to use alumina based used for high temperature. The system in the study was based on alumina with 55 mm inner diameter and 65 mm outer diameter. Alumina was surrounded by heating coils/rods (nichrome or supercanthol), which were used to heat the chamber.

(vii) Rotary pump: To maintain the vacuum and selective pressure, rotary or other types of pumps were used. Generally, in CVD rotary pumps are used because the vacuum is not high **(Figure 3-24 (a))**. These pumps are connected with electronic pressure controllers as shown in the layout diagram **(Figure 3-24 (b)).** The electronic pressure controller is further connected with pressure controller (VD9) in order to maintain the suitable pressure.

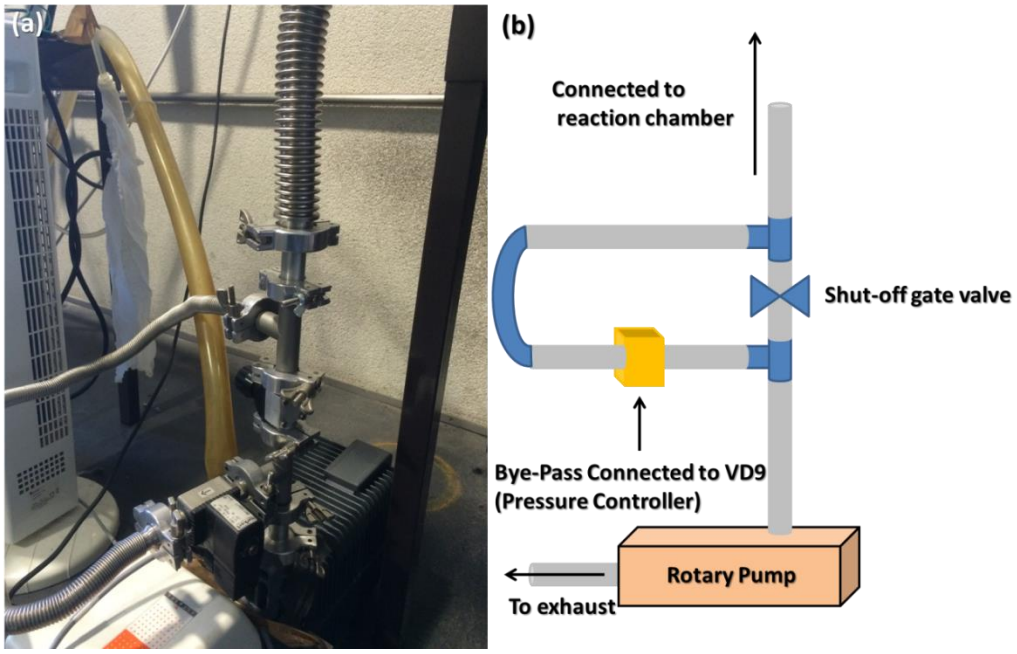

Figure 3-24: (a) Rotary pump system, with electronic bye-pass pressure controller connected for reducing the high pressure, and maintaining the suitable pressure.

Chapter 4:

Synthesis of pure graphene on copper

Abstract

This chapter describes the experimental strategy used in the present thesis work for the growth of pure graphene on copper (Cu) substrates adopting a methane-based CVD method. Different trial and error methods were screened for parameterizing the growth conditions. After numerous attempts, 35 torr pressures were found suitable for the growth of monolayer graphene on copper films and foils at 1080 ^{o}C on Cu foil of ~25μm thickness (Good Fellow, UK). The area of produced graphene on Cu foil was ~25 mm x 25 mm. The results from Raman, HR-XPS and HR-TEM showed excellent quality of graphene. The presence of very small D peaks confirmed the high quality of graphene crystals with strictly monolayer to a few layers thickness, and the sample can be considered as a pristine graphene. Additionally, HR-XPS analysis demonstrated the high quality graphene with C 1s in sp^2 configuration (284.8 eV). The standard quality of the samples was also reconfirmed by the absence of other components resembling the purity of graphene. The Raman mapping demonstrated a full coverage of the large area graphene on copper substrate. In addition, high crystallinity of graphene was confirmed by HR-TEM.

4. Synthesis of pure graphene on copper

4.1. Graphene on different metallic substrates

Metals play a crucial role in graphene depositions, where they act as catalysts for the growth process, and hence form a honeycomb like structures in/on different substrates. There are numerous reports in the literature on transitions metals that can be used for graphene deposition. Various metals such as ruthenium (Ru) [11, 202], iridium (Ir) [13, 203], cobalt (Co) [204], nickel (Ni) [2, 205], platinum (Pt) [204, 206] and palladium (Pd) [45, 204] are considered good for the growth process. The metal carbon solubility and the growth conditions determine the deposition mechanism. Metals are also responsible for the morphology along with the thickness of the graphene films. Graphene grown on Co(0001) and Ni(111) surfaces was reported to exhibit a lattice mismatch of less than 1% [26]. However, the mismatch can be more than 1% for Pt(111) [204], Pd(111) [204], Ru(111) [202], and Ir(111) [203]. In the case of Pt, it has higher catalytic ability of hydrocarbon (CH_4) which was previously confirmed by theoretical calculations [207]. Furthermore, it has stronger catalytic ability for hydrogen-dissociation for forming active atomic H.

Ni and Cu were reported to exhibit the promising results for graphene deposition. In particular, as compared to other transition metals, Cu can give good results because the electron transferred from CH bonds to fill 3d orbitals leads to only one unpaired electron available for interaction (the electronic configuration of Cu is [Ar] $3d^{10}4s^{1}$). However, in the case of Ni, one can find two 3d unpaired electrons. This is quite important as the electron passes from the 4d-orbital to 3d to generate a filled 3d electron shell to form most stable configuration [208]. Furthermore, the low solubility is also a key factor for suitable substrate. For example, Cu has solubility of 0.001 – 0.008 wt % at ~1080 ^{o}C; Co - 0.9 wt % at ~1320 ^{o}C and Ni has 0.6 wt % at ~1320 ^{o}C. Due to this low solubility and low catalytic activity, Cu creates soft bonds with carbon via charge transfer from the π electrons in the sp^2- hybridized carbon to the vacant 4s states of Cu [10, 209, 210]. Additionally, Ni and Cu are the most widely used due to their low cost and easy availability.

Taking these above facts in account, Cu and Ni were chosen for graphene depositions in the present thesis work. Graphene growth on Ni seems to limit the control of the number of layers, thus resulting in a single to a few layer graphene [211]; whereas the used Cu provided the growth of uniform and high-quality single layer over a large area. The previously mentioned quality and

uniformity were later checked by different techniques like Raman, XPS and TEM, which are discussed in the sections followed hereafter.

4.1.1. Growth conditions and characterization of the pure graphene on copper

As mentioned above we chose Cu and Ni as growth substrates for graphene. Depositions were performed using a vacuum with a vacuum pump at one corner, an introduction of gases step at the opposite corner and an alumina tube in the center surrounded by a cylindrical furnace. The vacuum pump was used for removing the atmosphere inside the alumina tube in order to replace it by high quality gases at the desired pressure. Thus, after *in-situ* cleaning the substrate by H_2/Ar gases at high temperature, the C-rich molecular precursor was added to the atmosphere. These precursors react with the Cu surface and decompose on it. Furthermore, the carbon atoms spontaneously reorganize on the surface forming the graphene sheet.

The growth process can be divided into five stages as described in **Figure 4-1**.

During the first stage, the metal substrate (Cu) was kept at room temperature (RT) inside the chamber for annealing in the Ar and H_2 (Ar:H_2::120:40, sccm) atmosphere till 900 ^oC under the pressure of 35 torr.

At stage II, at 900 ^oC, the flow of Ar was shut down and only H_2 was flown with 100 sccm till 1050 ^oC. This process was used to crystallize the metal substrates in order to form large grains.

During stage III, the furnace was tuned at the rate of 0.5 ^oC from 1050 ^oC to 1080 ^oC, and methane along with hydrogen (CH_4:H_2::10:50 sccm) was passed for the cracking and formation of methyl radicals from methane, which was the precursor of graphene, which later led to formation of high quality graphene.

After deposition (~70 min) in stage IV, the furnace and methane was closed; however, the flow of hydrogen and argon was continued (H_2:Ar::10:85 sccm) till 300 ^oC.

In the final stage V, the hydrogen flow was shut down and only argon (Ar:85 sccm) was continued till room temperature is reached and finally at room temperature the sample was taken out.

The as synthesized graphene, grown on Cu substrates was of high quality with the least number of defects, that was confirmed by different techniques, such as Raman, HR-TEM and HR-XPS.

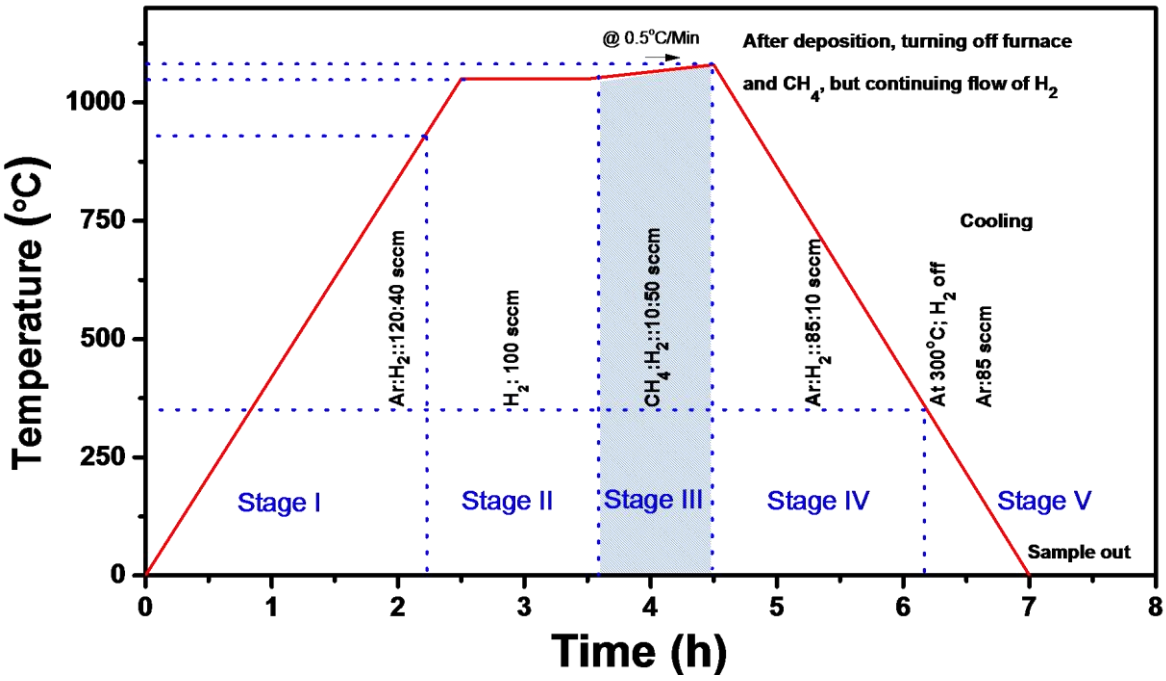

Figure 4-1: Growth process diagram for the large area pure graphene on metal substrates by modified thermal Chemical Vapor Deposition setup.

4.1.2. Characterization of as-synthesized graphene

4.1.2.1. *Raman spectroscopy:*

The as-synthesized graphene was characterized using non-destructive Raman spectroscopy, which has been considered the best method for quantifying the defect density and crystallographic quality of carbonaceous products [166]. This fast and non-destructive technique also allows us to distinguish graphene from graphite and a few-layer graphene and to probe doping level, strain, disorder, chemical derivatives and the atomic arrangement at the edges.

There are various bands/peaks like *G, 2D, D or D'*, which determine the nature and quality of the graphene synthesized.

Figure 4-2 shows the Raman spectroscopy results for pure graphene grown on 25µm thick Cu substrates (inset show the optical image). The spectra were recorded at different time intervals in the range from 10 to 1000s. The peak intensities related to *D*, *G*, *D'* and *2D* features were

collected and fitted with Lorentzian functions. As widely accepted, we refer to their heights as peak intensities and these are denoted as I_D, I_G, $I_{D'}$, I_{2D} for the *D*, *G*, *D'*, and *2D* peaks, respectively.

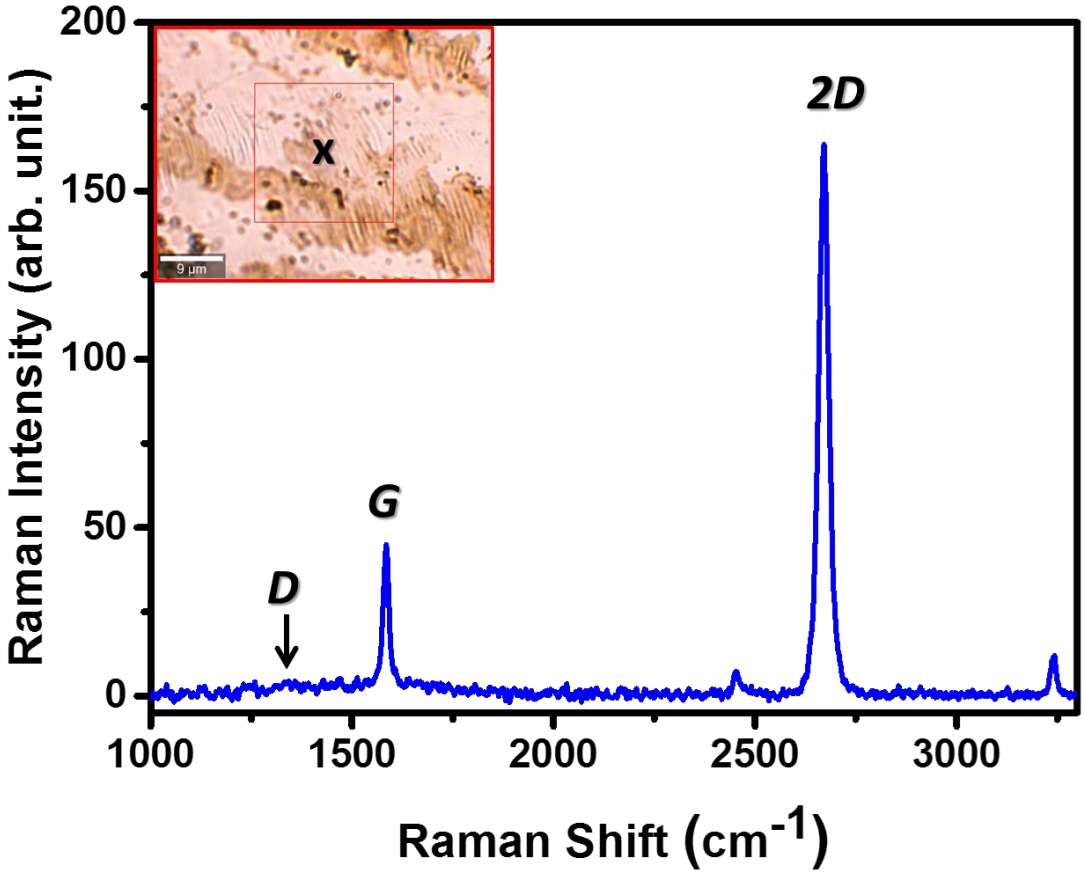

Figure 4-2: Full Raman spectra of pure graphene on copper substrate. The spectra show major peaks associated with graphene namely *D*, *G* and *2D*. The inset shows the optical image taken using 100x objective lens in Confocal – Raman equipment.

G and *2D* peaks must satisfy the Raman selection rules making Raman spectroscopy one the most important tools for probing the structural defects. Single-phonon intervalley and intravalley scattering processes activate the first two peaks. The defect peaks *D* and *D'* located as shoulder peaks on *G* peak provide the missing momentum in order to satisfy the momentum conservation in the Raman scattering process [167, 169].

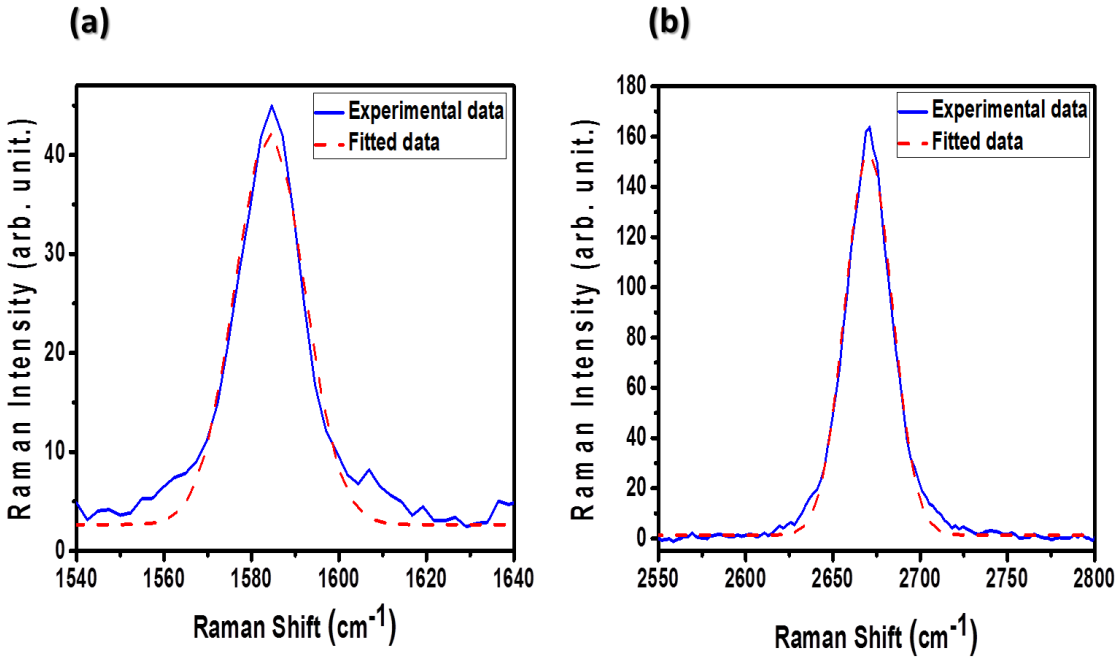

Figure 4-3: *G* and *2D* peaks of pure graphene on copper (Cu). The blue and red (dotted) spectra are respectively the experimental and fitted data obtained by Lorentzian mathematical function.

From the above spectra (**Figure 4-3**), the *G* peak was found to be at ~1584 cm^{-1} (full width at half maxima: *FWHM* ~18) for the graphene deposited on 25 µm thick Cu substrates. This peak is due to the E_{2g} phonon at the Brillouin zone center. The *2D* peaks, located at ~2694 cm^{-1} (*FWHM* ~30), are assigned to the second orders of D peak.

In the present work, we did not find *D* peak but small peaks were found (located at the concerned region) after magnifying in the range of 1280 – 1400 (cm^{-1}). Moreover, a minor peak (negligibly weak) was also located at 1350 cm^{-1} with the intensity I_D ~ 2.78. The latter band originated from the breathing modes of six-membered rings that are activated by defects. All these mentioned above parameters were acquired at 100 s acquisition time during Raman measurements.

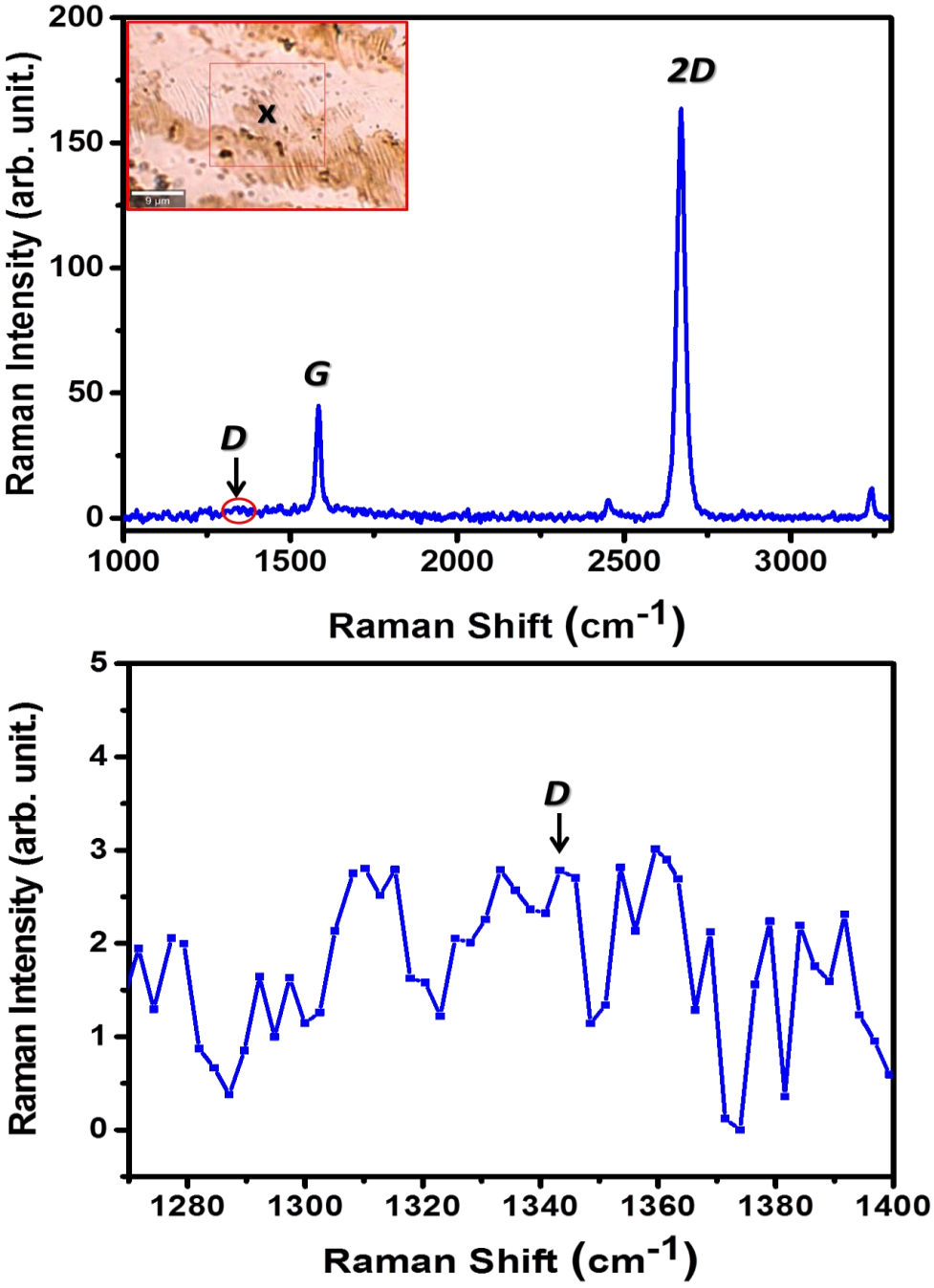

Figure 4-4: (a) Full Raman spectra with highlighted *D* Peak, and (b) Magnified *D* peak (with the range of 1280 – 1400 cm^{-1}) along with fitted data using Lorentzian mathematical function.

4.1.2.2. *Transmission Electron Microscopy*

Transmission Electron Microscopy (TEM) is the best possible technique to view and to detail any nanostructure, for example to study the morphology of graphene at the nanoscale. It was extensively used to determine the presence of rotational stacking faults [32, 91, 212]. Furthermore, TEM is quite relevant and fast tool for direct imaging the atomic structural and also the rotational misorientation in the few layer graphene (FLG) giving rise to definitive patterns [213]. TEM has been reported to provide the information about structural aspects, phases, impurities, elemental analyses and dislocations. Beside this, Selected Area Electron Diffraction (SAED) is also required to calculate the lattice parameter and to observe the crystallinity of the sample.

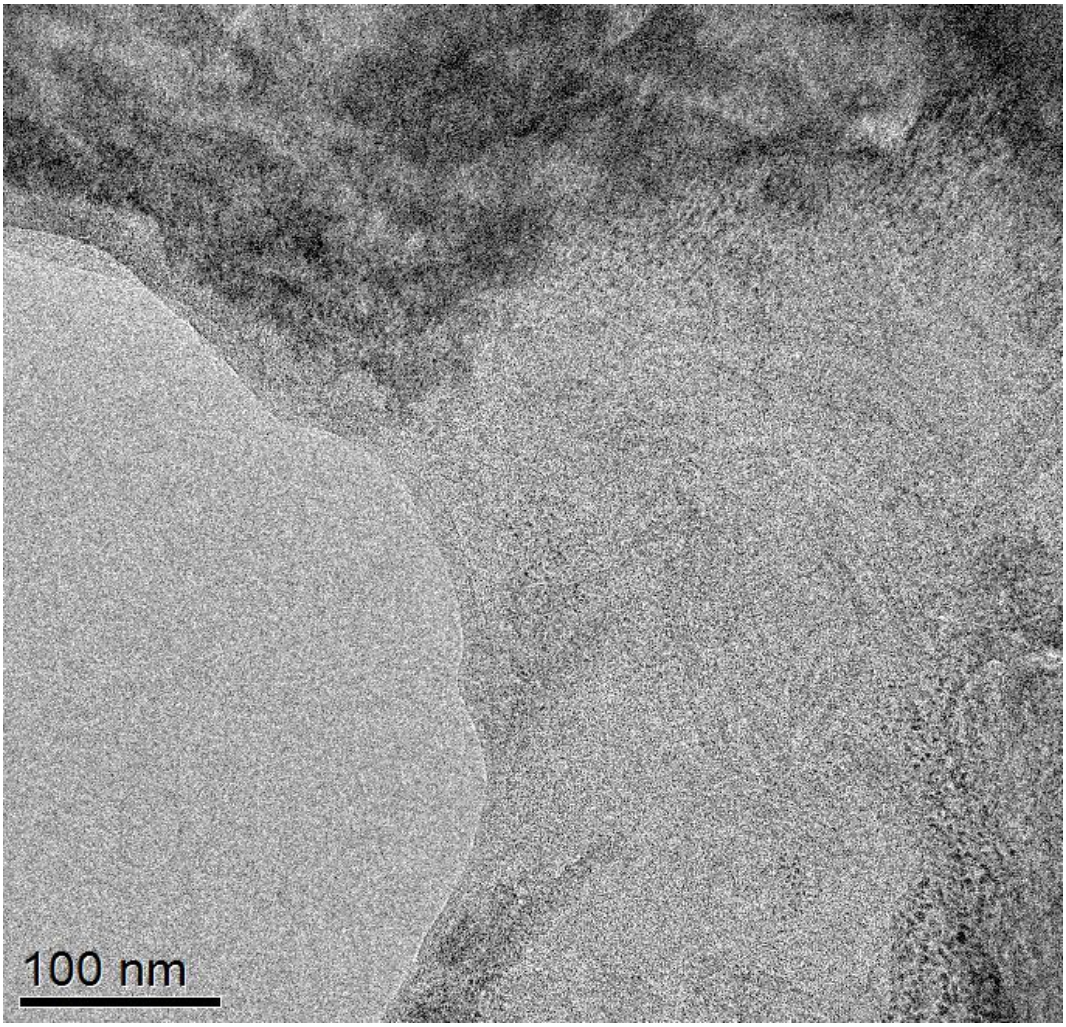

Figure 4-5: Bright-field HR-TEM images of graphene deposited on copper (Cu) substrate, taken on a Cu grid of 400 Mesh (Agar Scientific, G6210).

Figure 4-5 (above) shows the bright field TEM image, the uneven distribution of dark black and grey shows that upper and a lower secondary electrons detector, also a mix detection using both graphene is quite thick and amorphous with different layer. It was difficult to get the crystalline planes but, fortunately, they were found in HR-TEM image (**Figure 4-6**).

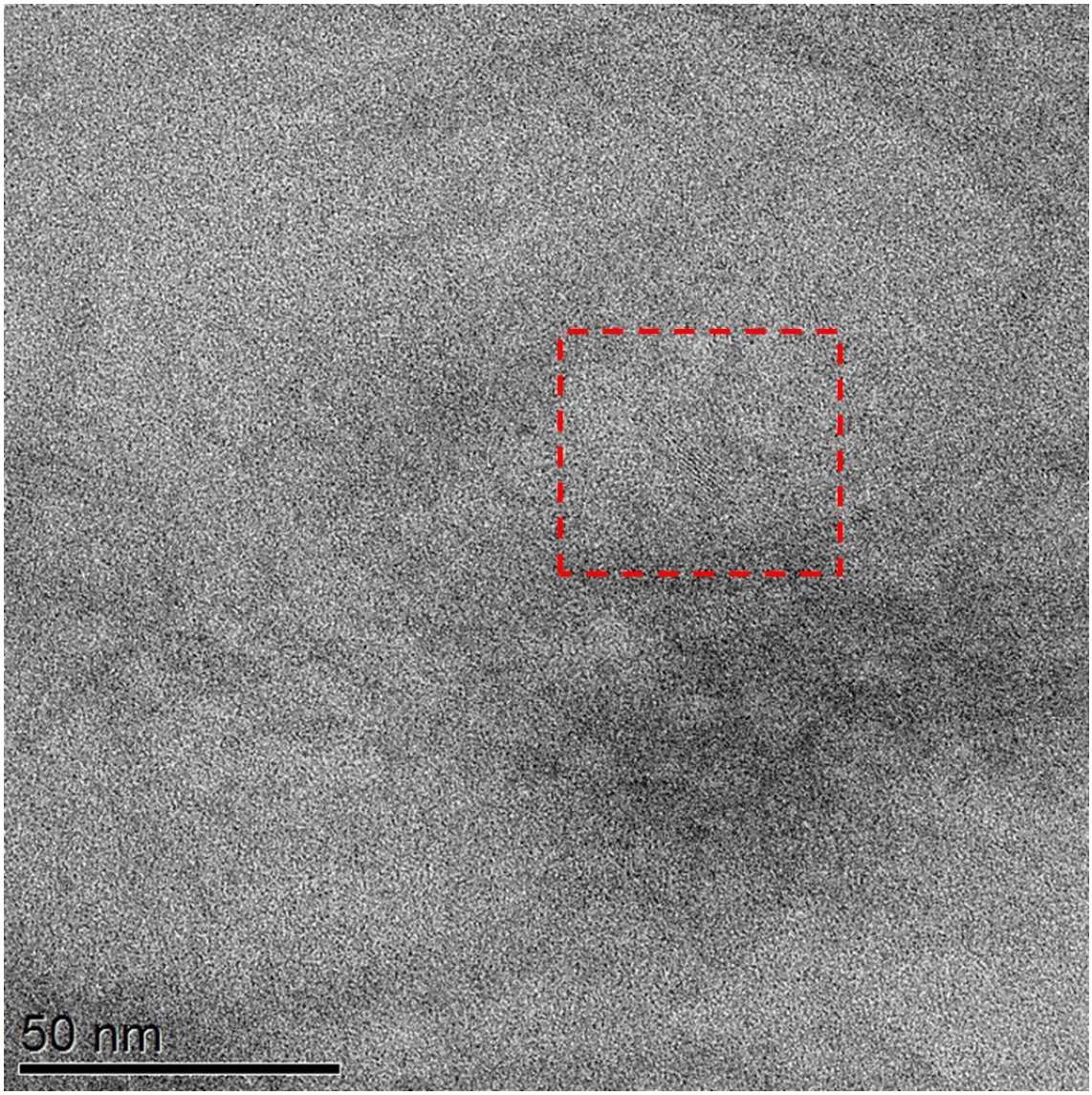

Figure 4-6: HR-TEM picture of bright field image, where inset (red box) shows the set of planes.

Figure 4-7 shows the HR-TEM of graphene. The red region (shown in the inset) represents a set of planes. Afterwards, FFT and inverse FFT were performed for processing the image (reducing unwanted noise and applying a mask). A line profile was also performed to analyze the set of

planes, the d spacing of the inter lattices was calculated and shown in the Table 4-1: Information related the d spacing and *hkl* from HR-TEM**Table 4-1**.

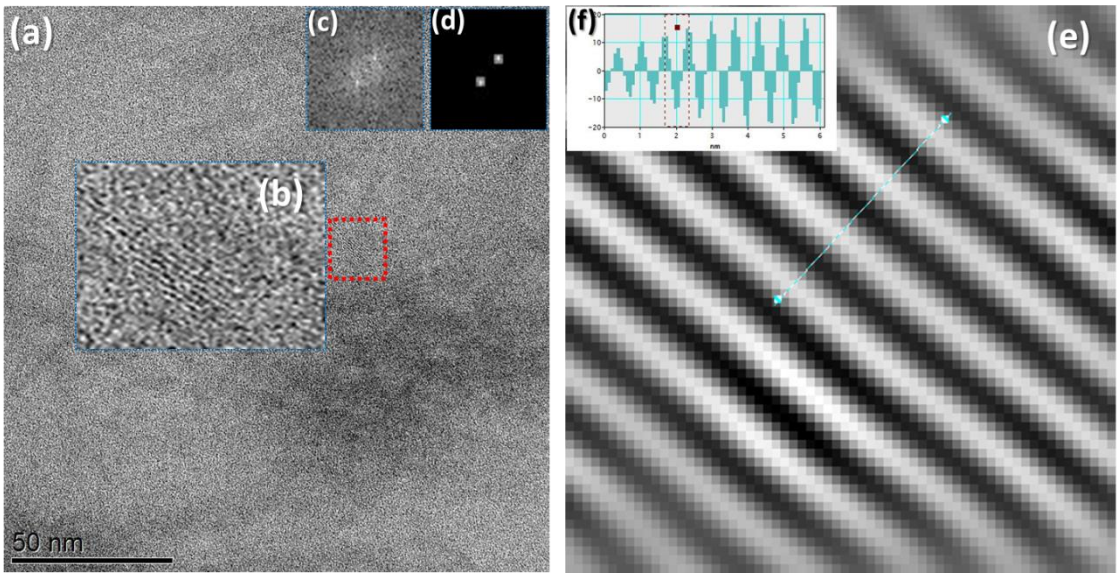

Figure 4-7: HR-TEM image of the large area indicated with a red box in (a) Bright field image. (b) Shows the set of planes. (c) Shows the FFT image of the region indicated in (a), (d) Masked applied FFT image corresponding to (c), (d) Unwanted noise reduced image of (c). (e) Inverse FFT image of the (d) with line profile. (f) Line profile showing the distribution.

4.1.2.2.1 Line profile of HR-TEM

The total distance of d spacing between the two-consecutive set of planes are found to be 6.69 Å.

Taking this data into account and comparing the value with database one from CaRine crystallography v3.1, it was possible to attribute it to [0 0 1] corresponding to the zone axis where electron diffraction pattern was acquired.

Table 4-1: Information related the d spacing and *hkl* from HR-TEM

d	*d* spacing (Å)	*hkl*
d	6.69	001

4.1.2.2.2 From Dark Field: Electron Diffraction

Electron diffraction performed on the same region shows two-hexagonal structures with radii r_1 and r_2, assuming the distance from the center to the spot a and b, respectively. There can be different possibilities for the measurements of SAED patterns. Since the measurements are performed in reciprocal space, it is recommended to use the ratio method as mentioned below. We cannot use the reciprocal measurement for the calculation as this may involve the error due to lens and camera constant. Keeping this in mind, the distance (in terms of pixels) from the center was calculated and found to be 76.446 and 133 pixels by using ImageJ software.

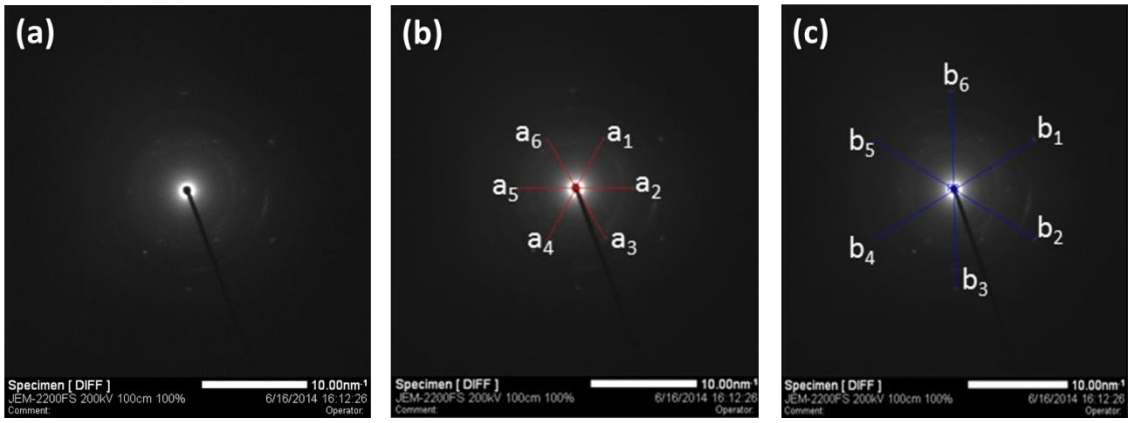

Figure 4-8: (a) Electron Diffraction showing six hexagonal spots with different planes (b) with (1 -2 0) and (c) with (1 -1 0) family of planes.

Applying the relation:

$$\boldsymbol{r_1\, d_1 = L\lambda = constant = r_2\, d_2\ ,} \qquad \text{(Eq. 4-1)}$$

where, r_1 and r_2 are the distance from the center of the spot, $d_1$and d_2 are the d spacing.

Hence from **Equation 4-1**, we have

$$\frac{r_2}{r_1} = \frac{133.71}{76.446} = \mathbf{1.749} \qquad \text{(Eq. 4-2)}$$

After simulation from CaRine crystallography v3.1, and the values taken from it, we have:

$$\frac{\boldsymbol{d\ values\ of\ (1{-}2\ 0)\ plane}}{\boldsymbol{d\ values\ of\ (1{-}1\ 0)\ plane}} = \frac{\mathbf{2.139}}{\mathbf{1.235}} = \mathbf{1.739} \qquad \text{(Eq. 4-3)}$$

The ratio of d spacing for (1 -2 0) and (1 -1 0) was found to be the most nearest to the ratio obtained in **Equation 4-2** which also says that the assumption of two planes was right.

Table 4-2: Information related the d spacing, radius, ratio and *hkl* from both experiment and database.

d	Radius *(in pixel)*	*hkl*	d spacing *(Data base)*	Ratio r_2 & r_1 *(experimental)*	Ratio d_1 & d_2 *(ICDD file)*
r_1	76.446	1-20	1.235	**1.749**	**1.739**
r_2	133.71	1-10	2.139		

Furthermore, reciprocal lattices from (-3 -3 -3) to (3 3 3) has been shown in the **Figure 4-9**. The zone axis was found to be [0 0 1]. The two hexagons are shown with the green and red dotted line presenting (1 -2 0) and (1 -1 0) planes.

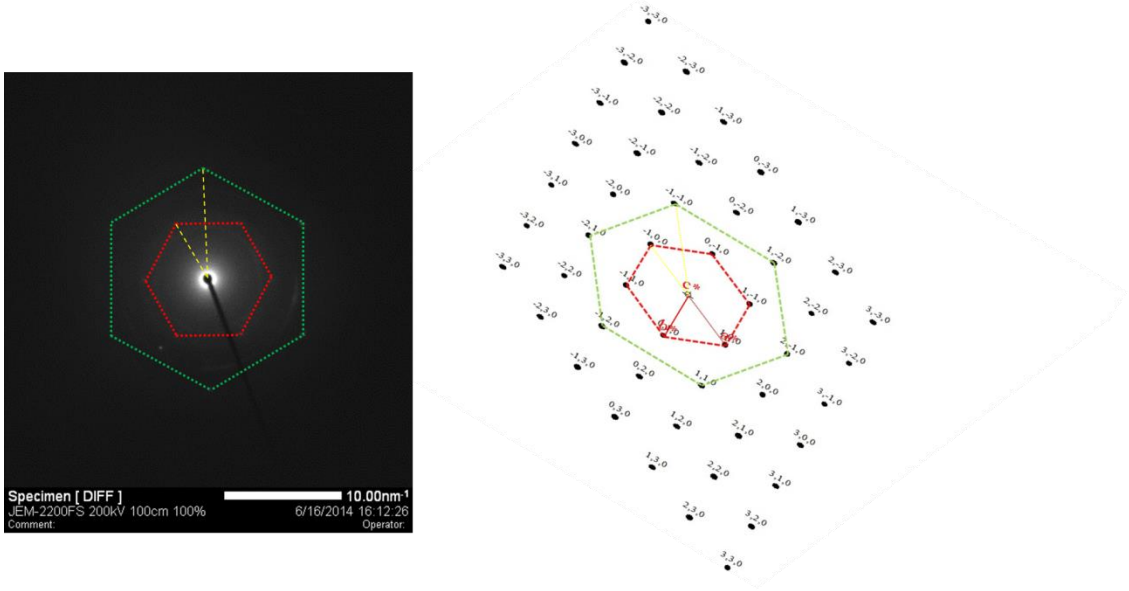

Figure 4-9: (a) Electron Diffraction showing six hexagonal spots of (1 -2 0) and (1 -1 0) family of planes, (b) The two set of planes with green and red dotted line (hexagonal shape) in reciprocal space.

4.1.2.2.3 Contaminations

During ED imaging mode, a few nanoparticles were observed very near to hexagonal structure. To confirm the same, dark field image acquisition was performed which showed the presence of copper oxide (CuO) or iron chloride ($FeCl_3$) nanoparticles. **Figure 4-10** presents the dark field image of the same region corresponding to bright field image **Figure 4-6**.

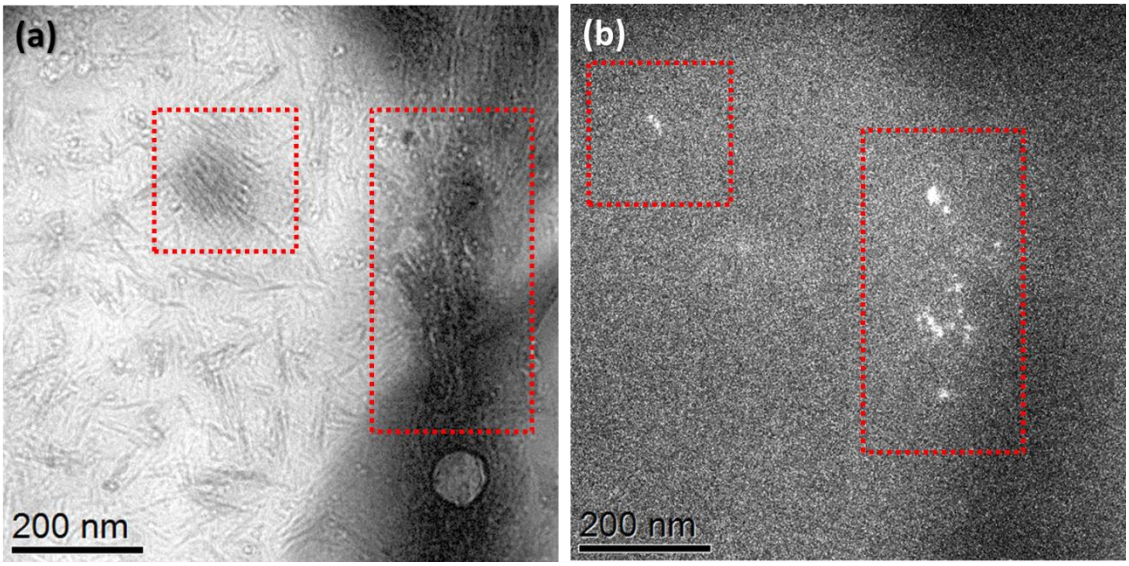

Figure 4-10: (a) Bright field image and (b) dark field image of contaminations. The inset showing CuO or $FeCl_3$ nanoparticles.

From the bright, dark, electron diffraction and HR-TEM modes, the graphene was found to be mostly thick and wrinkle based; although in some regions, it exhibited crystalline structure (hexagonal). The electron diffraction pattern resembled two hexagonal structure of (1 -2 0) and (1 -1 0) family of planes. From the simulation (CaRine crystallography), the zone axis was calculated and found to be [0 0 1]. In case of HR-TEM image, by applying FFT to the image and calculating the d spacing, (0 0 1) plane was found, which says that probably during the HR-TEM image mode, the area which showed the crystalline structure was the zone axis in the ED mode. The same set of planes was viewed in HR-TEM and ED but in ED the sample was tilted to have better spots.

4.1.2.2.4 Extra carbon depositions

It would be interesting to mention here that it was very difficult to perform more HR-TEM images with much higher resolution because there was a huge carbon deposition due to strong electron beam **(**Figure 4-11: (a, b) Extra carbon depositions (in forms of rings) formed due to high energy electron beam during transmission electron microsocopy studies.**Figure 4-11)**. The dark rings shown in the inset correspond to carbon deposition due to high energy. Keeping this in the mind, one has to perform TEM measurements at comparatively low electron beam energies.

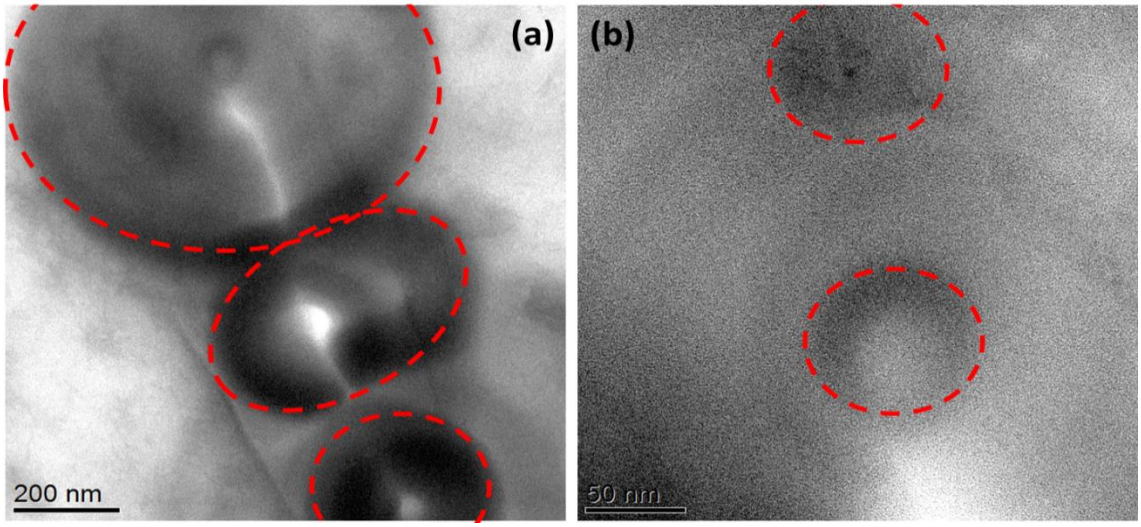

Figure 4-11: (a, b) Extra carbon depositions (in forms of rings) formed due to high energy electron beam during transmission electron microsocopy studies.

4.1.2.3. *X-ray Photoelectron Spectroscopy*

X-ray Photoelectron Spectroscopy (XPS) is a well suited technique for characterizing graphene samples on different substrates [173]. **Figure 4-12** shows the overview XPS spectrum of the as-grown graphene on Cu substrate. Clear signals were identified related to Cu atoms from the substrate and carbon from graphene in a good agreement with literature. Only a small feature appears at a binding energy that corresponds to oxygen atoms.

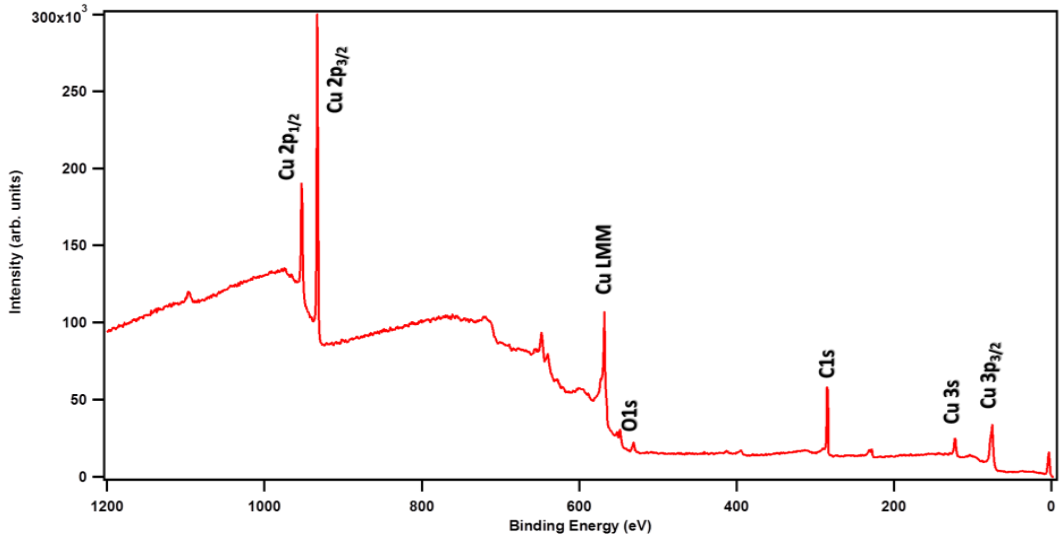

Figure 4-12: Overview of the XPS spectrum of graphene on copper (Cu) substrate along with major elements indicated.

Interestingly, it can be seen that the C 1s core level of graphene on Cu is very sharp and centered at a BE (binding energy) of 284.5 eV. This attributes it to the C sp^2 bond and can be fitted by only one component; hence, high-quality graphene deposition on Cu substrate is confirmed.

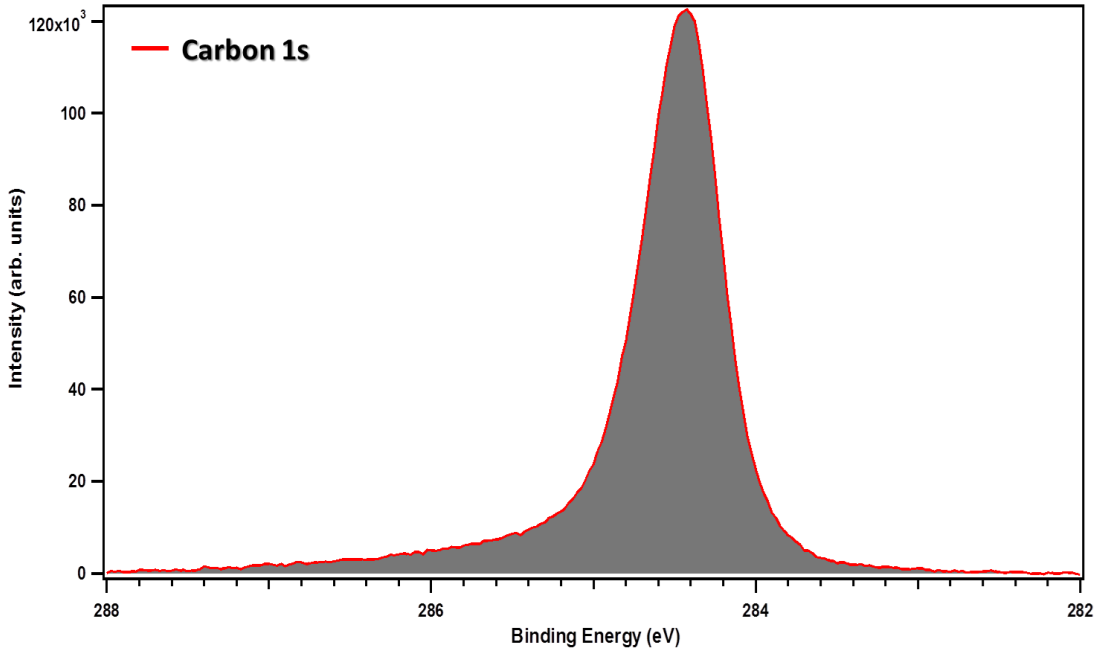

Figure 4-13: High Resolution XPS showing C 1s core levels peak. The as–grown graphene can be fitted by a single C sp^2 component.

4.1.2.4. *Homogeneity of the graphene layer: Raman mapping*

The Raman mapping was performed to check the homogeneity of the deposited samples. **Figure 4-14** shows the Raman mapping of the *D, G* and *2D* band intensity of the graphene grown on Cu substrate. The color contrast confirms that the graphene was more or less homogeneously deposited. However, the bright color contrast may differ from point to point due to the presence of some defects or uneven surface of Cu substrate, which occurred because of its annealing at relatively high temperature (~1080°C).

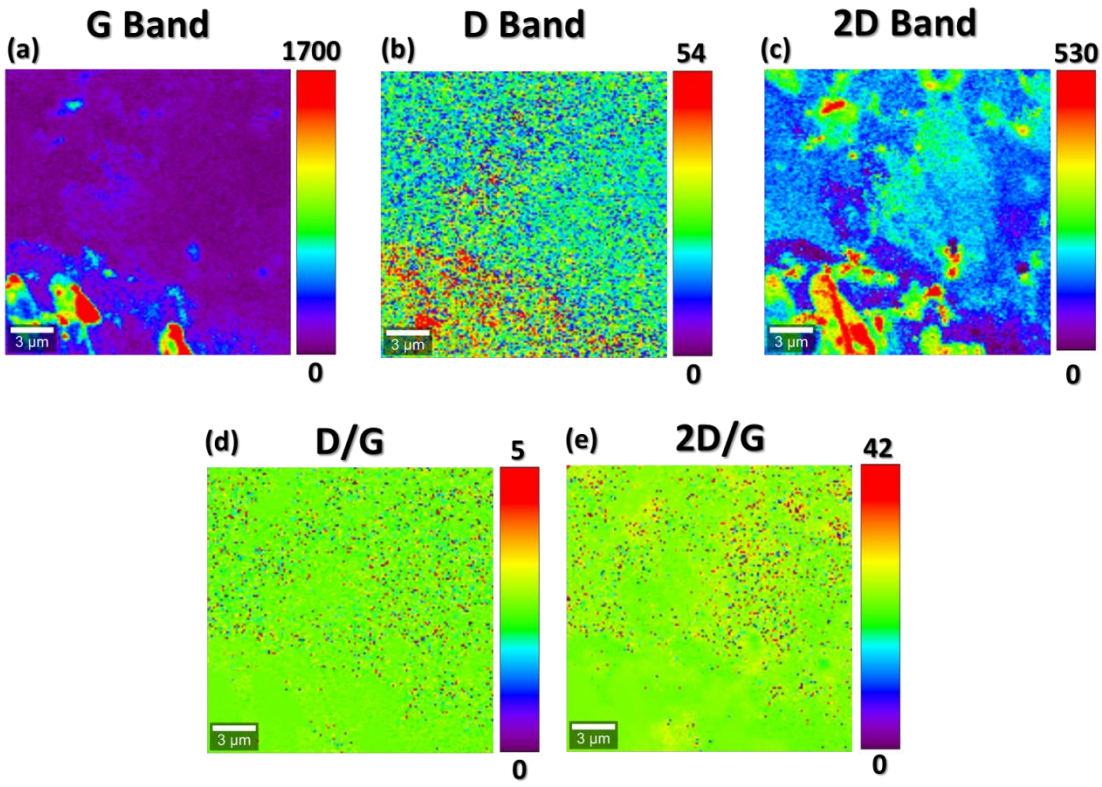

Figure 4-14: Raman mapping integrated intensities of the (a) *G*, (b) *D* and (c) *2D* using 532 nm laser source of graphene grown on Cu substrates. (d) and (e) shows the calculation of integrated intensities of I_D/I_G and I_{2D}/I_G respectively. The vertical bars show the color profile in the Raman mapping, with scale in CCD counts.

The mapping also assumes that the graphene was deposited on the entire surface of the substrate. This result suggests that the CVD process is able to produce large area graphene.

4.1.3. Quantification of defects

Although graphene is generally considered as a perfect honeycomb crystals real samples may have defects created during the growth process [214]. Using Raman spectroscopy, one can easily probe the defects concentration since it is a suitable technique that always obeys the Raman selection rule (due to presence of *G* and *2D* peaks). In spite of the previous facts, the emergence of *D* and *D'* is also natural because it provides the missing momentum that satisfies the Raman scattering process [167-169].

By the intensive use of local activation model [215-217], the intensity of any defect activated peak $I(x)$, where $x = D\ or\ D'$, as compared to the *G* peak intensity $I(G)$, is given by:

$$\frac{I(x)}{I(G)} = C_A \frac{(r_A^2 - r_S^2)}{(r_A^2 - 2r_S^2)} \left[e^{-\pi r_S^2/L_D^2} - e^{-\pi(r_A^2 - r_S^2)/L_D^2}\right] + C_S\left[1 - e^{-\pi r_S^2/L_D^2}\right]. \quad \text{(Eq. 4-4)}$$

It can be seen that above equation is dependent on the intensity of defect activated peaks which further depends on the two length scales, r_S and r_A . These are the radii of the two circular areas measured from the defect site.

r_S corresponds to radius of the structurally disordered area around the defect; hence, this might change from defect to defect [217]. For distances larger than r_S but shorter than r_A, the lattice structure is preserved; however, the proximity to a defect causes a mixing of Bloch states near the ***K*** and ***K'*** valleys of the graphene Brillouin zone, hence causing the breaking of selection rules, and this will lead to an enhancement of the *D* band [215, 217].

r_A corresponds to the disk, where the *D* peak scattering takes place and it defines the activated area.

C_A depends only on the Raman mode, being roughly given by the ratio of the electron-phonon coupling between the two phonons considered [215, 217]. C_S is the factor assumed to depend only on the geometry of the defect for a fixed phonon mode.

It is important to mention that Eq. 4-4 can also be applied to the integrated area. In the case of low defect concentration, the use of integrated area or intensity is equivalent [215, 217, 218]. However in the case of high defect concentration, one must consider the peak intensity obtained from full width at half maximum [216].

Using the Taylor expansion of Eq. 4-4, the same equation can be modified and, using the concerned values of different variables (r_S ~3 nm, r_A ~1 nm, C_A = 4.2 and C_S = 0 [216, 217]), the defect density can be calculated as:

$$n_D = 10^{14} / \pi L_D^2 , \quad \text{(Eq. 4-5)}$$

where n_D is the defect density (in cm^{-2}) and L_D is the mean distance between two defects.

Hence, from the above equation we have:

n_D = 1.8 x 10^{10} cm^{-2}

However, this defect concentration calculated by the use of Raman spectroscopy can come from several reasons and one cannot confirm that these defects are directly related to carbon-carbon bonds. There might be other reasons such as effect of copper substrate etc. [219, 220].

4.1.4. Conclusions

From the above characterization results, it can be said that the use of methane as a precursor in the CVD can yield the growth of pure graphene on Cu substrate. The presence of very small *D* peaks confirmed high quality of graphene crystals with either a monolayer or a few layers graphene and the sample can be considered as pristine graphene. HR-XPS analysis confirm also the high-quality graphene with C 1s in sp^2 configuration (284.8 eV). The absence of other components reflects the purity of graphene and again shows the absence of defects. Furthermore, from the Raman mapping image, full coverage of large area graphene on Cu substrate was demonstrated. HR-TEM results also corroborated the above conclusions and confirmed high crystallinity of the obtained graphene with two-type of rotational planes. This can be due the presence of wrinkles formed during the transfer of graphene sheet on TEM grids. However, it is common to have such type of wrinkles upon transfer of graphene from Cu on any arbitrary substrate such SiO_2/Si, Au, Si_3N_4 etc. To this end, it can be concluded that CVD can be further extended to dope graphene with heteroatoms (H, N, B, etc.) and combine graphene with a wide variety of functional materials for intended applications. In principle, CVD is not only applicable for graphene, but also can be extended to other functional materials on industrial scale.

Chapter 5:

Synthesis of *in-situ* ammonia doped graphene

Abstract

This chapter describes the experimental strategy used for *in-situ* ammonia doped graphene growth on copper substrates using a methane-based CVD method. Various trial and error depositions were performed for parameterizing the growth conditions. After numerous attempts, 35 torr pressures were found to be suitable for doping of graphene. Several Cu substrates were used with different thicknesses (10, 20 and 25 μm). This chapter also describes the role of copper substrate thickness in the *in-situ* doping of graphene with ammonia. We convincingly show that the standard copper foil widely used for graphene deposition is not very efficient, and smaller thickness (10 μm) has to be used for the successful heteroatom engineering of graphene, which is strongly needed for many electronic applications of this material. The results from Raman, HR-XPS and HR-TEM demonstrate the efficient doping and defects created in graphene. The evidence of *D* and *D'* peaks confirm the defects formation in graphene. High Resolution X-ray Photoelectron Spectroscopy (HR-XPS) precisely affirms ~0.4 atomic % of nitrogen intercalations in graphene. Our results show that the substitutional type of nitrogen doping dominates over the pyridinic configuration. In addition, X-ray diffraction (XRD) pattern displays all the XRD peaks associated with carbon. However, the peak at ~24° is suppressed by the substrate peaks (Cu). Furthermore, using Raman mapping, we demonstrate large area graphene deposition on copper substrates.

5. Synthesis of *in-situ* ammonia doped graphene

To build graphene-based circuits for microelectronic applications, the modulation of electronic properties of this material is required. One way to achieve this is to induce defects by doping with *n*- or *p*-type doping elements. Doping is a common technique for tuning the electronic properties of any material. Previous reports show that carbon nanotubes (CNTs) can be efficiently doped with *n*-type and *p*-type using nitrogen and boron atoms, respectively [221-223]. Similarly, in the case of graphene, doping can also significantly change its electronic properties. Theoretical and experimental studies [224] revealed that substitutional doping should modify the electronic band structure of graphene [225-227] which enhances the possibilities of its applications [228-230]. Doped graphene promises several breakthroughs and widespread potential applications due to predicted superconductivity [231], ferromagnetism [232], etc. Given this, intensive research is now focusing on the possibility of graphene doping under controlled conditions.

During this PhD work the focus was given on an *in-situ* nitrogen doping of graphene by the use of ammonia as a source of nitrogen atoms in the home made CVD setup.

5.1. Growth of *in-situ* ammonia doped graphene by CVD

Graphene growth on copper substrates was very similar to the synthesis of pure graphene on the same substrate. The growth process can be divided into six stages as described in **Figure 5-1**.

Ammonia (NH_3) gas was used *in-situ* to supply nitrogen atoms during growth in a CVD setup within the alumina tube furnace (see the schematic diagram).

During the first stage, the metal substrate was annealed inside the chamber in the Ar and H_2 (Ar:H_2::120:40 sccm) atmosphere from RT till 900 ^oC under the pressure of 35 torr.

At stage II, at 900 ^oC the flow of Ar was shut down during this process and only H_2 was flown with 100 sccm for 1h, this process was required for crystallizing the metal substrate in order to form large grains.

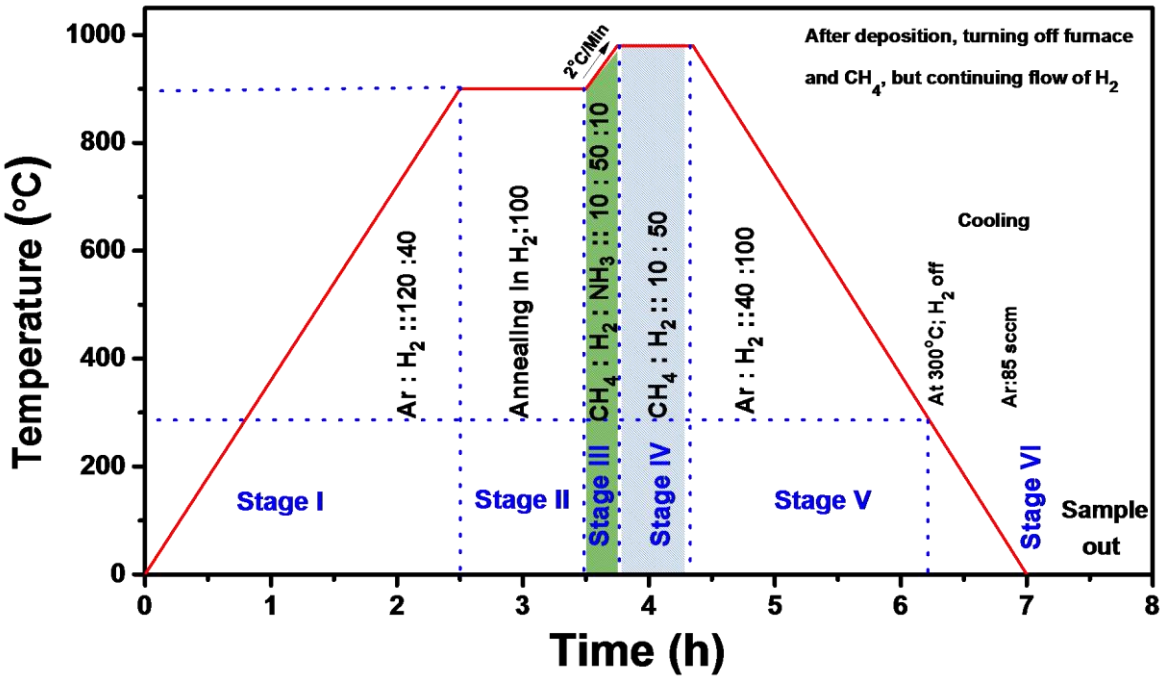

Figure 5-1: Growth process diagram for the large area *in-situ* ammonia doping of graphene on metal substrates by modified thermal chemical vapor deposition setup.

During stage III, the furnace was heated at the rate of 2 °C from 900 °C to 980 °C and ammonia along with methane and hydrogen (CH_4:H_2:NH_3:: 10:50:10 sccm) was passed for 15 min for the cracking, doping and formation of methyl radicals from methane, which was the precursor of graphene which later led to the formation of high quality coating. During this, ammonia was the source for the nitrogen atoms for doping. This created additional nitrogen atoms involved in the methyl radicals and formed the nitrogen bonds with the carbon atoms. These enhanced the possible sites for N intercalation in graphene sheets. Mainly three types of bonding were found in graphene with incorporated nitrogen, namely, substitutional, pyridinic and pyrrolic ones [224].

After providing the sufficient amount of nitrogen for doping, the supply of ammonia was stopped as too much of ammonia will act as an etchant for graphene and copper substrate. At stage IV, only methane and hydrogen (CH_4:H_2::10:50 sccm) were passed for supplying more methyl radicals and sufficient carbon atoms for 20 min.

After deposition (~15-20 min) at stage V, the furnace and methane flow were closed, however the flow of hydrogen and argon was continued (H_2:Ar::10:85 sccm) till 300 °C, so that the copper substrate should not get oxidized.

At stage VI At (at around 300 °C) the hydrogen flow was shut down and only argon (Ar: 85 sccm) was continued till room temperature (RT) was reached and finally the samples were taken out.

5.2. Characterization of as-synthesized ammonia doped graphene

5.2.1.1. *Raman Spectroscopy*

Raman spectra of as-synthesized *in-situ* ammonia doped graphene were measured **(see Figure 5-2)** using non-destructive Raman spectroscopy, which is commonly used to quantify the defect density and crystallographic quality of carbonaceous products. It is the best fingerprint technique for analyzing the properties of the carbon related materials including graphene [166]. This technique allows distinguishing among single layer, a few layers graphene and graphite. It is also sensitive to defects, excess charge, strain and atomic arrangement of the edges. Various peaks such as *G, 2D, D or D'* which can determine the nature and quality of the graphene were measured and fitted using mathematical Lorentzian function.

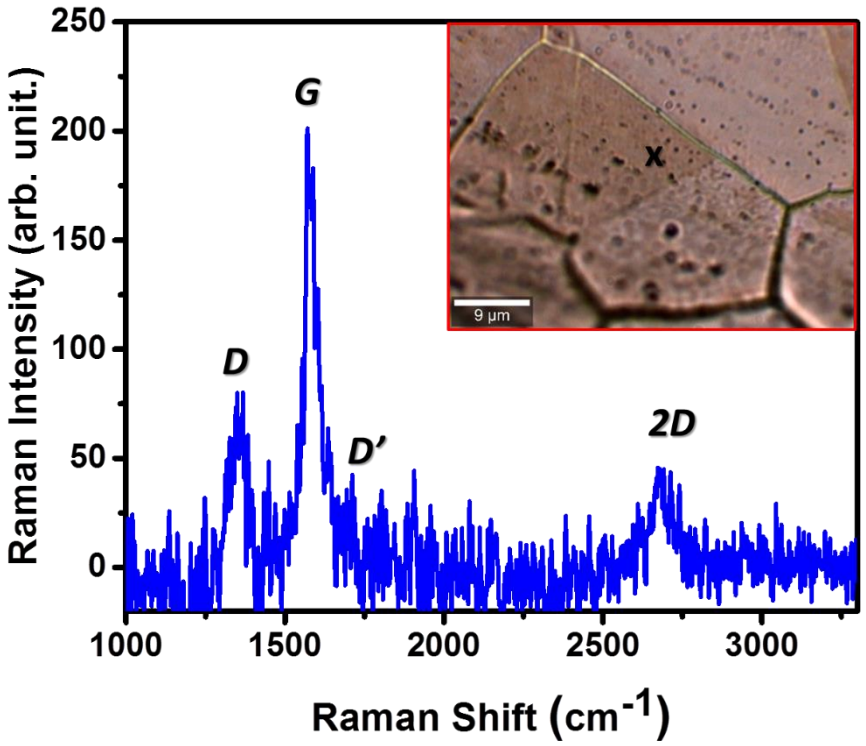

Figure 5-2: Full Raman spectra of *in-situ* ammonia doped graphene on copper substrate. The spectra shows major peaks associated with graphene namely *D, G, D'* and *2D*. The inset showing the optical image taken using 100x objective lens in Confocal – Raman equipment.

The *G* peak **(see Figure 5-3 (a))** corresponding to the E_{2g} phonon at the Brillouin zone center (Γ point) was found at ~1580 cm^{-1} with *FWHM* around 50. The overtone peak *2D* peak **(see Figure 5-3 (c))** which is associated with the breathing modes of six-atom rings (it comes from TO phonons in the vicinity of the *K* point and activated by a resonant intervalley scattering process) was found at ~2685 cm^{-1} with *FWHM* of 109. The *D* peak (at ~1350 cm^{-1}, *FWHM* of 100) **(see Figure 5-3 (b))** and *D'* peak (at ~1630 cm^{-1}, *FWHM* of 24) **(see Figure 5-3 (a))** were related to single phonon intervalley scattering events. As it is well known, these defects provide the missing momentum in order to satisfy momentum conservation during the Raman scattering process.

The as synthesized graphene was doped on 20µm copper substrate using ammonia. The ammonia gas is rich in nitrogen (N) atoms which contain one additional electron and, when replacing the carbon atom in the graphene lattice, novel electronic properties can be envisaged.

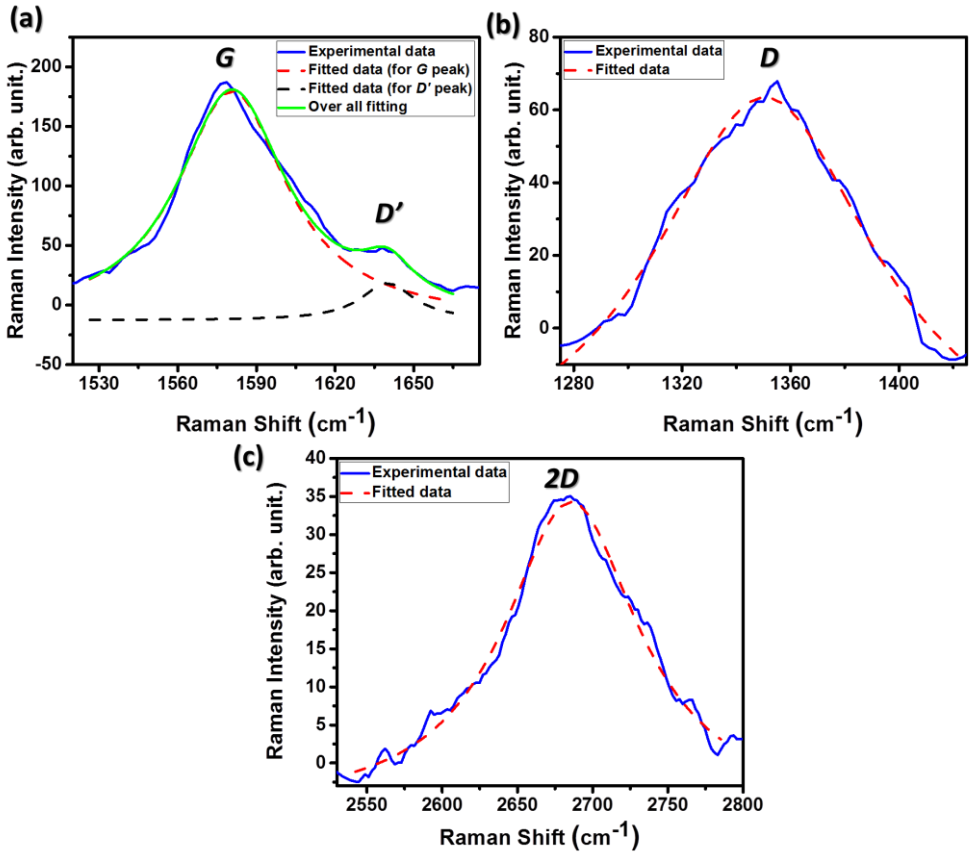

Figure 5-3: Experimental (blue line) and fitted data using Lorentzian mathematical function (dotted lines). (a) *D*, (b) *G* and *D'*, (c) *2D* peaks associated with the *in-situ* ammonia doped graphene on Cu.

This incorporation of nitrogen into a matrix of carbon is a necessity to reach the desirable semiconducting properties [233-237].

5.2.1.2. *X-ray Photoelectron Spectroscopy*

HR-XPS was performed on as synthesized *in-situ* ammonia doped graphene to study and to identify chemical environments associated with the incorporation of nitrogen atoms into the sp^2 hybridized structure of carbon. **Figure 5-4** shows the normalized overview of XPS spectra for the as-grown *in-situ* ammonia doped graphene. In the spectra, all the main core level peaks are indicated which are associated with carbon (C), copper (Cu) and nitrogen (N). The spectrum also describes the presence of oxygen, which was probably due to the fact of formation of oxides that were removed later by annealing of the samples at 873 °C.

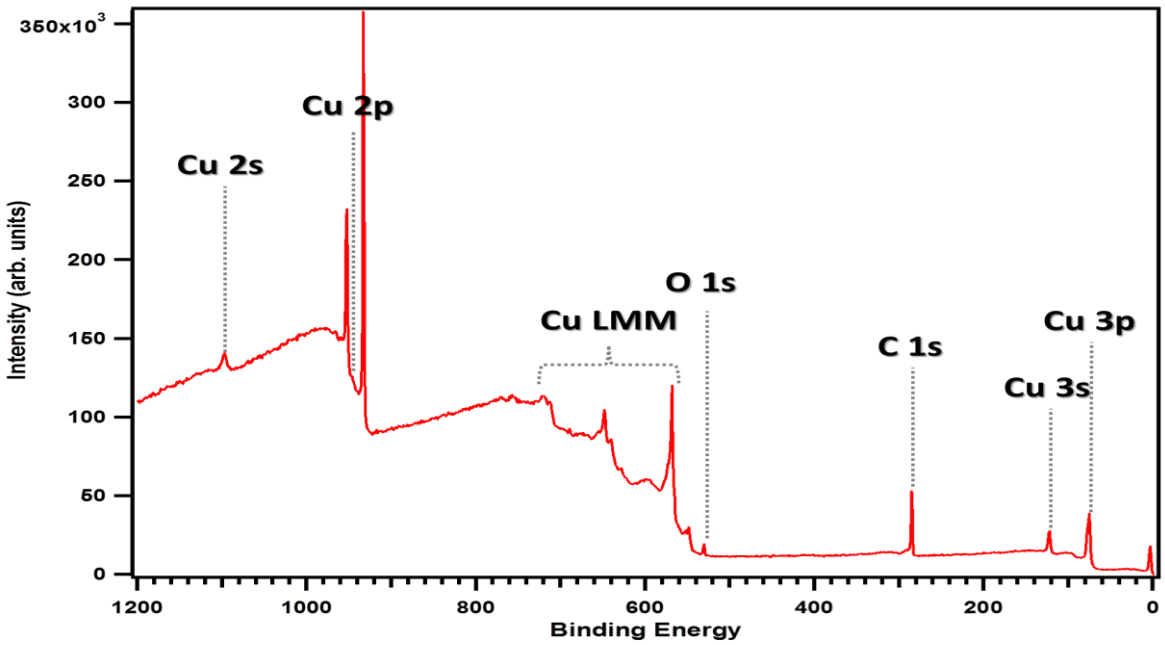

Figure 5-4: Normalized overview of XPS spectra of the *in-situ* ammonia doped graphene grown on copper substrate. The main core levels related to substrates (Cu, Si and O) are indicated together with C 1s.

Figure 5-5 shows the high resolution core level peak associated with *in-situ* ammonia doped graphene as C 1s, this was quite similar to C 1s of pure graphene grown on copper substrate. Moreover, the peak can be fitted with only one component centred at BE of 284.5 eV, which can

be related to C sp^2 [173]. In the spectra, the red line is the experimental data, the grey peaks are the mathematical fitting and finally the black line is the overall resultant fitting. The fitting was performed by the speciallized software (CasaXPS).

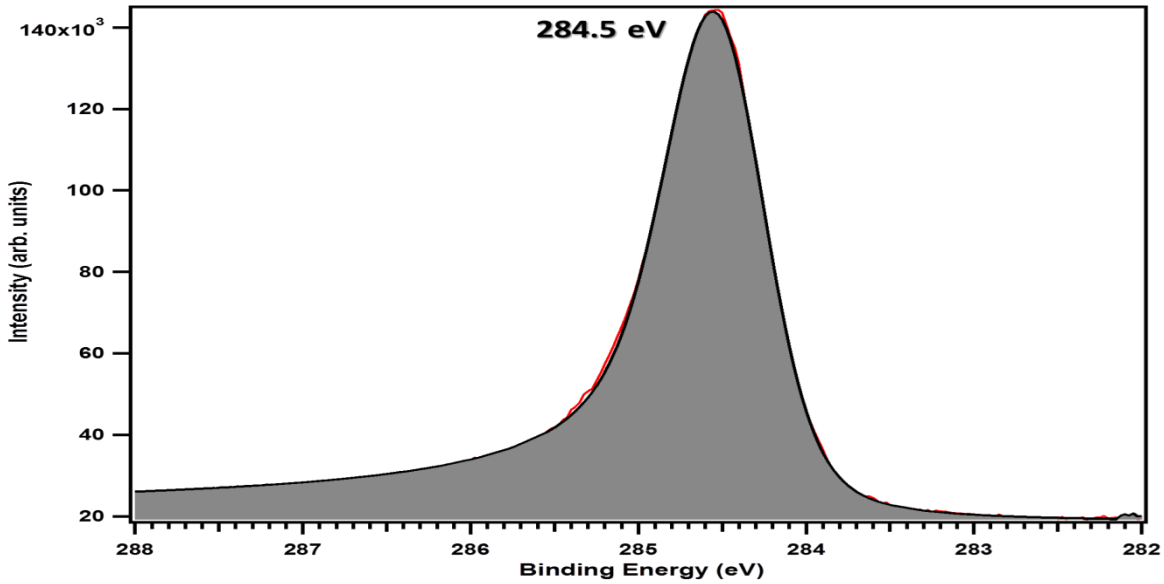

Figure 5-5: Showing the C 1s core levels obtained by high resolution XPS of the as grown *in-situ* ammonia doped graphene. The peak can be fitted by a single C sp^2 component.

Figure 5-6 shows the core level peak of nitrogen (N 1s) of the as grown *in-situ* ammonia doped graphene on a Cu substrate. It also presents peak deconvolution into two individual subcomponents, indicating two types of nitrogen incorporation into the graphene framework. The feature appearing at lower binding energy (~398.5 eV) is commonly assigned to the pyridinic configuration, while the component located at higher BE (~401 eV) suggests graphitic nitrogen, where N directly substitutes sp^2 hybridized carbon. From the ratio between both components in the *in-situ* ammonia doped graphene we can reveal a predominance of the desired graphitic N (substitutional) over the pyridinic type of substitution.

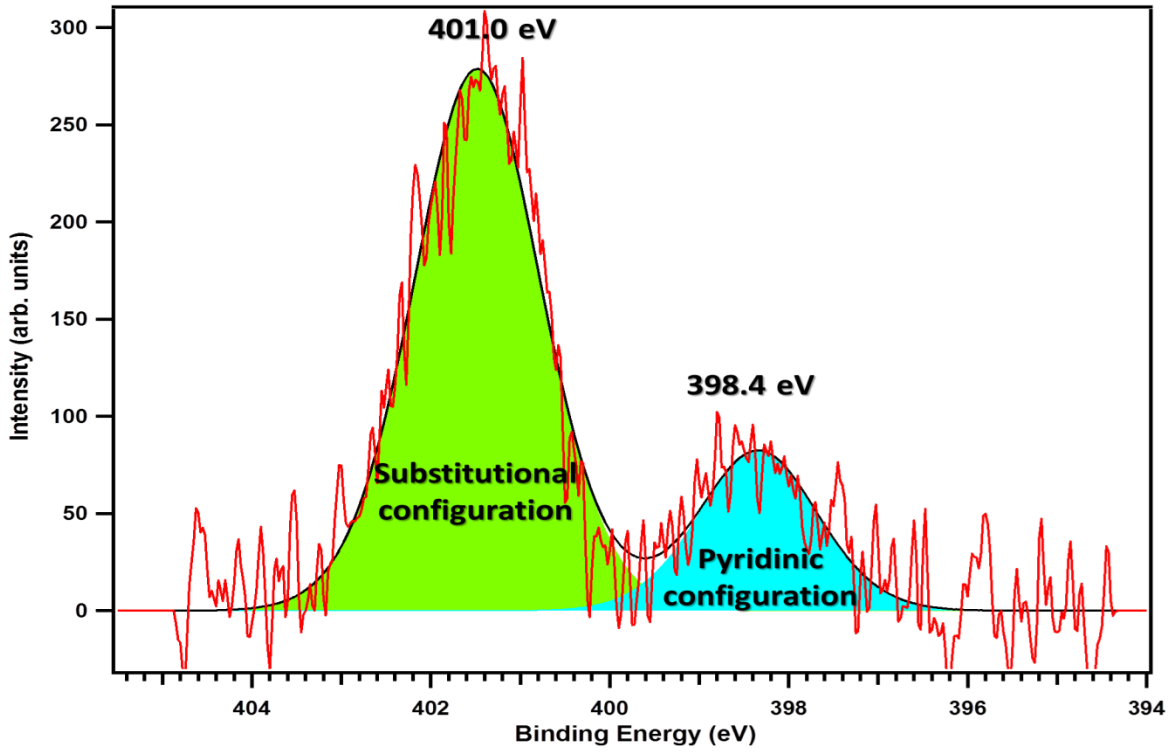

Figure 5-6: High resolution XPS spectrum showing the core level of N 1s of *in-situ* grown ammonia doped graphene on Cu substrate.

5.2.1.3. *Transmission Electron Microscopy*

After the CVD process of the *in-situ* ammonia doped graphene growth was completed, SEM images in transmission mode (**Figure 5-7**) were acquired. In can be seen from the TEM image that the majority of the areas covered by graphene looks like largely crumpled (**Figure 5-8: TEM image showing the crumbled like structure of** *in-situ* ammonia doped graphene on TEM grid.) paper on the lacey carbon TEM grid, which clearly indicates the flexibility of the sample. This crumpling is very common and can be seen in the majority of places on the TEM grid. It can be concluded that these are coming from both growth and post-treatment processes and can be also observed in the graphene produced by CVD in the absence of NH_3 [236, 238]. **Figure 5-10 - Figure 5-14** shows the HR-TEM image of *in-situ* ammonia doped graphene and we were able to find numerous crystalline planes (as marked in image).

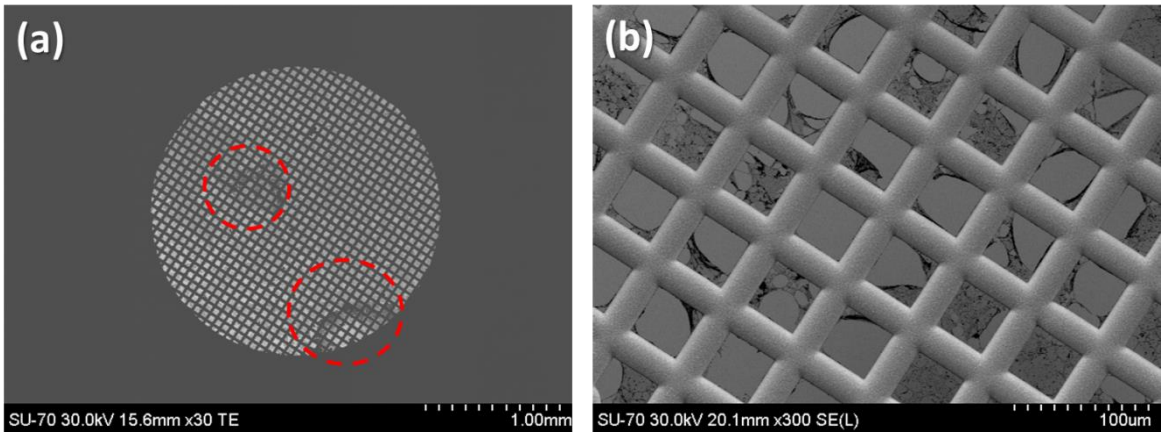

Figure 5-7: The images of *in-situ* ammonia doped graphene from (a) upper (b) lower secondary electrons detectors in Transmission mode.

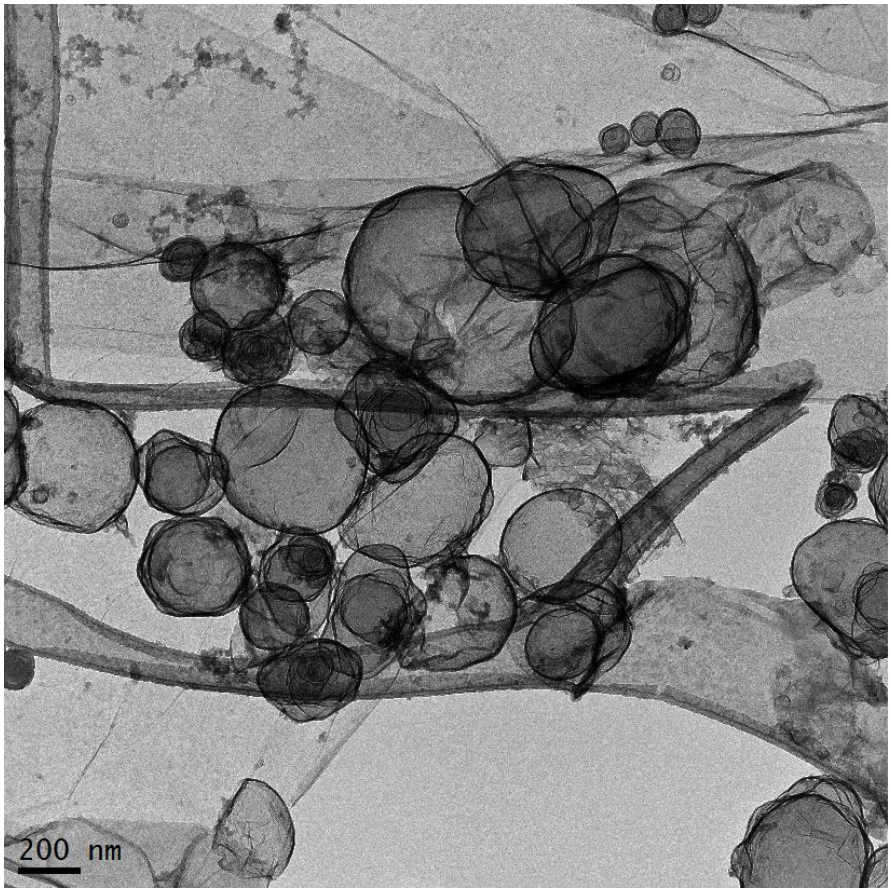

Figure 5-8: TEM image showing the crumbled like structure of *in-situ* ammonia doped graphene on TEM grid.

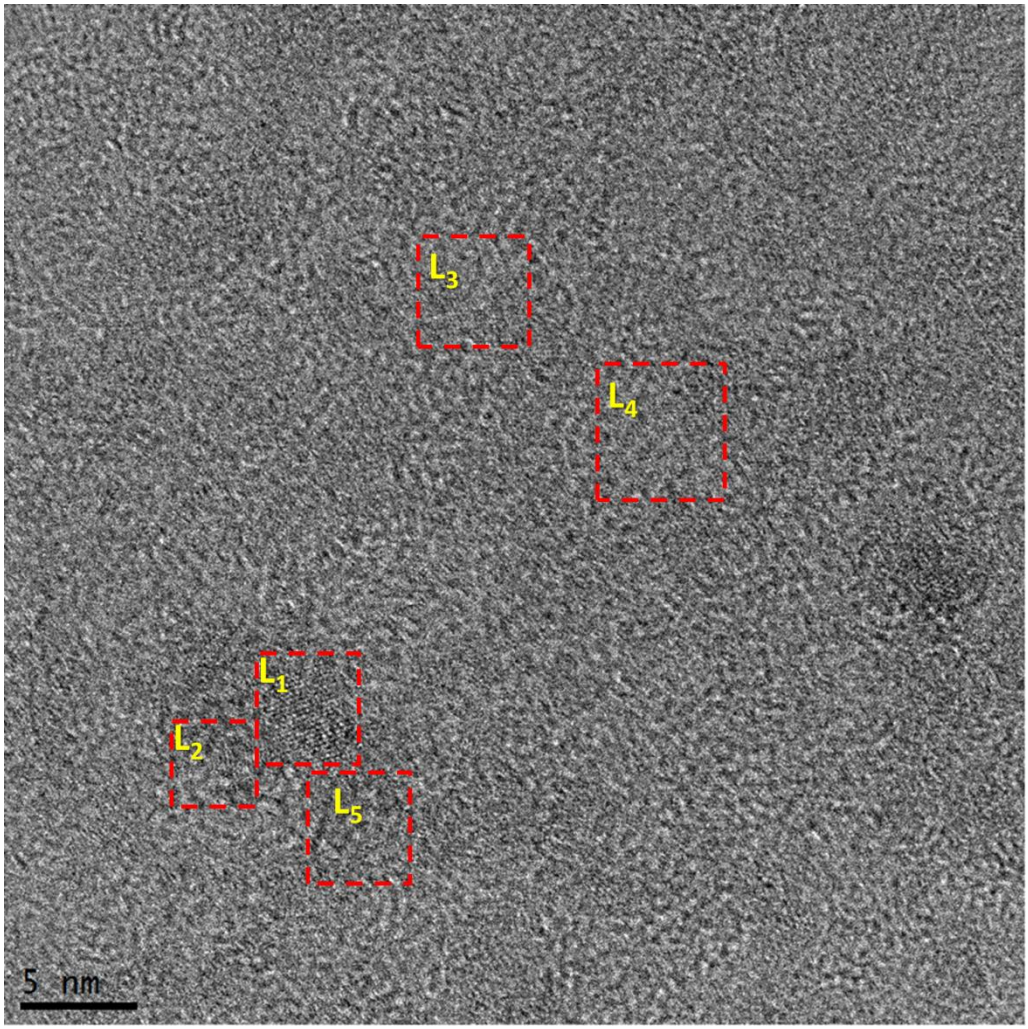

Figure 5-9: HR-TEM bright field image. Inset (red box) shows the set of planes located at various places marked as labels.

Location 1 (L_1)

Figure 5-10 shows the HR-TEM image of an *in-situ* ammonia doped graphene. The red box shows a set of planes. After processing the image (reducing unwanted noise and applying the mask) it was possible to perform FFT and inverse of FFT. A line profile was performed to analyze the set of planes, the d spacing of the inter lattices was calculated and shown in **Table 5-1**.

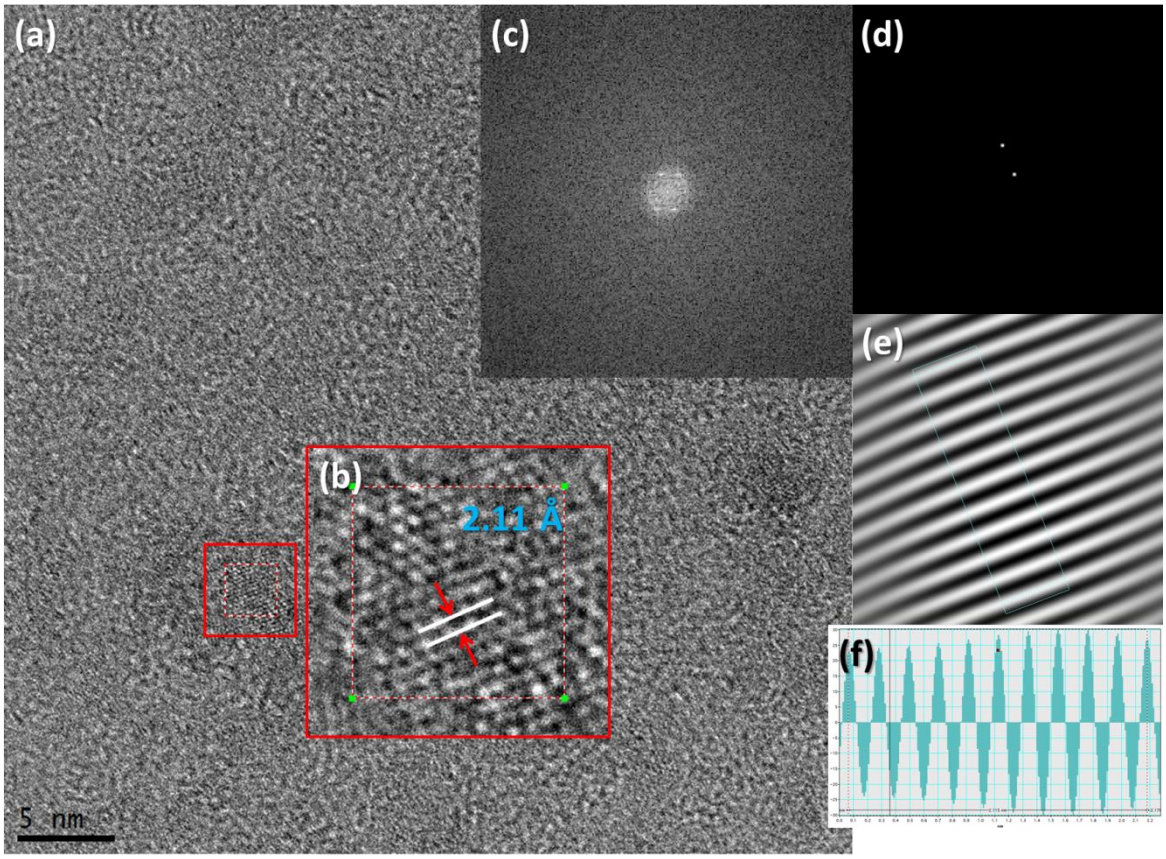

Figure 5-10: HR-TEM image of the large area location (L_1) indicated with a red box, (a) Bright field image. (b) Shows the set of planes. (c) Shows the FFT image of the region indicated in (a), (d) Masked applied FFT image corresponding to (c), (d) Unwanted noise reduced image of (c). (e) Inverse FFT image of the (d) with line profile. (f) Line profile showing the distribution.

5.2.1.3.1 Line profile of HR-TEM

The total distance of d spacing between 10 consecutive planes was found to be 2.11 nm, so for each set of consecutive planes, it was 2.11 Å

Comparing the above value with the database from CaRine crystallography v3.1, it was found that it belongs to a [100] plane, which corresponds to the zone axis when we acquired the electron diffraction pattern.

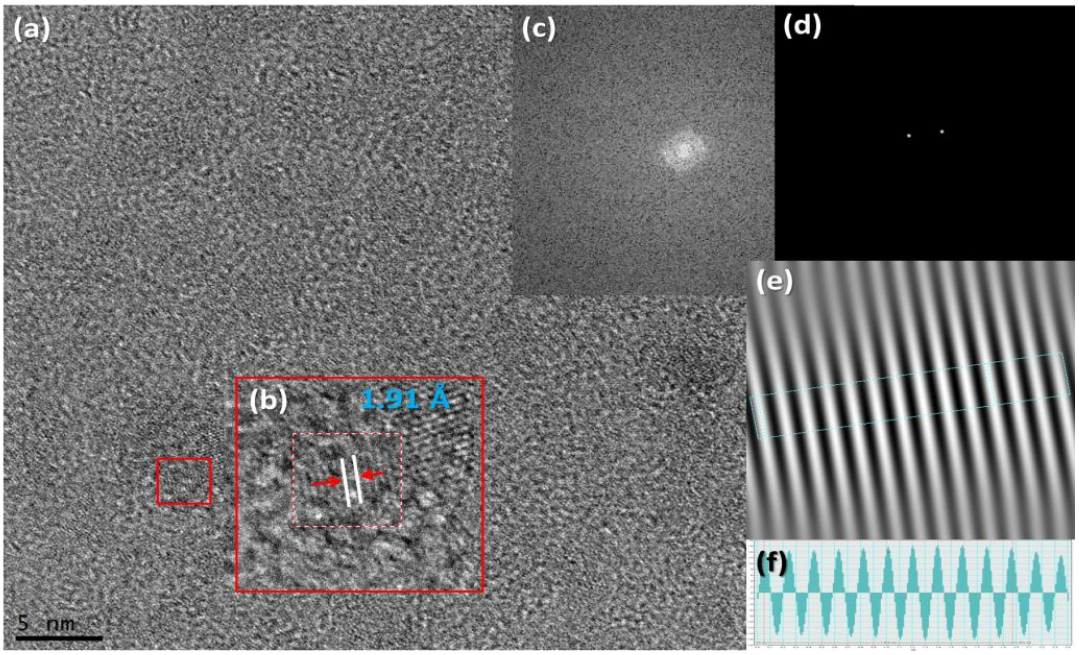

Figure 5-11: HR-TEM image of the large area location (L_2) indicated with a red box, (a) Bright field image. (b) Shows the set of planes. (c) Shows the FFT image of the region indicated in (a), (d) Masked applied FFT image corresponding to (c), (d) Unwanted noise reduced image of (c). (e) Inverse FFT image of the (d) with line profile. (f) Line profile showing the distribution.

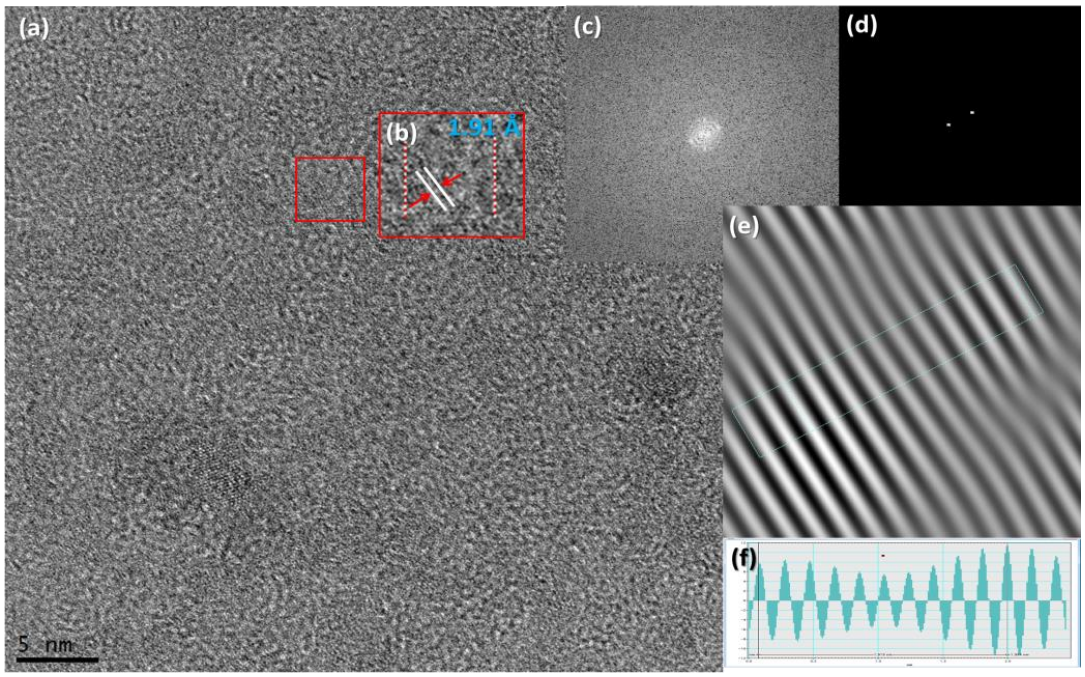

Figure 5-12: HR-TEM image of the large area location (L_3) indicated with a red box, (a) Bright field image. (b) Shows the set of planes. (c) Shows the FFT image of the region indicated in (a), (d) Masked applied FFT image corresponding to (c), (d) Unwanted noise reduced image of (c). (e) Inverse FFT image of the (d) with line profile. (f) Line profile showing the distribution.

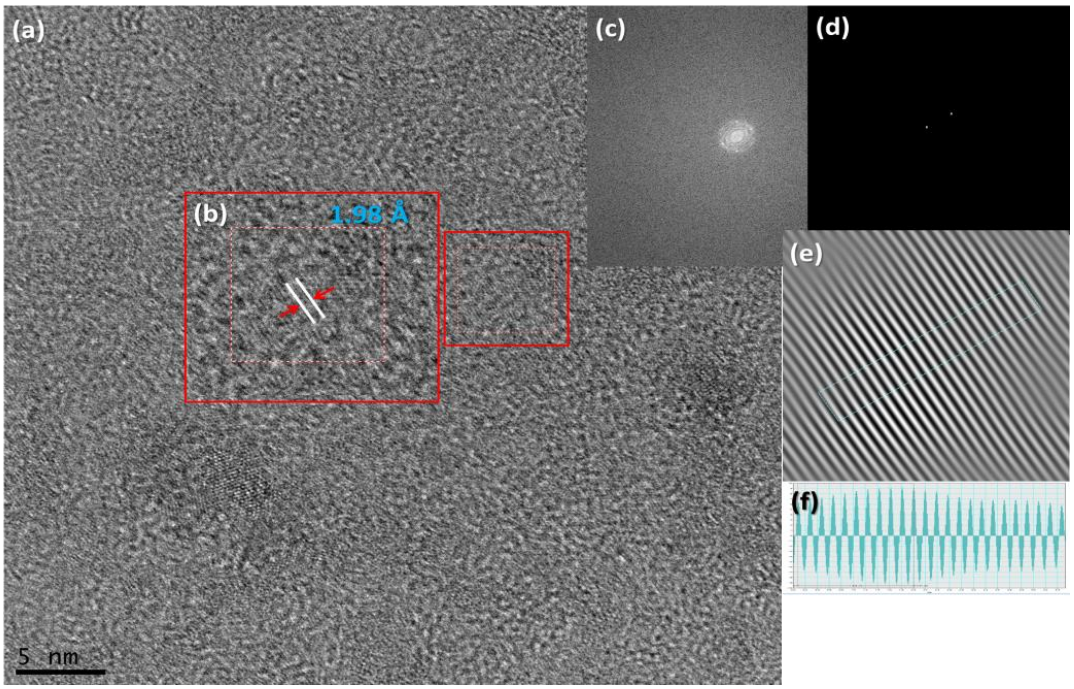

Figure 5-13: HR-TEM image of the large area location (L_4) indicated with a red box, (a) Bright field image. (b) Shows the set of planes. (c) Shows the FFT image of the region indicated in (a), (d) Masked applied FFT image corresponding to (c), (d) Unwanted noise reduced image of (c). (e) Inverse FFT image of the (d) with line profile. (f) Line profile showing the distribution.

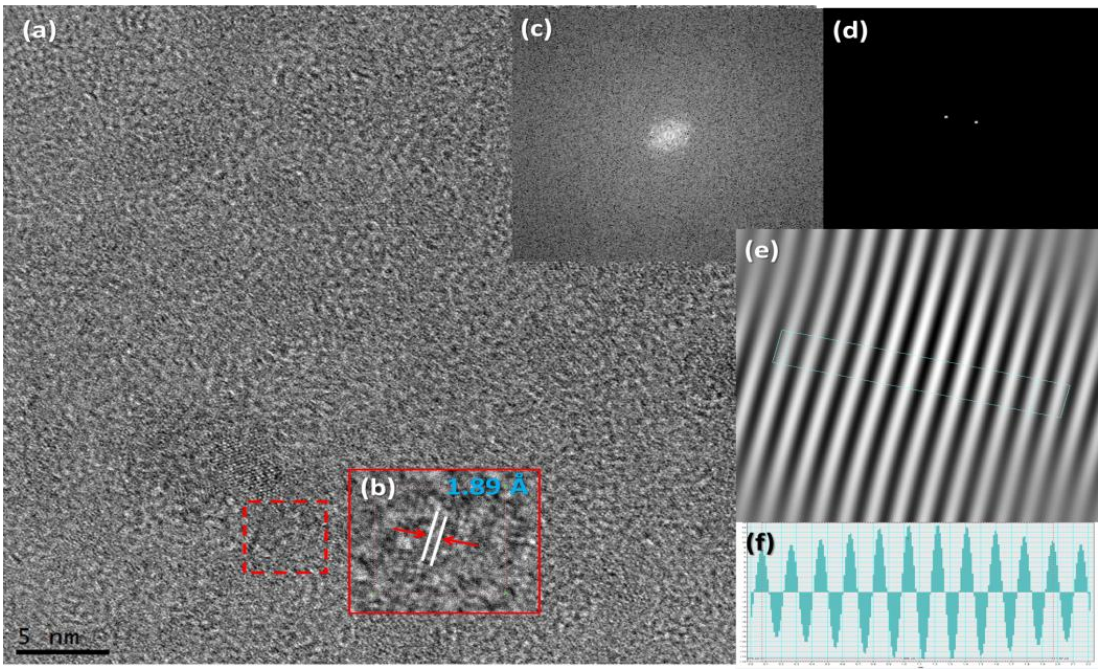

Figure 5-14: HR-TEM image of the large area location (L_5) indicated with a red box, (a) Bright field image. (b) Shows the set of planes. (c) Shows the FFT image of the region indicated in (a), (d) Masked applied FFT image corresponding to (c), (d) Unwanted noise reduced image of (c). (e) Inverse FFT image of the (d) with line profile. (f) Line profile showing the distribution.

Table 5-1: Information related about the d spacing and *hkl* from HR-TEM image at different locations.

Location	d spacing (Å)	*hkl*
L_1	2.11	100
L_2	1.91	101
L_3	1.91	101
L_4	1.98	101
L_5	1.89	101

5.2.1.3.2 Selected Area Electron Diffraction

Electron diffraction was performed on the sample, showing two hexagonal structures, r_1 and r_2, assuming the distance from centre to spot a and b, respectively. Using ImageJ software, the distance (in terms of pixels) from the center was calculated to be about 988 and 1727 pixels.

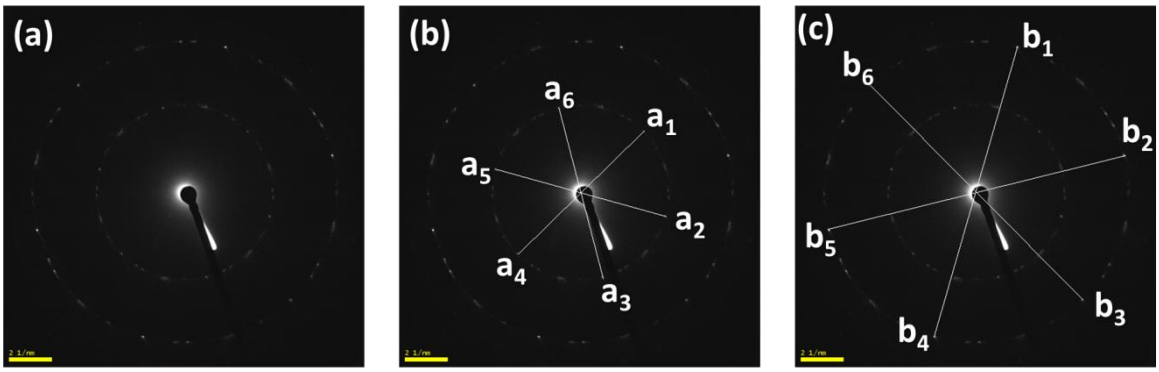

Figure 5-15: (a) Electron Diffraction showing 6 hexagonal spots with different planes (b) with (110) and (c) with (032) family of planes.

Applying the relation:

$$r_1 d_1 = L\lambda = constant = r_2 d_2 \ , \qquad \text{(Eq. 5-1)}$$

where r_1 and r_2 are the distances from the center of the spot, d_1 and d_2 are the d spacings.

Hence from $\boldsymbol{r1\, d_1 = L\lambda = constant = r_2\, d_2}$,

(Eq. **5-1**, we have

$$\frac{r_2}{r_1} = \frac{1727}{988} = \mathbf{1.747}.$$

After simulation from CaRine crystallography v3.1, and the values taken from it, we have:

$$\frac{\boldsymbol{d\ values\ of\ (110)\ plane}}{\boldsymbol{d\ values\ of\ (032)\ plane}} = \frac{1.231}{0.695} = \mathbf{1.771}$$

The ratio of d spacing for (110) and (032) was found to be the nearest to the ratio obtained in **Equation 5-1** which also says that these are two assumed planes.

Table 5-2: d spacing, radius, ratio and *hkl* from both experimental and database.

d	Radius *(in pixel)*	*hkl*	d spacing *(Data base)*	Ratio r_2 & r_1 *(experimental)*	Ratio d_1 & d_2 *(ICDD file)*
r_2	1727	110	1.231	**1.747**	**1.771**
r_1	988	032	0.695		

Furthermore, reciprocal lattices from (-5, -5, -5) to (5, 5, 5) are shown in the **Figure 5-16**. The zone axis was found to be [1 0 0]. The two hexagonal structures are shown with the green and red dotted lines for (1,1,0) and (0,3,2) planes, respectively.

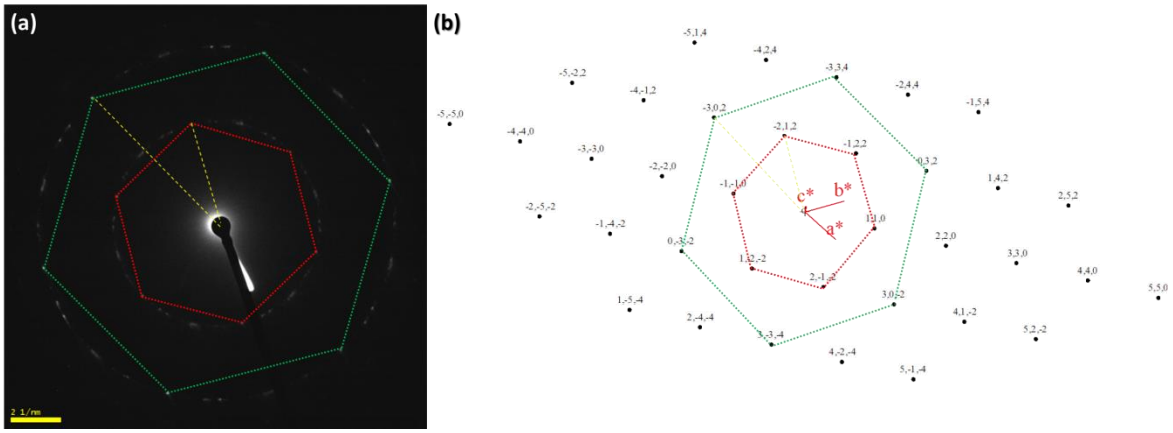

Figure 5-16: (a) (a) Electron Diffraction showing 6 hexagonal spots of (0,3,2) and (1,1,0) family of planes, (b) The two sets of planes with green and red dotted line (hexagonal shape) in reciprocal space.

5.2.1.3.3 Extra carbon deposition

As observed earlier in the case of pure graphene, it was quite difficult to perform HR-TEM images with much higher resolution as there was huge carbon deposition due to strong electron beam (see, **Figure 5-17**). The rings (dotted lines) shown in the image correspond to carbon deposition due to high energy. Keeping this in the mind, we performed the HR-TEM with the energy less than 200kV. This was an optimum for the high resolution TEM images and we were able to see the planes in the locations.

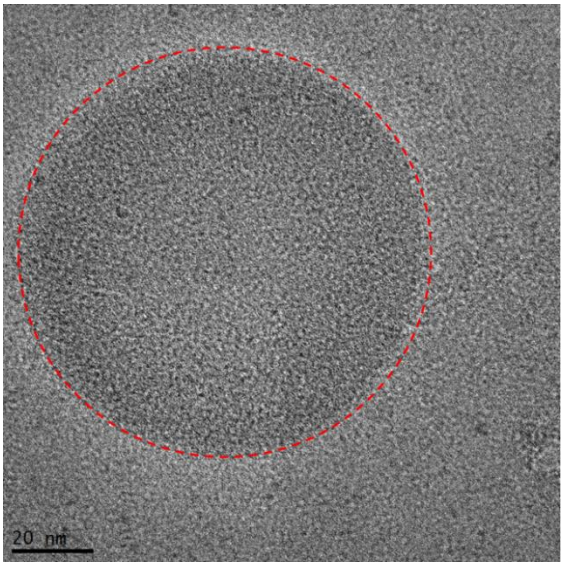

Figure 5-17: Extra carbon depositions (in forms of rings) formed due to high energy electron beam during Transmission Electron Microscopy measurements.

5.2.1.3.4 Energy Dispersive X-ray Spectroscopy

To have a better insight and to reconfirm the elements presented (the existence of the crystalline planes), Energy Dispersive X-ray Spectroscopy (EDS) measurements were performed exactly at the same location where previously HR-TEM and SAED were recorded. EDS relies on an interaction of some source of X-ray excitation and a sample. Its characterization capabilities are due in large part to the fundamental principle that each element has a unique atomic structure allowing a specific set of peaks in its electromagnetic emission spectrum. **Figure 5-18** shows the EDS spectrum obtained from the *in-situ* ammonia doped graphene transferred on TEM grid. The spectrum shows the peaks of carbon (C), nitrogen (N), oxygen (O), and iron (Fe). The presence of Fe in the sample is due to $FeCl_3$ used for catalytic reaction of the substrate required for transfer process. This Fe was also observed in HR-XPS and the result was reported in the literature [239]. On the other hand, the peaks from Cu are coming from the TEM grid.

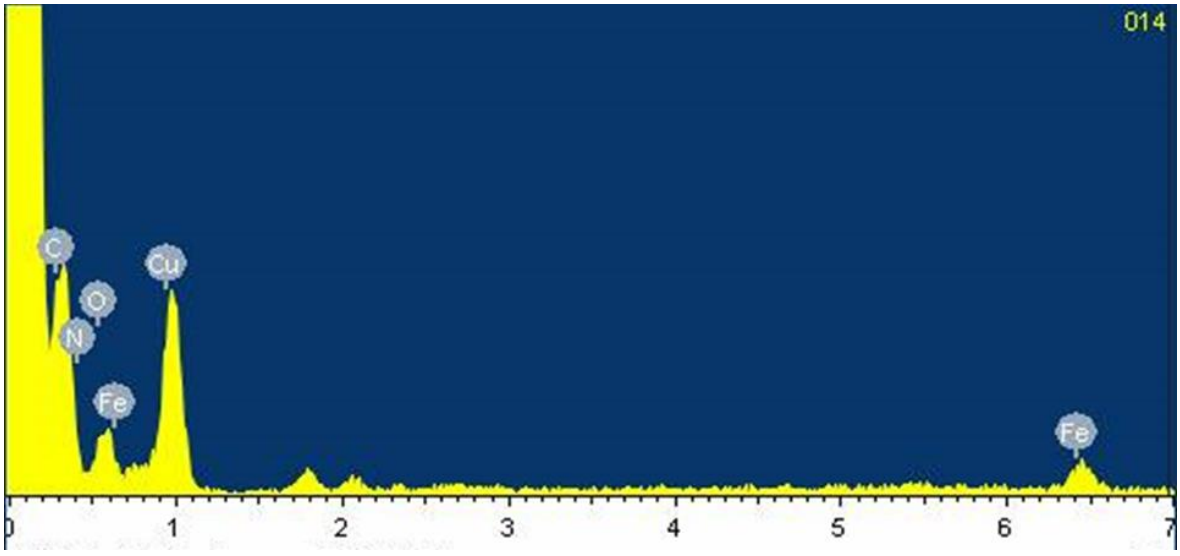

Figure 5-18: Energy dispersive X-ray spectroscopy (EDS) spectrum of the *in-situ* ammonia doped graphene on TEM grid.

From the above EDS pattern, we found two hexagonal of (0,3,2) and (1,1,0) family of planes. After simulation from CaRine crystallography software, the zone axis was calculated, and it was found to be [1 0 0]. In case of HR-TEM, after applying FFT to image and calculating the d spacing, we found two planes of (1,0,0) and (1,0,1). And this was also compared with JCPDF XRD file (file reference is #C–00–056–0159 and #C–00–056–0160). Upon comparing the data, simulating using CaRine, and extracting the zone axis we came to the conclusion that the planes noticed in HR-TEM

image, are (1,0,0) and (1,0,1) whereas in the case of SAED we observed (0,3,2) and (1,1,0) family of planes. The zone axis obtained from the SAED pattern was [1 0 0]. The above calculation and observation lead us to the conclusion that the crystallinity in the *in-situ* ammonia doped graphene was maintained. The same set of planes was viewed in HR-TEM and ED but in EDS the sample was tilted to have better spots.

5.2.1.4. *Homogeneity of the graphene layer: Raman mapping*

To check the homogeneity of the sample, we performed Raman mapping. Figure 4-14 Raman mapping of the *D, G* and *2D* band intensity of the graphene grown on Cu substrate can be seen in **Figure 5-19**. The color contrast depicts that the graphene flake deposited on Cu was sufficiently homogeneous. However, in some areas the contrast was absent due to defects and uneven surface of Cu substrate that was possibly due to the substrate annealing at high temperature (~1000 °C).

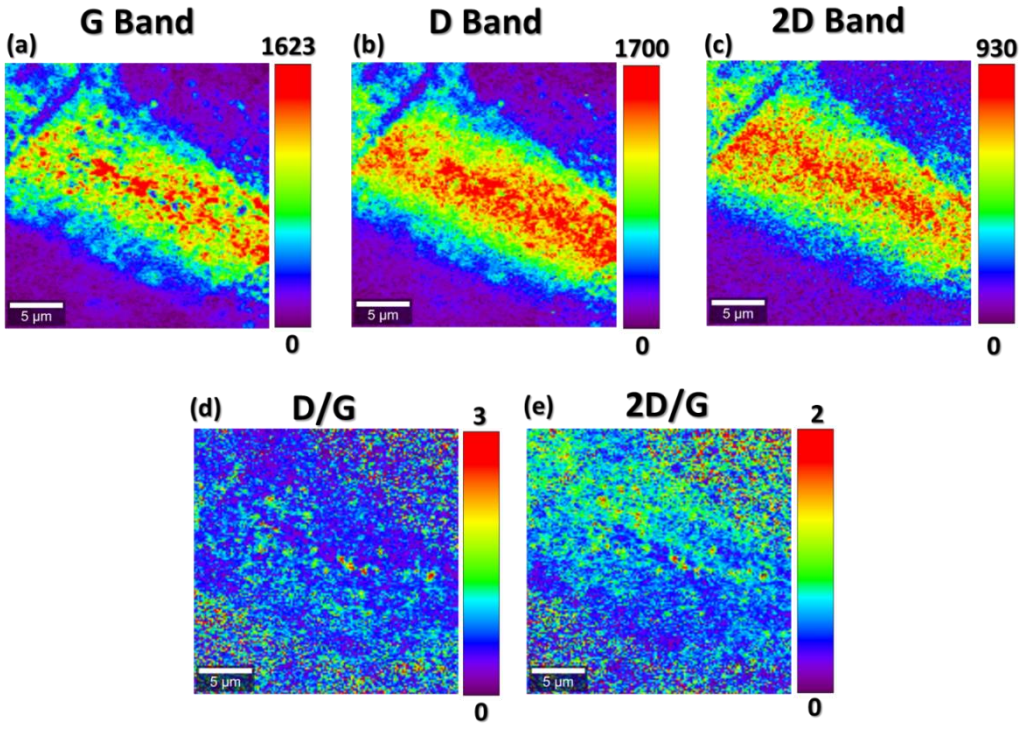

Figure 5-19: Raman mapping integrated intensities of the (a) *G*, (b) *D* and (c) *2D* band using 532 nm laser source of *in-situ* ammonia doped graphene grown on Cu substrates. (d) and (e) show the calculation of integrated intensities of I_D/I_G and I_{2D}/I_G, respectively. The vertical bars show the color profile in the Raman mapping with scale in CCD counts.

5.3. Defect concentration dependence on substrate thickness[†]

Tuning the band-gap of graphene is a current need for real device applications. Copper (Cu) as substrate plays a crucial role in graphene deposition. Here we report the fabrication of *in-situ* nitrogen (N) doped graphene via CVD technique and the effect of Cu substrate thickness on the growth mechanism. The ratio of intensity ratio of *G* and *D* peaks was used to evaluate defect concentration based on the local activation model associated with the distortion of the crystal lattice due to incorporation of nitrogen atoms into graphene lattice. The results suggest that Cu substrate of 20 µm in thickness exhibits higher defect density (1.86 x 10^{12} cm^{-2}) as compared to 10 and 25 µm thick substrates (1.23 x 10^{12} cm^{-2} and 3.09 x 10^{11} cm^{-2}, respectively). Furthermore, High Resolution -X-ray Photoelectron Spectroscopy (HR-XPS) precisely affirms ~0.4 atomic % of nitrogen intercalations in graphene. Our results show that the substitutional type of nitrogen doping dominates over the pyridinic configuration. In addition, X-ray diffraction (XRD) shows all XRD peaks associated with the carbon. However, the peak at ~24° is suppressed by the substrate peaks (Cu). These results suggest that nitrogen atoms can be efficiently incorporated into the graphene using thinner copper foils, rather than the standard 25 µm thick substrates. This is important for tailoring the properties of graphene required for microelectronic applications.

Ni and Cu substrates are the most widely used due to low cost and ease of availability. Kim *et al.* reported high optical transparency (80%), low sheet resistance and greater electron mobility of 3700 cm^2/V.s for the graphene grown by CVD on polycrystalline Ni, and transferred onto SiO_2 substrate [3]. Recently Li *et al.* have demonstrated that using Ni foil limits the control of the number of layers, resulting in a single to a few layer graphene [211]. In the case of Cu, graphene grows as uniform and high-quality single layer over a large area. The studies of Sutter *et al.* have demonstrated uniform high quality single layered graphene growth over a large area up to 30-inches on polycrystalline substrates [7]. Their study further confirmed 95% of the copper surface covered by a single layered graphene while the remaining area was coated by 2-3 layer graphene. Copper, as a substrate, has shown catalytic behavior for several carbon allotropes, such as graphite [240], diamond [241], carbon nanotubes [242, 243] and graphene [7], as was unintentionally achieved in 1991 in an experiment designed to catalyze the growth of diamond by CVD.

[†] Parts of this chapter have been published as Physica B 513 (2017) 62–68).

Given the extensive applications of graphene related materials and based on the success of graphene growth on the large areas of Cu substrates, we aimed to grow doped thin films by CVD. We performed the growth of highly homogenous *in-situ* nitrogen doped graphene on these substratess in its single layer form. The effect of substrate thickness on structure is studied by calculating defect concentrations based on local activation model associated with the distortion of the crystal lattice upon introduction of nitrogen atoms. By means of confocal Raman spectroscopy and XPS we further confirmed the existence of defects created by nitrogen atoms on different Cu substrates. Our studies reveal that graphene grown on 20µm Cu exhibits higher concentration of defects, as compared to 10 and 25µm substrates.

5.3.1. Results and discussions

5.3.1.1. *High Resolution X-Ray Diffraction*

HR-XRD pattern of nitrogen doped graphene grown on different Cu substrates is depicted in **Figure 5-20**. The XRD patterns of Cu substrate (before and after deposition of nitrogen doped graphene on 10, 20 and 25µm thick substrates) can be seen in the figure. The results show the presence of strong peaks associated with Cu, which suppress the carbon (graphene) peak, typically expected around $2\Theta \sim 24^{o}$. This could be due to the fact that only a few layers of graphene were grown on the substrate; such observation is reported in literature for graphene films on various metal substrates. From our XRD results three distinct diffraction peaks at approximately $2\Theta \sim 43$, 50, and 74^{o}, which correspond to (003), (202) and (220) reflections of carbon [244] and the crystallographic plane of Cu (111), (200) and (220), respectively [245]. The absence of other peaks confirms that no other elements are present in our sample as an impurity.

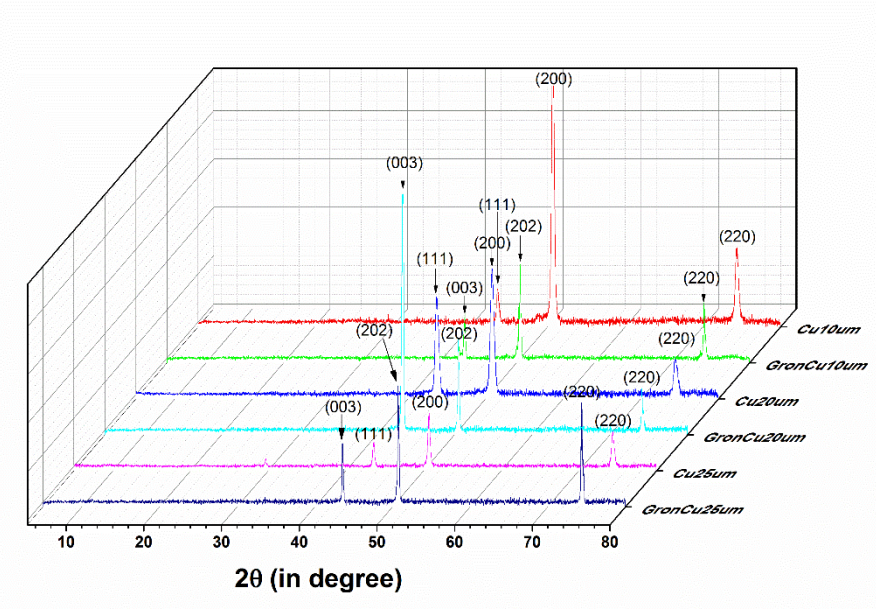

Figure 5-20: XRD patterns with corresponding peaks of Cu substrate (before deposition) and after deposition of nitrogen doped graphene.

5.3.1.2. *Raman spectroscopy and defect calculation*

Raman spectroscopy is the best fingerprint technique for analyzing the properties of the carbon related materials including graphene [166]. This technique allows distinguishing among single layer, a few layers graphene and graphite. It is also sensitive to defects, excess charge, strain and atomic arrangement of the edges. **Figure 5-21** shows the Raman spectroscopy results of nitrogen doped graphene grown on 10, 20 and 25µm thick Cu substrates. The spectra were recorded at different time intervals in the range from 10 to 1000 s. The peak intensities related to *D*, *G*, *D'* and *2D* features were collected and fitted with Lorentzian functions. As widely accepted we refer to peak intensities their height and these are denoted as I_D, I_G, $I_{D'}$, I_{2D} for the *D*, *G*, *D'*, and *2D* peaks, respectively.

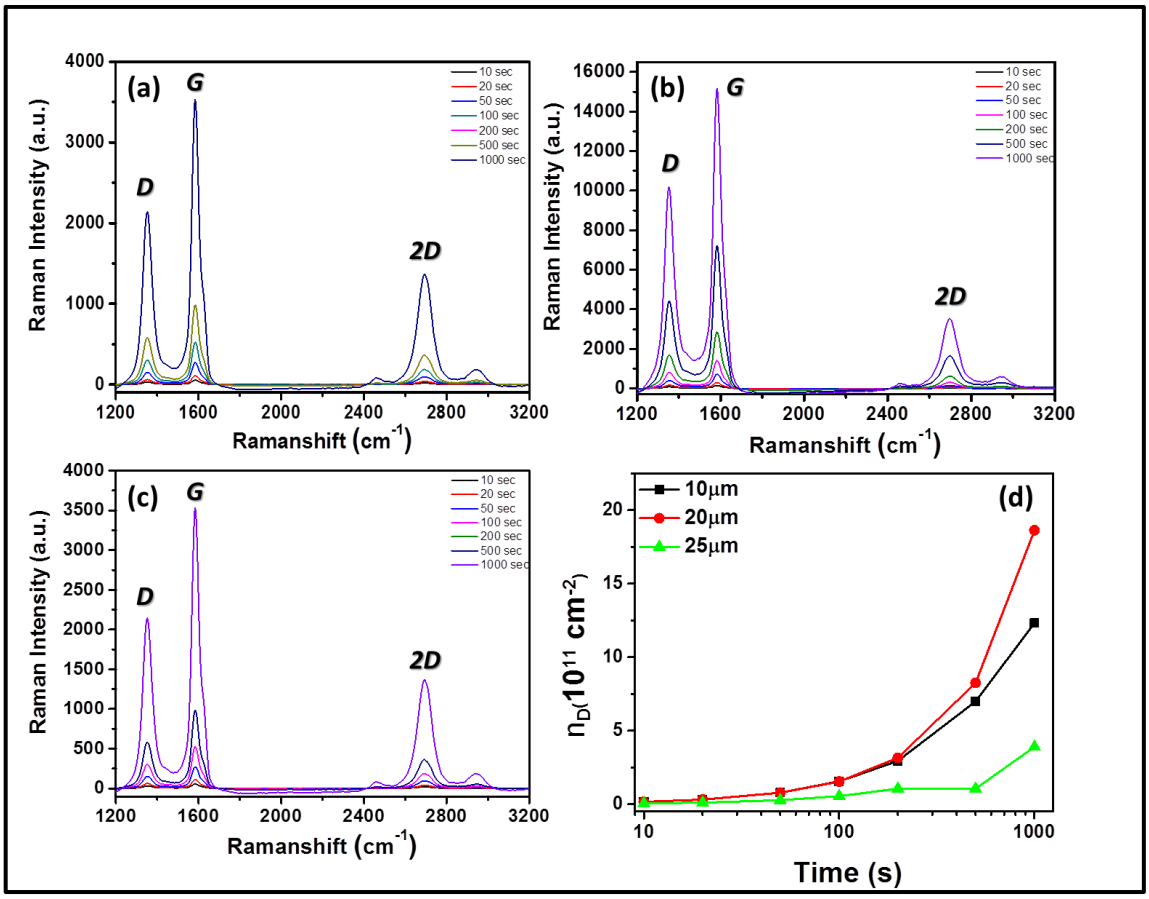

Figure 5-21: Raman spectra of graphene grown on (a) 10, (b) 20 and (c) 25µm Cu substrate showing the distinct peaks *D*, *G* and *2D* respectively. (d) Spectra showing the defect density with respect to time of acquisition for the graphene grown on 10, 20 and 25µm Cu substrates.

G and *2D* peaks must satisfy the Raman selection rule and this makes Raman spectroscopy one the most important tools for probing the structural defects. The first two peaks are activated by single-phonon intervalley and intravalley scattering processes, and the defect peaks *D* and *D'* provide the missing momentum in order to satisfy the momentum conservation in the Raman scattering process [167, 169]. In our case *D* peak was found almost at the same position in all the samples (~1354 cm^{-1}). However, the values of *FWHM* were found to be around 43, 53 and 53 for 10, 20 and 25µm thick substrates, respectively. This band originates from the breathing mode of six-membered rings that are activated by defects. The *G* peak was found to be at ~1583 cm^{-1} (*FWHM* ~47), ~1584 cm^{-1} (*FWHM* ~45) and ~1585 cm^{-1} (*FWHM* ~42) for 10, 20 and 25 µm thick Cu substrates, respectively, which are due to the E_{2g} phonon at the Brillouin zone center. Finally, 2D peaks at ~2694 cm^{-1} (*FWHM* ~63), ~2697 cm^{-1} (*FWHM* ~100) and ~2695 cm^{-1} (*FWHM* ~87) for 10, 20 and 25µm thick Cu substrates, respectively, are assigned to the second orders of D peak. All

these parameters were acquired at 100 s acquisition time during Raman measurements. Lucchese *et al.* have made extensive efforts to study the relationship between the amount (and nature) of defects and the intensities of *D* and *D'* peaks [217]. A simple formula was proposed to calculate the defect density n_D (in cm^{-2}) with the help of mean distances in graphene (L_D, nm) with relation to I_D/I_G.

$$\frac{I_{(x)}}{I_{(G)}} = C_A \frac{r_A^2 - r_S^2}{r_A^2 - 2r_S^2} \left[e^{\frac{-\pi r_S^2}{L_D^2}} - e^{\frac{-\pi (r_A^2 - r_S^2)}{L_D^2}} \right], \qquad \text{(Eq. 5-2)}$$

where $x = D$ or D'; r_S (1 nm) and r_A (3.1 nm) are the radii of the "structurally disordered" area and the "activated area" around the defects, respectively [217].

C_A correlates with the electron-phonon matrix elements and it was found to be 4.2 using the green laser excitation (532 nm). From the above equation, the defect densities n_D (in cm^{-2}) were calculated as follows:

$$n_D = 10^{14} / \pi L_D^2 \qquad \text{(Eq. 5-3)}$$

Figure 5-21 (d) shows the defect densities calculated for the substrates with different thicknesses. From the measured spectra it was concluded that the highest defect density is observed for 20µm thick Cu substrate. Possible reason for this effect could be the increased surface roughness due rolling process used for the commercial fabrication of Cu substrates [246]. Due to strong *D* peak seen in graphene grown on 20µm Cu substrate and because of the defect density, the "activated" area starts to coalesce and the structurally disordered area dominates in the graphene sheets [247]. **Figure 5-21 (d)** shows the summary of defect densities calculated over different laser time acquisitions starting 10s to 1000s. To check the homogeneity of the sample, we perform Raman mapping. **Figure 5-22** shows the Raman mapping of the *G* band intensity, *D* peak intensity and *2D* peak of the graphene grown on 10, 20 and 25µm respectively. The color contrast depicts that the graphene was homogeneously deposited on the Cu, though the quality differs due to different Cu substrates used during experiment. The mapping also confirms the overall uniform deposition of nitrogen doped-graphene on over most of the substrate surface. This result suggests that the CVD process is able to produce large areas of graphene.

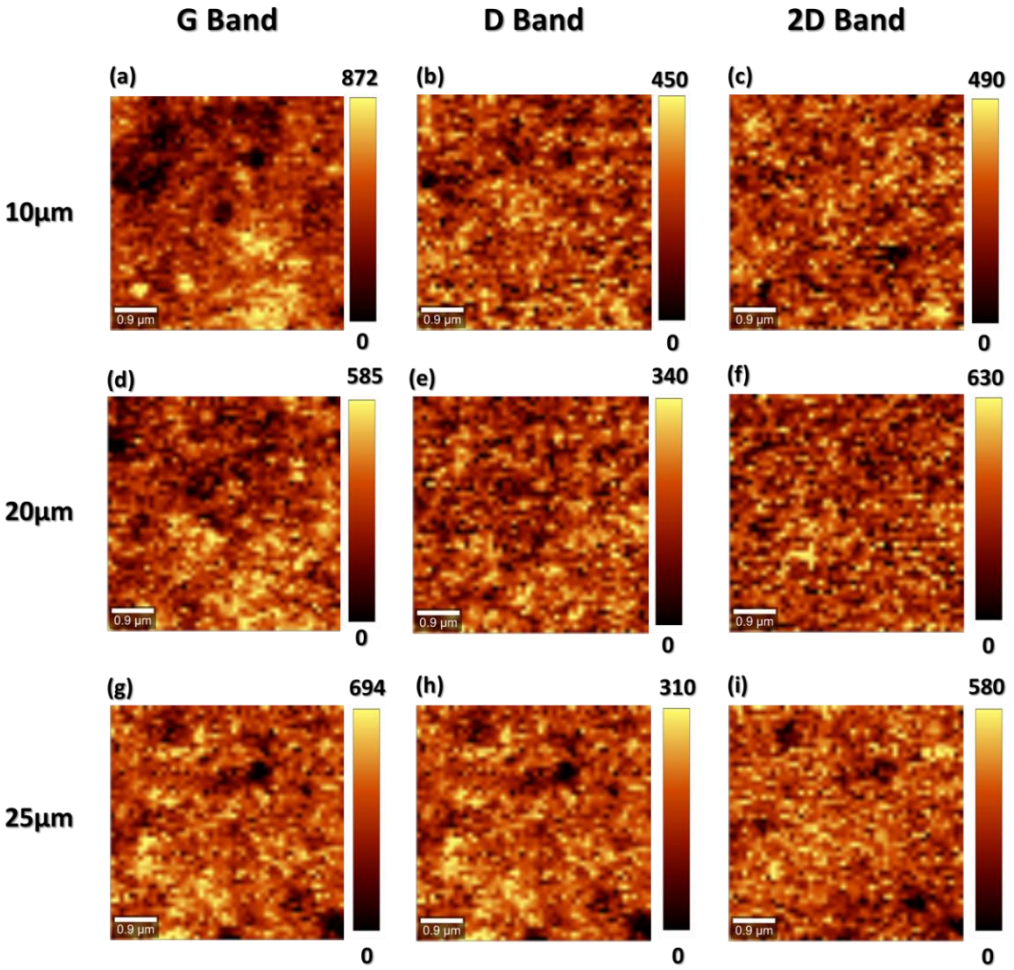

Figure 5-22: Raman mapping of the *G*, *D* and *2D* band intensity of the graphene grown on 10, 20 and 25µm thick Cu substrates, respectively. The values in the scale are in CCD counts.

5.3.1.3. *High-Resolution X-Ray Photoelectron Spectroscopy*

Furthermore, we performed HR-XPS to re-confirm the nature of defects created by doping of graphene. XPS is a well-established technique used for revealing the elemental composition and the chemical environment of the detected elements. **Figure 5-23 (a)** shows the overview spectrum of as grown N doped graphene on 10, 20 and 25µm thick foils. **Figure 5-23 (b)** shows carbon (C) 1s and **(c)** nitrogen (N) 1s core levels.

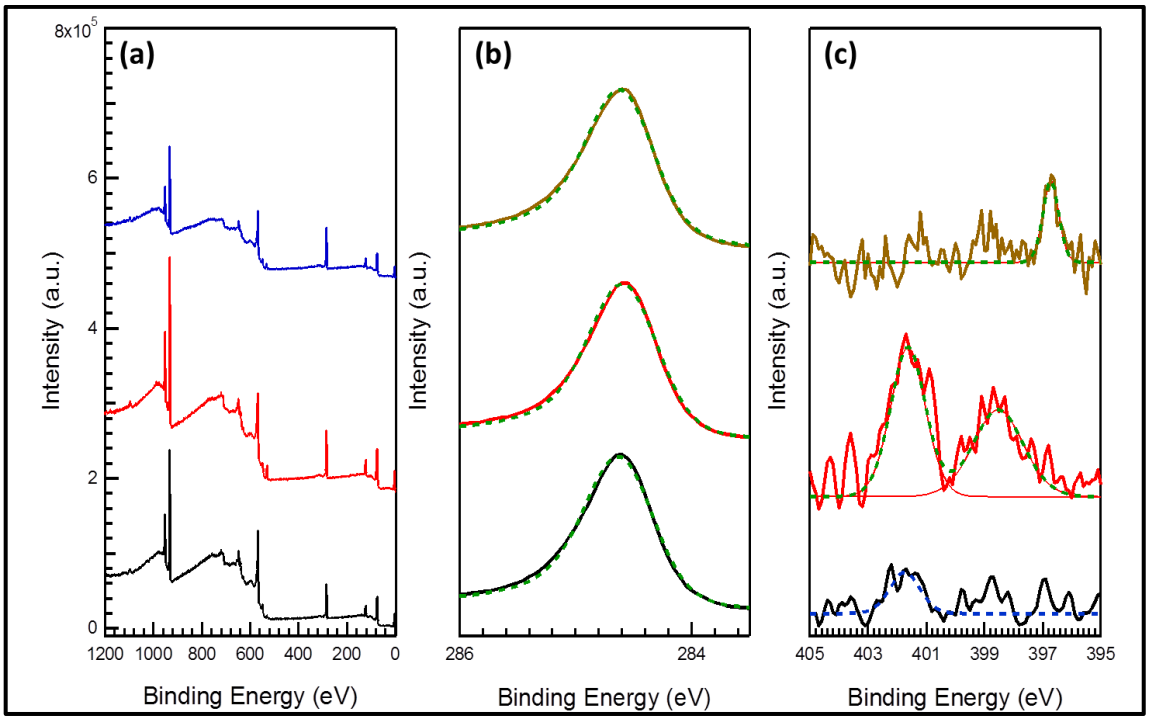

Figure 5-23: HR-XPS comparison of nitrogen (N) – doped graphene grown on copper (Cu) substrate of 10 (brown), 20 (black spectra) and 25 (red) µm in thickness. (a) Shows the overview spectra of *n*-doped graphene. (b) C 1s and (c) N 1s core levels. The best fits are also included in green. In the case of the N 1s spectra of graphene grown on 25µm Cu substrate sample (bottom spectra) the blue line is a guide for the eyes.

C 1s core level (**Figure 5-23 (b)**) can be fitted by a single component centered at a BE of 284.5 eV and can be ascribed to C sp^2 [173]. Thus, from the XPS point of view C 1s seems to be almost the same in all the samples. On the contrary, significant changes were detected in the N 1s core level (**Figure 5-23 (c)**). Under the same growth conditions the quantity of nitrogen is almost zero in the case of the 25µm copper substrate (bottom spectra). The blue dashed line that is included in the bottom spectra is only a guide for the eye, fixed at the BE that we could expect substitutional nitrogen in graphene. On the other hand, the nitrogen intercalation in the graphene sheets is clear in the upper spectra, corresponding to the sample grown on the 20 µm thick copper substrate. Two components are clearly distinguished in the respective N 1s core level. The first one, centered at BE of 401.7 eV, is attributed to substitutional nitrogen atoms in a graphene sheet, whereas the second component (BE = 398.5 eV) is attributed to nitrogen atoms in a pyridinic configuration [224]. In this sample the amount of nitrogen quantified by XPS is about 0.4 atomic %. Finally, in the case of the sample grown on 10µm thick copper substrate a sharp N peak is detected at 396.7 eV. This value of BE is too low for the substitutional nitrogen in the graphene

sheet. On the contrary, it can be related to the atomic nitrogen bonded to the copper substrate [239]. **Figure 5-24 (b)** shows the possible sites for N intercalation in graphene sheets. There are mainly three types of bonding found in graphene with incorporated nitrogen, namely substitutional, pyridinic and pyrrolic ones. However, in our graphene (grown on a 20µm thick copper substrate) we found only substitutional and pyridinic configurations of bonding. In substitutional type of configuration, three nitrogen valence electron form three σ– bonds, one electron fills the π–states, and the fifth electron enters the π*–states of the conduction band, providing a strong doping effect.

5.3.1.4. *Surface analysis*

Commonly, 25 µm Cu substrates are mostly used for the deposition of graphene. In our experiment, we used 10, 20 and 25 µm thick Cu foils and studied the effect of substrate thickness. As discussed earlier, we found that 20µm Cu substrates are the best for doping of graphene. The graphene grown on it has larger defect concentration as compared to that grown on 25µm thick foil. The conceivable mechanism can be as follows: it is well known that Cu sheets are prepared using a rolling process. This rolling technique creates lines with sufficiently high roughness (average roughness of highly smooth Cu sheet can be as high as 100 nm) [246]. Since Cu surface plays an important and crucial role for the grain growth during annealing process (during deposition) [248], we infer that thinner Cu substrates are likely to have higher surface roughness that will create more nucleation sites for graphene growth and subsequent doping. As in the case of 20µm, the results show that the number of grains is higher than that for 25 µm substrates. On the contrary 10 µm substrate might have even higher number of grains but, since the deposition is done around 1000 ^{o}C, it leads to evaporation of Cu atoms from the surface (because of the melting temperature of Cu ~1085^{o}C). This is deleterious for the graphene deposition and its doping. It is worth mentioning that we tried the same experiment around ~1050 ^{o}C and it was surprising that 10µm Cu substrate was completely evaporated due to high temperature, as also confirmed by Ago *et al*. [248].

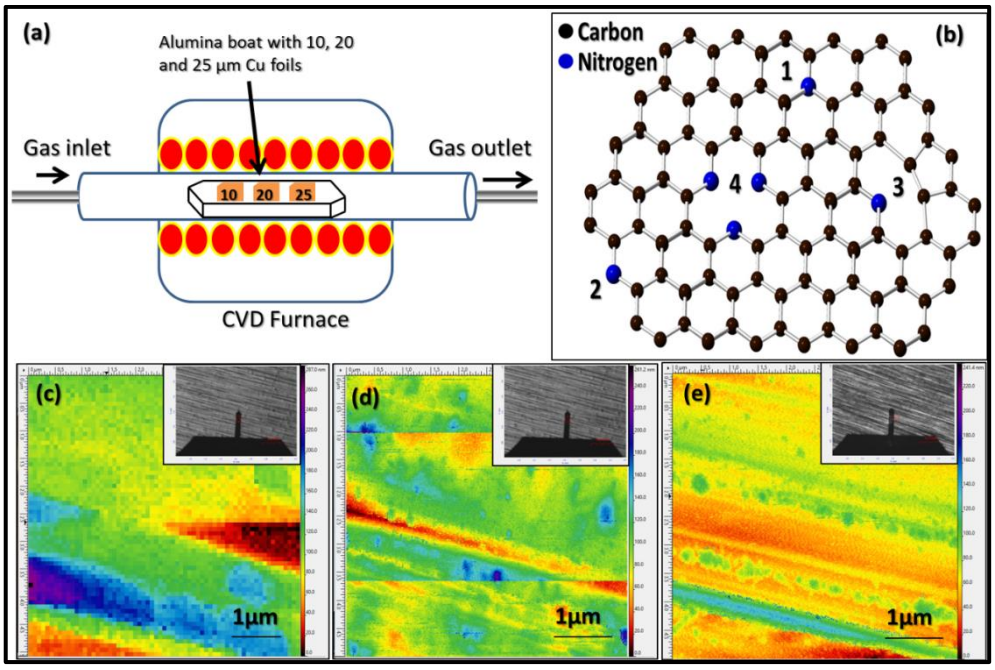

Figure 5-24: (a) Schematic diagram of the experiment showing the 10, 20 and 25µm copper (Cu) substrates placed in alumina boat in CVD furnace, (b) Possible nitrogen (N) incorporation in graphene structure showing (1) substitutional or graphitic N, (2) pyridine-like N, (3) single N pyridinic vacancy, (4) triple N pyridinic vacancy, (c–e) Atomic Force Microscopy (AFM) image for average RMS surface of virgin Cu substrates of 10, 20 and 25µm respectively (inset showing the optical image captured during AFM).

Atomic Force Microscopy (AFM) was used to quantify the root mean square (RMS) roughness in a semicontact mode using a cantilever with force constant 3 Nm^{-1} of all as-received Cu foils (Good Fellow, 99.97+%) and the results are presented in **Figure 5-24 (c-e)**. The graphene films grown on 10, 20, and 25µm Cu substrates have a uniform thickness with an RMS roughness of 46, 25 and 18 nm, respectively. Hence, from the above observation we infer that thinner Cu substrates have higher roughness as compared to thicker substrates; consequently, it is the roughness that controls the grain number and doping efficiency.

5.4. Conclusions

In conclusion, we argue that the use of ammonia along with methane as a precursor in the CVD can yield the N-doped graphene on copper substrates. The presence of *D* peaks confirms the doping of graphene and, moreover, we were able to control the amount of doping by varying the

time duration. HR-XPS analysis shows the growth of high quality graphene with C 1s in sp^2 configuration (284.8 eV). Furthermore, we were able to determine the type of doping and amount of nitrogen intercalations in the graphene sheets. Moving further, the Raman mapping image demonstrated the full coverage of large area *in-situ* ammonia doped graphene on copper substrate. Lastly, from the HR-TEM results, we identified the crystalline plane, which reconfirmed the crystallinity of the sample. However, the sheet (transferred on TEM grids) was crumbled like paper due to the flexibility and thin nature of the material. Further, we also observed the apparent effect of Cu substrate thickness on *in-situ* nitrogen doping of graphene by using NH_3 as precursor. In general, 25 µm thick Cu foils are the standard substrates for the growth of pristine epitaxial graphene. Our results based on Raman spectroscopy, HR-XPS, HR-XRD and AFM indicate that the use of a thinner copper substrate (20µm) rather than the standard one (25µm) is preferred to significantly increase the efficiency of doping of graphene sheets with nitrogen. Thus, this study provides a clue for heteroatom engineering of graphene, which is required for the electronic applications of graphene.

Chapter 6

Graphene growth on nickel substrates

Abstract

This chapter describes the experimental strategy used for pure graphene growth on various nickel substrates using a methane-based CVD method. Trial and error method was applied for parameterizing the growth conditions. After many attempts, 35 torr pressures was found to be suitable for the pure graphene deposition. The deposition of graphene on nickel substrates involves two major processes, initially the dissolution of the (released) carbon atoms into the metal at high temperature followed by the crystallization of carbon atoms on the metal surface to form graphene. The as synthesized graphene was found to be multilayer graphene (MLG) due to high amount of carbon absorbing on nickel. This was confirmed by Raman spectroscopy. MLG were found to be highly crystalline in nature, with sharp G peak at ~1560 cm^{-1} (with *FWHM* as ~24). However, we were able to see the D peak due to possible wrinkle formation in MLG. This was proved by SEM images. Moreover, the results from HR-XPS show that the peak can be fitted by only one component centered at 284.4 eV, which firmly confirms the sp^2 nature of carbon. Also, the Raman mapping shows the overall coverage of the sample on the large area.

In addition, we have calculated the charge injection as well as subsequent charge diffusion with time on the MLG/nickel surface by using Kelvin Probe Force Microscopy. The results unveiled that: (i) MLG surface can be either positively or negatively charged through the injection process using Pt coated Si-based AFM probes; (ii) the charges accumulated and eventually reached the saturated concentrations of (+4.45 ±0.1) $\mu C/m^2$ and (−1.3 ±0.1) $\mu C/m^2$; (iii) the charge diffusion coefficients on graphene surface were measured to be (1.50 ±0.05) × 10^{-16} m^2/s and (0.64 ±0.05) × 10^{-16} m^2/s for the positive and the negative charges, respectively.

6. Graphene growth on nickel substrates

Graphene growth on the catalytic transition metal substrates seems to be the most promising during the past decades and found to be the best for delivering high quality and large area crystalline graphene. By using thermal decomposition of carbon-based gaseous precursors such as methane or ethylene in CVD technique allowed us to achieve the high-quality graphene. Nickel exhibits significant carbon solubility and additionally has a high carbon diffusivity [249]. It is worth noting that Ni as a catalyst allows the faster growth of graphene layers as compared to copper [250].

Growth of graphene on nickel substrate evolves in two major steps, initially the dissolution of the (released) carbon atoms into the metal at high temperature (700–1000 ^{o}C) and, secondly, the crystallization of carbon atoms onto the metal surface to form graphene. The crystallization step may take place during the high-temperature period of the treatment or during cooling [1, 3, 11, 13, 250-252]. In these phenomena, the metals used as catalysts which dehydrogenate the hydrocarbons (such as methane, ethylene) used, thus leaving only carbon on the surface. Noble metals such as Au (gold) and Ag (silver) does not exhibit high enough catalytic activities for the dehydrogenation, but in some cases Au was used as catalyst and growth of graphene was demonstrated under appropriate conditions [253]. It is quite relevant to state that metal type and temperature play a crucial role for the growth of graphene on any surface. This controls the amount of diffusivity into the bulk. The amount of carbon in the bulk depends on the carbon solubility of the metal and this property is important to determine whether graphene grows on the surface of the metal at high temperatures, as it is the case for copper, or carbon dissolves into the bulk at high temperatures, as it is the case for nickel [254]. Ni and other materials (mainly metals) dissolving larger quantity of carbon in the bulk are likely to form graphitic layers or multilayers of graphene upon cooling from high temperatures. High carbon solubility in nickel makes difficult conditions for monolayer growth in Ni and also the formation of graphene at low temperatures is complicated by the presence of another carbon containing surface phases such as carbon forming a surface-carbide, i.e. a single atomic monolayer ordered Ni_2C phase on the Ni(111) surface [255, 256]. Furthermore, lattice mismatch and metal–graphene interaction are also important regarding the growth of the graphene. Typically, Ni(111) surface is the closest matched interface with respect to graphene of all transition metals. This close lattice match enables the formation of a 1 x 1 structure of graphene on Ni(111) under vacuum growth

conditions, while on all the other metals a periodic lattice matching condition results in a Moiré superstructure.

6.1. Graphene growth on nickel substrate

Graphene on Ni as substrate can be easily grown in ultra-high vacuum (UHV) using hydrocarbon precursors, typically methane, ethylene or propylene, with low pressures in the 10^{-9} to 10^{-6} Torr range. It is interesting to mention that the thickness of the Ni substrate determines the amount of carbon dissolvability. Another parameter playing a role is the duration of reaction with the hydrocarbon at a given high temperature. In particular, carbon content in the substrate strongly affects the growth of graphene on Ni.

Graphene was grown on Ni substrates (GoodFellow, 99.95+%) of 30 μm in thickness. The process was similar to that performed for pure and *in-situ* ammonia doped graphene on copper substrates. The growth parameters were quite similar to the parameters used by Hawaldar *et al.* **[173]** As usual, the growth process can be divided into six stages as described in Figure 6-1.

During the first stage Ni metal substrate was heated from RT to 1050 ^{o}C inside the chamber in the Ar and H_2 mixture (Ar:H_2::120:40, sccm) under the pressure of 35 Torr.

In stage II, the flow of Ar was shut down at 900 ^{o}C, during this process only H_2 was flown with 100 sccm till 1050 ^{o}C. This process played a critical role for crystallizing the metal substrate and combining the small size grains in order to form a larger grain.

During stage III, the furnace was heated to 1050 ^{o}C from 900 ^{o}C (with predefined rate) and methane along with hydrogen (CH_4:H_2::10:50 sccm) was passed for the cracking and formation of methyl radicals from methane (which was the precursor of graphene) which later led to the formation of high quality graphene. This was done only for a few minutes (max ~10 min) as Ni has higher carbon solubility as compared to Cu (in case of Cu it was 60 min).

After deposition (~10 min) at stage IV, the furnace with methane was closed, however the flow of hydrogen and argon was maintained (H_2:Ar::10:85 sccm) till 300 ^{o}C. This was done to remove the access methyl radicals in order to avoid the formation of too many layer graphene.

During stage V the hydrogen flow was shut down and only argon (Ar:85 sccm) was continued till room temperature (RT) and finally at room temperature the sample was taken out.

The as synthesized graphene grown on Ni substrates was found to have sufficiently high quality with some defects, which were confirmed by different techniques, such as Raman, HR-TEM and HR-XPS.

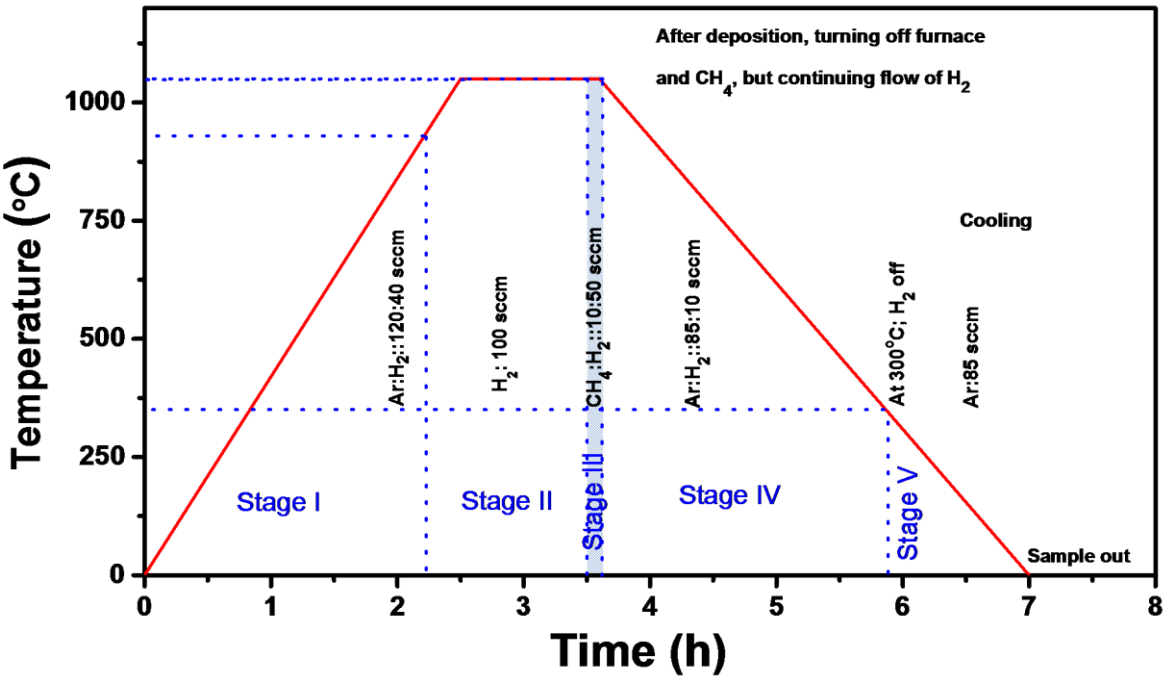

Figure 6-1: Growth process diagram for the large area pure graphene on Ni substrate by modified chemical vapor deposition setup.

6.2. Characterization of graphene grown on Ni

6.2.1.1. *Raman spectroscopy*

Raman spectra of as-synthesized graphene grown on Ni substrates were acquired (see **Figure 6-2**) using Raman spectrometer. This technique allows distinguishing among single layer, a few layer graphene and graphite. It is also sensitive to defects, excess charge, strain and atomic arrangement of the edges. Various peaks including *G*, *2D* and *D* were measured and fitted using mathematical Lorentzian function.

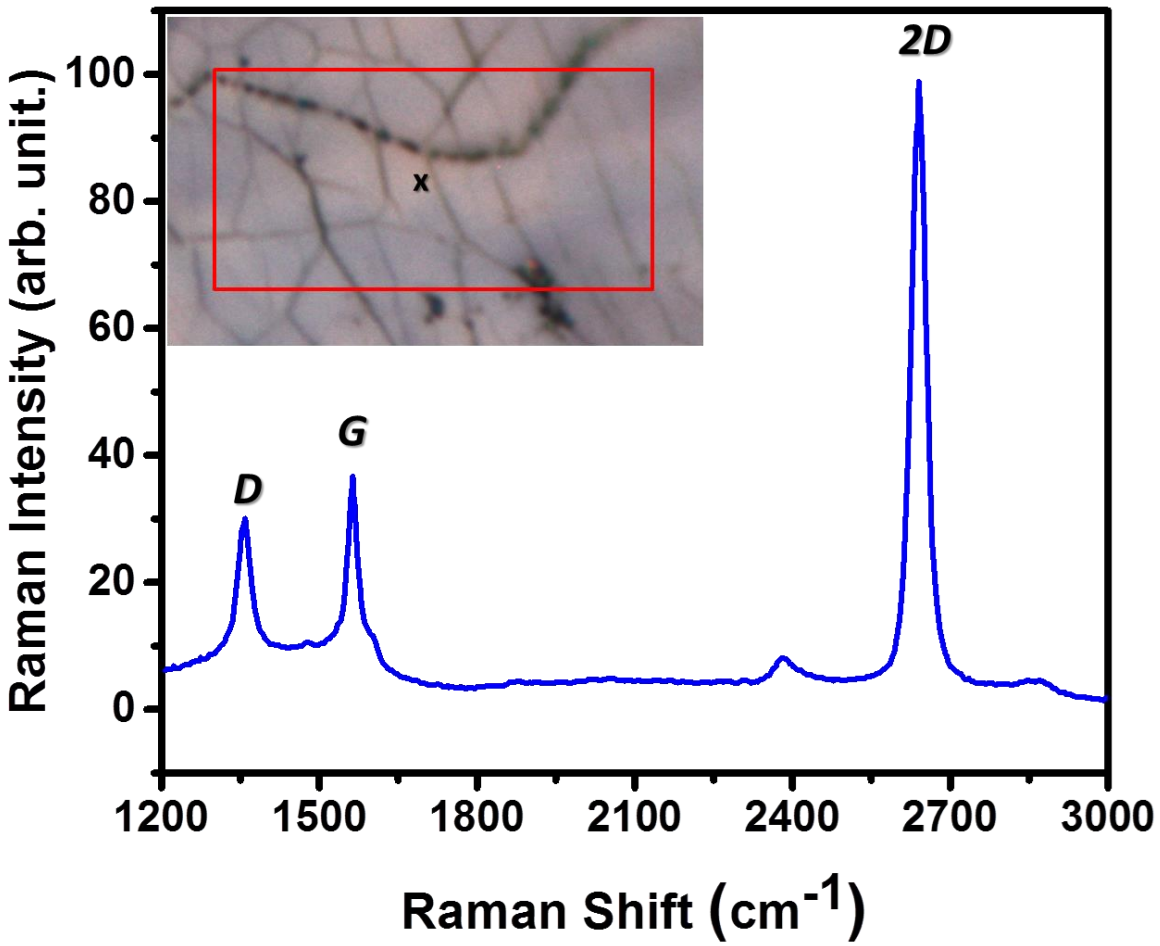

Figure 6-2: Full Raman spectra graphene on Ni substrate. Inset shows the optical image with the mark where the spectrum was taken. The spectra show major peaks associated with graphene, namely D, G and 2D.

The *G* peak (see **Figure 6-3(a)**) was found to be at ~1563 cm^{-1} with *FWHM* of ~24. The overtone peak *2D* peak (see **Figure 6-3 (c)**) was found at ~2640 cm^{-1} with *FWHM* of 33. *D* peak (defect peak) was found to be at ~1359 cm^{-1} with *FWHM* of 29 (see **Figure 6-3 (b)**). However, we also found a small shoulder *D'* peak at ~1604 cm^{-1} having *FWHM* of 24 (see **Figure 6-3 (a)**) that was related to the single phonon intervalley scattering events. Also, both the *D* and *D'* defects provide the missing momentum in order to satisfy momentum conservation during e Raman scattering process.

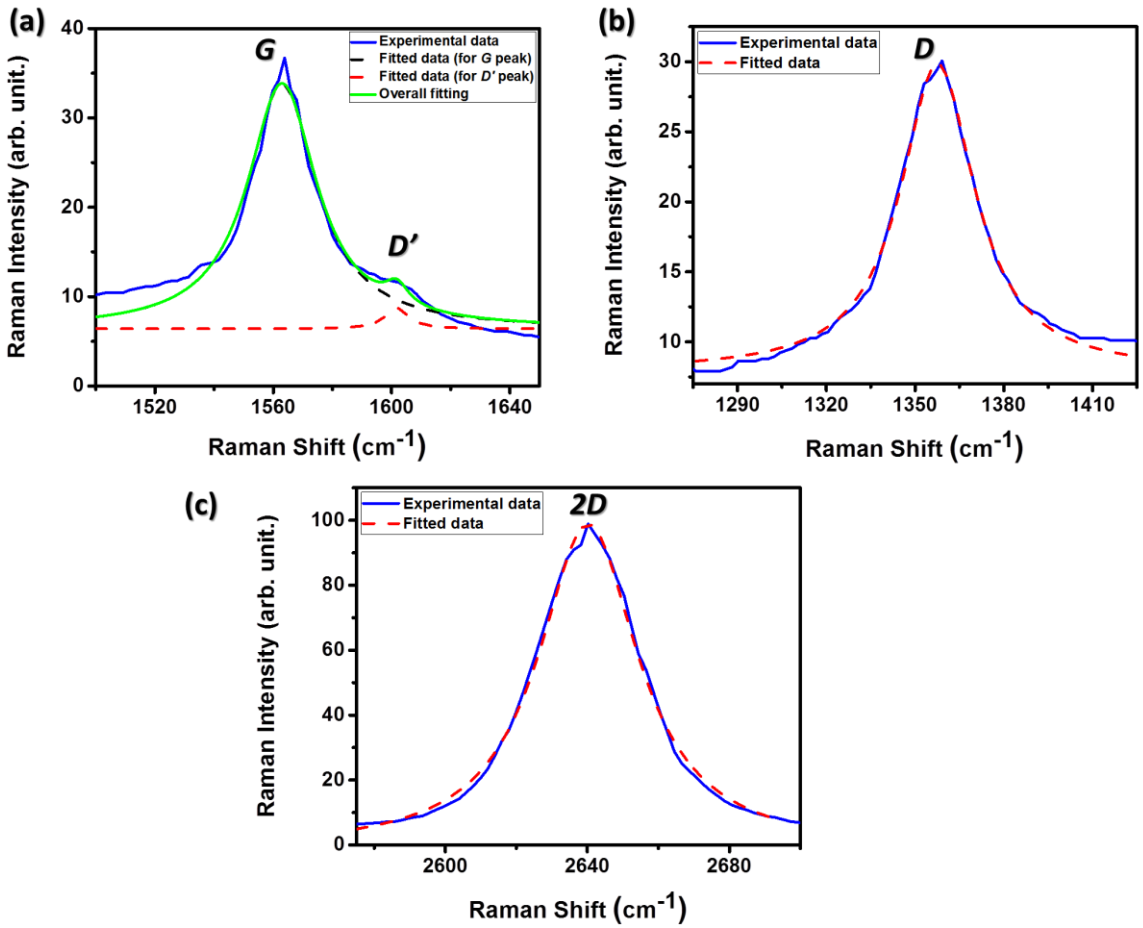

Figure 6-3: Experimental (blue line) and fitted data of Raman spectra using Lorentzian mathematical function (dotted line). (a) *G* and *D'*, (b) *D*, (c) *2D* peaks associated with the as synthesized graphene on Ni substrate.

6.2.1.2. *X-ray Photoelectron Spectroscopy*

The as synthesized graphene on Ni substrate was characterized by HR-XPS. The spectrum in **Figure 6-4** shows the overview XPS scan. It can be clearly seen that the C 1s peak is dominant. This confirms the fact that multilayer graphene was deposited on Ni substrate. However, we were still able to find small minor peaks associated with the substrate of Ni 2p and Ni 2s at 855 and 1011 eV, respectively. Beside this we found O1s peak that can come from the atmospheric oxygen. This peak was later removed by annealing the sample at around 800 °C.

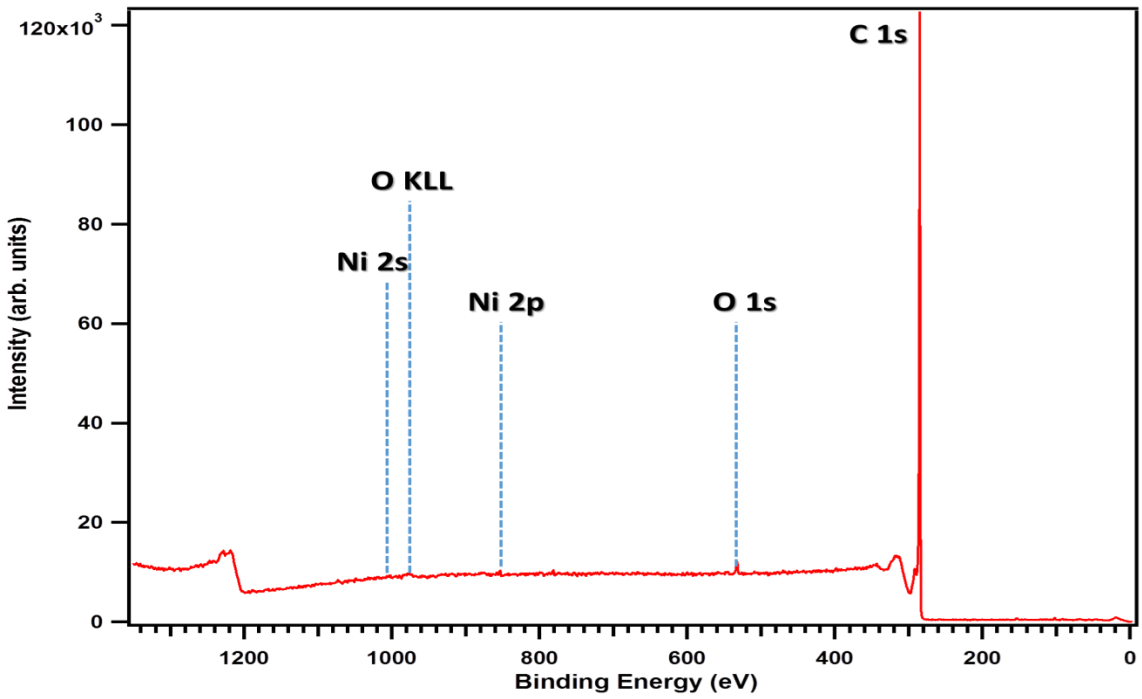

Figure 6-4: X-ray Photoelectron Spectroscopy result showing the overview scan of as-synthesized graphene on Ni substrate.

Figure 6-5 shows the high-resolution core level peak associated with carbon (in the form of graphene) deposited on Ni. It must be noted that in the case of carbon, we need to used DS (Doniach-Sunjic) with DS(α, n) with a Gaussian profile with the width characterized by an integer $0 \leq n \leq 499$. This fitting was performed by the specialized software (CasaXPS). It can be seen that the peak can be fitted by only one component centered at 284.4 eV confirming its C sp^2 nature. These results are in accordance with the earlier literature data [173].

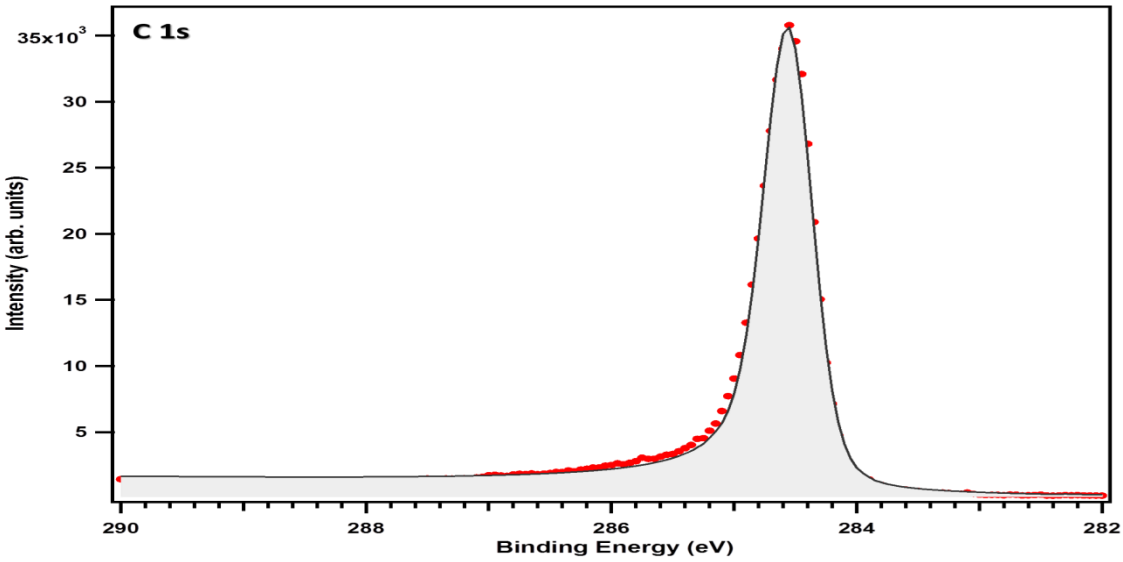

Figure 6-5: High-resolution XPS scan for the C 1s core level peak of graphene on Ni. The main core levels peaks can be deconvoluted in three components. In the spectra dots are the experimental data points, black line is the overall fitting performed with the CasaXPS .

Figure 6-6 displays the oxygen-related components of O 1s level deconvoluted into two peaks. The presence of oxygen most likely originates from the residual oxygen in low-vacuum chamber of our CVD system. The O 1s spectrum shows peaks at 532.33 (1) and 532.3 eV (2), which could be assigned to C-OH/C-O and hydroxides, respectively.

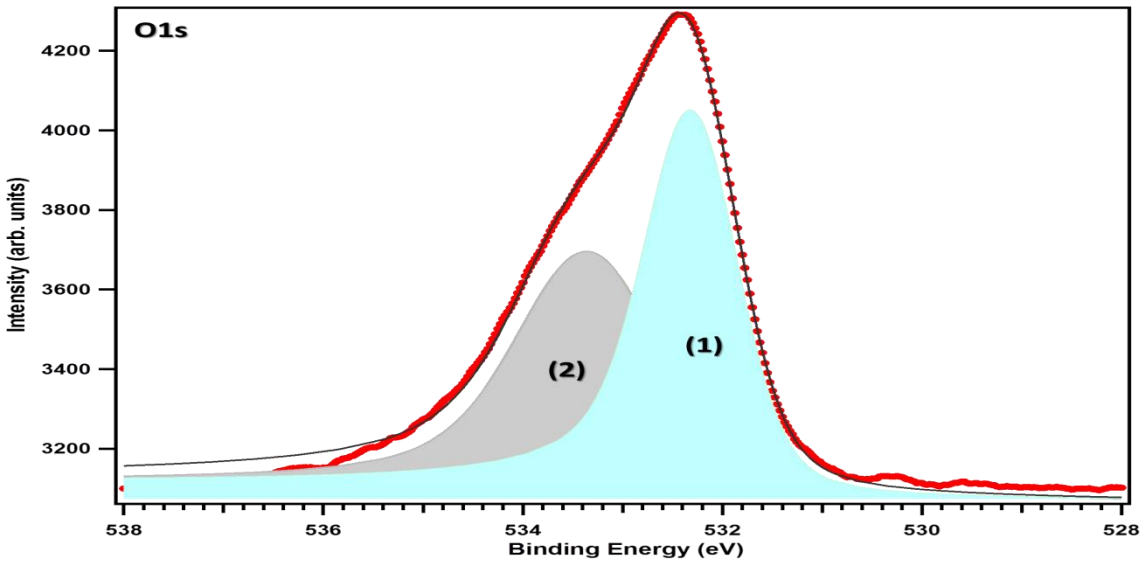

Figure 6-6: High-resolution XPS scan for the O 1s core level peak of the graphene grown on Ni.

6.2.1.3. *Homogeneity of the graphene layer: Raman mapping*

To check the homogeneity of the deposited graphene, we performed Raman mapping. Raman mapping of the *D*, *G* and *2D* band intensity of the graphene grown on Ni substrate is shown in **Figure 6-7**. The color contrast confirms that the graphene was homogeneously deposited on Ni. Some variation of the color contrast may be due to the presence of defects (e.g. wrinkles) or uneven surface of Ni substrate, which occurs because of annealing the Ni substrate at high temperature (~1000 ^{o}C).

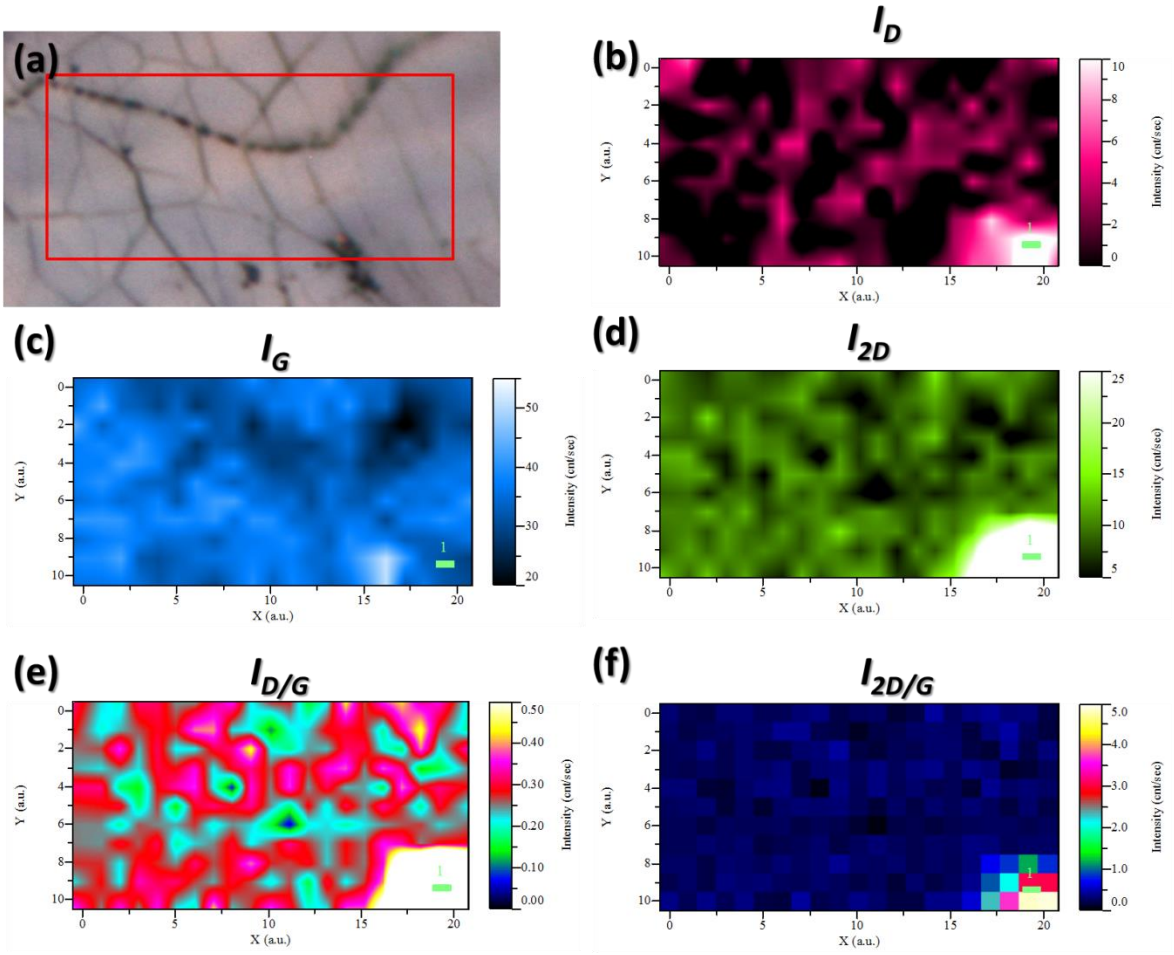

Figure 6-7: (a) Optical image, Raman mapping of integrated intensities of (b) *D*, (c) *G* and (d) *2D* band of the graphene grown on Ni. (e) and (f) show the calculation of integrated intensities of I_D/I_G and I_{2D}/I_G, respectively. The vertical bars show the color profile in the Raman mapping (scale in CCD counts).

6.3. Studies of charge injection in multilayer graphene using ambient Kelvin Probe Force Microscopy‡

This study presents the method for quantitative characterization of nanoscale electrostatic properties of as-grown multilayer graphene (MLG) sheets on nickel by a combination of Atomic Force Microscopy (AFM) and Kelvin Probe Force Microscopy (KPFM). Large area epitaxial MLG sheets were grown on nickel by using Chemical Vapor Deposition technique describe in the previous sections. High crystallinity MLG sheets on nickel were confirmed by Raman spectroscopy that revealed average *G*-bandwidths of about 20. Herein, the charge injection as well as subsequent charge diffusion in the MLG/nickel surface was studied for the first time. The results unveiled that: (i) MLG surface can be either positively or negatively charged through the injection process using Pt coated Si-based AFM probes; (ii) the charges were accumulated and eventually reached saturated concentrations of (+4.45 ±0.1) μC/m^2 and (−1.3 ±0.1) μC/m^2; (iii) the charge diffusion coefficients on graphene surface were measured to be (1.50 ±0.05) × 10^{-16} m^2/s and (0.64 ±0.05) × 10^{-16} m^2/s for the positive and the negative charges, respectively. The discovery of charge injection in MLG may pave the way for designing a new class of microelectronic devices. Additionally, our study demonstrated a technique for nano-patterning/charge lithography of surface charges by contact electrification, which could be a promising approach to create controlled nanostructures for next generation of graphene based nanoelectronic devices [257].

From both scientific and technological points of view, charge injection on insulating films has been of great interest for the development of multiple devices including triboelectric nanogenerators for building self-powered portable electronics, large-scale energy harvesting, and also to develop data storage devices [258]. In particular, charge injection measured using Kelvin Probe Force Microscopy (KPFM) technique was reported to be a useful method to study the electrostatic properties of materials at the nanoscale level [259]. Determination of the interface in carbon nanotubes (CNTs) based devices or distinguishing the metallic and semiconducting nature of CNTs with the same diameters, silicon nanoparticles, and semiconducting quantum nanorods are the major examples of the application of KPFM technique. In addition, KPFM has also been used to study different charge states of single metal atoms, molecules, atomic point defects, and imaging of the charge percolation pathways in two-dimensional quantum dot arrays [260].

‡ Parts of this chapter have been published as Applied Materials Today 8 (2017) 18–25).

Recently, KPFM was used for the imaging of charge distribution in different complex systems such as semiconducting quantum dots, carbon nanotubes, graphene on SiO_2, organic molecules, and even bacterial protein filaments [261-273]. Besides direct KPFM measurements, researchers have also performed nanolithography and manipulation of graphene by using AFM. For example, conductive Atomic Force Microscopy (c-AFM) [271] has been used to analyze the local current mapping and patterning of reduced graphene oxide. Sibel *et al.* used Electrostatic Force Microscopy (EFM) technique for the elucidation of the charge transport mechanisms in progressively deposited reduced graphene oxide [273]. With these measurements, it is possible to correlate the detailed morphology of graphene (e.g., wrinkles, multilayer regions, and local defects) with its nanoscale electrical characteristics, reading/writing charges, and local electronic behavior at graphene-metal interface.

In this particular direction, present study has shown successful charge injection (both positive and negative) and the subsequent visualization of charge distribution, as well as charge diffusion over time on the large area as-grown MLG surface. In addition to this, stable charged nanosized areas were created using so-called “charge nanolithography” These findings provide new insights in understanding the electronic charge behavior in large area MLG on nickel surface at the nanoscale. We assumed that this phenomenon arises due to low conductivity, and may be originated from MLG-nickel interface (which often introduces various defects into the mono- and a few layers graphene-nickel interface, so-called “defective regions”) [274, 275]. These include misorientation within the graphene layers, point defects, grain boundaries, wrinkles or ripples of the MLG sheets. Indeed it has been already proven that the sensitivity of electronic systems directly correlates with the defects and/or deformation in two-dimensional graphene lattice [276].

6.3.1. Results and discussion

6.3.1.1. *Scanning Electron Microscopy*

Figure 6-8 (a) shows representative Scanning Electron Microscopy (SEM) image of CVD-grown large-area MLG-nickel foil, which acts as a catalyst for graphene growth as well as bottom electrical contact during KPFM measurements. The inset shows some typical wrinkles on large area MLG sheet grown on nickel.

6.3.1.2. *Raman Spectroscopy*

To confirm the identity and quality of our as deposited MLG sheets on nickel foil, we performed detailed micro-Raman studies (see **Figure 6-8** (b)). Raman mapping over different areas with 1 µm steps (not shown) as well as individual spectra were obtained from MLG-Ni sample. **Figure 6-8** (b) reveals the Raman spectra taken of the grown sample clearly showing strong *G* peak (~1580 cm^{-1}), which indicates the formation of hexagonal lattice of carbon atoms. The high crystalline quality of MLG sheets on nickel is indicated by Raman spectroscopy revealing average *G* bandwidths as low as 20 at 488 nm excitation. Furthermore, the absence of disorder-induced *D* peak (~1360 cm^{-1}) also indicates extremely low density of defects in as-grown MLG sheets. We note that no *D* peak has been found in any area of the sample. The *2D* peak (~2700 cm^{-1}) is weaker compared to the *G* peak and has a wide line width of ~60, and its position is slightly up shifted compared to monolayer graphene. It is worth to mention that the Raman data presents the information only about the top graphene layers, which are away from MLG/nickel interface due to the low penetration depth of Raman excitation source into the sample. Thus, the top graphene layers (several nanometers) are free from any crystal defect as evidenced by the absence of Raman D peak mentioned above.

6.3.1.3. *High Resolution X-Ray Photoelectron Spectroscopy*

High Resolution X-Ray Photoelectron Spectroscopy (HR-XPS) was performed to reconfirm the quality of MLG-nickel sample and also to detect any contamination on the surface. XPS is a well-established technique used for revealing the elemental composition and the chemical environment of the detected elements. **Figure 6-8(c)** shows the overview spectrum of as grown MLG/nickel (in which only carbon is detected) and the inset displays the C 1s core level. C 1s spectrum demonstrates a quite sharp peak centered at a binding energy (BE) of 284.5 eV, which can be due to the high quality of sp^2 carbon.

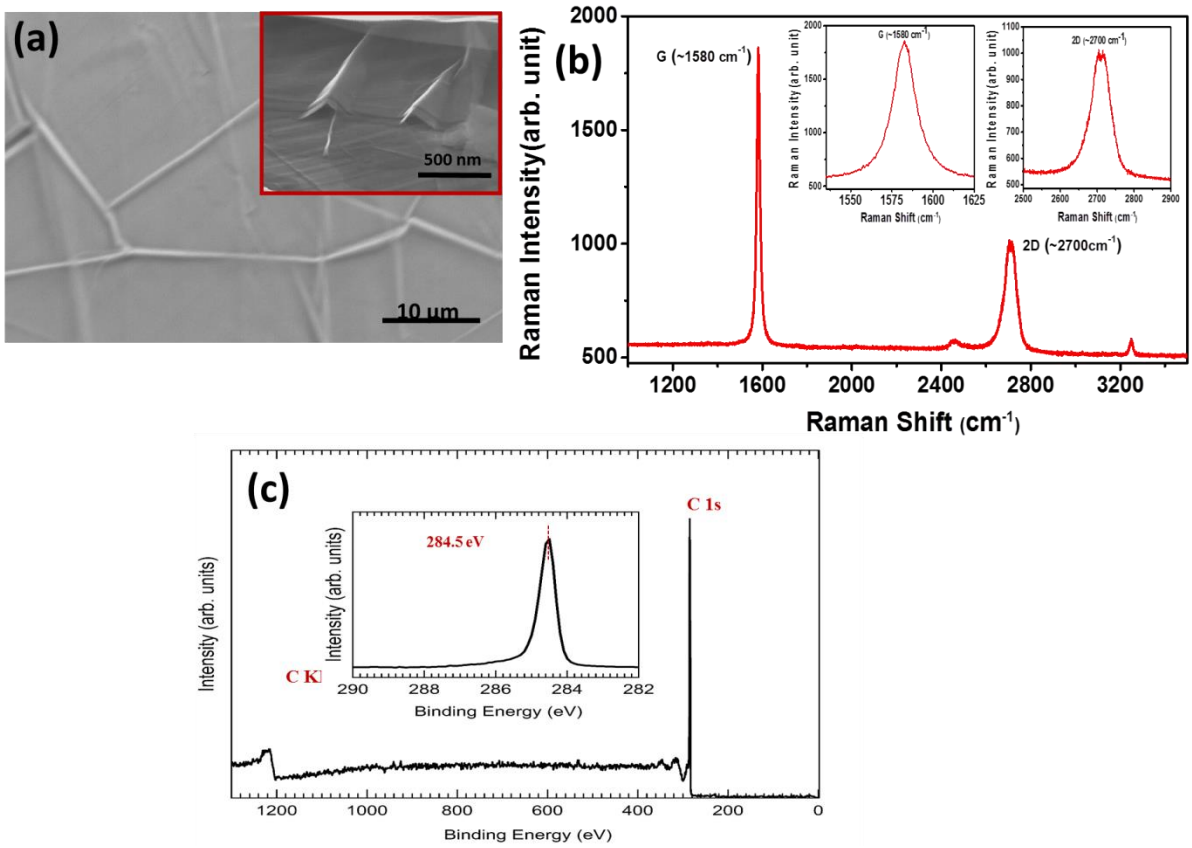

Figure 6-8: (a) Scanning electron microscopy (SEM) image of CVD-grown large-area MLG on nickel foil (inset shows the ripple), (b) Raman spectra of as-grown MLG on nickel, clearly showing the strong *G* peak (~1580 cm^{-1}) Inset is the zoom of the *G* and *2D* peaks, (c) X-ray photoelectron spectroscopy of as-synthesized MLG on nickel, inset shows high-resolution XPS of C 1s core level of MLG on nickel.

Moreover, its *FWHM* is 0.5, which clearly indicates a high-quality sample from the XPS point of view. Furthermore, an extra proof of the quality of the graphene sample is the lack of XPS peaks that could be ascribed to contaminants such as oxygen species (C-O or C=O) [266]. Finally, we notice that XPS did not detect any signature of the nickel substrate, indicating that several graphene layers grew on it.

Thus, the full set of characterization techniques (SEM, Raman spectroscopy and XPS) confirmed the high quality and defect free MLG/nickel sample. Additionally, the thickness of the MLG sheet was estimated by analyzing the AFM images of transferred samples (not shown) and found to be ~150 nm.

6.3.1.4. *Kelvin Probe Force Microscopy*

KPFM was done by using the two-pass technique for imaging of the contact potential difference between the sample and the AFM tip (see **Figure 6-9**). The principle of the KPFM is to match the probe bias V_{dc} with the contact potential difference between the sample and the probe V_{cpd} by nullifying the vibration of the probe, which is initially driven (with frequency ω) by the electrostatic force (F_{es}) as described by the equation below.

$$F_{es} = -\frac{dC}{dz}\left\{\frac{1}{2}\left[\left(V_{dc} - V_{cpd}\right)^2 + \frac{1}{2}V_{ac}^2\right] + \left(V_{dc} - V_{cpd}\right)V_{ac}\sin(wt) - \frac{1}{2}V_{ac}^2\cos(2wt)\right\}, \quad \text{(Eq. 6-1)}$$

where, C, z, V_{ac}, and t are the equivalent capacitance between the tip and sample, the tip−sample distance, the magnitude of ac voltage applied to the probe, and the time, respectively. V_{dc} is the tip bias voltage and V_{cpd} is the contact potential difference. .

Figure 6-9 shows detailed schematics of the charge injection experiments on MLG/nickel sample by KPFM. The local charge injection was performed by applying various dc voltages to the conducting tip, and followed by KPFM imaging (**Figure 6-9**). A representative topographic image with the superimposed surface charge potential (color coded) of the selected area is shown in **Figure 6-9(b)**. In the chosen region, the dc biases of V_{inj} = +10V (on the right) and -10 V (on the left) were applied between the conductive tip and the bottom electrode. The injection time (t_{inj}) was about 10 s, and the time interval between positive and negative applications was about 100 s. Immediately after the charge injection step, the tip was lifted around 20 nm away from the surface and the surface potential image was obtained in the KPFM mode.

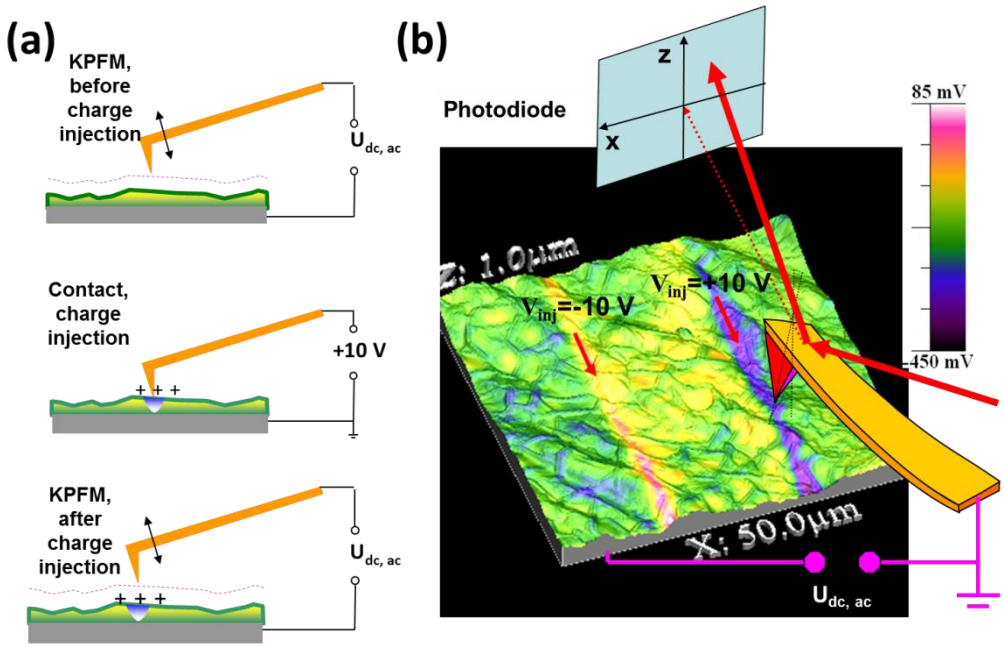

Figure 6-9: Charge injection experiments on MLG/nickel surface based on AFM. (a) Schematic illustration of KPFM and contact mode for charge injection process. (b) 3D example of charge injection schematic presentation. The topography is mapped onto the third dimension (z-axis) and the recorded surface potential is color coded.

The observed KPFM image reveals two stripes with a clear contrast due to the local potential difference and surface charge redistribution (see **Figure 6-9(b)**). It is worth mentioning that the contact potential difference of the area induced by the applied bias voltage is several times greater than that of the applied voltage.

Macroscopically, the injection occurs via the local area in the situation where the electric field is uniform. The RMS roughness of MLG/nickel obtained by AFM is around 3 nm (for 3x3 μm^2 scan) confirming high quality and uniformity of the MLG film. Therefore, the injection averaged over the entire region under the electrode. In surface potential experimental conditions, the electric field is strongly localized and inhomogeneous, and, therefore, the injection starts with the nucleation of a small area just under the AFM tip. Under the applied voltage, this area elongates to the bottom electrode and simultaneously expands in lateral directions until reaching an equilibrium size, which depends on the value of the maximum applied voltage. Saturation of the injection is achieved, when the size of the area is much larger than the contact tip-surface area. The threshold voltage describes the voltage at which a stable injected area is formed below the tip.

Figure 6-9(b) shows the effect of the voltage applied to the AFM conducting tip on the surface potential signal. The size and stability of injected area is directly related to macroscopic properties such as conductivity and its anisotropy, effective tip diameter and contact conditions. The calculations of the electric field distribution under the AFM tip with effective diameter ~10 nm and applied voltage of ±10 V corresponds to an electric field of ~0.006 V/Å for MLG sheet thickness of ~150 nm.

In the present work, the topography of the scanned area was checked each time before and after local charge injection, and no changes were revealed even after the application of dc voltages up to +12 V. **Figure 6-10 (a-f)** shows charge injection experiment along linear paths on MLG/nickel sample. **Figure 6-10** shows the topographic image before **(a)** and after **(b)** the charge injection with V_{inj}=−5 V and +5 V, injection time (t_{inj})=10 s, and scanning tip velocity of 3.5 $\mu m s^{-1}$. Immediately after the charge injection step the AFM tip was lifted 20 nm to measure the surface potential (see **Figure 6-10 (d)**. For better clarity **Figure 6-10 (e)** represents the difference between the images of **Figure 6-10 (c)** and **(d)**. The areas in which the charge injection was done are clearly recognized. Furthermore, the profile presented in **Figure 6-10 (f)** resembles the potential contrast between the charged and non-charged areas.

The difference in SP values (ΔV) was correlated to the surface charge density σ using a parallel capacitor model, as given in **Eq. 6-2**, since the scale of the charged area (~4 μm^2) is much larger than the thickness of the MLG sheet.

$$\boldsymbol{\sigma = \frac{\Delta V \varepsilon_0 \varepsilon_{MLG}}{t_{MLG}}},$$ (Eq. 6-2)

where ε_0 (8.854187817 x 10^{-12} Fm^{-1}) is the vacuum dielectric constant and ε_{MLG} and t_{MLG} are the relative dielectric constant and thickness of MLG sheets, respectively. Recently, Santos *et al.* studied the effect of electric field on the effective dielectric constant in n-layer graphene and noted that the values of out-of-plane ($\varepsilon_\perp$) and the in-plane ($\varepsilon_\parallel$) dielectric constant are nearly constant (~3 and ~1.8, respectively) under applied electric field (~0.005 V/Å) [277]. In the case of ΔV_+ = 0.025 V, σ is calculated to be (+4.45 ± 0.1) μCm^{-2} and ΔV_- = 0.007 V, σ is (-1.3 ± 0.1) μC/m^{-2}.

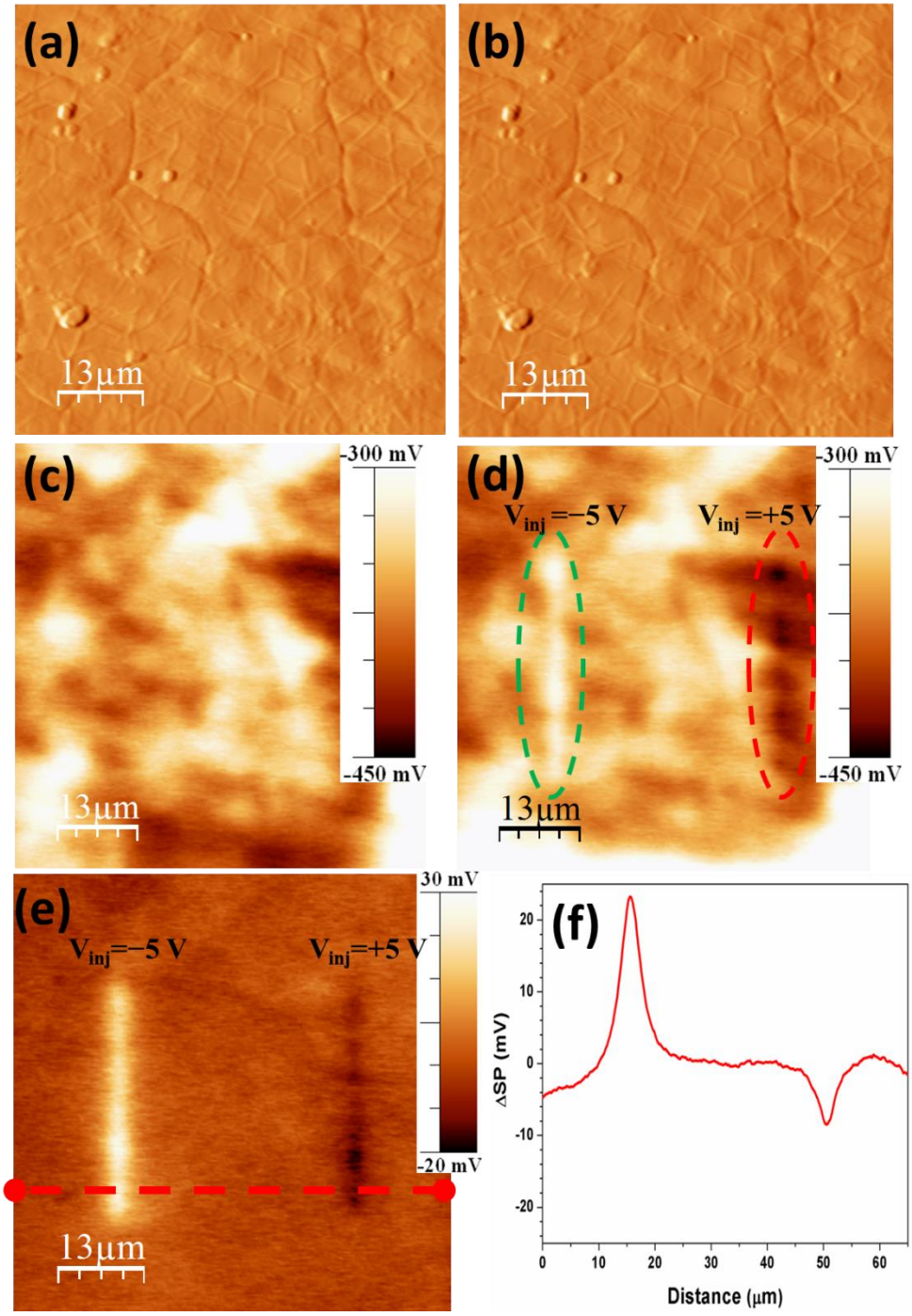

Figure 6-10: Charge injection experiments on MLG/nickel. AFM topography image before (a) and after (b) charge injection, performed with the conducting tip (Vinj=−5 V, Vinj=+5 V; and injection time tinj=10 s). Surface potential image before (c) and after (d) injection. (e) represents the difference between images (c) and (d) for more clarity. (e & f) Profile of the surface potential signal across red dotted lines.

Besides this, we studied the surface stability of MLG-Ni film under higher voltage injection via the AFM tip (**Figure 6-11**). **Figure 6-11 (a)** and **(b)** show the topography before and after injection, respectively, while (c) represents the surface potential image before injection. In our experiment, we created a pattern of dark lines by applying bias voltages of V_{inj}= +2.5, +5.0, +7.5, +10.0 and +12.5 V, from left to right in **Figure 6-11 (d-f)**, with scanning tip velocity of 3.5 $\mu m s^{-1}$ and injection time of 10 s. **Figure 6-11 (e)** shows the profile along the red line indicated in (d), while (f) shows the surface potential as a function of the applied voltage. The difference in the injected charges in the parallel lines leads to the variation in contrast, which can be explained by charging the capacitance (polarization). Interestingly, we observed that the MLG-Ni surface topography is stable even at the highest tip voltages (**Figure 6-11 (b)**).

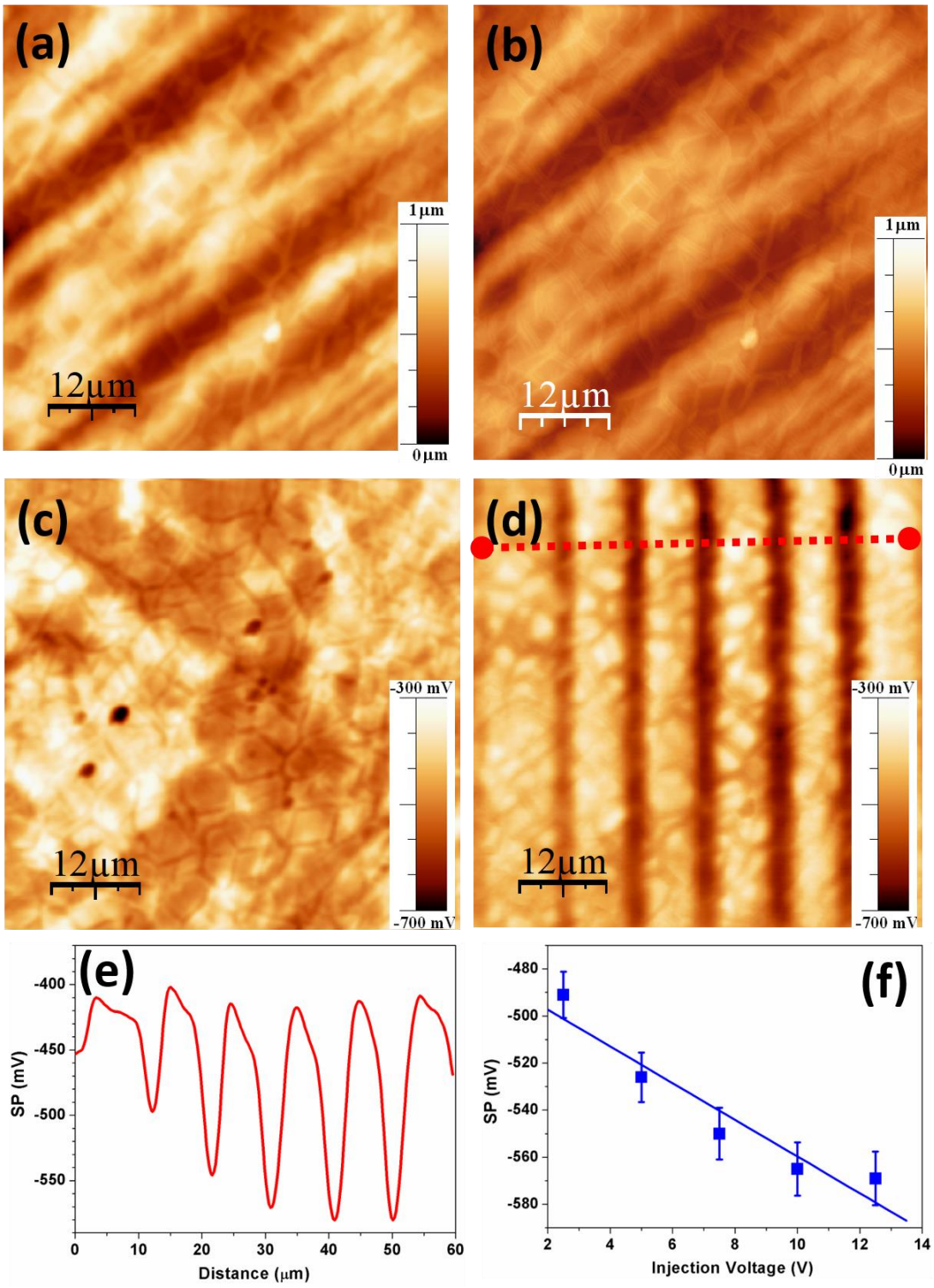

Figure 6-11: Surface stability of MLG films under higher voltage injection through the AFM tip. (a) Surface topography of as-grown MLG film before and (b) after injection. (c) Surface potential image before injection and (d) Surface potential images of the electric-field-induced contrast on MLG films obtained after the application of Vinj=+2.5, +5.0, +7.5, +10.0, and +12.5 V to the tip (dark lines from left to right). (e) profile along the red dotted line showed in (d). (f) SP intensity vs applied voltage obtained from (e).

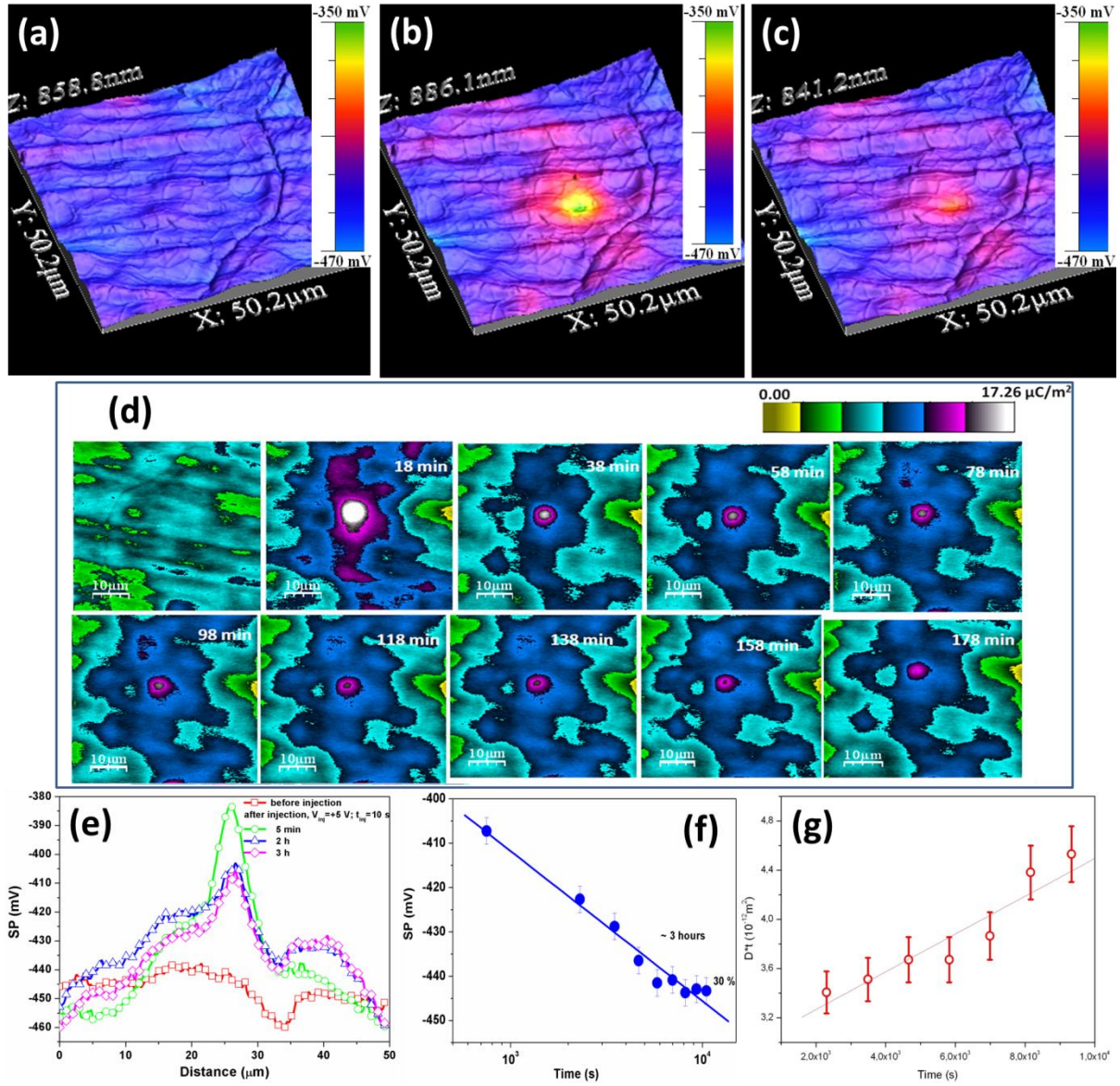

Figure 6-12: Topography with KPFM image over-imposed (colored coded) before (a), immediately after (b) poling, +5 V, 10 s, and (c) after prolonged aging 3h (c). (d) Charge relaxation starting before injection till 180 min after injection, with the intervals of 20 min.(e) Profile of the images taken before, immediately after poling, and after 2-3 hrs. (f and g) SP intensity vs. time obtained from (e) and (g) D*t vs time.

Moreover, taking the advantage of the nanometer scale resolution of AFM and KPFM, the method is able to study the charge propagation by monitoring the surface potential distribution on two-dimensional MLG/nickel surface. In our experiment (**Figure 6-12 (a-g)**), we examined the

evolution of induced surface potential as a function of time by measuring the potential immediately after charging (**Figure 6-12 (b)**), and after prolonged aging time (**Figure 6-12 (c)**). For this particular experiment, the charge was injected (V_{inj}=+5 V, and t_{inj}=10 s) at a point and the subsequent charge relaxation was monitored (**Figure 6-12 (d)**) during nearly 3 hrs with the time intervals of 20 min. From the **Figure 6-12 (e-f)**; it is clearly seen that the initial pattern is not really stable and reduces about 30% of the initial value of surface potential after about 3 h (t = 300 s is the time needed for a single scan). The fitting was done with the Kohlrausch–Williams–Watts formula (Eq. 6-3) commonly used to describe relaxation in the system with dipole–dipole interactions, as described below [278].

$$\boldsymbol{SP = SP_0 \exp[-(t/t_0)b],} \qquad \text{(Eq. 6-3)}$$

where t is the time, bt_0 is the effective relaxation time and b is the parameter. For b = 1 the **Eq. 6-3** reduces to simple Debye relaxation formula. For our case, we obtained effective relaxation time ~ 1 hr (see **Figure 6-12 (e, f)**). This parameter is much higher than 10^{-9} s, which is obtained from the simple formula (**Eq. 6-4**) for Maxwell relaxation time. Moreover, Maxwell's equation actually reproduces Ohm's law for the case when the initial potential difference is given and discharge as the function of relaxation time (τ) is studied. For the case of constant voltage (conductivity does not change) relaxation time and conductivity are related as described in **Eq. 6-4**.

$$\boldsymbol{\tau = 4\pi\varepsilon\varepsilon_0\rho,} \qquad \text{(Eq. 6-4)}$$

where, ε_0 is the vacuum dielectric constant and ε dielectric constant. Based on the conductivity measurement from the recent report published by Rani *et al.* [279], the Maxwell relaxation time (from **Eq. 6-4**) is estimated to be ~10^{-9} s. It means that the locally induced charge states decay with a characteristic time that is many orders of magnitude greater than the expected Maxwell relaxation time of uncharged surface material. Moreover, charges diffuse laterally on the surface in two-dimensions as well as vertically into the bulk [280, 281]. In our charge injection experiment, we noticed that the charge migration is mostly in two dimensions and very low in vertical direction. It is due to some charges leaked into the bottom electrode rather than spreading over the surface. Since the characteristic length of the charge diffusion on the surface (~5 μm) is much larger than the thickness of the MLG film (~150 nm) we can employ the model

for a two-dimensional diffusion to estimate the surface charge diffusion coefficient on MLG sheet from a point source (x_0, y_0), as described in **Eq.6-5** [282, 283].

$$\boldsymbol{\sigma(x,y,t) = \frac{A}{t-t_0}\exp[-\frac{(x-x_0)^2+(y-y_0)^2}{4D\,(t-t_0)}]},\qquad \text{(Eq. 6-5)}$$

where, $\sigma(x,y,t)$is the surface charge density of a point (x,y) at a time (t), A is the magnitude constant and D is the diffusion coefficient on the given surface [282]. This equation represents the modified theoretical distribution of the applied electric field outside the moving tip in the frame of the spherical model and point charge approximation first developed by Mele *et al.* [284-286]. Furthermore, **Figure 6-12 (d)** represents the series of images of charge distribution as a function of time after positive charge injection. The surface potential/charge distribution was monitored by KPFM every 20 min. By fitting the data at different diffusion times (as illustrated in **Figure 6-12 (e-f)**), we can calculate the slope of the curve "D" **Figure 6-12 (g)**. From the fitting, the positive surface charge diffusion coefficient D = (1.50 ± 0.03) × 10^{-16} m^2s^{-1} was obtained. Using the same method, the negative surface charge diffusion coefficient on the MLG film was estimated to be (0.64 ± 0.05) × 10^{-16} m^2s^{-1}. The difference in the surface diffusion coefficients may be related to difference in the mobilities of charge carriers and the structure of the surface. Interestingly, after several hours KPFM signals from locally modified areas were still visible.

We assume that the charge in the locally modified areas is stabilized due to low conductivity, multi-layer graphene nature, and may be originated from MLG/nickel interface (often introduce significant defects into the mono and a few layers graphene-nickel interface layer, so-called “defective region”) [274, 275, 287].

Another reason of the slow relaxation of the charge may be the strain on MLG film on nickel, which arises due to different thermal expansion coefficients for nickel and graphene [+13x10^{-6}/°C and −8x10^{-6}/°C, respectively] [288]. We estimated the total strain on multi-layer graphene film after cooling from 1000 °C to room temperature is ~2%. This strain produces high degree of ripples, and boundary conditions (domain-like structures) on the atomically flat surface of the MLG sheets (clearly observed in **Figure 6-10 (a)**). In addition, differences in work functions and charge density under mechanical deformation [289] could be also responsible for the stabilization of the injected states in MLG films. For example, contact with metal and doping modifies the work function of single and MLG graphene sheet [290-292]. In the case of nickel, the reported value is 0.125 eV [293]. We also performed this experiment with monolayer graphene samples fabricated

in our lab, and did not observe these phenomena. We assume that this is due to the high-conducting nature of monolayer graphene sheet.

Using demonstrated capability of controlled charge injection process, we can investigate the local charge transfer at the interface. This can be also used for the patterning of surface charges at the nanoscale. The polarity of the written charges could be controlled simply by positive and negative voltage pulses.

6.3.2. Conclusions

The experiment described above resulted in the deposition of thick graphene layers on nickel substrates. The as synthesized graphene was found to be multilayer graphene (MLG) due to high carbon absorbing nature of nickel. The results from Raman spectroscopy confirm that MLG is highly crystalline in nature, with sharp G peak at ~1560 cm^{-1} (with *FWHM* of ~24). The *D* peak (~1350 cm^{-1}) confirms the existence of defects present in the form of wrinkles. This was further proven by SEM images. Moreover, the results from HR-XPS show that the C sp^2 nature and the peak can be fitted by only one component centered at 284.4 eV. In addition, results obtained from Raman mapping demonstrates the overall coverage of the sample on the large area.

Lastly, in the charge injection experiments, nanoscale electrostatic properties of as-grown MLG sheets on nickel were performed by a combination of contact mode AFM and KPFM. By using this method, we systematically investigated the charge injection (by applying positive or negative potential to the AFM tip) and subsequent charge diffusion. From the above measurements, we elucidated that after injection, charge area is quite stable (even after 3 h) and the relaxation time is much longer than the expected Maxwell relaxation time required for the charge equilibration. The outcomes of this study could be promising for nano-patterning of surface charges with clear potential for directed self-assembly of charged nanostructures for nanoelectronic devices such as super-capacitors, and in the field of energy-harvesting devices.

Chapter 7

Transfer of pure and *n*-doped graphene on different substrates

Abstract

This chapter describes the results concerning transfer of graphene flakes on SiO_2/Si substrates done in this work. Transfer of graphene is essential for its utilization in many applications. We have studied the transfer methods and optimized the procedures to obtain clean and mechanically robust graphene on rigid substrates. Observed Raman lines are all belonging to the known peaks of pure and *in-situ* ammonia doped (*n*-doped) graphene. Moreover, the mapping obtained by micro Raman spectroscopy demonstrated sufficiently uniform layers deposited over the large area by using our standard transfer method (without any polymer, such as PMMA). Results from HR-XPS spectra show the carbon (sp^2) nature of the peak of the transferred graphene. However, for the case of *in-situ* ammonia doped graphene on SiO_2 we found C-O peak (along with C sp^2). In the as grown *n*-doped graphene a predominance of desired graphitic nitrogen (N) was revealed. The dominance of pyridinic N at the expense of substitutional N evidences again the generation of defects on the graphene sheet during growth. We also report the iron intercalation in graphene sheets upon the transfer process. This was confirmed by HR-XPS and stabilization was checked by the heat treatment in ultra-high vacuum.

7. Transfer of pure and *n*-doped graphene on different substrates

Transfer of graphene is essential process because graphene sheets on different substrates are likely to be used in various industrial applications. Depending upon the growth method the transfer process varies, e.g. graphene from graphite samples requires micromechanical cleavage etc. Hence, different transfer processes come into play and plays a crucial role in the formation of final structure. Literature reports describe graphene transfer on various substrates such as SiO_2 [4], Al_2O_3 [25], WO_3 [91] etc. Beside these it has been also transferred on polymers such as polyethylene terephthalate (PET) [92], polydimethylsiloxane (PDMS) [93], polystyrene (PS) [94], polyimide (PI) [95]) etc. Moreover, a few metallic substrates have been also reported including Au [96], Ti [97], NiFe [43], nanostructured Ag [98], and Li [99]). Substrates such as boron nitride [100], SiC [101], SiN_x [102], sapphire [103], InAs/GaAs [105] and KBr [106] are considered for the transfer of graphene.

There are various methods which have been applied for the transfer of graphene on desired substrates. Reina *et al.* [294] used a polymeric layer for the support of graphene. It must be kept in mind that a single layer of graphene is so thin that perfect transfer without cracks or defects is extremely hard to do. Therefore, spin coating of polymeric layer on graphene/substrate film is used in order to manipulate it easily.

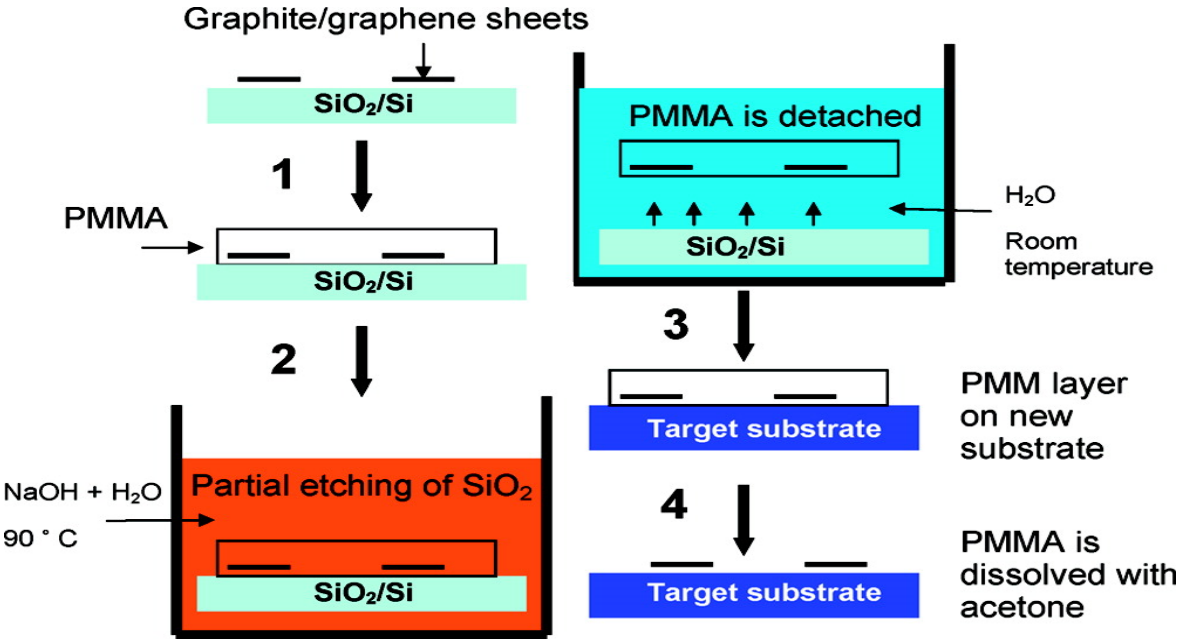

Figure 7-1: Schematic diagram highlighting the major procedure for the transfer of graphene using poly(methyl methacrylate)) (PMMA). Adapted from [294].

Figure 7-1 shows the transfer process used by Reina *et al.*[294]*,* in which a polymer PMMA (poly(methyl methacrylate)) is spin coated on graphene grown on a substrate. Afterwards, it is immersed in the etchant solution in order to etch the substrate away leaving freestanding PMMA/graphene. This freestanding graphene/PMMA is washed out in water to clean of the remaining etchant solution. Finally, the graphene/PMMA is transferred on the substrate. Upon this, the polymer layer is dissolved in the acetone leaving only graphene deposited on the desired substrate. This method is the most employed technique due to easy availability of PMMA. However, dissolving PMMA is a critical issue and, to our best knowledge, only three PMMA solvents are currently being used:

(i) Anisole (2% [108], 4 vol.% [111], 5% [101], 6–9 wt.% [110], 8 wt.% [112] or 50% [113]),

(ii) Chlorobenzene (3% [114], 10% [99], 20 mg/ml [109] or 46 mg/ml [115], 50 mg/ml [116])

(iii) Toluene (4 wt.% [117])

The influence of the PMMA residue on the graphene deteriorates the electrical conductivity and other properties of graphene. Hence, it is quite important to remove the residual PMMA after the graphene is transferred.

The use of PMMA to protect graphene layer is an easy technique for the graphene transfer on any desired substrate and many researchers tried to improve this process. In 2009, Li *et al.* used second layer of PMMA deposited on first layer by spin coating. This prevents the cracks, which were observed if only one layer of PMMA is used. During the second coating, a liquid PMMA solution was added to the first layer in order to dissolve the pre-coated PMMA. That involves mechanical relaxation at the interface between PMMA and graphene layer, which can be transferred more easily without cracks and tears [134]. In another work published in 2011 Suk *et al.* used to bake out their samples at 180 ^{o}C for 3 h to improve the graphene adhesion and its quality after transfer.

Beside this Regan *et al.* [295] used direct transfer of graphene on the desired substrate (see **Figure 7-2**). In this work, they used the mechanism of surface tension and evaporation in order to pull Cu-supported graphene into intimate contact with the targets, simultaneously achieving the desired graphene/target bond and providing a rigid graphene support (the target substrate) during subsequent Cu etching. The benefit of this direct transfer is that it is cleaner and gentler

than the polymer-based methods, which makes it ideal for the fabrication of a variety of optical, chemical, and electronic devices that utilize large, uniform graphene sheets. In the direct transfer methods, this support is provided by the target substrate, specifically TEM grid's a-C film in this case. For better bonding of graphene and a-C film, they placed the TEM grid just on the top of graphene/Cu and dropped the isopropanol (IPA) solution. Consequently, both the grid's a-C film and the underlying graphene film got wet. As the IPA evaporates, the surface tension draws the graphene and a-C TEM grid together into intimate contact.

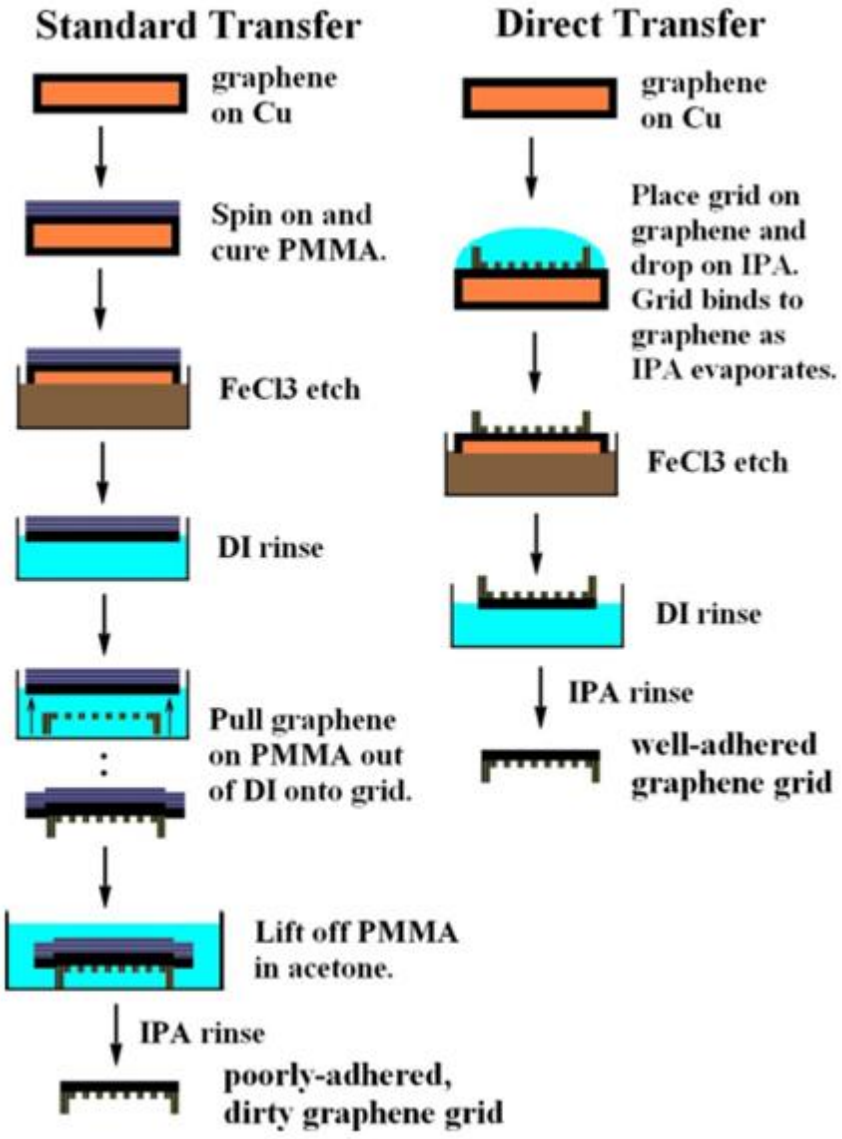

Figure 7-2: Schematic diagram and comparison between the standard, e.g., PMMA-based and direct transfer of layer-area graphene to hole of an a-C TEM grid. Adapted from [295].

Apart from this, Kim *et al.* [3] in their extensive work used CVD technique for the growth of a few layer graphene films and their successful transfer on arbitrary substrates without intensive mechanical and chemical treatments, in order to preserve their high crystalline quality. The transferred graphene films show very high conductivity and very low sheet resistance of 280 Ω per square (2cm x 2cm), 80% optical transparency (also at low temperatures), and high electron mobility (greater than 3,700 $cm^2 V^{-1} s^{-1}$).

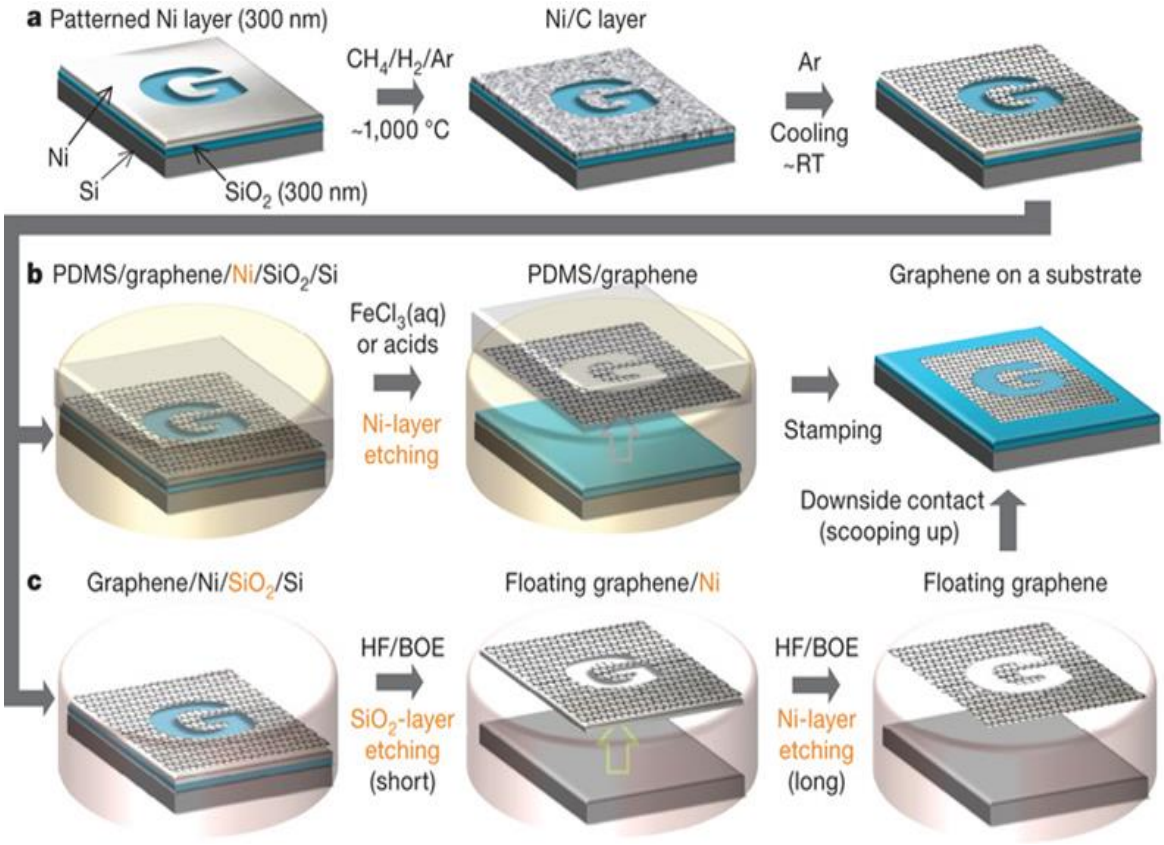

Figure 7-3: Schematic diagram of the synthesis, etching and transfer processes for the large scale and patterned graphene films. (a) Synthesis of patterned graphene films on thin nickel layers, (b) Etching using $FeCl_3$ and transfer of graphene films using a PDMS stamp, (c) Etching using BOE or hydrogen fluoride (HF) solution and transfer of graphene films. Adapted from [3].

The authors of Ref [3] initially deposited a very thin layer of nickel (thickness < 300 nm) on SiO_2/Si using an electron-beam evaporator, and then they grew graphene on this substrate (see **Figure 7-3 (a)**). Upon this, they etched away the nickel substrate using $FeCl_3$ as described elsewhere, leaving the adhered graphene film on the PDMS substrate (**Figure 7-3 (b)**). By using the pre-patterned nickel substrate (**Figure 7-3 (c)**), they were able to transfer graphene of various sizes

and shapes on any arbitrary substrate. This dry-transfer process turns out to be very useful in making large-scale graphene electrodes and devices without additional lithography process [3].

In addition, it is interesting to mention that various etchant solutions were used to etch the metal substrates. For copper substrate: ammonium persulfate (0.05M [296], 0.2M [297], 0.5M [298][129], 0.05 g/ml [299], 1 wt.% [300], ammonium sulfate (0.1M [301]), iron (III) chloride (0.4 g/ml [302], 1M [303], iron (III) nitrate (0.05 g/ml [304], 0.7M [305], iron (III) chloride (0.25M) followed by HF (10%) [306], and commercial etchant from Transene: 49-1 [307], CE-100 [308], CE 100/200 [309], CE-100 followed by HCl (10%) [310], CE-100 followed by HNO_3 (10 min) [311] were used. For the nickel substrates hydrogen fluoride [233], hydrochloric acid (3w.% [250], 15% [312], and nickel etchant from Transgene (90◦C – 2 h) [313] were used.

7.1.1. Results and discussions

7.1.1.1. *Optical data, Raman spectra and Raman mapping*

In our case, we used standard procedure, i.e. graphene films grown on Cu substrates were put in $FeCl_3$ aqueous solution (1M) for etching the underlying copper. After the removal of copper substrate, the floating graphene film was washed in DI (deionized distilled water) for the removal of etchant residues. Finally, fresh clean graphene was ready to be transferred directly on Si/SiO_2 (300 nm) substrates (see **Figure 7-4**). It is worth mentioning that, since graphene was transferred on these substrates, it made a clear optical contrast seen by the eye.

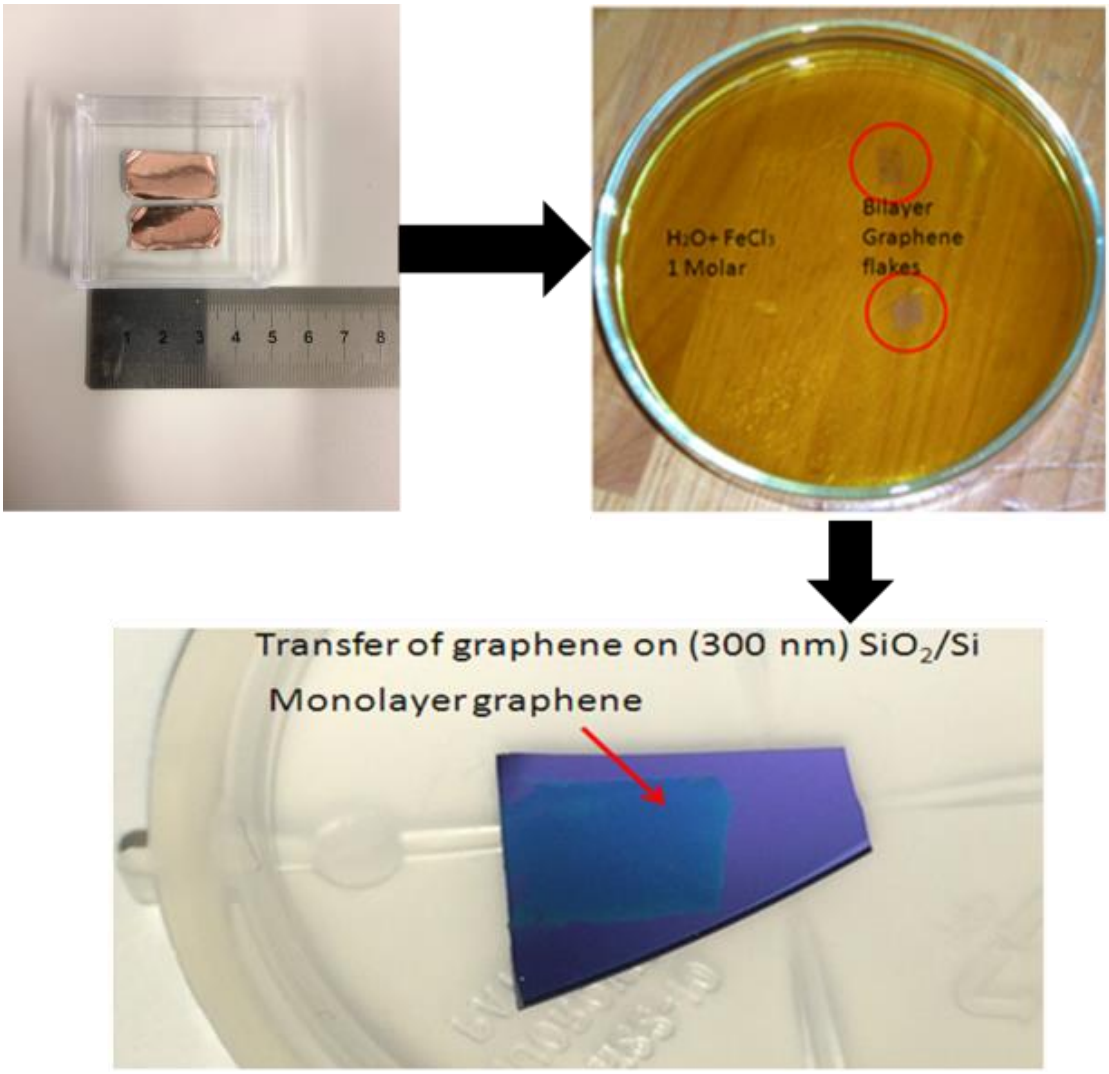

Figure 7-4: Major transfer processes for the large-scale graphene films: Large-scale graphene film grown on copper (Cu) substrate, floating graphene film after etching the copper layers in (1M) $FeCl_3$ aqueous solution. After the removal of the copper layers, the floating graphene film can be transferred directly on Si/SiO_2 (300 nm) substrate.

7.1.1.1.1. Pure graphene transferred on SiO_2/Si

Silicon dioxide (SiO_2/Si) substrates were used to transfer both pure and *n*-doped graphene grown on Cu substrates using CVD technique. Silicon wafer is the most common material and widely used for a variety of high-tech industries, including integrated circuits, detector/sensor devices, MEMS, opto-electronic components, solar cells etc. This substrate has a native oxide layer of ~300 nm in thickness, which makes them optically blue. This feature enables us to see directly the quality of the transferred samples.

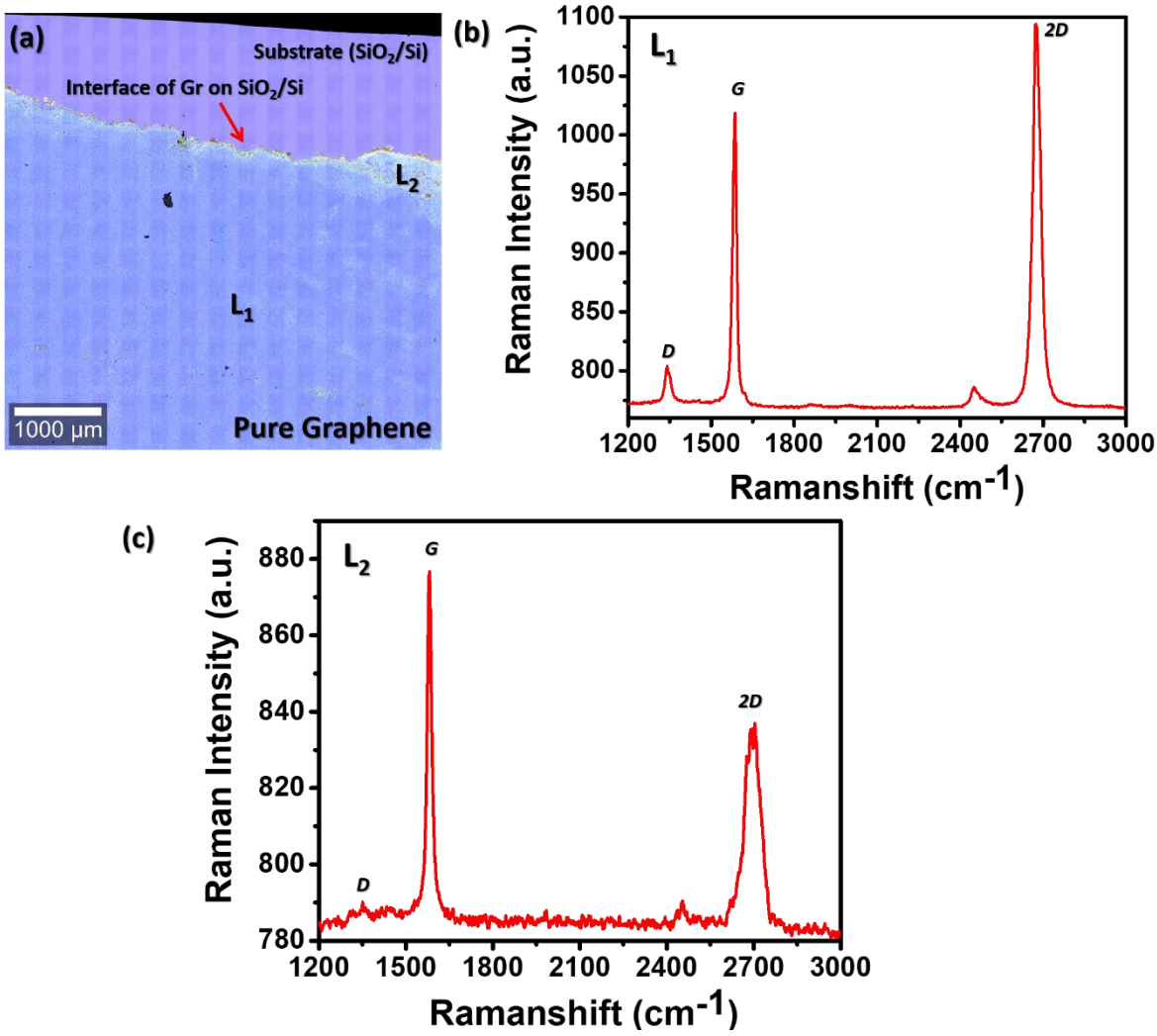

Figure 7-5: (a) Optical image of pure graphene deposited on SiO_2/Si taken using 10x objective for large area, (b) Raman spectrum of the graphene taken at point L_1 (marked on optical image), (c) Raman spectrum of the graphene taken at point L_2 (marked on optical image).

It can be seen from the optical image (**Figure 7-5 (a)**) that the graphene transferred on the substrate is quite good in quality and has sufficiently large area. The clear color contrast can distinguish the area covered by graphene and the interface between the graphene and SiO_2/Si. The Raman spectra were taken at different places as marked by **L_1** and **L_2** (shown on optical image). **Figure 7-5 (b)** shows the Raman spectrum recorded at "**L_1**" point and demonstrates the evidence of the good quality of the graphene upon transferring. The peak positions, intensities and *FWHM* related to *D*, *G*, and *2D* features were recorded and they are summarized in **Table 7-1**.

Table 7-1: Positions, intensities and *FWHM* of the Raman peaks acquired from pure graphene transferred on SiO_2/Si

Locations	Peaks	Position (cm^{-1})	*FWHM*	Intensity (a. u.)
L_1	*D*	1340.57	12.62	790
	G	1586.62	18.62	876
	2D	2673.00	63.18	63
L_2	*D*	1350.77	23.63	804
	G	1581.00	17.50	1018
	2D	2703.96	34.00	1095

To check the homogeneity of the deposited layers, we performed Raman mapping. **Figure 7-6** (a-c) presents the Raman mapping of the *G* peak, *D* peak and *2D* peak intensities of the graphene transferred on SiO_2/Si, respectively. The color contrast clearly depicts that the graphene was relatively homogeneous, however the intensity changed in the right upper corner of the image (*G* and *2D* band) possibly due to defects. However, relative intensities (*D*/*G* and *2D*/*G*) were uniform, indicating the overall good coverage of the sample on large area.

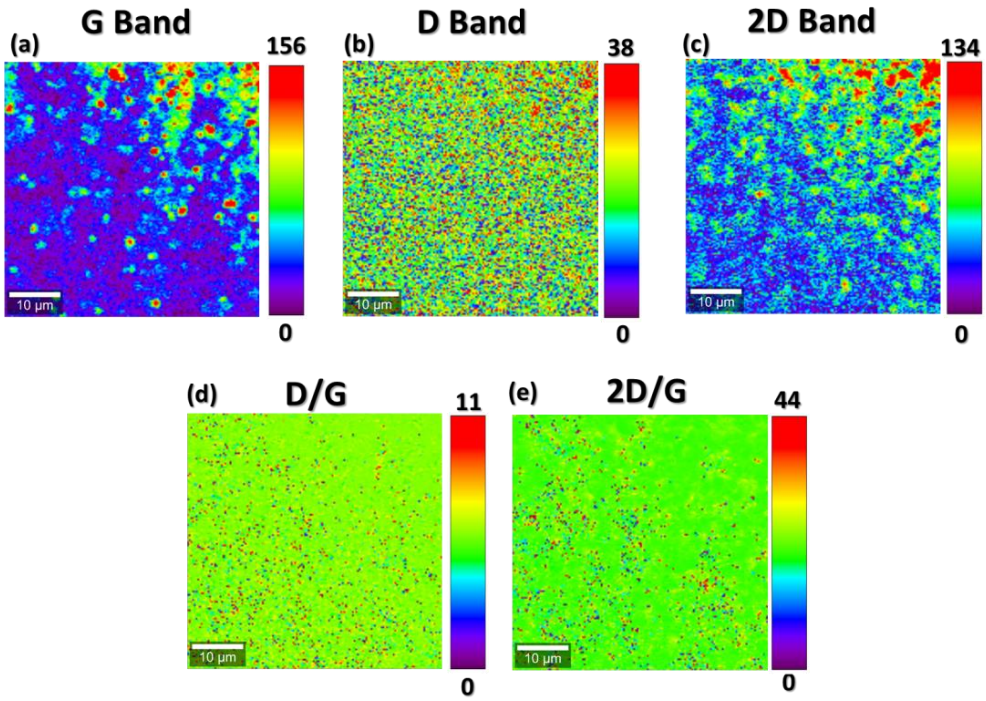

Figure 7-6: Raman mapping of (a) *G*, (b) *D* and (c) *2D* band intensities of the pure graphene transferred SiO_2/Si. Maps of relative intensities I_D/I_G (d) and I_{2D}/I_G (e) are also shown on the figure.

7.1.1.1.2. In-situ ammonia doped graphene transferred on SiO_2/Si

Similarly, to the case of pure graphene *in situ* ammonia doped graphene was transferred on SiO_2/Si. **Figure 7-7** (a) shows the optical image of the sample and its uniformity on large area. However, a few cracks have been detected and presented as dotted lines (red color). The clear contrast between the graphene and the substrate is seen, as well as the interface between the two. The Raman spectra were taken at randomly different places and are marked as **L_1**, **L_2** and **L_3** in the optical image. **Figure 7-7** (b) displays the Raman spectrum recorded at "**L_1**", which is a signature of good quality of graphene upon the transfer.

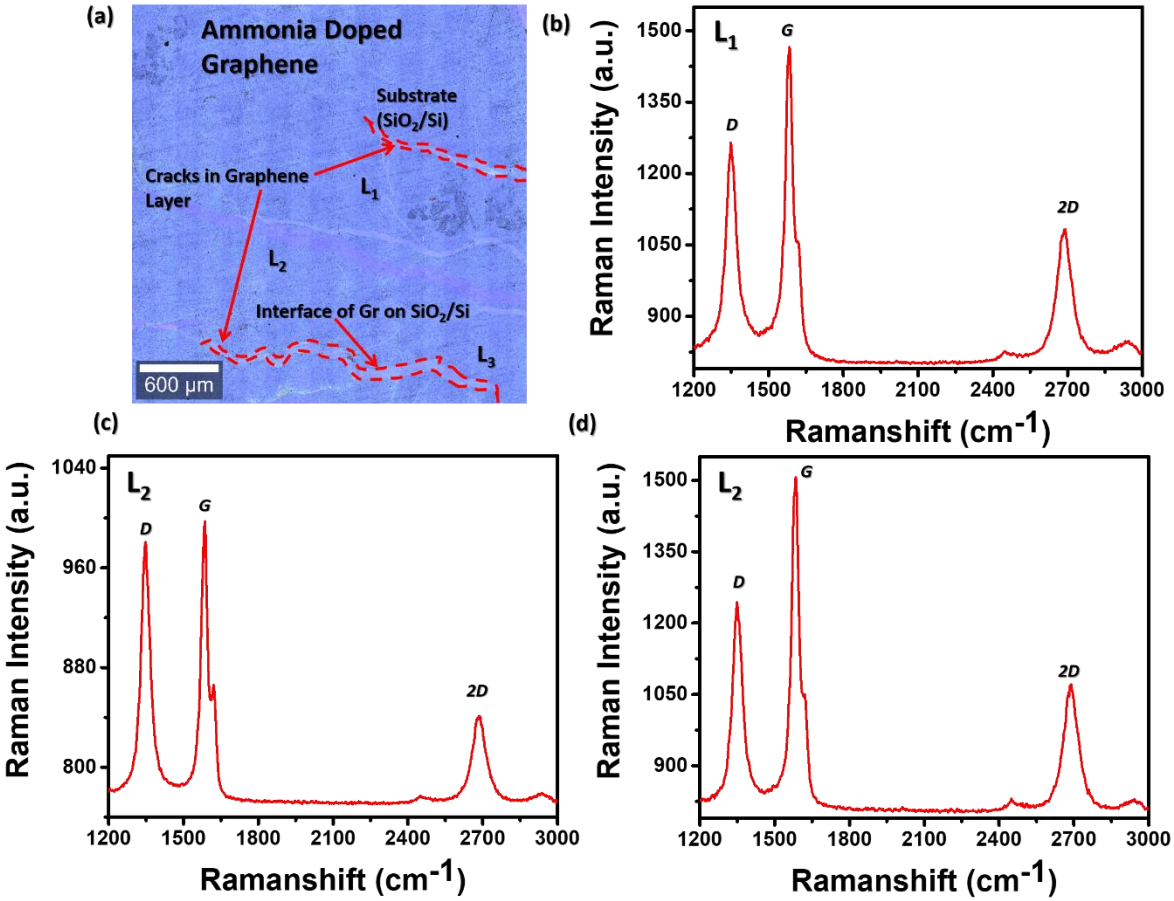

Figure 7-7: Optical image and Raman spectra of pure graphene transferred on SiO_2/Si using standard procedure without polymer such as PMMA. (a) Optical image taken using 10x objective to see large area, (b) Raman spectrum of the graphene taken at point L_1 (marked on optical image), (c) Raman spectrum of the graphene taken at point L_2 (marked on optical image), (d) Raman spectrum of the graphene taken at point L_3 (marked on optical image).

The peak intensities and *FWHM* related to *D*, *G*, and *2D* features were collected and are summarized in **Table 7-2**. The table clearly shows that the region covered by **L_1** are in the agreement of good quality *n*-doped graphene transferred on the substrate. The lower values of *FWHM* shows high sharpness of the peak directly confirms the quality of the sample. Additionally, the intensities of the G, D and 2D peaks are also high which re-confirms the quality of the sample.

Table 7-2: Positions, intensities and *FWHM* of Raman peaks acquired from an *in-situ* ammonia doped graphene transferred on SiO_2/Si.

Locations	Peaks	Position (cm^{-1})	*FWHM*	Intensity (a. u.)
L_1	*D*	1348.22	45	1264
	G	1584.15	35	1465
	2D	2691.13	70	1080
L_2	*D*	1348.22	44	1243
	G	1584.15	33	1506
	2D	2688.98	67	1071
L_3	*D*	1348.22	40	980
	G	1586.62	30	977
	2D	2684.70	62	840

Similar to the previous case, we performed Raman mapping to check the homogeneity of the transferred layers. **Figure 7-8 (a-c)** shows the Raman maps of the *G*, *D* and *2D* peak intensities of the graphene transferred on SiO_2/Si, respectively. The color contrast clearly depicts that the graphene covers large area on the substrate, however, intensity of the peaks may vary due to some wrinkle formation upon transfer.

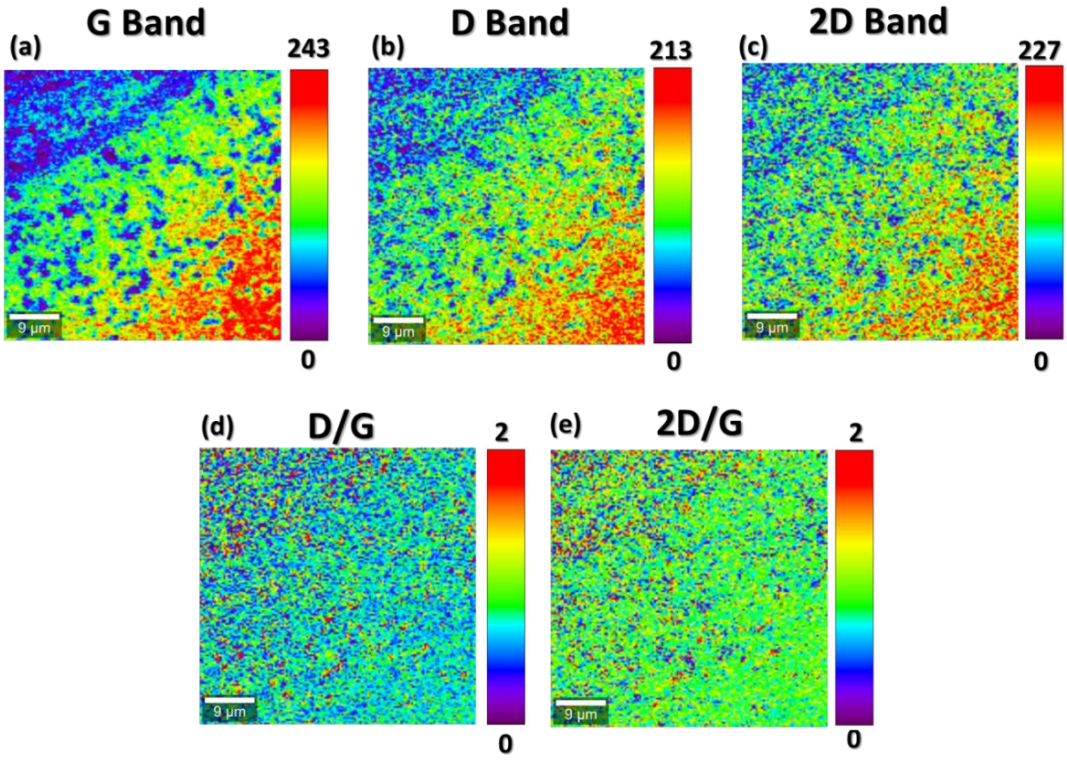

Figure 7-8: Raman mapping of the (a) *G*, (b) *D* and (c) *2D* band intensities of nitrogen doped graphene transferred SiO_2/Si substrates, respectively. It also shows the maps of the peak intensity ratios, I_D/I_G (d) and I_{2D}/I_G (e), respectively.

7.1.1.2. *X-Ray Photoelectron Spectroscopy*

As mentioned above, XPS is a useful technique for characterizing graphene samples on different substrates. **Figure 7-9** compares the overview XPS spectra of the as-grown graphene (Gr) and *in-situ* ammonia doped graphene (N-Gr) on Cu substrate before and after their transfer to SiO_2/Si substrates. Both spectra, are almost identical in the XPS wide scans (see black and green lines in **Figure 7-9**). Clear signals are identified and related to copper atoms from the substrate and carbon from graphene in a good agreement with literature reports [173].

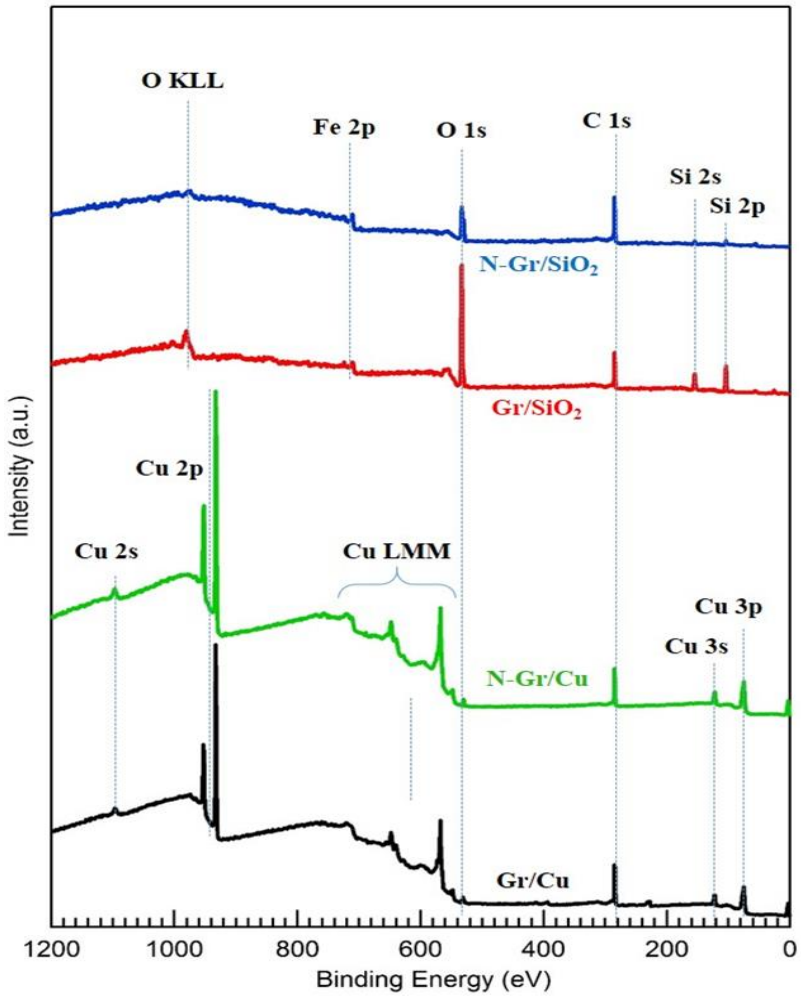

Figure 7-9: Normalized overview XPS spectra of pure and *in-situ* ammonia doped graphene before and after their transfer to SiO_2/Si. The main core levels related to substrate (Cu, Si and O) are indicated together with C 1s peak for carbon. Furthermore, a small quantity of iron atoms is detected on the transferred sample that were incorporated into the graphene sheets during the transfer process.

Only a small feature appears at a binding energy that corresponds to oxygen atoms. Small concentration of nitrogen atoms in the *in-situ* ammonia doped graphene samples was not detected in the wide XPS scans. After transferring the samples to SiO_2 (red and blue spectra of **Figure 7-9**) XPS wide scan detects several peaks that can be ascribed to carbon, silicon and oxygen atoms related to graphene sheets and substrates. Copper substrate peaks completely disappeared as can be seen in the red and blue spectra of **Figure 7-9.** Interestingly, a clear feature appears in the overview scans at binding energies (BEs) of around 710 eV, which is ascribed to Fe atoms that were incorporated into graphene during the transfer process.

Figure 7-10 presents more detailed comparison of the C 1s core levels obtained by high resolution XPS.

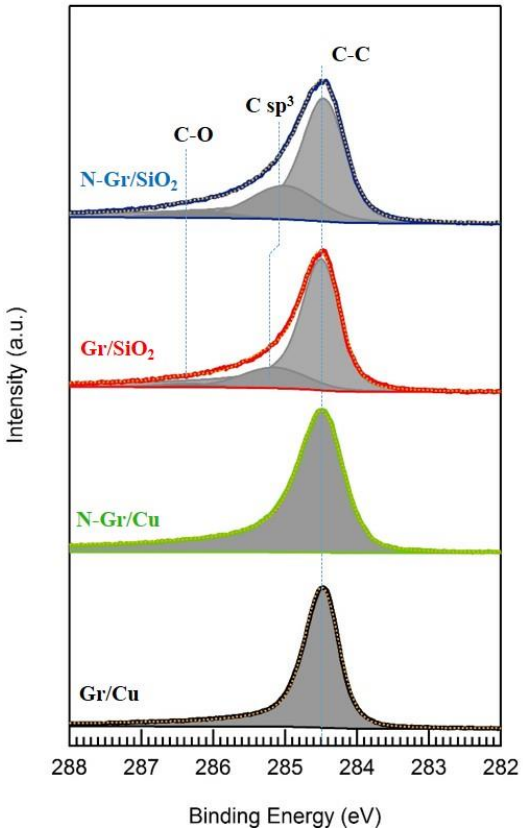

Figure 7-10: Comparison of the C 1s core levels obtained by high resolution XPS in pure and *n*-doped graphene. The as grown graphene can be fitted by a single C sp^2 component (black and green spectra). After transferring the samples, two new components appear that can be related to C sp^2 and C-O bonds (red and blue spectra).

C 1s core level of pure and *in-situ* ammonia doped (*n*-doped) graphene on copper are very similar. Both can be fitted by only one component, centred at a BE of 284.5 eV, which can be related to carbon (C) sp^2 level [173]. Thus, from the XPS point of view, the quantity of defects in the C-C bonds in the as grown (*n*-doped) graphene sheets can be neglected. On the contrary, upon the transfer to SiO_2 three peak components were necessary to perform the curve fitting. The difference between the C 1s core levels before and after transfer the samples is clear in the comparison reported in supplementary information of [173]. After the transfer, first component corresponds to the C-C bond as in the case of the spectra obtained before the transfer. The second component appears at BEs of 285.15 eV and 285.05 eV for the pure and *n*-doped graphene on SiO_2, respectively. This component can be ascribed to C sp^3 [224] and it typically

appears in the XPS spectra because of the generation of defects in the graphene sheets during the transfer. Finally, the last component is centred at the BE of 286.3 eV and can be related to C-O bond [173].

In case of *n*-doped samples further information can be obtained by characterizing the N 1s core level. **Figure 7-11** shows the N 1s peak and its deconvolution into two individual subcomponents, indicating two types of nitrogen incorporation into the graphene lattice. The feature appearing at lower binding energy (~398.5 eV) is commonly assigned to the pyridinic configuration, while the component located at higher BE (~401 eV) suggests graphitic nitrogen, where N directly substitutes sp^2 hybridized carbon [224].

The ratio between both components in the as grown *n*-doped graphene reveals a predominance of desired graphitic nitrogen over the pyridinic one. On the contrary, this aspect ratio is swapped in the N 1s spectra of the samples transferred to SiO_2. The increase of pyridinic N at the expense of substitutional N during transfer evidences again the generation of defects in the graphene sheet upon this process. This fact agrees with the emergence of the carbon sp^3 component in the C 1s spectra of the transferred samples in literature reports [173, 224].

As it was mentioned above, the only element not related to the graphene sheets and substrates detected by XPS was Fe.

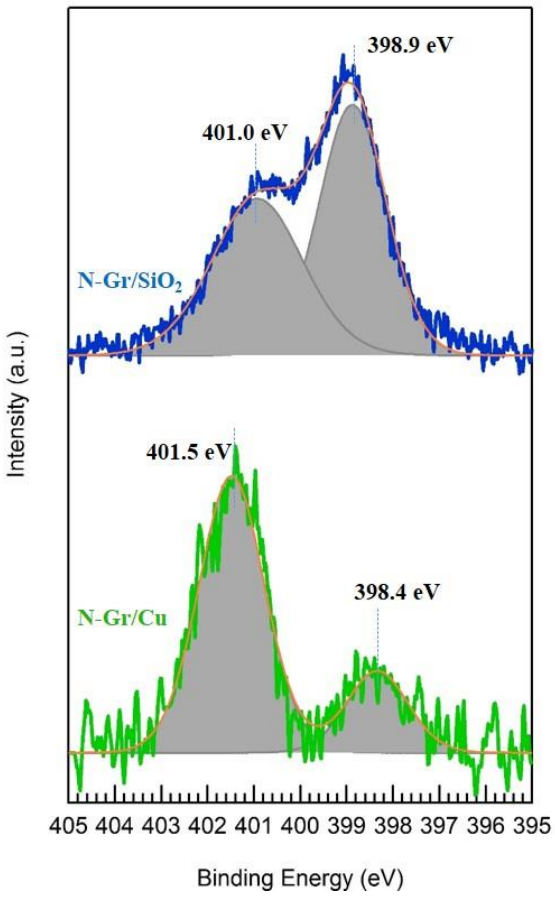

Figure 7-11: Comparison between the N 1s high-resolution XPS spectra of (*n*-doped) graphene on Cu foil (green) and that transferred onto a SiO_2 substrate (blue).

Previous experimental and theoretical studies revealed the existence of interactions between graphene and single metal atoms including iron [314-316]. In particular, the report by Zhao *et al.* mentioned the inclusion of iron atoms in the graphene sheets during the transfer process [239]. Their study based on low-voltage spherical aberration-corrected TEM (LVACTEM) demostrated the interaction between graphene and Fe atom under electron-beam irradiation. The transferred samples typically consist of large areas of monolayer graphene in which some regions contain remnant material from the transfer process, including Fe species from decomposed $FeCl_3$. Under close inspection, pure Fe can be found as small nanocrystals formed on the surface of the graphene, as single atoms or small clusters at the edge of pores in clean graphene, or as 2D crystalline membranes suspended across perforations in the graphene. **Figure 7-12 (a)** shows typical a HR-TEM image of graphene pore holding the one of these suspended Fe membranes in- as BCC and HCP atomic structure and their image simulation as an inset (bottom left of b and c), respectively.

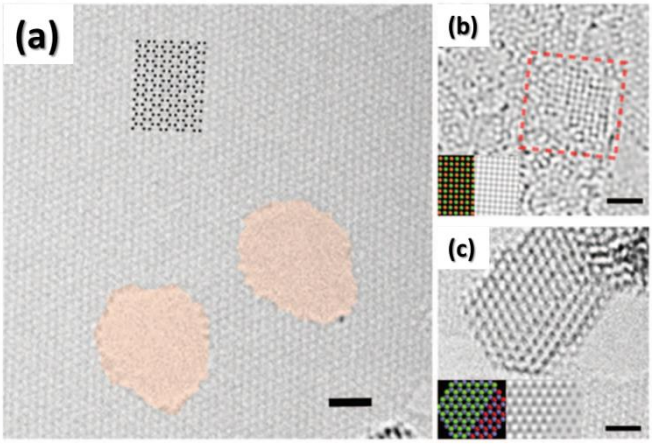

Figure 7-12: (a) Low-voltage spherical aberration-corrected transmission electron microscopy (LVACTEM) images of graphene perforations. (b) BCC and (c) HCP Fe nanocrystals, with atomic structure and image simulation shown as insets [239].

Furthermore, for better understanding, they performed after Fourier transform filtering (to reduce the noise) as shown in **Figure 7-13** and the inner reflexes correspond to the (100) plane of Fe where as the outer reflexes arise from the (1-100) plane of graphene. In addition, the (110) plane for Fe almost overlaps the (1-100) graphene planes. This indicates preferential alignment of the Fe(110) plane with the graphene (1-100) plane.

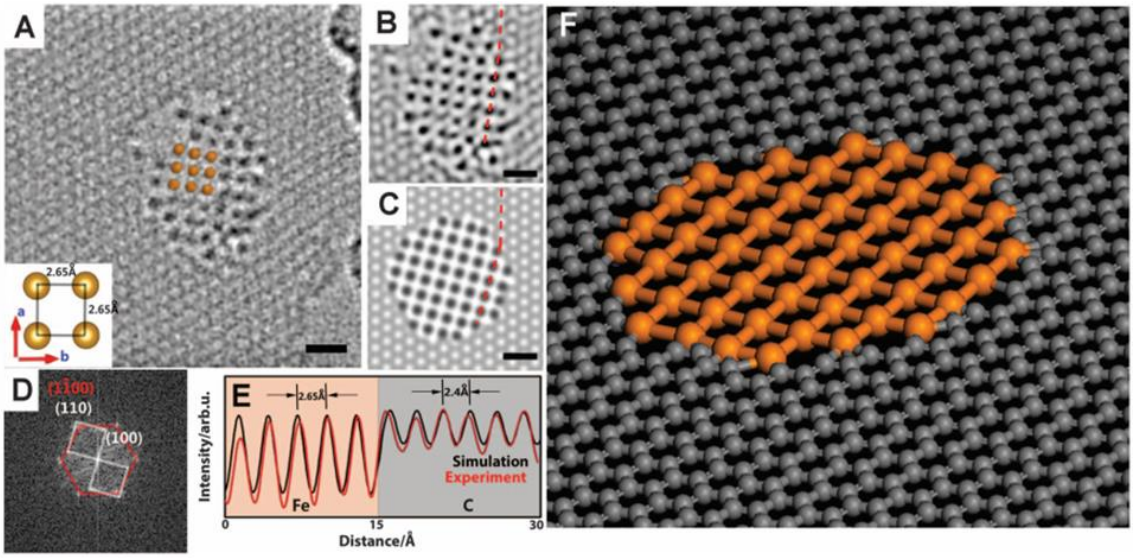

Figure 7-13: (A) LVACTEM image of monoatomic Fe layer. Inset shows the interatomic spacing of the square unit cell. (B) Smoothed image of (A). (C) Image simulation of a monoatomic Fe layer. (D) Fast Fourier transform of the structure in (A). (E) Normalized intensity profiles from the image simulation (black line) and experimental image (red line). (F) Atomic structure of a suspended monoatomic Fe layer in a graphene pore. All scale bars 0.6 nm. Adapted from [239].

Moreover, they performed simulation and two profiles (experimental and simulated) matched each other extremely well. The image simulation of single atomic layer of Fe atoms is shown in **Figure 7-13** thus confirming that the suspended Fe structure was single-atom-thick Fe layer. Therefore, individual atoms, small metallic cluster or even single-atom-thick 2D membranes can be trapped in graphene defects and pores.

In our case, in order to study the oxidation state of the iron atoms incrusted in the graphene sheets during the transfer process we performed high resolution XPS of the Fe 2p core level as a function of the temperature by heating the samples under UHV condition. The evolution of the shape and BEs of the Fe 2p level as a function of temperature is shown in **Figure 7-14.** Fe 2p core level has two sublevels (Fe $2p_{3/2}$ and Fe $2p_{1/2}$) and a satellite between them.

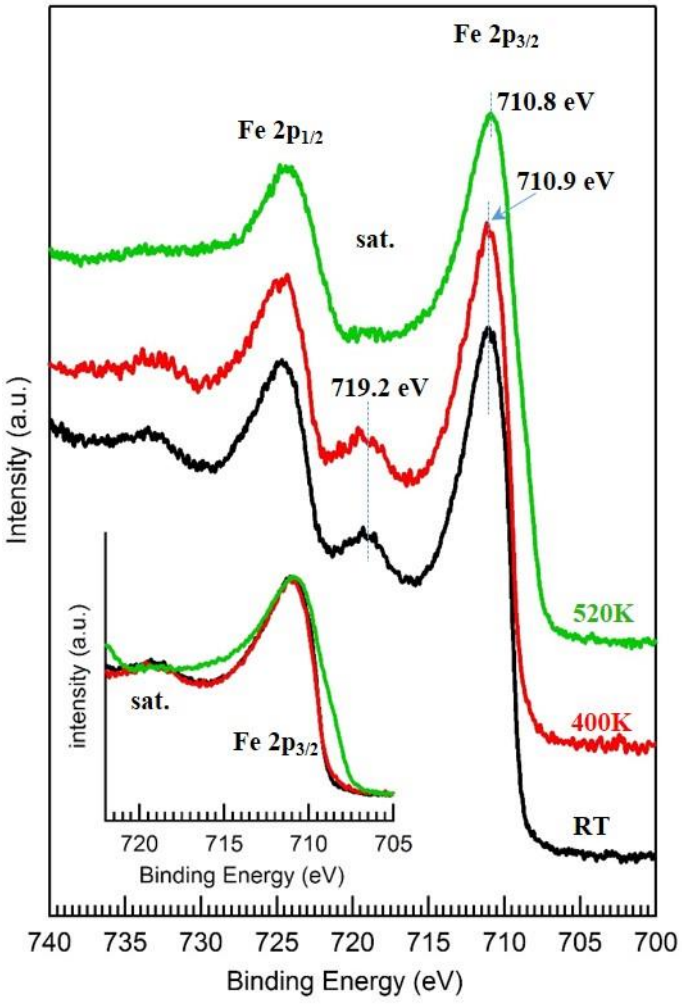

Figure 7-14: Fe 2p core levels obtained by XPS of a transferred graphene sample as a function of temperature. The inset shows Fe $2p_{3/2}$ level in detail.

At room temperature, Fe $2p_{3/2}$ and Fe $2p_{1/2}$ asymmetric peaks are centred at BEs of 710.9 eV and 724.5 eV, respectively. Furthermore, a clear satellite peak appears at 719.2 eV. Thus, XPS indicates that iron atoms are oxidized as Fe^{3+}, this state remains stable even after heating the sample to 600 K (black and red spectra in the inset of **Figure 7-14**). A significant change occurs after heating the sample to 520 K (green spectra in **Figure 7-14**). The position of the centre of the main peaks (Fe $2p_{3/2}$) is almost the same as before the annealing but significant changes occur in the shape of the core level. On one hand the satellite strongly diminishes and a shoulder appears at lower binding energies than the main peak. This information altogether strongly indicates a partial reduction of the iron from Fe^{3+} to Fe^{2+}. Both, Fe^{3+} and Fe^{2+}, probably, coexist in the sample after heating to 520 K. This experimental results from HR-XPS reconfirm the results obtained by Zhao *et al.* [239] and we can say that there can be an inclusion of iron atoms in the graphene sheets during the transfer process. In order to reaffirm the existence of Fe atoms as a result of transfer process, we performed the graphene transfer on Au substrates, as discussed in the following section.

7.1.1.2.1. Pure and in-situ ammonia doped graphene on Au

7.1.1.2.1.1 Raman Spectroscopy

Pure and *n*-doped graphene were transferred to gold coated substrates using a standard technique (i.e. without using polymer such as PMMA). The substrate was 100 nm gold coated silicon (http://www.amsbio.com/productpage.aspx?code=AU.1000.SL1). The purpose of the transfer of the graphene on this substrate was to see if we are still able to find Fe atoms in the pores of graphene or not. Initially we recorded the Raman spectrum to see the existence of the graphene on the Cu substrate and latter it was tranferred. **Figure 7-15** shows the optical image and Raman spectra acquired at various locations. Optical image on **Figure 7-15 (a)** verifies that the graphene was indeed transferred on a large scale and it was found to be quite stable. We were able to clearly see the interface between graphene and Au substrate. **Figure 7-15 (b)** shows the Raman spectra recorded at vairous locations namely $\mathbf{L_1}$, $\mathbf{L_2}$, $\mathbf{L_3}$ and $\mathbf{L_4}$. A brief summary is shown in **Table 7-3.**

Table 7-3: Peak positions, intensities and *FWHM* of Raman spectra of pure graphene transferred on Auric.

Locations	Peaks	Position (cm^{-1})	*FWHM*	Intensity (a. u.)
L_1	*D*	1332.25	119	38
	G	1568.85	127	355
	2D	2680.97	50	93
L_2	*D*	1332.25	80	32
	G	1568.85	52	452
	2D	2674.53	50	109
L_3	*D*	1342.46	66	23
	G	1573.81	66	170
	2D	2678.83	83	87
L_4	*D*	1332.25	62	39
	G	1573.81	46	344
	2D	2678.83	114	121

Figure 7-15 (c) shows the Raman maps of the *G*, *D* and *2D* peak intensities of the Raman spectra of graphene transferred on Au substrate. The ratios of I_D/I_G and I_{2D}/I_G are also shown. The color contrast clearly depicts that the graphene was homogeneously transferred, though there are some variations in the peak intensities due to defects.

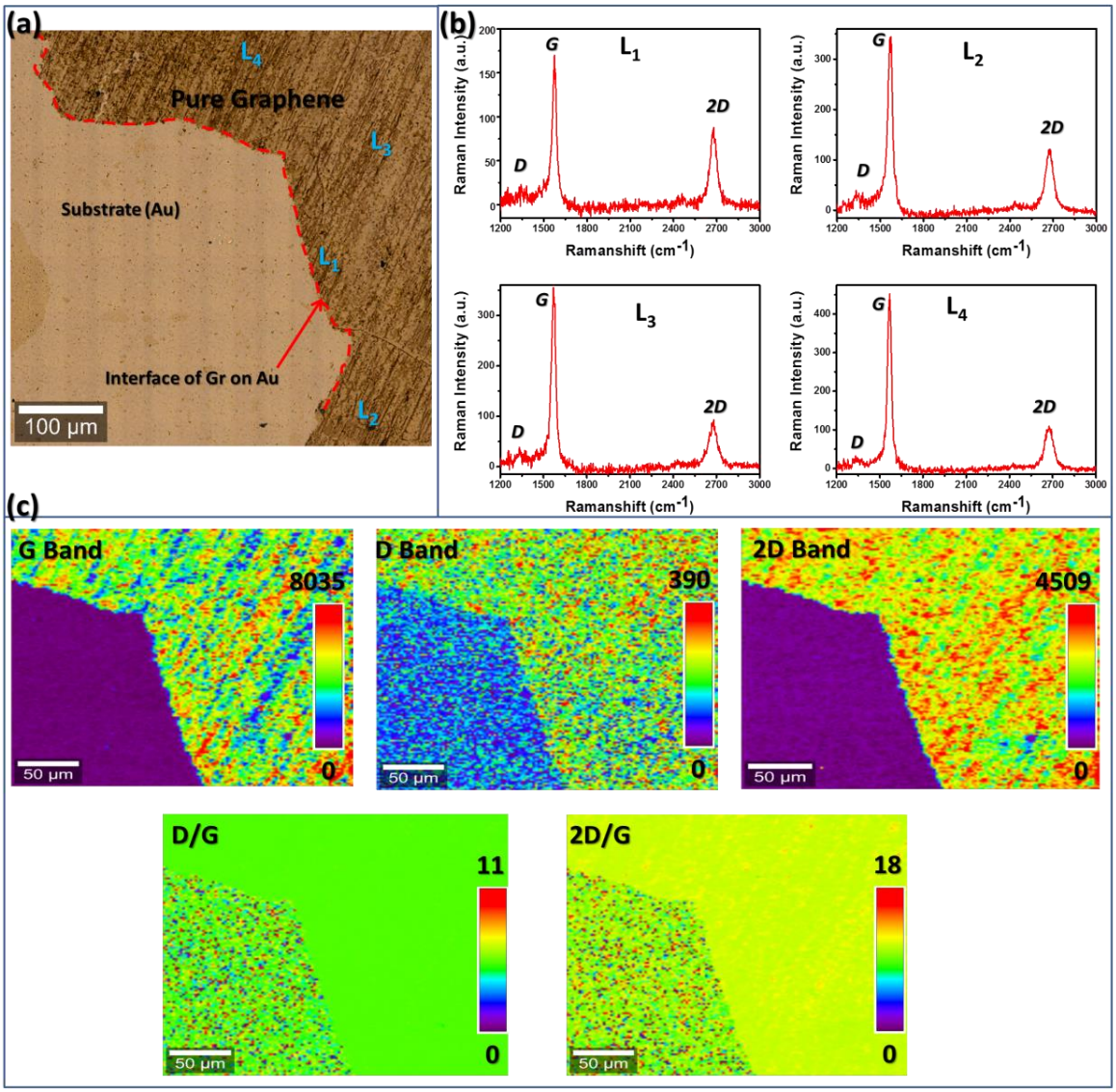

Figure 7-15: Optical image and Raman spectra of pure graphene transferred on Au/Si using standard procedure without using polymer such as PMMA. (a) Optical image using 10x objective to see large area, (b) Raman spectrum of the graphene taken at various location namely L_1, L_2, L_3 and L_4 (marked on optical image). (c) Raman mapping of *G*, *D* and *2D* band intensities of the pure graphene transferred Au/Si. Maps of relative intensities I_D/I_G and I_{2D}/I_G are also shown.

Similaryly to pure graphene, as discussed above *n*-doped graphene was transferred on Au substrate in order to corroborate the existence of Fe (discussed earlier in XPS). **Figure 7-16** shows the optical image and Raman spectra recorded at various locations. The optical image as shown in (**Figure 7-16 (a)**), cleary confirms the presence of sample on the Au substrate. The sample was even distributed on the large scale upon transfer. As in the case of pure graphene, we were still able to see the interface between *n*-doped graphene and Au substrate. Similarly, vairous locations, namely, L_1, L_2, L_3 and L_4 were marked and the corresponding spectra were recorded.

Figure 7-16 (b) shows the spectrum acquired at different locations namely at **L_1**, **L_2**, **L_3** and **L_4**. The summary of these measurements is shown in **Table 7-3**.

Table 7-4: Peak positions, intensities and *FWHM* of Raman spectra of *n*-doped graphene transferred on Auric.

Locations	Peaks	Position (cm^{-1})	*FWHM*	Intensities
L_1	*D*	1316.91	119	193
	G	1571.33	127	200
	2D	2680.97	53	18
L_2	*D*	1352.65	82	50
	G	1573.81	52	87
	2D	2663.79	61	22
L_3	*D*	1352.65	66	265
	G	1581.24	45	386
	2D	2689.55	83	92
L_4	*D*	1350.11	62	487
	G	1583.72	46	713
	2D	2685.28	114	99

Figure 7-16 (c) shows the Raman maps of the *G*, *D* and *2D* peak intensities of the Raman spectra of graphene transferred on Au substrate. The ratio of I_D/I_G and I_{2D}/I_G are also shown. The color contrast clearly depicts that the graphene was homogeneously transferred on the substrate, though there are some minor variations in the peak intensities.

However, while acquiring the Raman mapping the high laser (~7.5mW) the sample area which was scanned was found to be burnt. The burnt sample area is marked in rectangle, as shown in the **Figure 7-16 (d)**.

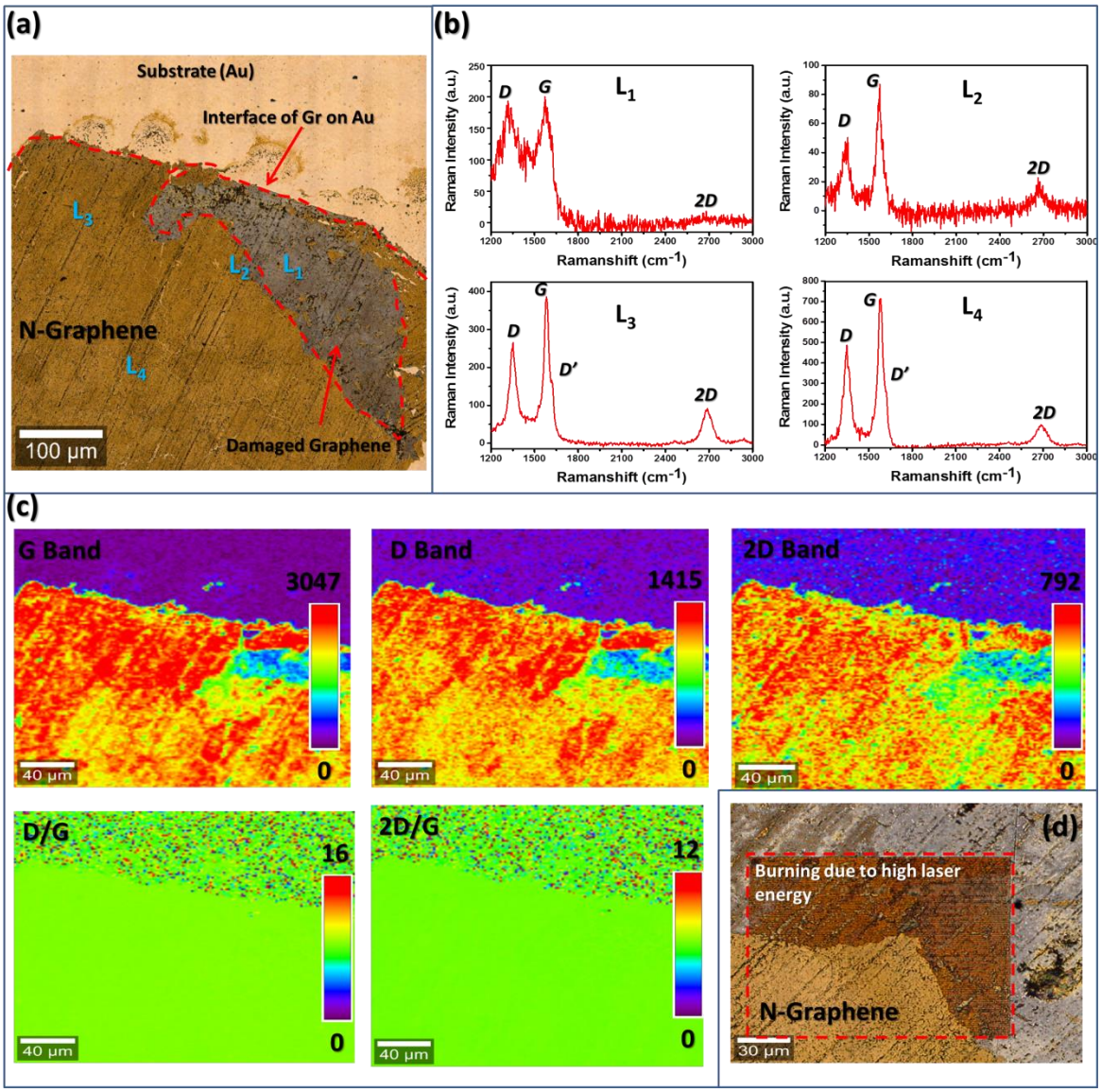

Figure 7-16: Optical image and Raman spectra of *n*-doped graphene transferred on Au/Si using standard procedure without using polymer such as PMMA. (a) Optical image using 10x objective to see large area, (b) Raman spectrum of the graphene taken at various location namely L_1, L_2, L_3 and L_4 (marked on optical image). (c) Raman mapping of *G*, *D* and *2D* band intensities of the *n*-doped graphene transferred Au/Si. Maps of relative intensities I_D/I_G and I_{2D}/I_G are also shown. (d) Burnt sample area marked in rectangle.

7.1.1.2.1.2 High-Resolution X-ray Photoelectron Spectroscopy

As discussed earlier, to verify the existence of Fe in the graphene sheet HR-XPS measurements were performed and similar resullts were found as compared to those transferred on SiO_2/Si. **Figure 7-17** shows the overview XPS spectra for the as-grown on Cu and *n*-doped graphene transferred on Au/Si substrate.

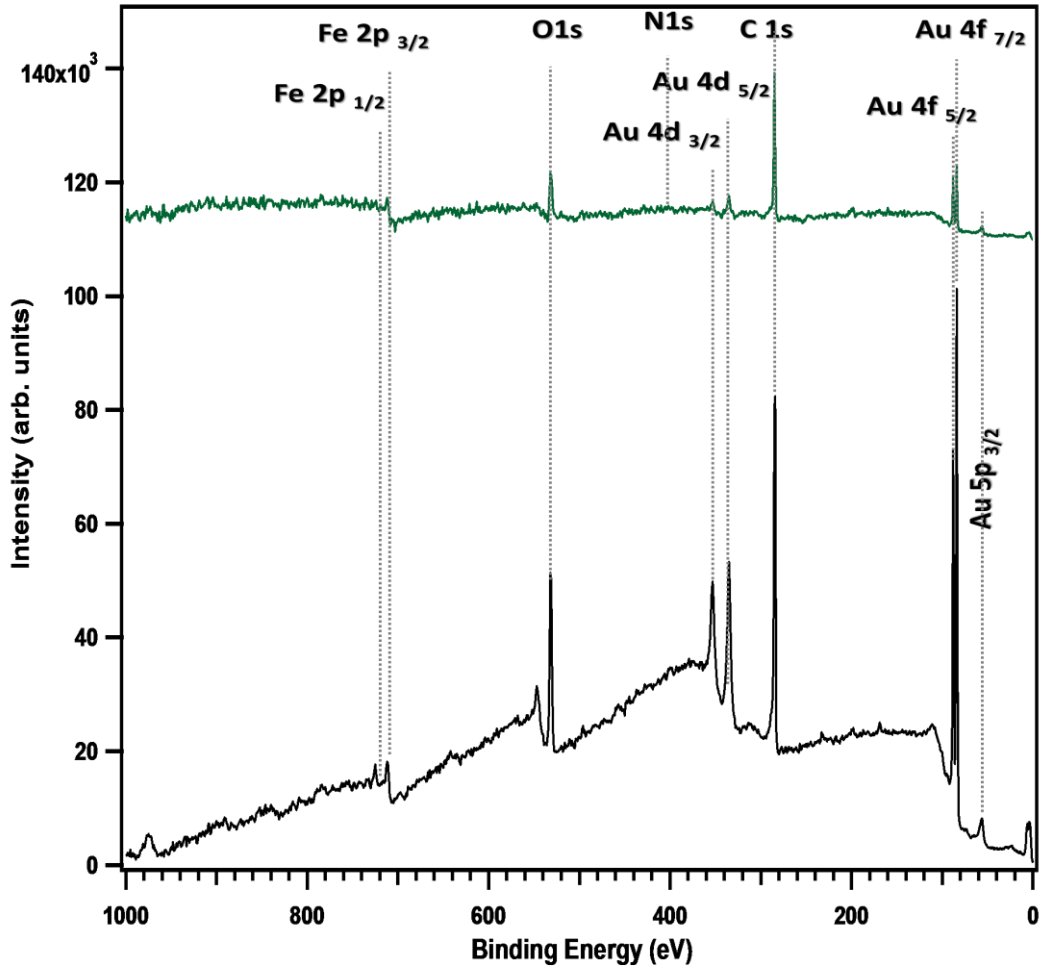

Figure 7-17: Normalized overview XPS spectra of pure (black line) and *n*-doped (green line) graphene on copper substrate and after their transfer to Au/Si substrates. The main core levels related with the substrates (Cu, Au and O) are indicated together with C 1s. Furthermore, a small quantity of iron atoms is detected on the transferred samples that were incorporated to the graphene sheets during the transfer process.

Both, pure and *n*-doped graphene transferred on Au/Si are almost identical in the XPS wide scans (see black and green spectra of **Figure 7-17**). Clear peaks are identified and marked. The peaks are in good agreement with previous works [173]. In the overview scan it was difficult to observe the

small quantity of nitrogen atoms in the *in-situ* ammonia doped graphene samples. Since the samples were transferred on the Au/Si substrate, we did not find any Cu peaks. On the contrary, huge peaks of Au $4d_{3/2}$ and $4d_{5/2}$ were found at 353 and 335 eV in the pure graphene transferred on Au whereas in the *n*-doped graphene on Au these were comparatively small.

Figure 7-18 shows a comparison between the C 1s core levels obtained by high resolution XPS. In the case of pure graphene the core level peak was observed at 284.4 eV where in the *n*-doped graphene it was shifted to higher binding energy by 0.2eV. This can be due to the presence of nitrogen Intercalation in the graphene sheet.

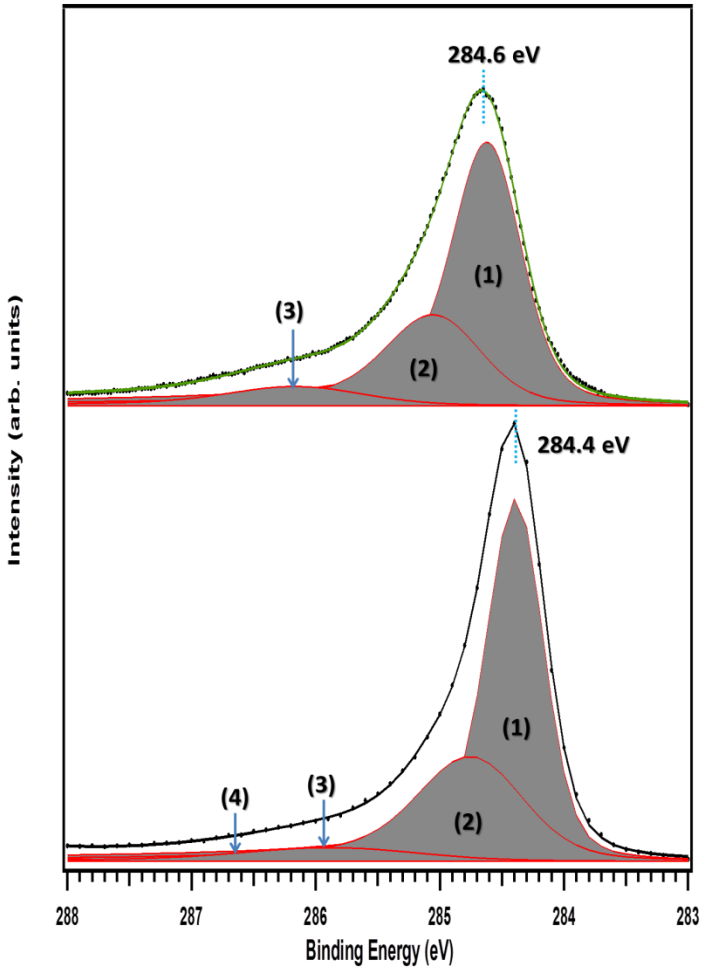

Figure 7-18: Comparison between the C 1s core levels obtained by high resolution XPS. The C 1s peak of pure graphene can be fitted by four components (bottom) whereas in the case of *n*-doped graphene it was fitted by only 3 components (top figure).

Various components used to fit in pure graphene were marked as (1), (2), (3), and (4) corresponding to C sp^2, C-OH, C-O, and C=O bonds, at 284.4, 284.7, 285.7 and 286.6 eV, respectively [173]. The O bonds with C are due to the presence of oxygen which arised as a consequence of transfer process. We did not annealed the sample to remove the oxygen due to presence of Si (as a substrate) and quality of Au was not that good. In the case of *n*-doped graphene we observed only 3 components which were attributed to: component (1) to C sp^2, component (2) to C-OH and component (3) to C-O.

As discussed above, we observed Fe 2p peak in both pure and *n*-doped graphene (see **Figure 7-19**). The spectra were recorded at room temperature due to low quality of Au deposited on Si substrate.

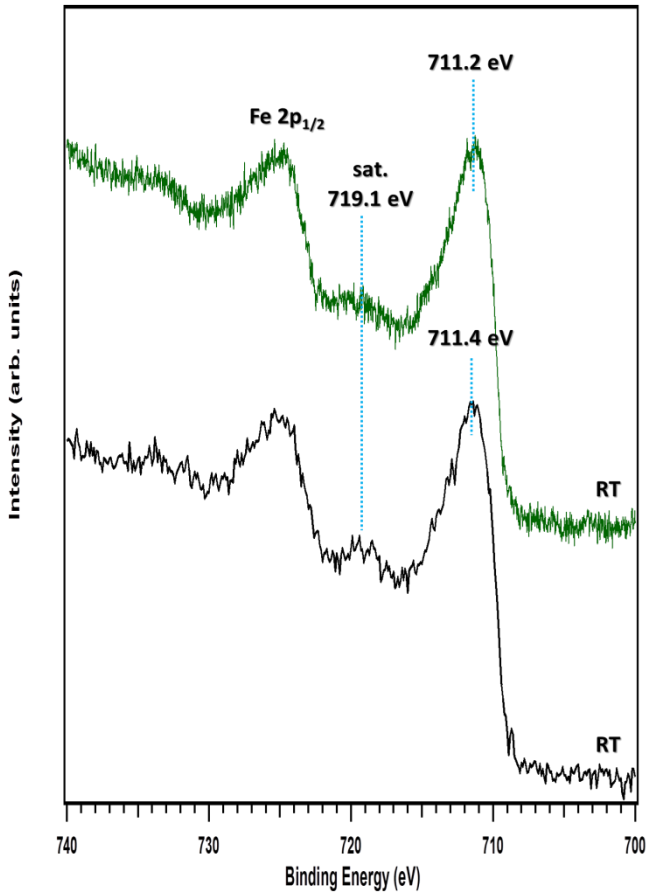

Figure 7-19: Fe 2p core levels obtained by XPS of pure (black line) and *n*-doped (green line) graphene on Au/Si.

Similar to the case of graphene transferred on SiO_2/Si the iron atoms appeared during the transfer process. High resolution XPS of the Fe 2p core level of both pure and *in-situ* ammonia doped

graphene were recorded, as shown in **Figure 7-19.** Both spectra were identical and it was found that Fe 2p core level has two sublevels (Fe $2p_{3/2}$ and Fe $2p_{1/2}$) at 711.2 and 711.4 eV, respectively, with a satellite between them at 719.1 eV. This assumed the appearance of iron in 2D form in graphene sheet during the transfer process irrespectively of substrate used.

Conclusion

For any real application of graphene, the key factor is the transfer process. Different transfer processes have been reported in the literature resulting in uniform and large area coatings. In this work, a standard procedure without using polymer was applied to transfer the graphene on different substrates, namely SiO_2/Si and Au/Si. The optical images of both pure and *n*-doped graphene demonstrated an evidence of the successful transfer of graphene on these substrates. In both cases, Raman spectra acquired at different locations show typical features of a few layer graphene. However, some non-uniformity was found in the Raman intensity maps, which are due to wrinkles formed during transfer process. In addition, the sharpness of the peaks (low *FWHM* values) corroborates good quality of pure graphene transferred on SiO_2/Si. In the case of *in-situ* ammonia doped graphene, the Raman results substantiate the existence of *D'* and *D* peaks due to doping.

Moreover, based on XPS measurements the core level peak of C1s was found to contain two different components, namely, C-C sp^2 and C sp^3 for transferred pure graphene, whereas in the case of *in-situ* ammonia doped graphene it can be deconvoluted into three different components, namely, C-C sp^2, C sp^3 and C-O. In the case of N 1s spectra were deconvolute into two individual subcomponents, indicating two types of nitrogen assembling, namely, pyridinic and substitution types in the graphene framework. The ratio between both components in the as grown and *in-situ* ammonia doped graphene revealed a predominance of desired graphitic nitrogen over the pyridinic impurities which switches upon the transfer process.

Finally in the HR-XPS spectrum, we found the inclusion of iron atoms in the graphene sheets due to the transfer process. The core level peak of Fe 2p was deconvoluted into two parts, namely, Fe $2p_{3/2}$ and Fe $2p_{1/2}$ peaks centred at BEs of 710.9 eV and 724.5 eV, respectively, with satellite peak at 719.2 eV. In order to check the stability of the Fe atoms, we measured the spectra with respect to temperature increase and the results indicate that these iron atoms remain stable even after heating the sample to 400 K.

Furthermore, we performed the same transfer process of pure and *n*-doped graphene on Au/Si in order to reaffirm the results obtained on SiO_2/Si and we got similar results as expected. The experiments confirm our previous conclusions and show clear evidence of the incorporated iron atoms in the form of nanocrystals.

Chapter 8

Deposition and investigation of MoS_2

Abstract

In recent few years, monolayers of transition metal dichalcogenides (TMDs) have attracted significant attention of researchers due to their potential applications in the new generation of optoelectronic and nanoelectronic devices. In particular, molybdenum disulfide (MoS_2) as one of the TMDs was found to be a good substitution of graphene in the next generation of nanoelectronics. This chapter describes the experimental strategy used for the growth of large area MoS_2 from monolayer to a few layers using Chemical Vapor Deposition (CVD) at different pressures. After several trials and errors, we came to conclusion that using 50 mbar is an optimum pressure for the growth of large area MoS_2. The as synthesized MoS_2 was found to have a direct bandgap of 1.6 eV, as calculated using UV-Visible spectroscopy data. The results of micro-Raman spectroscopy clearly show the presence of distinct E^1_{2g} and A^1_g peaks. High-Resolution X-ray Photoelectron Spectroscopy substantiated high quality of MoS_2 by examining different Mo and S core level peaks. Electrical measurements show both ohmic and semiconducting behavior of the crystals. Demonstrated growth of high-quality single-layer MoS_2 is important in view of their further application in microelectronics as it has a capacity to replace graphene in near future.

8. Emergence of MoS_2[§]

Graphene, being a semi-metallic material due to its special π-π* band structure, has sparkled the dramatic increase in the 2D materials research [17, 122, 145]. Extremely high mobility value of graphene ($\sim 10^5$ cm^2 V^{-1} s^{-1}) which is higher than in the parent material (graphite) makes it much more attractive for semiconductors industry. The conduction band and valence band of graphene are symmetrical about the Dirac point; hence its electronic properties can be described via Dirac equation, not the Schroedinger one. The Fermi surface is just the intersection point of the conduction and valence bands, making graphene to be a zero bandgap material. This unique structure provides outstanding electrical properties, but it limits its application in logical circuits for low-power electronic switching [32]. As a result, the electric current in graphene cannot be turned off and it is deemed unfavourable for the development of transistors [32, 122]. Since the invention of graphene researchers have started focusing on graphene-like 2D materials aiming at overcoming the disadvanatges of graphene and broadening the range of their applications [16, 317].

Generally, 2D insulating and semi-conducting materials are more likely to be obtained due to the intrinsic chemical activity of most metallic materials. Graphite, hexagonal boron nitride (hBN) and molybdenum disulfide (MoS2) stand out in this competition. Due to its widespread nature as molybdenite, MoS_2 has been one of the most studied layered transition metal dichalcogenides (TMDCs). Monolayer MoS_2 is a semiconductor with a direct bandgap of 1.8 eV [16], which makes it possible a substitution of gapless graphene, providing a possibility for 2D materials to be used in the next generation switching and optoelectronic devices. So far, MoS_2 has achieved primary progress in several application areas, such as energy conversion and storage [19, 318] and hydrogen evolution reaction (HER) [319]. Additionally, MoS_2 with odd number of layers could produce notable piezoelectric voltage and current outputs, indicating its potential applications in powering nanodevices and stretchable electronics [320].

8.1. CVD upgrade for MoS_2 growth

To implement MoS_2 to be used for semiconductor industries, the materials should have: (i) large surface area, (ii) possibilities to controlling the thickness, and (iii) high crystallinity along the planes and high yield in fabrication.

[§] Parts of this chapter have been published as Materials Research Bulletin, 97, pp. 265-271 (2017).

Just like in graphene case a common method used to obtain monolayer TMDs is the scotch-tape based micromechanical cleavage technique as reported in early publications [17, 145]. However, this method has various limitations, such as the lack of control over the flake thickness and size, which is likely to be crucial for nanoelectronics and optoelectronics. Keeping this in mind, a bottom-up method which envolves Chemical Vapor Deposition (CVD) technique has emerged in recent years. CVD is the most common and desired technique for the synthesis of MoS_2 because it allows easy control of deposition parameters by regulating the temperature and the carrier gas flow. Also, these CVD methods are able to synthesize reasonably good quality material with typical flake sizes from hundreds of nanometers to a few micrometers.

In CVD synthesis, the method for achieving the final product may differ depending on the precursor and temperature used. For example, one can use initially pure sulfur (S) and MoO_3 powder for the deposition directly on the substrate or one can predeposit the MoO_3 and then perform functionalization using S in the next step.

The key parameter for large area synthesis of MoS_2 is the control of the reaction between between MoO_3 and S. MoO_3 compounds go through the transition from $MoO_{(3-x)}$ species with S interaction to form the final composition (MoS_2) with stepwise reaction as shown below.

$$\boldsymbol{MoO_3 + x/2\, S \;\rightarrow\; MoO_{3-x} + x/2\, SO_2} \qquad \text{(Eq. 8-1)}$$

$$\boldsymbol{MoO_{3-x} + (7-x)/2\, S \;\rightarrow\; MoS_2 + (3-x)/2\, SO_2} \qquad \text{(Eq. 8-2)}$$

where $x < 1$ is the arbitrary number. When there is an incomplete reaction, an intermediate product such as MoO_x can be found which further might react with S.

In our case, we used modified CVD equipment and optimized the best growth condition. The modification of the existing CVD system was performed for controlling the temperature of two different regions of the CVD system at the same time. **Figure 8-1 (a)** shows a schematic diagram of the upgraded experimental facility used for the growth of the samples.

The standard CVD system was modified by including a second heater near one of the corners of the quartz tube. In particular, a heating belt was installed in the position indicated in **Figure 8-1 (a)** and its temperature was calibrated by the use of a thermocouple. By this way, this particular section of the quartz tube can be heated independently of the central part of the CVD system,

allowing the sublimation of different products at different temperatures at the same time. The range of temperatures allowed by the heating belt is between room temperature and 150°C.

For the growth of MoS_2 samples, sulfur and MoO_3 powders under a full set of different experimental conditions were used. In particular, the temperatures of both products, the pressure of the system, the growth time and the flow of the carrier gases (argon) were systematically changed in order to obtain high quality MoS_2 samples. The following section will describe the best growth conditions that were found in our modified CVD system.

Step 1: Installation of the powders and substrate. In the central part of the quartz tube an alumina boat is installed with MoO_3 powder and a substrate for the growth. The substrate was ~300 nm of SiO_2 on Si(111) of the size ~10 × 10 mm^2. In our experiment, the distance between S and MoO_3 was ~20 cm. When the heating of S takes place with the help of a heating belt, it will create more pressure which enhances the overall pressure in the CVD system. This will further reduce the vapor of MoO_3 and hence lead to a reduction in the reaction of both compounds. Moreover, the substrate is located in the upper part of the alumina boat, providing a bridge between its lateral walls while the MoO_3 powder is located at the bottom of the boat. With this configuration, upon heating, the sublimated MoO_3 is directly deposited on the substrate. On the other hand, the sulfur is installed in a second alumina boat, located just in the region heated by the heating belt, near the inlet region of the carrier gases. In this way, upon heating, the sublimated sulfur can be carried by the argon gas (with Ar:150 sccm).

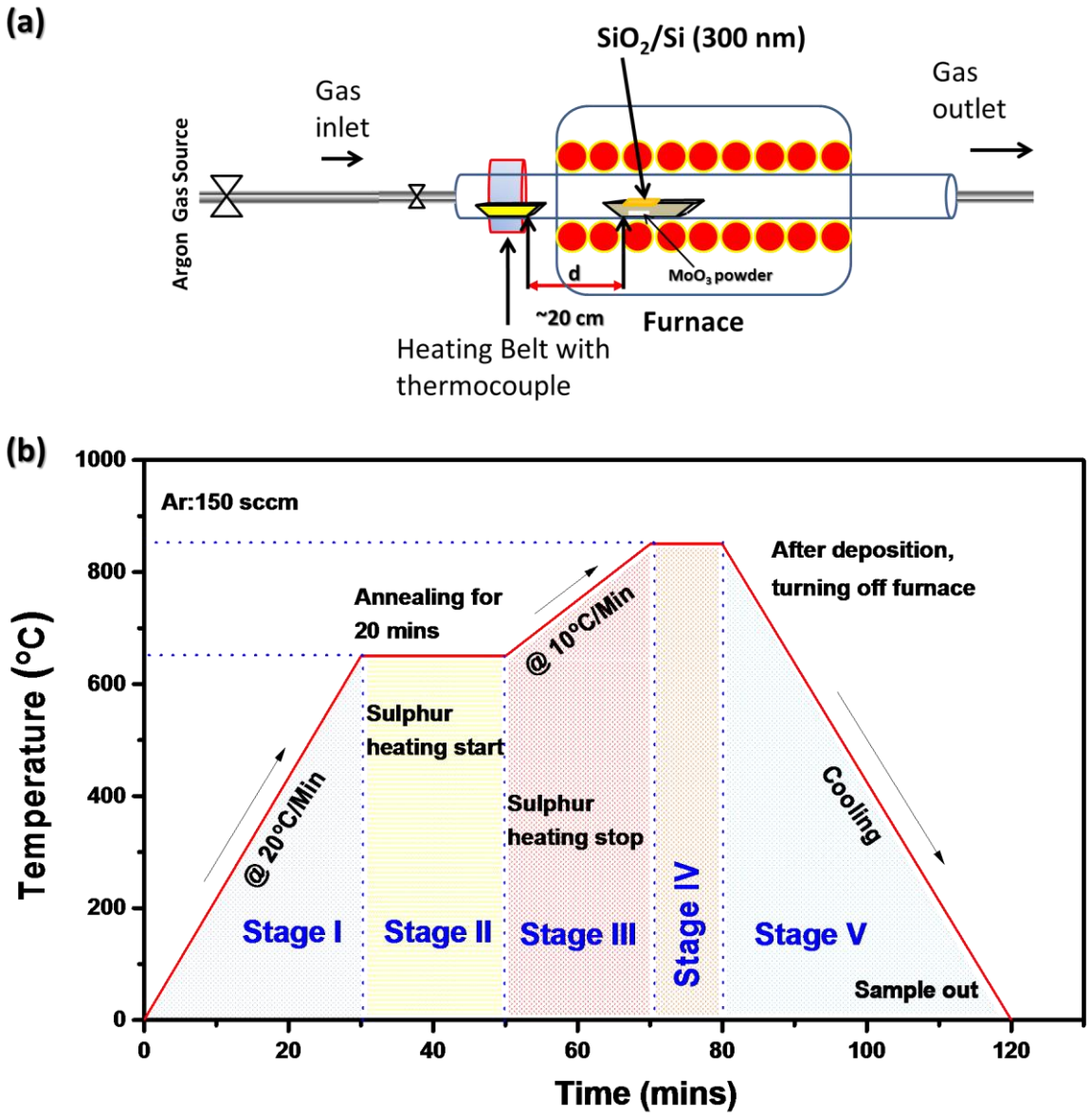

Figure 8-1: (a) Schematic diagram of modified CVD equipment for the growth of MoS_2. (b) The temperature diagram for the growth process of large area MoS_2 by modified CVD.

Step 2: Purge of the system. After installing the products the system is closed and purged. First, a vacuum of 10^{-2} mbar was achieved in the CVD during 20 min. Then, the CVD is fulfilled with pure argon gas. By repeating up to three times, this procedure allows most of the atmospheric contaminants to be removed from the quartz tube.

Step 3: Heating Ramp – stage 1. The CVD furnace is heated in an argon atmosphere (50 mbar) at a rate of 20 °C /min until reaching a temperature of 650 °C.

Step 4: Heating Ramp – stage 2. The temperature of the furnace is maintained at 650 ^oC for 20 minutes, conditions in which the MoO_3 powder is slowly sublimated from the alumina boat. At the same time, during this stage, the heating belt is heated to 150 ^oC for sublimating the sulfur. This is a key in order to obtain single layer MoS_2 samples, and the optimization of it will be discussed below.

Step 4: Heating Ramp – stage 3. At the beginning of this stage the sulfur was completely sublimated from the alumina boat and the heating belt is switched off. On the contrary, the temperature of the CVD furnace is increased at a rate of 10 ^oC/min until reaching a temperature of 850 ^oC. This post annealing treatment drastically improved the quality of the samples.

Step 5: Heating ramp – stage 4. The sample is maintained at 850 ^oC during 20 min. After this time, all the heating elements are switched off. During the cooling (stage 5) of the system the atmosphere inside the quartz tube is maintained with pure argon in order to avoid any contamination of the sample.

The program steps used in the furnace for the growth of MoS_2 are the following:

TSP 1 (Target Set Point): 650^oC
RMP 1 (Ramp): 20.0
DWEL 1 (DWELL): 0:20
TSP 2 (Target Set Point): 850^oC
RMP 2 (Ramp): 10.0
DWEL 2 (DWELL): 0:20

The above code was used for the growth of MoS_2 on SiO_2/Si substrate. The heating rate used was 20 ^oC/min till 650 ^oC, there it will dwell for 20 mins (as a part of annealing). After annealing the temperature will increase with the rate of 10 ^oC until it reaches to 850 ^oC and then it will dwell for 20 min. Afterwards it cools slowly until room temperature is reached. Point to be noted is that we used natural cooling and the cooling rate was not controlled.

In our experiments we used trial and error method to vary the pressure and found that 50 mbar pressure is ideal for large area single layer growth of MoS_2 on SiO_2/Si. We tried various pressures keeping other conditions the same. After sorting out the data, we report the results for 3 pressures: 10, 50 and 100 mbar representative enough to be explained by the described above chemical reaction mechanism. In the beginning with the pressure around 10 mbar, the reaction time was very short and thus the compounds were unreacted. Hence we infer that intermediate

compound (probably $MoO_{(3-x)}$ crystal) is only formed instead of MoS_2. The rhombohedral shape of the $MoO_{(3-x)}$ crystals is clear in the optical image shown in **Figure 8-2 (a)** while two distinct Raman active peaks of MoS_2 do not appear in the Raman spectra presented in **Figure 8-4**. At this pressure, the as grown sample comprises some rhombohedral structures (as shown in figure).

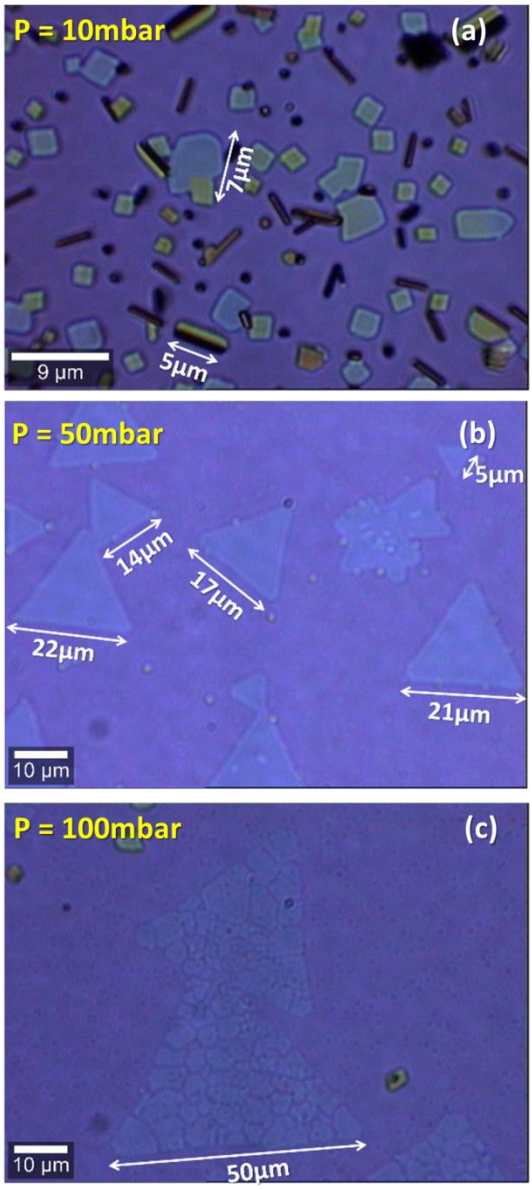

Figure 8-2: Optical image of as synthesized MoS_2 on SiO_2/Si (300 nm). (a) Synthesized at ~10mbar having ~5-7µm samples of $MoO_{(3-x)}$ with rhombohedral structure, (b) Synthesized at ~50 and (c) ~100 mbar with average size of 22 and 50 µm, respectively.

The average size of these rhombohedral structures was found to be around 5-7 µm. In the next series of experiments conducted at around 50 mbar pressure, triangular crystals were clearly

observed in the optical image. The average grains of MoS_2 crystals synthesized at this pressure were found to be in the range between 5 and 22 µm, see **Figure 8-2 (b)**. The shapes were quite similar to those reported by Zande *et al*. [321]. This pressure was found to be optimal for the growth of best MoS_2. At this pressure S evaporates and successfully reacts with MoO_3, leaving very small residue, hence less intermidiate $MoO_{(3-x)}$ is formed. We can say that the reaction leads to the nucleation of small triangular domains at random locations. Thus nucleated crystals continued to grow and formed boundaries until the favorable conditions are present (such as pressure and sufficient supply of precursors) [322]. Finally the results are compared with the samples grown under a pressure of 100 mbar. Under this condition MoS_2 triangular crystals were still obtained, but unpredictable cracks were created, and the average grain size was found to be a maximum (~50 µm), see Figure 8-2 (c). It iwas concluded that the reaction between compounds was fine but, due to high pressure, it leads to cracking of MoS_2 single crystals (see **Figure 8-2 (a)).** Similar result has been reported by Zande *et al*. [321].

Through this trial and error method, we conclude that the yield of the final product strongly depends on one of the growth parameters, i.e. the pressure. It is the pressure of the system during the sublimation of sulfur (step 4 of the growth protocol) that plays a key role. As an example, **Figure 8-4** shows a comparison of Raman spectra of the obtained samples by keeping 10 mbar of pressure during the growth in comparison with the sample obtained at the pressure of 100 mbar. During the growth of samples all the other growth parameters were kept the same.

8.2. Characterization of the MoS_2 samples

8.2.1.1. *Raman spectroscopy*

Raman spectroscopy based on the frequency shift or intensity change of the Raman modes of the inter-layer and in-plane vibration is the best technique not only to characterize the materials structure but also to study the electron-phonon-coupling effects. It can be used in almost all two dimenional TMDs to identify the number of the layers and other properties. Typically, MoS_2 has four distinct Raman-active modes (E_{1g}, E^1_{2g}, A_{1g} and E^2_{2g}) and two IR-active modes (A_{2u} and E_{1u}) [323-326]. E^1_{2g} is an in-plane mode resulting from the opposite vibration of two S atoms with respect to the Mo between them. On the contrary, the A_{1g} mode is attributed to the out-of-plane

vibration of only S atoms in opposite directions. When moving from single layer to multiple layers (bulk), the frequency of E^1_{2g} mode (see **Figure 8-3**) increases, whereas in the case of A_{1g} mode (see **Figure 8-3**), it moves towards lower frequencies [325, 327, 328]. Previous studies show that E^1_{2g} mode is controlled by the long-range interlayer Coulombic interaction between molybdenum atoms. On the other hand, A_{1g} mode is less affected by the interlayer interactions [329]. The A_{1g} mode is very sensitive to adsorbates on the MoS_2 surface [330] and electron doping [331]. Hence, due to stronger electron – phonon coupling of the A_{1g} mode, it shows a shift and an increase in the peak width with increasing doping level. This frequency or frequency-shift difference between these two modes on the Raman spectrum can be used to determine the layer number of a few-layer flakes [327]. Beyond this, there exist two low-frequency interlayer breathing (B^2_{2g}) and shear (E^2_{2g}) modes which are sensitive to the number layers and also can be used to examine the structural properties of a few-layer MoS_2 and to determine the number of layers [324, 332, 333]. It must be noted that both these modes disappear for single layer MoS_2 as they result from the interlayer interaction.

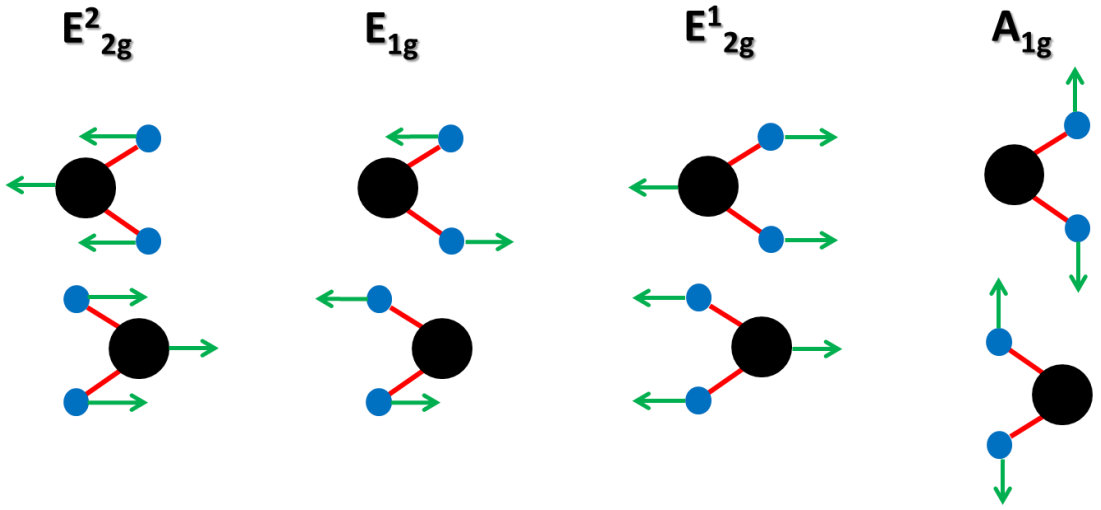

Figure 8-3: Typical four distinct Raman-active modes present in MoS_2 vibrational due in-plane and out-of-plane vibrations.

Figure 8-4 (a, b, and c) shows the Raman spectra of the sample grown at different pressures: 10, 50 and 100 mbar, respectively. Starting from the sample grown under ~10 mbar pressure, the Raman spectra (**Figure 8-4 a**) have no distinct peaks associated with Raman active mode (E^1_{2g} and A_{1g}) at ~380 cm^{-1} and ~409 cm^{-1} , respectively [16, 321, 328, 334, 335]. However, we detected minor peaks from $MoO_{(3-x)}$ and major peak from the Si substrate at ~520 cm^{-1}. On contrary, in the

case of the samples grown under 50 mbar pressure (**Figure 8-4 b**), Raman spectra display two distinct Raman active modes, E^1_{2g} at 380 cm^{-1} and A_{1g} at 409 cm^{-1} inherent to single layer MoS_2. The first peak (E^1_{2g}) is associated with the planar vibrations whereas the second peak is concerned with the vibration of sulfides in the out-of-plane direction. Both peaks are quite sharp with a difference (Δ) ~ 25.69 cm^{-1} while their full width at half maxima (*FWHM*) were 11.72 and 11.88, respectively. Finally, in the case of samples synthesized under about 100 mbar two distinct peaks of E^1_{2g} and A_{1g} are still observed. However, the peaks are slightly shifted towards lower wavenumber. They appear at ~ 375.18 and 406 cm^{-1} with a *FWHM* of 11.45 and 10.46 for E^1_{2g} and A_{1g}, respectively, with the difference (Δ) ~ 31.41 cm^{-1}. The Δ value in 50 and 100 mbar ssamples is similar to earlier results on CVD grown MoS_2 samples under similar pressure (40 – 10 mbar) [336]. The observed increase in the difference from 25.69 to 31.18 cm^{-1} is due to the increase of the number of layers [334]. Here, it is noteworthy to mention that Raman mode around 450 cm^{-1} for 50 and 100 mbar grown samples corresponds to two-phonon Raman process of successive emission of a dispersive quasi-acoustic phonon and a dispersionless transverse-optical phonon propagating along the *c*- axis [337]. These observations are clear indications that the grown MoS_2 consists of a few layers. It is interesting to mention that, while acquiring the Raman spectra (Figure not shown), we could see the excited PL (photoluminescence) response of the sample. As mentioned earlier this response was apparently weaker in the sample synthesized at ~100 mbar, as compared to ~50 mbar. Possible reason is the increase in the the number of layers in 100 over 50 mbar sample. This can be reasoned by the fact that the optical bandgap transforms from indirect to direct one when the dimension of MoS_2 is reduced from a multilayer layer form to a few layer sheet [149]. Here it is important to note that both E modes become broader when the pressure changes from 50 to 100 mbar and A_{1g} modes are shifted at 3 cm^{-1} that corresponds to 1.2 GPa hydrostatic pressure [338]. Thus, the change in Ar pressure and corresponding strain in S-Mo-S chains resuls in microstructural changes shown in the optical image (**Figure 8-2 b and c)**. Furthermore, Raman mapping was performed on the sample 50 and 100 mbar sintered samples.

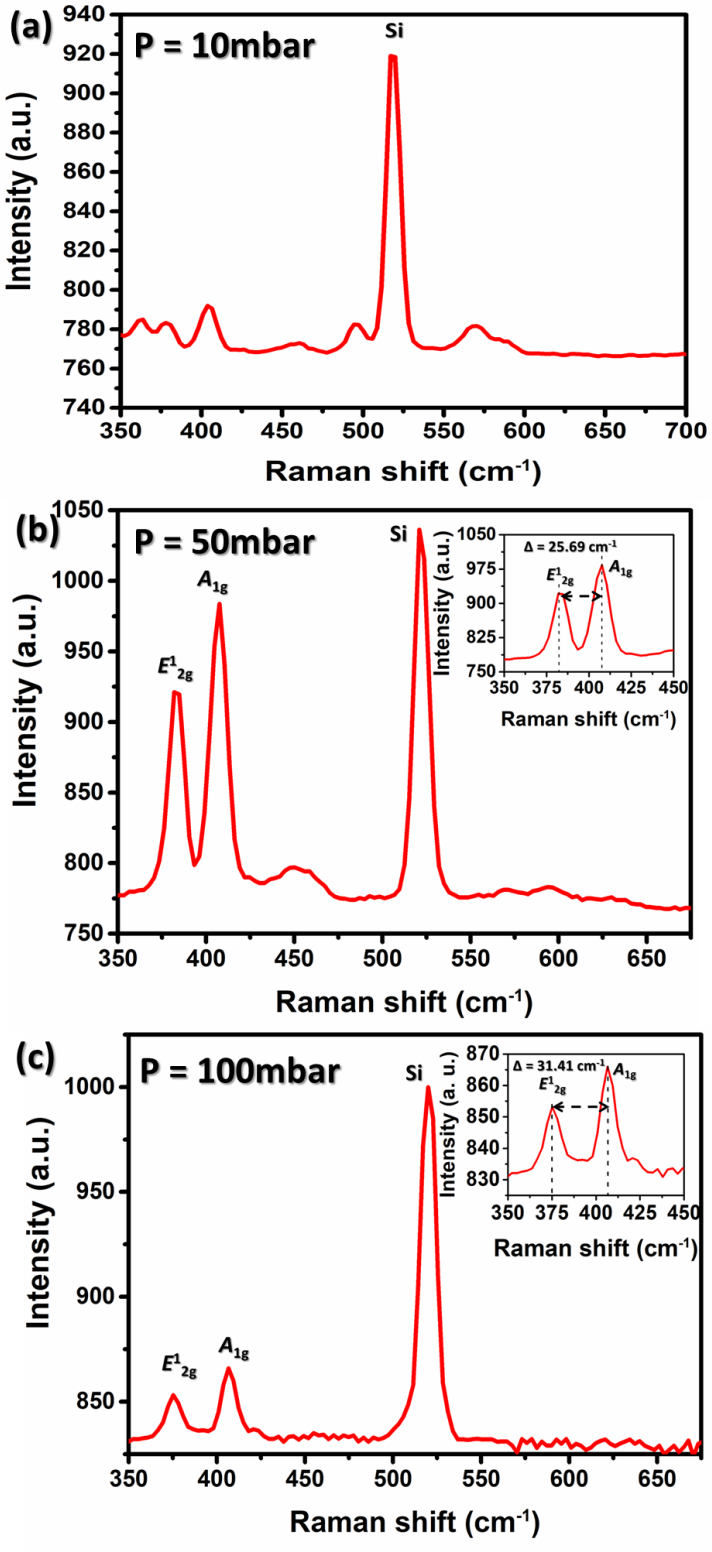

Figure 8-4: Raman spectra of the sample grown at (a) 10mbar, (b) 50mbar, and (c) 100mbar. The spectra clearly shows the distinct peaks E^1_{2g}, A^1_g and Si in sample synthesized at 50 and 100mbar pressure respectively. The inset (b and c) showing the E^1_{2g} and A^1_g peaks.

Figure 8-5 shows the combined Raman image using two distinct Raman lines. The blue spectra correspond to the average spectra of Si substrate (520 and 960 cm^{-1}). The red spectra correspond to MoS_2, where the two characteristic Raman bands are contributing from semiconductor/metallic (later confirmed by electrical characterization).The observed Raman bands from Si are apparently coming from the substrate used [334].

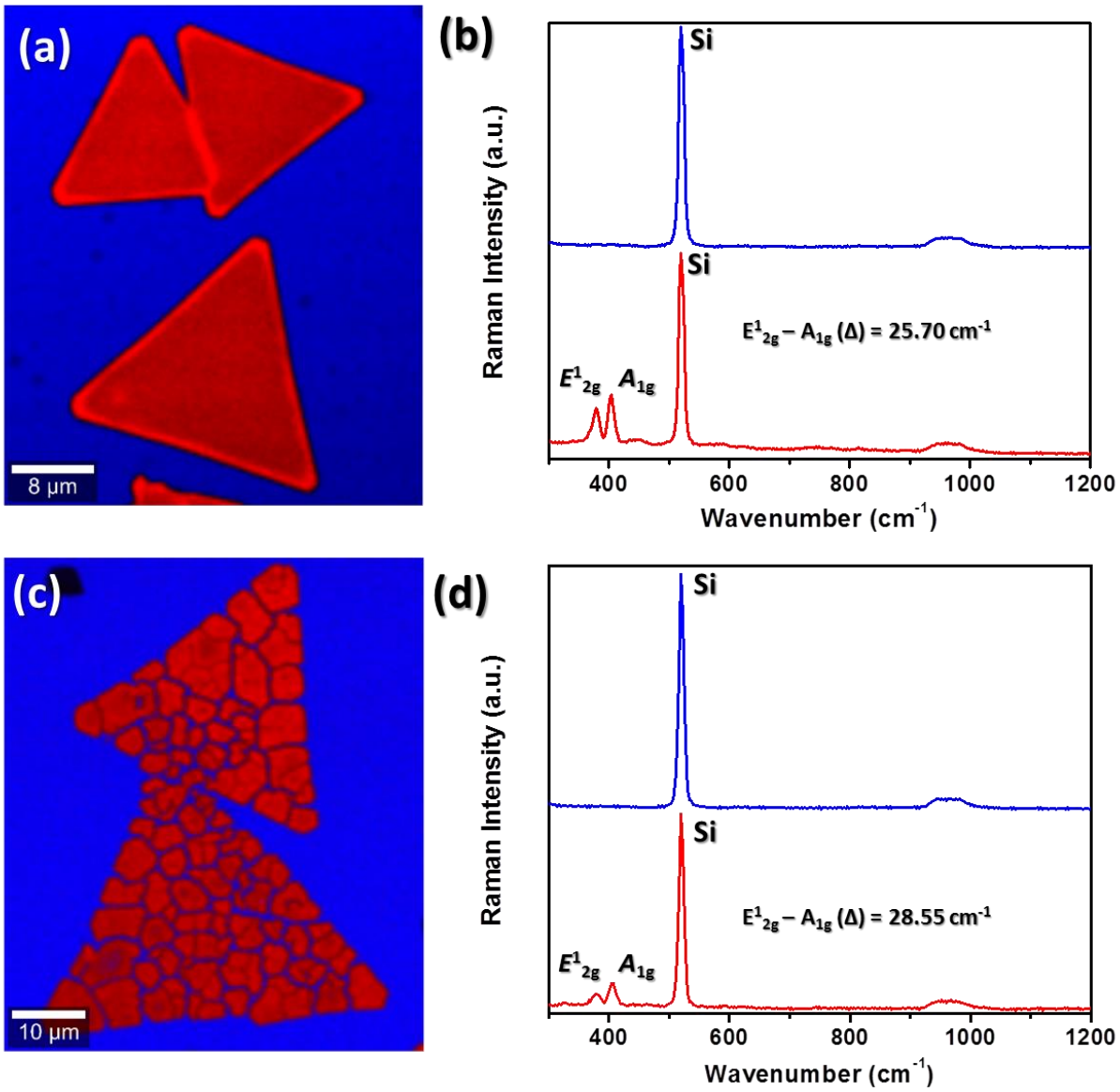

Figure 8-5: Combined Raman imaging using the distinct Raman spectra (left) and respective Raman spectra used for the combined Raman image (right) of the sample grown at 50 and 100 mbar. The blue spectra (b, d) correspond to the blue region (a, c) and the red spectra (b, d) correspond to the red region (a, c) in Raman imaging respectively. The differences (Δ) between (E^1_{2g} - A_{1g}) were found to be 25.7 and 28.55 cm^{-1} for the sample synthesized at 50 and 100 mbar respectively.

8.2.1.2. *X-ray Photoelectron Spectroscopy*

High-Resolution X-ray Photoelectron Spectroscopy (HR-XPS) is one of the most important techniques for evaluating chemical bonding states of the MoS_2 layers. It also allows us to study the surface chemistry of MoS_2 grown under different pressures by measuring the binding energies of both Mo and S. Thus, XPS is one of the best experimental techniques that allows to prove the formation of single layer MoS_2. We performed HR-XPS spectra of all the sintered samples. **Figure 8-6 (a and b)** shows the Mo 3d and S 2p core levels of all the samples grown under 10, 50 and 100 mbar. The fits were performed by a convolution of Gaussian and Lorentzian (70:30) functions after removing a Shirley type background. The binding energies in the XPS spectra were conventionally calibrated against the adventitious carbon C (1s) singlet (BE = 284.6 eV). **Figure 8-6 (a)** shows the core level peaks of Mo 3d of the sample grown at ~10, 50 and 100 mbar. The obtained spectra values were imported in CasaXPS and fitting was performed. The areas shown in green, blue, and cyan are the result of the overall fitting, while the red line shows the envelop obtained by fitting the experimental spectra (dotted points). Mo 3d spectra consist of two main peaks, namely Mo $3d_{3/2}$ (blue) and Mo $3d_{5/2}$ (cyan) at 232.6 and 229.4 eV, with a spin orbit splitting (Δ) of 3.2 eV. Their *FWHMs* were found to be around 0.95 and 1.17, respectively. However, in the spectra we were able to find the intermediate peak probably coming from $Mo3d^{6+}$ (expected area shown by green), from which we infer that the reaction was not completed during the growth [339]. The spectra do not show any significant S 2s peaks near the region of Mo. In the latter spectra of the samples grown at 50 and 100 mbar the scenario is completelly different. A clear peak appears at ~226.6 eV that can be ascribed to S 2s coming from MoS_2 [339, 340]. In the case of S, see **Figure 8-6 (b)** (sample grown under ~10mbar) we were not able to find any significant peak of S 2p, which indicates apparent absence of S on the surface of the sample, though we scanned over large range of energies (data not shown). **Figure 8-6 (a)** (~50 mbar) represents the highly resolved core level peaks for Mo $3d_{3/2}$ ~ 232.6 eV (blue) and Mo $3d_{5/2}$ ~ 229.4 eV (cyan) coming from $Mo3d^{4+}$. Their *FWHMs* were found to be 0.84 and 0.67 with the spin orbit splitting (Δ) of 3.2. As mentioned earlier, a small peak of S 2s was observed at 226.6 eV (yellow), with *FWHM* of 1.80. It is important to mention that no peak of intermediate compounds such as Mo $3d^{6+}$ were observed.

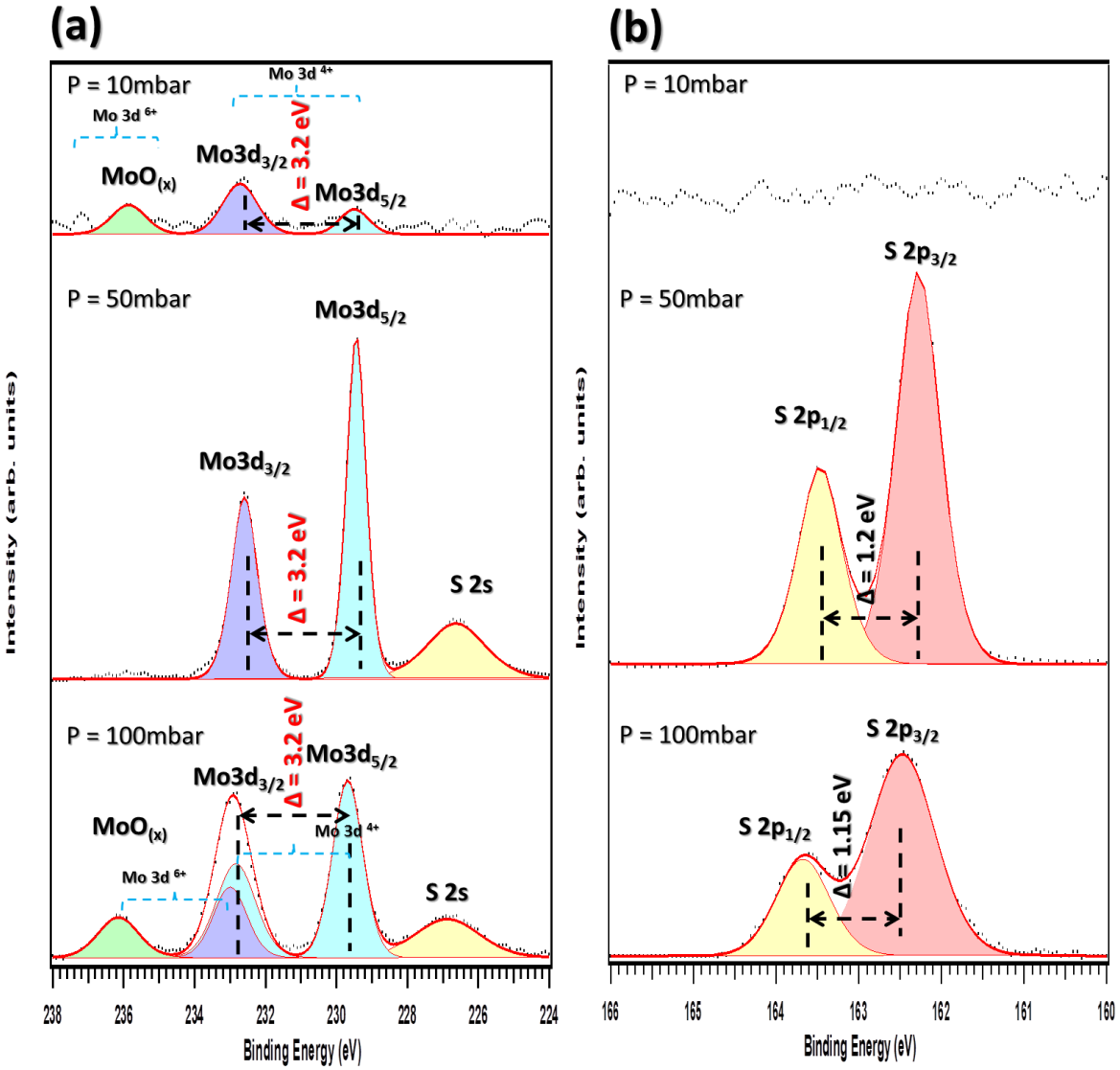

Figure 8-6: X-Ray photoelectron spectroscopy spectra of (a) Mo and (b) S respectively. The black dots are experimental data; red line is resultant fitting; green, blue, cyan and yellow are different components used for fitting.

In the case of S 2p peaks (**Figure 8-6 (b)** P = 50 mbar), two components are cleary detected and ascribed to S $2p_{1/2}$ and S $2p_{3/2}$ at 163.5eV (yellow) and 162.3eV (pink), respectively. Their *FWHMs* were found to be 0.67 and 0.64 for S $2p_{1/2}$ and S $2p_{3/2}$, respectively. Similar trends were found in the sample grown at ~100 mbar as shown in **Figure 8-6 (a)**. Thus obtained Mo 3d core peaks were deconvoluted into two parts, namely, for Mo3d 4+ and Mo3d 6+. The first part (marked as $MoO_{(x)}$) can be attributed to Mo $3d^{6+}$. However, the peak centered at BE = 233 eV shows a mixed contribution coming from Mo $3d^{6+}$ and Mo $3d^{4+}$ [339]. The peak centered at BE = 232. 8 eV is coming from Mo $3d^{4+}$. The spin orbit splitting between $Mo3d_{3/2}$ and Mo $3d_{5/2}$ was found to be 3.2

eV with *FWHM* of 1.20 and 0.99, respectively. The presence of Mo3d 6^+ clearly confirms the existence of intermediate oxidized state (green) Mo peak at 235.5 eV, which is indicative of incomplete reaction. As discussed earlier, the possible reason for it could be high pressure used during synthesis process. However, in this sample we found S 2s core level at around 226.7 eV (yellow), with *FWHM* of 2.24. In the case of S 2p core level (**Figure 8-6 (b)** ~100 mbar), the two components (S $2p_{1/2}$ and S $2p_{3/2}$) were observed at around 163.6 eV (*FWHM* ~0.79) and 162.6 eV (*FWHM* ~0.97), indicated by yellow and pink color, respectively. Thereon, we will now focus on the samples grown at 50 mbar as they showed the best quality as compared to the others.

8.2.1.3. *Ultraviolet Photoelectron Spectroscopy*

Ultraviolet Photoemission Spectroscopy (UPS), a photoemission spectroscopy using photons in the ultraviolet spectral range, is a powerful tool to detect a monolayer of an adsorbate or contaminant covering on the surface of the sample being examined due to its ultra-high surface sensitivity, especially sensitive to oxygen and carbon contaminations. Also, by applying UPS one can basically determine electronic band structure and work function of a solid since the energy of the photon source is low enough to just eject electrons form the valence/conduction bands of a material. Therefore, the energies of the ejected electrons are related to their original binding energies in the solid and also to their wave vector with their original states. The binding energy can be determined by measuring the observed kinetic energy using Einstein's photoelectric effect equation.

$$\boldsymbol{Binding\ Energy}\ (\boldsymbol{E_B}) = \boldsymbol{hv} - \boldsymbol{E_k} - (\boldsymbol{E_{vac}} - \boldsymbol{E_F})\,, \qquad \text{(Eq. 8-3)}$$

where h the Planck's constant; v is the frequency; E_k is the kinetic energy of an emitted photoelectron; E_F is the fermi energy.

The schematic diagram below (**Figure 8-7**) specifies the photoelectric phenomena associated with MoS_2.

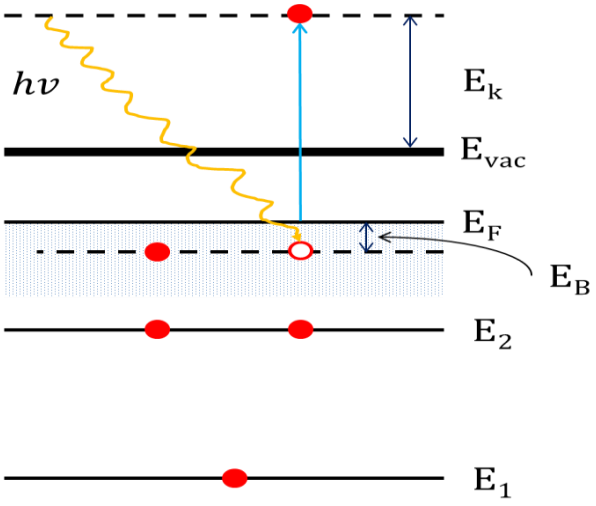

Figure 8-7: Schematic diagram of the Ultraviolet Photoelectron Spectroscopy associated with MoS_2

In our case we used He I 21.2 eV as the source for the excitation and calculated the work function of MoS_2 on SiO_2/Si.

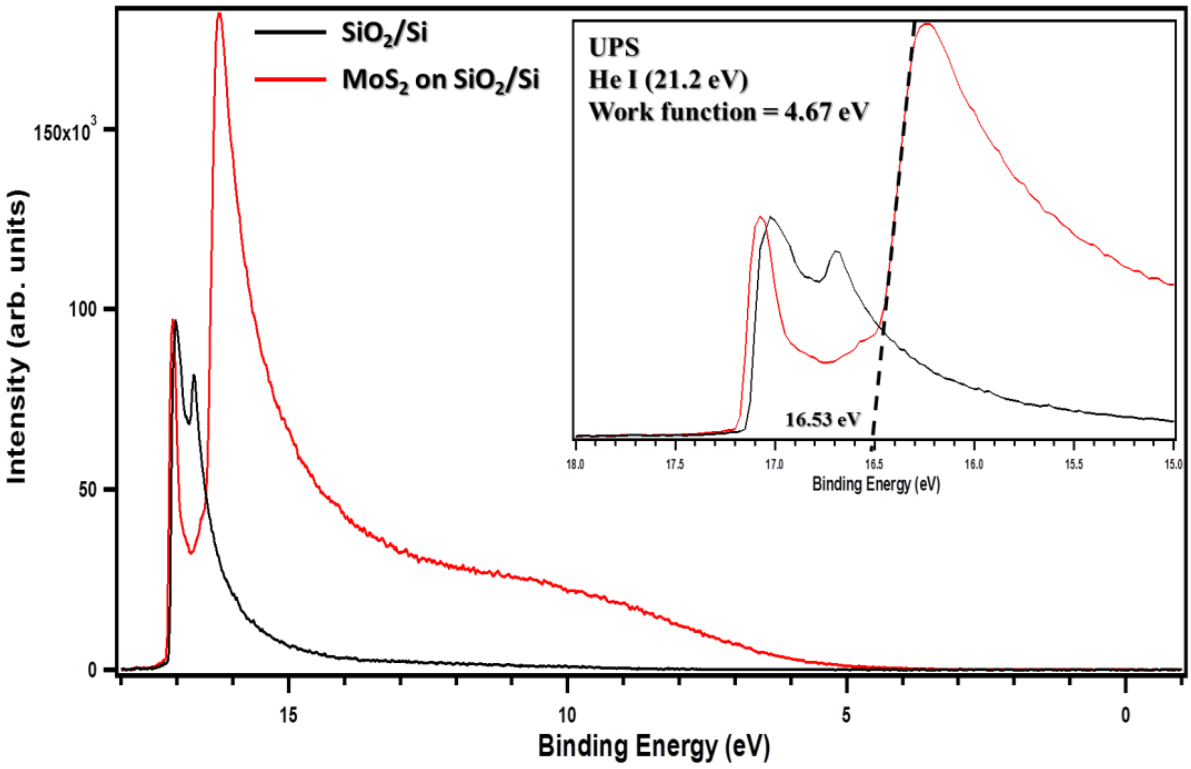

Figure 8-8: The figure shows the full UPS spectrum of MoS_2 on SiO_2/Si (red) and pristine SiO_2/Si (black) acquired with He I. The inset shows the broad scale to focus the shift, in order to have linear fitting (black dotted line). The obtained work function is 4.67 eV.

Figure 8-8 shows the full valence band (VB) spectrum of MoS_2 on SiO_2/Si (red) and pristine SiO_2/Si (black) acquired using XPS. To our best knowledge, we report for the first time VB spectra of MoS_2 on SiO_2/Si. The inset in the Figure highlights the magnified spectra of both pristine SiO_2/Si (fresh cleaned substrate without any sample) and MoS_2 grown on SiO_2/Si (synthesized at ~50 mbar). The Figure clearly shows two distinct peaks at ~17.075 and 16.25 eV. We consider the peak located at 17.075 eV to come from SiO_2/Si as this can also be seen in the pristine SiO_2/Si. On the contrary, the peak located at lower BE could be from MoS_2. The spectra indicate the shift of the peak towards higher BE from 17.025 to 17.075 eV. This could be due to the presence of MoS_2 on the substrate. A linear fitting was done in order to calculate the work function of MoS_2 on SiO_2/Si. The obtained work function was found to be 4.3 eV. Note that in the case of pristine SiO_2/Si substrate an unknown peak was observed at ~ 16.7 eV.

8.2.1.4. *UV-Visible Spectroscopy*

Photoluminescence (PL), along with Raman measurements, is the most used method to evaluate the quality of grown MoS_2, especially for monolayer samples [150, 322, 341-344]. In addition, by the extensive use of UV-visible absorption, we were able to calculate the direct band gap in MoS_2. In contrast to bulk samples, monolayer MoS_2 where the direct band gap is dominant, direct band radiative recombination becomes viable means for excitonic recombination [345]. Direct as well as indirect exciton transition in single to a few layers MoS_2 is found to be a result of the existence of in-plane excitons [346] and may help in understanding exciton-phonon interactions. In our case, using **Eq. 1**, we calculated the value of direct band gap.

$$(\boldsymbol{\alpha h v})^{\boldsymbol{n}} \propto \left(\boldsymbol{h v - E_g}\right) \quad , \qquad \text{(Eq. 8-4)}$$

where $n = 2$ for direct band-gap, α is the absorption coefficient, hv is the photon energy and E_g is the energy band-gap. When $(\alpha hv)^2 vs\, E_{plot}$ is plotted the value of the bandgap can be obtained. **Figure 8-9** shows the UV-visible diffuse reflectance spectrum of MoS_2 on SiO_2/Si. Inset to **Figure 8-9** displays $(\alpha hv)^2 vs\, E$ dependence [347]. The fitting parameter extrapolated at $(\alpha hv)^2 = 0$, indicates a bandgap of 1.6 eV for MoS_2 (shown in inset) which lies in the range of the previously reported literature values [149, 348-350]. For the bulk MoS_2 a band gap of 1.42 eV is expected while the present observation of 1.6 eV further hints to the formation of a few layer crystallites [351].

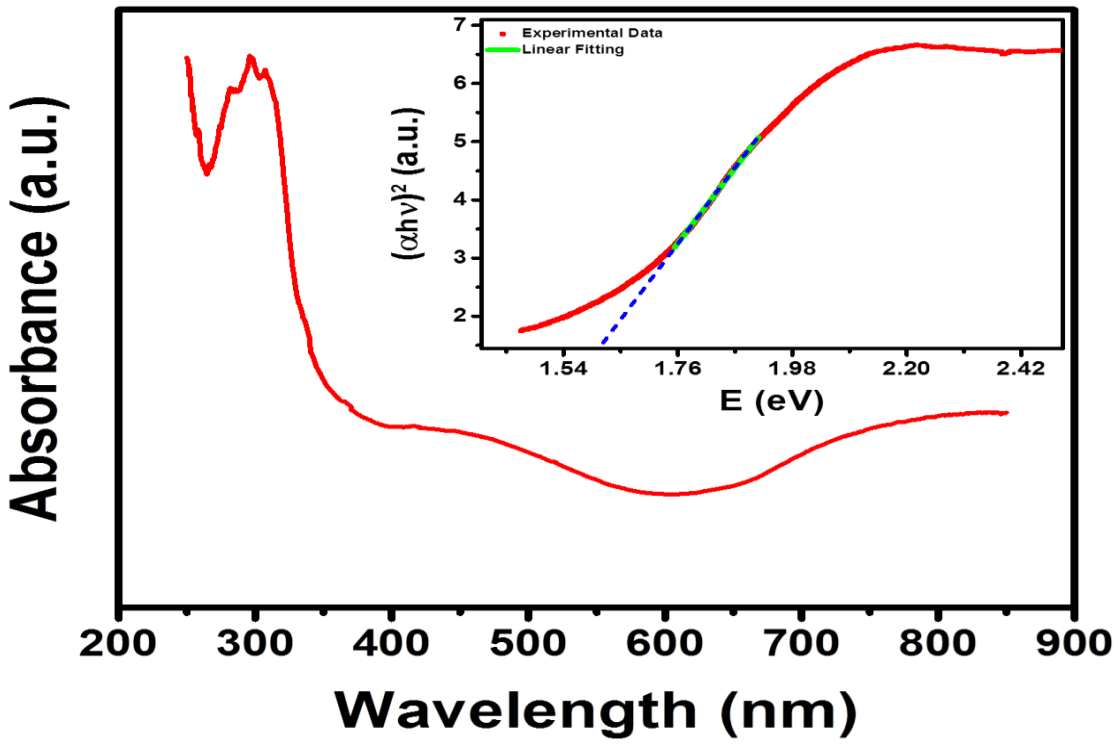

Figure 8-9: Shows the UV-visible diffuse reflectance spectrum of MoS_2 synthesized on SiO_2/Si substrate. Inset showing the $(\alpha h\nu)^2$ *vs* E plot for calculating the direct bandgap.

8.2.1.5. *Electrical properties*

The electrical conductance (G) and conductivity (σ) of the grown MoS_2 was mainly defined by two-terminal I-V measurements. **Figure 8-10** (a) shows focused ion beam scanning electron microscopy setup used for electroding of the sample while b and c shows the SEM image acquired after electroding the single grain and double triangular grain. Inset shows the captured image during the electroding process. **Figure 8-11** depicts the representative I-V curves measured by the two-probe method for our MoS_2. In order to check the electrical behavior of crystalline MoS_2 (having two triangles), we performed I-V measurements. Theoretically, electrical conductivity (*G*) can be described by:

$$G = \frac{I}{V} = \frac{\sigma A}{l} = \frac{\sigma w t}{l}, \qquad \textbf{(Eq. 8-5)}$$

where A is the electrode area for current transport, $l, w, and\ t$ are the length, width and thickness of the conductor, respectively.

The linear I-V relationship curve suggests an apparent Ohmic beahvior for the entire range of applied voltages, -40 V to +40 V. When the applied voltage was below ±10 V, MoS_2 showed Ohmic behavior and the current increased to 0.11 nA. This behavior of MoS_2 depends on the electronic structure of the boundary (individual sample area) which further depends on the atomic structure [352]. In the case of double/joint MoS_2 (having two triangles), the current versus voltage is linearly ranging from -40 V to +40 V, suggesting Ohmic contacts with our Pt electrodes. The forward current is approximately +6 nA at 40 V and -6 nA at -40 V.

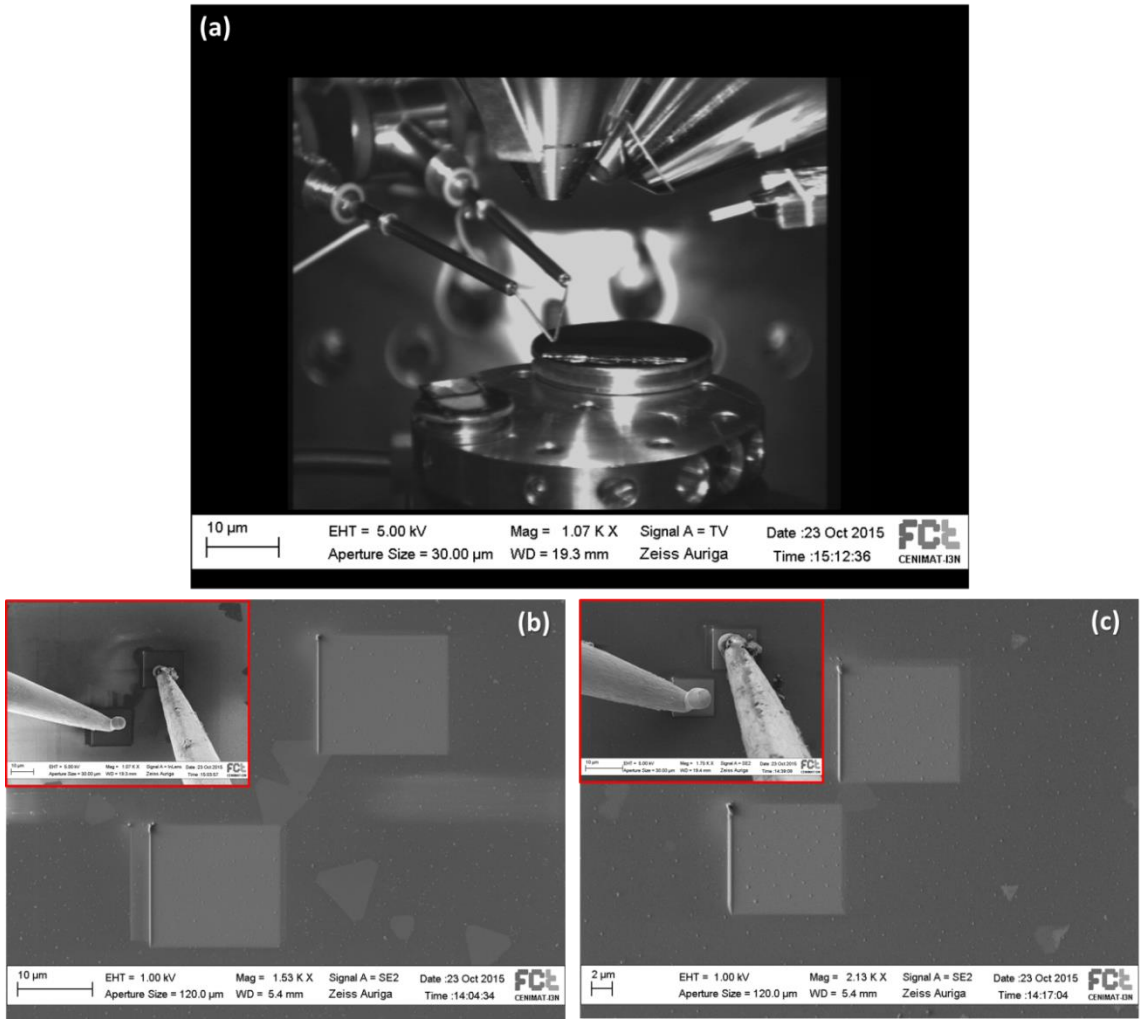

Figure 8-10: Electrical characterization of CVD synthesized MoS_2. (a) Showing Focused Ion Beam Scanning Electron Microscopes used for electroding of the sample. (b and C) Showing the SEM image acquired after electroding the single grain and double triangular grain. Inset showing the captured image while the electroding process.

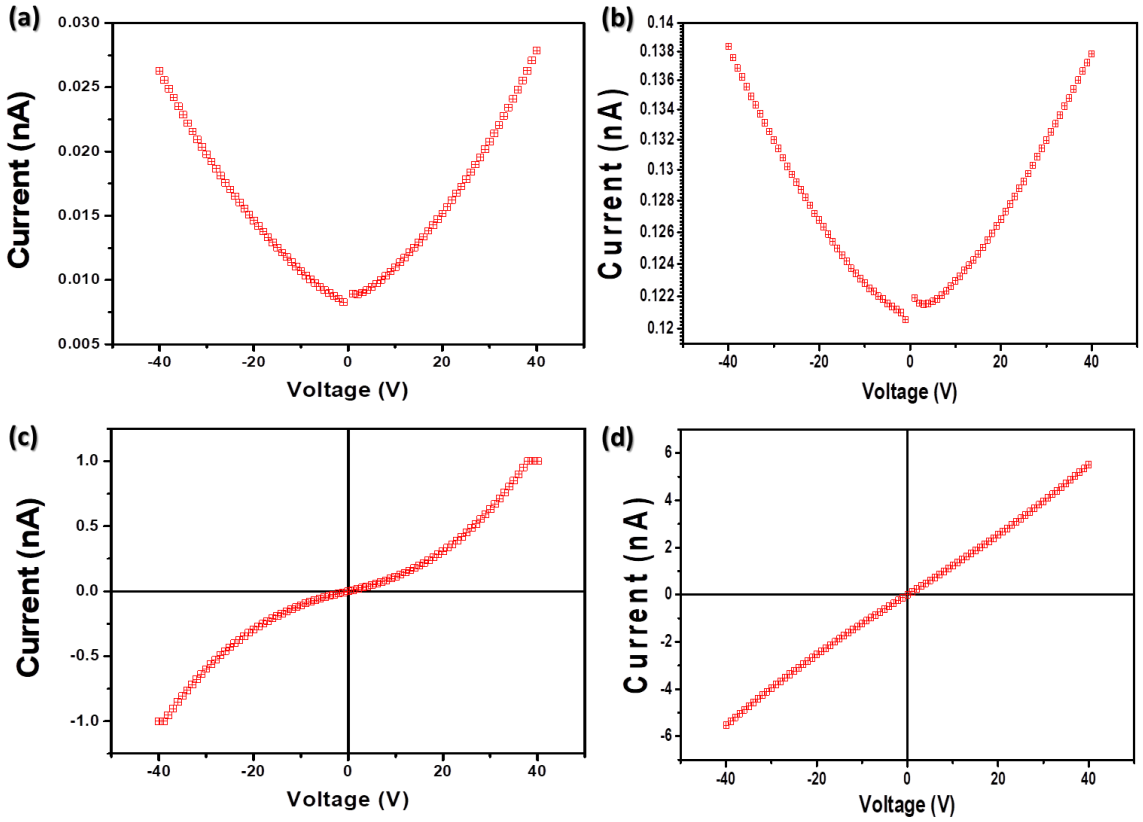

Figure 8-11: Shows the corresponding electrical measurement conducted horizontally with operating voltage in the range -40 V to +40 V which show (a and c) semiconducting and (b and d) Ohmic nature of single grain and double triangular grain, respectively.

8.2.1.6. *Conclusion*

After a decade of intensive investigations, graphene – related works are going to enter in matured zone. Hence, more and more research works are focused on other 2D materials. MoS_2 became one of the favorite compounds for the researchers from the large family of layered transition metal dichalcogenides due to its outstanding properties. Moreover, there exists massive potential to broaden this area by designing and producing 2D or 3D hybrid components by combining graphene and graphene-like 2D blocks. However, the growth of high quality MoS_2 for large area applications is still challenging. We have successfully demonstrated the growth of large-area continuous layers of MoS_2 on SiO_2/Si by using our home-made CVD technique. The role of pressure has been studied relevant to the sulfurization of molybdenum trioxide (MoO_3). The goal of the study was to find the suitable pressure for the highly crystalline MoS_2 to be formed. When

the pressure of the gas flow is low, 10 mbar, the ad-atoms retain insufficient kinetic energy due to fewer collisions during the transportation towards the surface of the substrate. When the pressure is increased to 50 mbar, the high surface mobility of ad-atoms gives rise to densely formed triangular grains, which is inherent to MoS_2. Further increase in pressure, however, hinders the mobility of atoms resulting in porously formed triangles inside the MoS_2 thin film. This will further affect the grain boundaries, which are essential for optimizing electronic and optical properties of MoS_2 based devices. The as synthesized MoS_2 layer on SiO_2/Si shows the direct band gap of 1.6 eV. Raman spectra and their maps clearly confirm the existence of large area material deposited on SiO_2/Si. Moreover, the XPS and UPS studies have been extensively used to distinguish the concerned core level peaks and also elucidated the mechanism of the growth procedure and its pressure dependence. In addition, we conclude that, band gap engineering of both graphene and MoS_2 can be used for achieving superior electrical performance and tunable band structure.

Chapter 9

General conclusions and future work

9. General conclusions and future work

Graphene, a single atomic layer of graphitic carbon, has attracted considerable interest as a new electronic material from many perspectives. It has a wide range of applications in electronics and it is a strong contender to replace silicon in future solid-state devices. However, most electronic applications are handicapped by the absence of a bandgap in the pristine graphene. For example, devices made from zero-band gap graphene are difficult to switch off the current through them. Therefore, pure graphene is fundamentally limited by its electronic properties and is not suitable for the digital circuitry that comprises the vast majority of devices. In this sense, it is highly desirable to introduce a bandgap in graphene in order to tailor its transport properties. Another task is to produce pristine or doped graphene of sufficiently high quality on technological substrates such as Si or Au.

Following this global task, the present thesis has made significant contributions toward the advancement of the process technology and the scientific understanding of the synthesis of pure and in-situ ammonia doped graphene by CVD on copper and nickel foils. The home-made CVD setup was built in the TEMA associate laboratory of the University of Aveiro for the dedicated growth of 2D materials. Besides assembling the deposition process was parameterized and characterization of the properties of graphene and other 2D material (MoS_2) was carried out. In order to tune the electronic properties of graphene, this work focused not only on the growth of high quality graphene but on *in-situ* heteroatom doping by ammonia (NH_3). Furthermore, the processing conditions were also parameterized for the synthesis of high quality TMD materials (such as MoS_2) by modifying the current CVD equipment. A thorough review of the fundamental properties as well as methods of synthesis and properties of 2D materials was also done in the present PhD work.

After establishing the home-made setup for the fabrication of large area graphene and other 2D materials, the thesis also presented the systematic study of *in-situ* ammonia doped graphene as a function of the thickness of the substrate used for the deposition. The novelty of this work is that it establishes and explains the thickness dependence mechanism for the defect creations by nitrogen atoms. As discussed in the corresponding chapter, 20 μm thick Cu foils should be used for this purpose. This conclusion was based on the detailed investigation by Raman, HR-XPS and AFM techniques. This thickness significantly increases the efficiency of doping of graphene sheets

with nitrogen as compared to standard 20 µm foils. This opens up an efficient way for heteroatom engineering of graphene, which is required for its electronic applications.

Further, the thesis describes a detailed study of the charge injection process into multilayer graphene (MLG) performed by Kelvin Probe Microscopy. For the first time, it is reported how the charge injection proceeds over time. The obtained results unveiled that: (i) MLG surface can be either positively or negatively charged through injection process using Pt coated probes; (ii) the charges accumulated can reach saturated concentrations as high as +4.45 and −1.3 $\mu C/m^2$ for positive and negative charges, respectively; (iii) the charge diffusion coefficients on graphene surface are about 1.50 and 0.64 × 10^{-16} m^2/s for the positive and the negative charges, respectively. This discovery of charge injection into MLG may pave the way for designing a new class of energy harvesting and memory devices. Additionally, we expect that our studies demonstrated a technique for nano-patterning/charge lithography of surface charges by contact electrification, which could be a promising application to create charged nanostructures for next generation nanoelectronic devices.

In addition to graphene study to the work was devoted to the fabrication of 2D materials such as MoS_2 using conventional home-made quartz based CVD equipment. Using sulfurization of MoO_3, the thesis provides an understanding of the effect of growth parameters (e.g. base pressure) on the quality of MoS_2 films on SiO_2/Si substrates. The as synthesized MoS_2 on ~10 × 10 mm^2 substrates were ready to be used for further device fabrication. The applications of MoS_2 are growing rapidly in many areas, such as transistors, photodetectors, solar cells, etc.

In the direction of future work, I would like to proceed with the fabrication of other 2D TMDs such as tungsten disulfide (WS_2), tungsten diselenide (WSe_2) and molybdenum diselenide ($MoSe_2$) etc. The CVD setup assembled in this work can be used for any TMD materials which are also very interesting for real device applications. I would like also to study the effect of transfer method on the properties of graphene. As reported in chapter 7 we observed significant predominance of pyridinic impurities over desired graphitic nitrogen after transferring the graphene on SiO_2. The increment of pyridinic N at the expense of substitutional N is probably due to the transfer process and evidences the generation of defects on the graphene sheet during this process. It would be interesting to conduct additional studies of this effect based on some theoretical modeling. A few literature reports have been found on this issue. Another interesting effect is the inclusion of iron atoms in the graphene sheets during the transfer process. The transferred samples typically consist of large areas of monolayer graphene in which some regions contain remnant material

from the transfer process, including Fe atoms from decomposed $FeCl_3$. As discussed in the corresponding chapter, pure Fe can be found as small nanocrystals forming on the surface of the graphene, as single atoms or small clusters at the edge of pores in clean graphene, or as 2D crystalline membranes suspended across perforations in the graphene. It will be interesting to carry out the investigation of the formation of Fe nanocrystals for nanotechnological purposes.

Further interest in this area is due to transfer of both pristine and in-situ ammonia doped graphene on specially prepared ferroelectric substrates (ferroelectric PMN-PT, PZN-PT, single crystals of $BiFeO_3$). These substrates have high polarization and electromechanical properties that could induce large mechanical deformations. The measurements of nanoelectromechanical effects and expected polar states in graphene will be accompanied by rigorous calculations of stress/strain distribution and evaluation of various accompanying effects e.g., flexoelectricity, Joule heating by the tip, defect formation under the tip force, etc. By this way, we can study the fully uniform external strain and local properties as a function of calibrated strain transferred from the substrate to graphene.

Bibliography

1. Yu, Q., et al., *Graphene segregated on Ni surfaces and transferred to insulators.* Applied Physics Letters, 2008. **93**(11): p. 113103.
2. Reina, A., et al., *Layer Area, Few-Layer Graphene Films on Arbitrary Substrates by Chemical Vapor Deposition.* Nano Letters, 2009. **9**(8): p. 3087-3087.
3. Kim, K.S., et al., *Large-scale pattern growth of graphene films for stretchable transparent electrodes.* Nature, 2009. **457**(7230): p. 706-710.
4. Orofeo, C.M., et al., *Synthesis of large area, homogeneous, single layer graphene films by annealing amorphous carbon on Co and Ni.* Nano Research, 2011. **4**(6): p. 531-540.
5. Ago, H., et al., *Epitaxial Chemical Vapor Deposition Growth of Single-Layer Graphene over Cobalt Film Crystallized on Sapphire.* ACS Nano, 2010. **4**(12): p. 7407-7414.
6. Varykhalov, A. and O. Rader, *Graphene grown on Co(0001) films and islands: Electronic structure and its precise magnetization dependence.* Physical Review B, 2009. **80**(3): p. 035437.
7. Li, X., et al., *Large-Area Synthesis of High-Quality and Uniform Graphene Films on Copper Foils.* Science, 2009. **324**(5932): p. 1312-1314.
8. Lee, Y., et al., *Wafer-Scale Synthesis and Transfer of Graphene Films.* Nano Letters, 2010. **10**(2): p. 490-493.
9. Bhaviripudi, S., et al., *Role of Kinetic Factors in Chemical Vapor Deposition Synthesis of Uniform Large Area Graphene Using Copper Catalyst.* Nano Letters, 2010. **10**(10): p. 4128-4133.
10. Mattevi, C., H. Kim, and M. Chhowalla, *A review of chemical vapour deposition of graphene on copper.* Journal of Materials Chemistry, 2011. **21**(10): p. 3324-3334.
11. Sutter, P.W., J.-I. Flege, and E.A. Sutter, *Epitaxial graphene on ruthenium.* Nat Mater, 2008. **7**(5): p. 406-411.
12. Yoshii, S., et al., *Suppression of Inhomogeneous Segregation in Graphene Growth on Epitaxial Metal Films.* Nano Letters, 2011. **11**(7): p. 2628-2633.
13. Coraux, J., et al., *Structural Coherency of Graphene on Ir(111).* Nano Letters, 2008. **8**(2): p. 565-570.
14. Murata, Y., et al., *Orientation-dependent work function of graphene on Pd(111).* Applied Physics Letters, 2010. **97**(14): p. 143114.
15. Singh, A.K., et al., *Molecular n-doping of chemical vapor deposition grown graphene.* Journal of Materials Chemistry, 2012. **22**(30): p. 15168-15174.
16. Ganatra, R. and Q. Zhang, *Few-Layer MoS2: A Promising Layered Semiconductor.* ACS Nano, 2014. **8**(5): p. 4074-4099.
17. RadisavljevicB, et al., *Single-layer MoS2 transistors.* Nat Nano, 2011. **6**(3): p. 147-150.
18. Li, X. and H. Zhu, *Two-dimensional MoS2: Properties, preparation, and applications.* Journal of Materiomics, 2015. **1**(1): p. 33-44.
19. Wi, S., et al., *Enhancement of Photovoltaic Response in Multilayer MoS2 Induced by Plasma Doping.* ACS Nano, 2014. **8**(5): p. 5270-5281.
20. Van Noorden, R., *Production: Beyond sticky tape.* Nature, 2012. **483**(7389): p. S32-S33.
21. Segal, M., *Material history: Learning from silicon.* Nature, 2012. **483**(7389): p. S43-S44.
22. Schmidt, C., *Bioelectronics: The bionic material.* Nature, 2012. **483**(7389): p. S37-S37.
23. Brody, H., *Graphene.* Nature, 2012. **483**(7389): p. S29-S29.
24. Dong, X., et al., *Electrical Detection of Femtomolar DNA via Gold-Nanoparticle Enhancement in Carbon-Nanotube-Network Field-Effect Transistors.* Advanced Materials, 2008. **20**(12): p. 2389-2393.

25. Fu, D., et al., *Differentiation of Gas Molecules Using Flexible and All-Carbon Nanotube Devices.* The Journal of Physical Chemistry C, 2008. **112**(3): p. 650-653.
26. Dong, X., et al., *Label-Free Electronic Detection of DNA Using Simple Double-Walled Carbon Nanotube Resistors.* The Journal of Physical Chemistry C, 2008. **112**(26): p. 9891-9895.
27. Park, S.J., et al., *Ultrasensitive Flexible Graphene Based Field-Effect Transistor (FET)-Type Bioelectronic Nose.* Nano Letters, 2012. **12**(10): p. 5082-5090.
28. Mohanty, N. and V. Berry, *Graphene-Based Single-Bacterium Resolution Biodevice and DNA Transistor: Interfacing Graphene Derivatives with Nanoscale and Microscale Biocomponents.* Nano Letters, 2008. **8**(12): p. 4469-4476.
29. Huang, Y., et al., *Graphene-based biosensors for detection of bacteria and their metabolic activities.* Journal of Materials Chemistry, 2011. **21**(33): p. 12358-12362.
30. Ang, P.K., et al., *Flow Sensing of Single Cell by Graphene Transistor in a Microfluidic Channel.* Nano Letters, 2011. **11**(12): p. 5240-5246.
31. Sparrow, G., *Carbon*. 1999, New York: Benchmark Books/Marshall Cavendish.
32. Novoselov, K.S., et al., *Electric field effect in atomically thin carbon films.* Science, 2004. **306**(5696): p. 666-9.
33. Petroski, H., 1989, The Pencil: A History of Design and Circumstance (Knopf, New York).
34. Wallace, P.R., *The Band Theory of Graphite.* Physical Review, 1947. **71**(9): p. 622-634.
35. Mayorov, A.S., et al., *Micrometer-Scale Ballistic Transport in Encapsulated Graphene at Room Temperature.* Nano Letters, 2011. **11**(6): p. 2396-2399.
36. Morozov, S.V., et al., *Giant Intrinsic Carrier Mobilities in Graphene and Its Bilayer.* Physical Review Letters, 2008. **100**(1): p. 016602.
37. Lee, C., et al., *Measurement of the Elastic Properties and Intrinsic Strength of Monolayer Graphene.* Science, 2008. **321**(5887): p. 385-388.
38. Liu, F., P. Ming, and J. Li, *\textit{Ab initio} calculation of ideal strength and phonon instability of graphene under tension.* Physical Review B, 2007. **76**(6): p. 064120.
39. Balandin, A.A., *Thermal properties of graphene and nanostructured carbon materials.* Nat Mater, 2011. **10**(8): p. 569-581.
40. Nair, R.R., et al., *Fine Structure Constant Defines Visual Transparency of Graphene.* Science, 2008. **320**(5881): p. 1308.
41. Bunch, J.S., et al., *Impermeable Atomic Membranes from Graphene Sheets.* Nano Letters, 2008. **8**(8): p. 2458-2462.
42. Moser, J., A. Barreiro, and A. Bachtold, *Current-induced cleaning of graphene.* Applied Physics Letters, 2007. **91**(16): p. 163513.
43. Elias, D.C., et al., *Control of Graphene's Properties by Reversible Hydrogenation: Evidence for Graphane.* Science, 2009. **323**(5914): p. 610-613.
44. Geim, A.K. and K.S. Novoselov, *The rise of graphene.* Nat Mater, 2007. **6**(3): p. 183-191.
45. Land, T.A., et al., *STM investigation of single layer graphite structures produced on Pt(111) by hydrocarbon decomposition.* Surface Science, 1992. **264**(3): p. 261-270.
46. Merino, P., et al., *Strain-Driven Moiré Superstructures of Epitaxial Graphene on Transition Metal Surfaces.* ACS Nano, 2011. **5**(7): p. 5627-5634.
47. Marchini, S., S. Günther, and J. Wintterlin, *Scanning tunneling microscopy of graphene on Ru(0001).* Physical Review B, 2007. **76**(7): p. 075429.
48. Wang, B., et al., *Coupling Epitaxy, Chemical Bonding, and Work Function at the Local Scale in Transition Metal-Supported Graphene.* ACS Nano, 2010. **4**(10): p. 5773-5782.
49. Sun, Z., et al., *Topographic and electronic contrast of the graphene moir\'e on Ir(111) probed by scanning tunneling microscopy and noncontact atomic force microscopy.* Physical Review B, 2011. **83**(8): p. 081415.

50. Paton, K.R., et al., *Scalable production of large quantities of defect-free few-layer graphene by shear exfoliation in liquids.* Nat Mater, 2014. **13**(6): p. 624-630.
51. Hummers, W.S. and R.E. Offeman, *Preparation of Graphitic Oxide.* Journal of the American Chemical Society, 1958. **80**(6): p. 1339-1339.
52. Tung, V.C., et al., *High-throughput solution processing of large-scale graphene.* Nat Nano, 2009. **4**(1): p. 25-29.
53. Stankovich, S., et al., *Synthesis of graphene-based nanosheets via chemical reduction of exfoliated graphite oxide.* Carbon, 2007. **45**(7): p. 1558-1565.
54. Williams, G., B. Seger, and P.V. Kamat, *TiO2-Graphene Nanocomposites. UV-Assisted Photocatalytic Reduction of Graphene Oxide.* ACS Nano, 2008. **2**(7): p. 1487-1491.
55. Wang, G., et al., *Facile Synthesis and Characterization of Graphene Nanosheets.* The Journal of Physical Chemistry C, 2008. **112**(22): p. 8192-8195.
56. Shin, H.-J., et al., *Efficient Reduction of Graphite Oxide by Sodium Borohydride and Its Effect on Electrical Conductance.* Advanced Functional Materials, 2009. **19**(12): p. 1987-1992.
57. Wang, H., et al., *Solvothermal Reduction of Chemically Exfoliated Graphene Sheets.* Journal of the American Chemical Society, 2009. **131**(29): p. 9910-9911.
58. Fan, Z.-J., et al., *Facile Synthesis of Graphene Nanosheets via Fe Reduction of Exfoliated Graphite Oxide.* ACS Nano, 2011. **5**(1): p. 191-198.
59. Hernandez, Y., et al., *High-yield production of graphene by liquid-phase exfoliation of graphite.* Nat Nano, 2008. **3**(9): p. 563-568.
60. Lotya, M., et al., *Liquid Phase Production of Graphene by Exfoliation of Graphite in Surfactant/Water Solutions.* Journal of the American Chemical Society, 2009. **131**(10): p. 3611-3620.
61. Qian, W., et al., *Solvothermal-assisted exfoliation process to produce graphene with high yield and high quality.* Nano Research, 2009. **2**(9): p. 706-712.
62. Jiang, B., et al., *Facile fabrication of high quality graphene from expandable graphite: simultaneous exfoliation and reduction.* Chemical Communications, 2010. **46**(27): p. 4920-4922.
63. Janowska, I., et al., *Microwave synthesis of large few-layer graphene sheets in aqueous solution of ammonia.* Nano Research, 2010. **3**(2): p. 126-137.
64. Singh, M.K., et al., *Atomic-scale observation of rotational misorientation in suspended few-layer graphene sheets.* Nanoscale, 2010. **2**(5): p. 700-708.
65. Sun, Z., et al., *Soluble graphene through edge-selective functionalization.* Nano Research, 2010. **3**(2): p. 117-125.
66. Pu, N.-W., et al., *Production of few-layer graphene by supercritical CO2 exfoliation of graphite.* Materials Letters, 2009. **63**(23): p. 1987-1989.
67. Behabtu, N., et al., *Spontaneous high-concentration dispersions and liquid crystals of graphene.* Nat Nano, 2010. **5**(6): p. 406-411.
68. Watcharotone, S., et al., *Graphene–Silica Composite Thin Films as Transparent Conductors.* Nano Letters, 2007. **7**(7): p. 1888-1892.
69. Becerril, H.A., et al., *Evaluation of Solution-Processed Reduced Graphene Oxide Films as Transparent Conductors.* ACS Nano, 2008. **2**(3): p. 463-470.
70. Wang, X., L. Zhi, and K. Müllen, *Transparent, Conductive Graphene Electrodes for Dye-Sensitized Solar Cells.* Nano Letters, 2008. **8**(1): p. 323-327.
71. Li, D., et al., *Processable aqueous dispersions of graphene nanosheets.* Nat Nano, 2008. **3**(2): p. 101-105.
72. De, S., et al., *Flexible, Transparent, Conducting Films of Randomly Stacked Graphene from Surfactant-Stabilized, Oxide-Free Graphene Dispersions.* Small, 2010. **6**(3): p. 458-464.

73. Blake, P., et al., *Graphene-Based Liquid Crystal Device.* Nano Letters, 2008. **8**(6): p. 1704-1708.
74. Zhu, Y., et al., *Transparent self-assembled films of reduced graphene oxide platelets.* Applied Physics Letters, 2009. **95**(10): p. 103104.
75. Biswas, S. and L.T. Drzal, *A Novel Approach to Create a Highly Ordered Monolayer Film of Graphene Nanosheets at the Liquid−Liquid Interface.* Nano Letters, 2009. **9**(1): p. 167-172.
76. Van Bommel, A.J., J.E. Crombeen, and A. Van Tooren, *LEED and Auger electron observations of the SiC(0001) surface.* Surface Science, 1975. **48**(2): p. 463-472.
77. Lin, Y.-M., et al., *100-GHz Transistors from Wafer-Scale Epitaxial Graphene.* Science, 2010. **327**(5966): p. 662-662.
78. R. Yakimova; C. Virojanadara; D. Gogova; M. Syväjärvi; D. Siche; K. Larsson; L. I. Johansson, *Analysis of the Formation Conditions for Large Area Epitaxial Graphene on SiC Substrates.* Materials Science Forum, 2010. **645-648**: p. 565-568.
79. Yazdi, G.R., et al., *Growth of large area monolayer graphene on 3C-SiC and a comparison with other SiC polytypes.* Carbon, 2013. **57**: p. 477-484.
80. Berger, C., et al., *Electronic Confinement and Coherence in Patterned Epitaxial Graphene.* Science, 2006. **312**(5777): p. 1191-1196.
81. Ohta, T., et al., *Controlling the Electronic Structure of Bilayer Graphene.* Science, 2006. **313**(5789): p. 951-954.
82. Riedl, C., et al., *Structural properties of the graphene-SiC(0001) interface as a key for the preparation of homogeneous large-terrace graphene surfaces.* Physical Review B, 2007. **76**(24): p. 245406.
83. Emtsev, K.V., et al., *Towards wafer-size graphene layers by atmospheric pressure graphitization of silicon carbide.* Nat Mater, 2009. **8**(3): p. 203-207.
84. Tairov, Y.M. and V.F. Tsvetkov, *Investigation of growth processes of ingots of silicon carbide single crystals.* Journal of Crystal Growth, 1978. **43**(2): p. 209-212.
85. Tairov, Y.M. and V.F. Tsvetkov, *General principles of growing large-size single crystals of various silicon carbide polytypes.* Journal of Crystal Growth, 1981. **52**: p. 146-150.
86. Berzelius, J.J., *Untersuchungen über die Flussspathsäure und deren merkwürdigsten Verbindungen.* Annalen der Physik, 1824. **77**(6): p. 169-230.
87. Acheson, F.G., *Edward g*. 1893, Google Patents.
88. Acheson, E., *On carborundum.* Chem. News, 1893. **68**: p. 179.
89. Yazdi, G., *Growth and Characterization of AlN: From Nano Structures to Bulk Material*. 2008, Linköping University Electronic Press.
90. Bostwick, A., et al., *Quasiparticle dynamics in graphene.* Nat Phys, 2007. **3**(1): p. 36-40.
91. Ferrari, A.C., et al., *Raman Spectrum of Graphene and Graphene Layers.* Physical Review Letters, 2006. **97**(18): p. 187401.
92. Somani, P.R., S.P. Somani, and M. Umeno, *Planer nano-graphenes from camphor by CVD.* Chemical Physics Letters, 2006. **430**(1–3): p. 56-59.
93. Ma, T., et al., *Repeated Growth–Etching–Regrowth for Large-Area Defect-Free Single-Crystal Graphene by Chemical Vapor Deposition.* ACS Nano, 2014. **8**(12): p. 12806-12813.
94. Stankovich, S., et al., *Graphene-based composite materials.* Nature, 2006. **442**(7100): p. 282-286.
95. Brodie, B.C., *On the Atomic Weight of Graphite.* Philosophical Transactions of the Royal Society of London, 1859. **149**: p. 249-259.
96. Marcano, D.C., et al., *Improved Synthesis of Graphene Oxide.* ACS Nano, 2010. **4**(8): p. 4806-4814.
97. Eigler, S., et al., *Wet Chemical Synthesis of Graphene.* Advanced Materials, 2013. **25**(26): p. 3583-3587.

98. Shim, M., et al., *Polymer Functionalization for Air-Stable n-Type Carbon Nanotube Field-Effect Transistors.* Journal of the American Chemical Society, 2001. **123**(46): p. 11512-11513.
99. Farmer, D.B., et al., *Chemical Doping and Electron−Hole Conduction Asymmetry in Graphene Devices.* Nano Letters, 2009. **9**(1): p. 388-392.
100. Liu, H., Y. Liu, and D. Zhu, *Chemical doping of graphene.* J. Mater. Chem., 2011. **21**(10): p. 3335-3345.
101. Wang, X., et al., *N-Doping of Graphene Through Electrothermal Reactions with Ammonia.* Science, 2009. **324**(5928): p. 768-771.
102. Zhao, L., et al., *Visualizing individual nitrogen dopants in monolayer graphene.* Science, 2011. **333**(6045): p. 999-1003.
103. Kim, Y.A., et al., *Raman Spectroscopy of Boron-Doped Single-Layer Graphene.* ACS Nano, 2012. **6**(7): p. 6293-6300.
104. Ito, Y., et al., *Chemical Vapor Deposition of N-Doped Graphene and Carbon Films: The Role of Precursors and Gas Phase.* ACS Nano, 2014. **8**(4): p. 3337-3346.
105. Schedin, F., et al., *Detection of individual gas molecules adsorbed on graphene.* Nat Mater, 2007. **6**(9): p. 652-655.
106. Wang, Y., et al., *Nitrogen-doped graphene and its application in electrochemical biosensing.* ACS Nano, 2010. **4**(4): p. 1790-8.
107. Ang, P.K., et al., *Solution-Gated Epitaxial Graphene as pH Sensor.* Journal of the American Chemical Society, 2008. **130**(44): p. 14392-14393.
108. Ohno, Y., et al., *Electrolyte-Gated Graphene Field-Effect Transistors for Detecting pH and Protein Adsorption.* Nano Letters, 2009. **9**(9): p. 3318-3322.
109. He, S., et al., *A Graphene Nanoprobe for Rapid, Sensitive, and Multicolor Fluorescent DNA Analysis.* Advanced Functional Materials, 2010. **20**(3): p. 453-459.
110. Lu, C.-H., et al., *A Graphene Platform for Sensing Biomolecules.* Angewandte Chemie International Edition, 2009. **48**(26): p. 4785-4787.
111. Xu, M., D. Fujita, and N. Hanagata, *Perspectives and Challenges of Emerging Single-Molecule DNA Sequencing Technologies.* Small, 2009. **5**(23): p. 2638-2649.
112. Postma, H.W.C., *Rapid Sequencing of Individual DNA Molecules in Graphene Nanogaps.* Nano Letters, 2010. **10**(2): p. 420-425.
113. Schneider, G.F., et al., *DNA Translocation through Graphene Nanopores.* Nano Letters, 2010. **10**(8): p. 3163-3167.
114. Merchant, C.A., et al., *DNA Translocation through Graphene Nanopores.* Nano Letters, 2010. **10**(8): p. 2915-2921.
115. Garaj, S., et al., *Graphene as a subnanometre trans-electrode membrane.* Nature, 2010. **467**(7312): p. 190-193.
116. Wehling, T.O., et al., *Molecular doping of graphene.* Nano Lett, 2008. **8**(1): p. 173-7.
117. Aufray, B., et al., *Graphene-like silicon nanoribbons on Ag(110): A possible formation of silicene.* Applied Physics Letters, 2010. **96**(18): p. 183102.
118. Lalmi, B., et al., *Epitaxial growth of a silicene sheet.* Applied Physics Letters, 2010. **97**(22): p. 223109.
119. Kara, A., et al., *A review on silicene — New candidate for electronics.* Surface Science Reports, 2012. **67**(1): p. 1-18.
120. Fleurence, A., et al., *Experimental Evidence for Epitaxial Silicene on Diboride Thin Films.* Physical Review Letters, 2012. **108**(24): p. 245501.
121. Bianco, E., et al., *Stability and Exfoliation of Germanane: A Germanium Graphane Analogue.* ACS Nano, 2013. **7**(5): p. 4414-4421.
122. Novoselov, K.S., et al., *Two-dimensional atomic crystals.* Proceedings of the National Academy of Sciences of the United States of America, 2005. **102**(30): p. 10451-10453.

123. Shahil, K.M.F., et al., *Crystal symmetry breaking in few-quintuple Bi2Te3 films: Applications in nanometrology of topological insulators.* Applied Physics Letters, 2010. **96**(15): p. 153103.
124. Goli, P., et al., *Charge Density Waves in Exfoliated Films of van der Waals Materials: Evolution of Raman Spectrum in TiSe2.* Nano Letters, 2012. **12**(11): p. 5941-5945.
125. Kim, K.K., et al., *Synthesis of Monolayer Hexagonal Boron Nitride on Cu Foil Using Chemical Vapor Deposition.* Nano Letters, 2012. **12**(1): p. 161-166.
126. Kong, D., et al., *Few-Layer Nanoplates of Bi2Se3 and Bi2Te3 with Highly Tunable Chemical Potential.* Nano Letters, 2010. **10**(6): p. 2245-2250.
127. Liu, D., et al., *Electronic origin of high-temperature superconductivity in single-layer FeSe superconductor.* Nature Communications, 2012. **3**: p. 931.
128. McTaggart, F. and A. Wadsley, *The sulphides, Selenides, and Tellurides of Titanium, Zirconium, Hafnium, and Thorium. I. Preparation and characterization.* Australian Journal of Chemistry, 1958. **11**(4): p. 445-457.
129. Bear, J. and F. McTaggart, *The sulphides, Selenides, and Tellurides of Titanium, Zirconium, Hafnium, and Thorium. II. Chemical properties.* Australian Journal of Chemistry, 1958. **11**(4): p. 458-470.
130. McTaggart, F., *The sulphides, Selenides, and Tellurides of Titanium, Zirconium, Hafnium, and Thorium. III. Electrical properties.* Australian Journal of Chemistry, 1958. **11**(4): p. 471-480.
131. Wilson, J.A. and A.D. Yoffe, *The transition metal dichalcogenides discussion and interpretation of the observed optical, electrical and structural properties.* Advances in Physics, 1969. **18**(73): p. 193-335.
132. Withers, R.L. and J.A. Wilson, *An examination of the formation and characteristics of charge-density waves in inorganic materials with special reference to the two- and one-dimensional transition-metal chalcogenides.* Journal of Physics C: Solid State Physics, 1986. **19**(25): p. 4809.
133. Furuseth, S.B., Leif; Kjekshus, Arne, *On the Crystal Structures of TiS3, ZrS3, ZrSe3, ZrTe3, HfS3, and HfSe3.* Acta Chemica Scandinavica, 1975. **29a**: p. 623-631.
134. Bjerkelund, E.K., Arne, *On the Crystal Structure of TaSe3.* Acta Chemica Scandinavica, 1965. **19**: p. 701-710.
135. Jaegermann, W. and H. Tributsch, *Interfacial properties of semiconducting transition metal chalcogenides.* Progress in Surface Science, 1988. **29**(1): p. 1-167.
136. Lesley E. Smart, E.A.M., *Solid State Chemistry: An Introduction*. 1993, CRC Press, Taylor & Francis Group.
137. Bullett, D.W., *Electronic structure of 3d pyrite- and marcasite-type sulphides.* Journal of Physics C: Solid State Physics, 1982. **15**(30): p. 6163.
138. Zhou, F.-C., et al., *Synthesis of SnFe2O4 as a novel anode material for lithium-ion batteries.* Solid State Ionics, 2016. **296**: p. 163-167.
139. Wang, Q., et al., *CoS2 Hollow Spheres: Fabrication and Their Application in Lithium-Ion Batteries.* The Journal of Physical Chemistry C, 2011. **115**(16): p. 8300-8304.
140. Denholme, S.J., *Novel nanostructures in transition metal chalcogenide systems*, in *University of Glasgow*. 2011, University of Glasgow: Glasgow.
141. Kuc, A., N. Zibouche, and T. Heine, *Influence of quantum confinement on the electronic structure of the transition metal sulfide TS${}_{2}$.* Physical Review B, 2011. **83**(24): p. 245213.
142. Sugai, S. and T. Ueda, *High-pressure Raman spectroscopy in the layered materials $2H$-Mo${\mathrm{S}}_{2}$, $2H$-Mo${\mathrm{Se}}_{2}$, and $2H$-Mo${\mathrm{Te}}_{2}$.* Physical Review B, 1982. **26**(12): p. 6554-6558.

143. Kumar, A. and P. Ahluwalia, *Electronic structure of transition metal dichalcogenides monolayers 1H-MX2 (M= Mo, W; X= S, Se, Te) from ab-initio theory: new direct band gap semiconductors.* The European Physical Journal B, 2012. **85**(6): p. 1-7.
144. Wieting, T.J., A. Grisel, and F. Lévy, *Interlayer bonding and localized charge in MoSe2 and α-MoTe2.* Physica B+C, 1980. **99**(1–4): p. 337-342.
145. Wang, Q.H., et al., *Electronics and optoelectronics of two-dimensional transition metal dichalcogenides.* Nat Nano, 2012. **7**(11): p. 699-712.
146. Fang, H., et al., *Degenerate n-Doping of Few-Layer Transition Metal Dichalcogenides by Potassium.* Nano Letters, 2013. **13**(5): p. 1991-1995.
147. Radisavljevic, B. and A. Kis, *Mobility engineering and a metal–insulator transition in monolayer MoS2.* Nat Mater, 2013. **12**(9): p. 815-820.
148. Yoon, Y., K. Ganapathi, and S. Salahuddin, *How Good Can Monolayer MoS2 Transistors Be?* Nano Letters, 2011. **11**(9): p. 3768-3773.
149. Mak, K.F., et al., *Atomically Thin ${\mathrm{MoS}}_{2}$: A New Direct-Gap Semiconductor.* Physical Review Letters, 2010. **105**(13): p. 136805.
150. Splendiani, A., et al., *Emerging Photoluminescence in Monolayer MoS2.* Nano Letters, 2010. **10**(4): p. 1271-1275.
151. Cheng, R., et al., *High-frequency self-aligned graphene transistors with transferred gate stacks.* Proceedings of the National Academy of Sciences, 2012. **109**(29): p. 11588-11592.
152. Wang, H., et al., *Integrated Circuits Based on Bilayer MoS2 Transistors.* Nano Letters, 2012. **12**(9): p. 4674-4680.
153. Chang, H.-Y., et al., *High-Performance, Highly Bendable MoS2 Transistors with High-K Dielectrics for Flexible Low-Power Systems.* ACS Nano, 2013. **7**(6): p. 5446-5452.
154. Radisavljevic, B., M.B. Whitwick, and A. Kis, *Integrated Circuits and Logic Operations Based on Single-Layer MoS2.* ACS Nano, 2011. **5**(12): p. 9934-9938.
155. Radisavljevic, B., M.B. Whitwick, and A. Kis, *Small-signal amplifier based on single-layer MoS2.* Applied Physics Letters, 2012. **101**(4): p. 043103.
156. Kim, S., et al., *High-mobility and low-power thin-film transistors based on multilayer MoS2 crystals.* Nat Commun, 2012. **3**: p. 1011.
157. Lopez-Sanchez, O., et al., *Ultrasensitive photodetectors based on monolayer MoS2.* Nat Nanotechnol, 2013. **8**(7): p. 497-501.
158. Yin, Z., et al., *Single-Layer MoS2 Phototransistors.* ACS Nano, 2012. **6**(1): p. 74-80.
159. Li, H., et al., *Fabrication of Single- and Multilayer MoS2 Film-Based Field-Effect Transistors for Sensing NO at Room Temperature.* Small, 2012. **8**(1): p. 63-67.
160. Jing, W. and M. Lundstrom. *Does source-to-drain tunneling limit the ultimate scaling of MOSFETs?* in *Digest. International Electron Devices Meeting*. 2002.
161. Frindt, R.F., *Single Crystals of MoS2 Several Molecular Layers Thick.* Journal of Applied Physics, 1966. **37**(4): p. 1928-1929.
162. Frindt, R.F., *Superconductivity in Ultrathin Nb${\mathrm{Se}}_{2}$ Layers.* Physical Review Letters, 1972. **28**(5): p. 299-301.
163. Consadori, F., et al., *CONSTRUCTION AND PROPERTIES OF WEAK-LINK DETECTORS USING SUPERCONDUCTING LAYER STRUCTURES.* Applied Physics Letters, 1971. **18**(6): p. 233-235.
164. http://en.wikipedia.org/wiki/Raman_spectroscopy.
165. http://www.horiba.com/us/en/scientific/products/raman-spectroscopy/tutorial-faqs/raman-tutorial/the-theory-of-raman-spectroscopy/.
166. Tuinstra, F. and J.L. Koenig, *Raman Spectrum of Graphite.* The Journal of Chemical Physics, 1970. **53**(3): p. 1126-1130.
167. Thomsen, C. and S. Reich, *Double Resonant Raman Scattering in Graphite.* Physical Review Letters, 2000. **85**(24): p. 5214-5217.

168. Basko, D.M., *Theory of resonant multiphonon Raman scattering in graphene.* Physical Review B, 2008. **78**(12): p. 125418.
169. Venezuela, P., M. Lazzeri, and F. Mauri, *Theory of double-resonant Raman spectra in graphene: Intensity and line shape of defect-induced and two-phonon bands.* Physical Review B, 2011. **84**(3): p. 035433.
170. http://www.witec.de/techniques/raman/.
171. Hertz, H., *Ueber einen Einfluss des ultravioletten Lichtes auf die electrische Entladung.* Annalen der Physik, 1887. **267**(8): p. 983-1000.
172. Moulder, J.F. and J. Chastain, *Handbook of X-ray Photoelectron Spectroscopy: A Reference Book of Standard Spectra for Identification and Interpretation of XPS Data*. 1992: Physical Electronics Division, Perkin-Elmer Corporation.
173. Hawaldar, R., et al., *Large-area high-throughput synthesis of monolayer graphene sheet by Hot Filament Thermal Chemical Vapor Deposition.* Scientific Reports, 2012. **2**: p. 682.
174. David B. Williams, C.B.C., *Transmission Electron Microscopy*. 1997: Springer US. 775.
175. http://en.wikipedia.org/wiki/File:Scheme_TEM_en.svg.
176. http://www.ems.psu.edu/~ryba/coursework/zhong%20shan%20da%20xue%20-%20course%20materials/class%20slides/TEM.ppt.
177. Joseph Goldstein, D.E.N., David C. Joy, Charles E. Lyman, Patrick Echlin, Eric Lifshin, Linda Sawyer, J.R. Michael, *Scanning Electron Microscopy and X-ray Microanalysis*. Third Edition ed. 2003: Springer US. 689.
178. http://www.jeol.co.jp/en/science/sem.html.
179. Binnig, G., C.F. Quate, and C. Gerber, *Atomic Force Microscope.* Physical Review Letters, 1986. **56**(9): p. 930-933.
180. Garcıa, R. and R. Perez, *Dynamic atomic force microscopy methods.* Surface science reports, 2002. **47**(6): p. 197-301.
181. http://ip.physics.leidenuniv.nl/index.php/theses.
182. Vilarinho, P.M., *Functional Materials: Properties, Processing and Applications*, in *Scanning Probe Microscopy: Characterization, Nanofabrication and Device Application of Functional Materials: Proceedings of the NATO Advanced Study Institute on Scanning Probe Microscopy: Characterization, Nanofabrication and Device Application of Functional Materials Algarve, Portugal 1–13 October 2002*, P.M. Vilarinho, Y. Rosenwaks, and A. Kingon, Editors. 2005, Springer Netherlands: Dordrecht. p. 3-33.
183. http://www.emrl.de/r_m_2.html.
184. Kelvin, L., *Contact electricity of metals.* Philosophical Magazine Series 5, 1898. **46**(278): p. 82-120.
185. Zisman, W.A., *A NEW METHOD OF MEASURING CONTACT POTENTIAL DIFFERENCES IN METALS.* Review of Scientific Instruments, 1932. **3**(7): p. 367-370.
186. McClelland, G.M., R. Erlandsson, and S. Chiang, *Atomic Force Microscopy: General Principles and a New Implementation*, in *Review of Progress in Quantitative Nondestructive Evaluation*, D.O. Thompson and D.E. Chimenti, Editors. 1987, Springer US: Boston, MA. p. 1307-1314.
187. http://universe-review.ca/F13-atom.htm.
188. Warren, B.E., *X-Ray Diffraction*. 1969: Courier Dover Publications.
189. Choy, K.L., *Chemical vapour deposition of coatings.* Progress in Materials Science, 2003. **48**(2): p. 57-170.
190. Bryant, W.A., *The fundamentals of chemical vapour deposition.* Journal of Materials Science, 1977. **12**(7): p. 1285-1306.
191. Fischer, R.A., *Chemical Vapor Deposition. Principles and Applications. Herausgegeben von M. L. Hitchman und K. F. Jensen. Academic Press, London, 1993. 677 S., geb. 75.00 £. - ISBN 0-12-349670-5.* Angewandte Chemie, 1994. **106**(9): p. 1062-1063.

192. Blocher, J.J.M., *Vapor Deposition*. 1966, Wiley, New York: John Wiley & Sons. 725.
193. Srinivasan, A. and G.S. Sandhu, *Catalytic breakdown of reactant gases in chemical vapor deposition*. 2001, Google Patents.
194. Puddephatt, R.J., *Reactivity and mechanism in the chemical vapour deposition of late transition metals.* Polyhedron, 1994. **13**(8): p. 1233-1243.
195. Spencer, J.T., *Chemical Vapor Deposition of Metal-Containing Thin-Film Materials from Organometallic Compounds*, in *Progress in Inorganic Chemistry*. 2007, John Wiley & Sons, Inc. p. 145-237.
196. Zhang, Y., S.W.K. Choi, and R.J. Puddephatt, *Catalyst Enhanced Chemical Vapor Deposition: Effects on Chemical Vapor Deposition Temperature and Film Purity.* Journal of the American Chemical Society, 1997. **119**(39): p. 9295-9296.
197. Hideki, M., *Catalytic Chemical Vapor Deposition (CTC–CVD) Method Producing High Quality Hydrogenated Amorphous Silicon.* Japanese Journal of Applied Physics, 1986. **25**(12A): p. L949.
198. Maruyama, S., et al., *Low-temperature synthesis of high-purity single-walled carbon nanotubes from alcohol.* Chemical Physics Letters, 2002. **360**(3–4): p. 229-234.
199. *Gas regulators for pipeline connections.*; Available from: http://www.terapeak.com/worth/air-products-e11-n515b-gas-regulator/232068030463/.
200. *Pressure Controller (VD9)*. Available from: http://thyracont-vacuum.com/.
201. *PID (Proportional intergral derivative) Controller (Eurotherm)*. Available from: https://eurothermonline.com/eurotherm-3216.html.
202. Himpsel, F.J., et al., *Adsorbate band dispersions for C on Ru(0001).* Surface Science, 1982. **115**(3): p. L159-L164.
203. Kholin, N.A., E.V. Rut'kov, and A.Y. Tontegode, *The nature of the adsorption bond between graphite islands and iridium surface.* Surface Science, 1984. **139**(1): p. 155-172.
204. Hamilton, J.C. and J.M. Blakely, *Carbon segregation to single crystal surfaces of Pt, Pd and Co.* Surface Science, 1980. **91**(1): p. 199-217.
205. Eizenberg, M. and J.M. Blakely, *Carbon monolayer phase condensation on Ni(111).* Surface Science, 1979. **82**(1): p. 228-236.
206. Zi-Pu, H., et al., *Leed theory for incommensurate overlayers: Application to graphite on Pt(111).* Surface Science, 1987. **180**(2): p. 433-459.
207. Au, C.-T., C.-F. Ng, and M.-S. Liao, *Methane Dissociation and Syngas Formation on Ru, Os, Rh, Ir, Pd, Pt, Cu, Ag, and Au: A Theoretical Study.* Journal of Catalysis, 1999. **185**(1): p. 12-22.
208. Losurdo, M., et al., *Graphene CVD growth on copper and nickel: role of hydrogen in kinetics and structure.* Physical Chemistry Chemical Physics, 2011. **13**(46): p. 20836-20843.
209. Gao, L., et al., *Repeated growth and bubbling transfer of graphene with millimetre-size single-crystal grains using platinum.* Nature Communications, 2012. **3**: p. 699.
210. Alan Earnshaw, T.J.H., *The Chemistry of Transition Elements*. 1973: Clarendon Press, Oxford.
211. Obraztsov, A.N., et al., *Chemical vapor deposition of thin graphite films of nanometer thickness.* Carbon, 2007. **45**(10): p. 2017-2021.
212. Jung, I., et al., *Simple Approach for High-Contrast Optical Imaging and Characterization of Graphene-Based Sheets.* Nano Letters, 2007. **7**(12): p. 3569-3575.
213. Fujimoto, H., et al., *The estimation of the rotational misorientation by the projected probability function of a displacement of carbon layer planes.* Carbon, 1996. **34**(9): p. 1115-1118.
214. Vogt, M.C.R.K.C.G.G.M.B.L.H., *Light Scattering in Solids II*, ed. M.C.G. Güntherodt. 1982: Springer-Verlag Berlin Heidelberg. 254.

215. Martins Ferreira, E.H., et al., *Evolution of the Raman spectra from single-, few-, and many-layer graphene with increasing disorder.* Physical Review B, 2010. **82**(12): p. 125429.
216. Cançado, L.G., et al., *Quantifying Defects in Graphene via Raman Spectroscopy at Different Excitation Energies.* Nano Letters, 2011. **11**(8): p. 3190-3196.
217. Lucchese, M.M., et al., *Quantifying ion-induced defects and Raman relaxation length in graphene.* Carbon, 2010. **48**(5): p. 1592-1597.
218. Eckmann, A., et al., *Probing the nature of defects in graphene by Raman spectroscopy.* Nano Lett, 2012. **12**(8): p. 3925-30.
219. Zhang, Y., et al., *Defect-like Structures of Graphene on Copper Foils for Strain Relief Investigated by High-Resolution Scanning Tunneling Microscopy.* ACS Nano, 2011. **5**(5): p. 4014-4022.
220. Zhang, Y., et al., *Invisible growth of microstructural defects in graphene chemical vapor deposition on copper foil.* Carbon, 2016. **96**(Supplement C): p. 237-242.
221. Xiao, K., et al., *n-Type Field-Effect Transistors Made of an Individual Nitrogen-Doped Multiwalled Carbon Nanotube.* Journal of the American Chemical Society, 2005. **127**(24): p. 8614-8617.
222. Terrones, H., et al., *New Metallic Allotropes of Planar and Tubular Carbon.* Physical Review Letters, 2000. **84**(8): p. 1716-1719.
223. Czerw, R., et al., *Identification of Electron Donor States in N-Doped Carbon Nanotubes.* Nano Letters, 2001. **1**(9): p. 457-460.
224. Usachov, D., et al., *Nitrogen-doped graphene: efficient growth, structure, and electronic properties.* Nano Lett, 2011. **11**(12): p. 5401-7.
225. Deifallah, M., P.F. McMillan, and F. Corà, *Electronic and Structural Properties of Two-Dimensional Carbon Nitride Graphenes.* The Journal of Physical Chemistry C, 2008. **112**(14): p. 5447-5453.
226. Martins, T.B., et al., *Electronic and Transport Properties of Boron-Doped Graphene Nanoribbons.* Physical Review Letters, 2007. **98**(19): p. 196803.
227. Cervantes-Sodi, F., et al., *Edge-functionalized and substitutionally doped graphene nanoribbons: Electronic and spin properties.* Physical Review B, 2008. **77**(16): p. 165427.
228. Calandra, M. and F. Mauri, *Electronic structure of heavily doped graphene: The role of foreign atom states.* Physical Review B, 2007. **76**(16): p. 161406.
229. Roldán, R., M.P. López-Sancho, and F. Guinea, *Effect of electron-electron interaction on the Fermi surface topology of doped graphene.* Physical Review B, 2008. **77**(11): p. 115410.
230. Wehling, T.O., et al., *Molecular Doping of Graphene.* Nano Letters, 2008. **8**(1): p. 173-177.
231. Uchoa, B. and A.H. Castro Neto, *Superconducting States of Pure and Doped Graphene.* Physical Review Letters, 2007. **98**(14): p. 146801.
232. Peres, N.M.R., F. Guinea, and A.H. Castro Neto, *Coulomb interactions and ferromagnetism in pure and doped graphene.* Physical Review B, 2005. **72**(17): p. 174406.
233. Lin, Y.-C., C.-Y. Lin, and P.-W. Chiu, *Controllable graphene N-doping with ammonia plasma.* Applied Physics Letters, 2010. **96**(13): p. 133110.
234. Jin, Z., et al., *Large-Scale Growth and Characterizations of Nitrogen-Doped Monolayer Graphene Sheets.* ACS Nano, 2011. **5**(5): p. 4112-4117.
235. Sun, Z., et al., *Growth of graphene from solid carbon sources.* Nature, 2010. **468**(7323): p. 549-552.
236. Wei, D., et al., *Synthesis of N-doped graphene by chemical vapor deposition and its electrical properties.* Nano Lett, 2009. **9**(5): p. 1752-8.
237. Ayala, P., et al., *Chemical vapor deposition of functionalized single-walled carbon nanotubes with defined nitrogen doping.* physica status solidi (b), 2007. **244**(11): p. 4051-4055.

238. Johansson, A.-S., J. Lu, and J.-O. Carlsson, *TEM investigation of CVD graphite on nickel.* Thin Solid Films, 1994. **252**(1): p. 19-25.
239. Zhao, J., et al., *Free-Standing Single-Atom-Thick Iron Membranes Suspended in Graphene Pores.* Science, 2014. **343**(6176): p. 1228-1232.
240. Ong, T.P., et al., *Nucleation and growth of diamond on carbon-implanted single crystal copper surfaces.* Journal of Materials Research, 1992. **7**(09): p. 2429-2439.
241. Constant, L., C. Speisser, and F. Le Normand, *HFCVD diamond growth on Cu(111). Evidence for carbon phase transformations by in situ AES and XPS.* Surface Science, 1997. **387**(1): p. 28-43.
242. Zhou, W., et al., *Copper Catalyzing Growth of Single-Walled Carbon Nanotubes on Substrates.* Nano Letters, 2006. **6**(12): p. 2987-2990.
243. Ding, L., et al., *Selective Growth of Well-Aligned Semiconducting Single-Walled Carbon Nanotubes.* Nano Letters, 2009. **9**(2): p. 800-805.
244. *Inorganic Crystal Structure Database, [PDF#01-075-9130(RDB)]*.
245. *Inorganic Crystal Structure Database, [PDF#03-065-9743(RDB)]*.
246. Luo, Z., et al., *Effect of Substrate Roughness and Feedstock Concentration on Growth of Wafer-Scale Graphene at Atmospheric Pressure.* Chemistry of Materials, 2011. **23**(6): p. 1441-1447.
247. Zhong, J.-H., et al., *Quantitative Correlation between Defect Density and Heterogeneous Electron Transfer Rate of Single Layer Graphene.* Journal of the American Chemical Society, 2014. **136**(47): p. 16609-16617.
248. Ago, H., et al., *Catalytic Growth of Graphene: Toward Large-Area Single-Crystalline Graphene.* J Phys Chem Lett, 2012. **3**(16): p. 2228-36.
249. *Solubility and Diffusion Coefficient of Carbon in Nickel: Reaction Rates of Nickel-Carbon Alloys with Barium Oxide.* Journal of Applied Physics, 1952. **23**(12): p. 1305-1309.
250. Reina, A., et al., *Large Area, Few-Layer Graphene Films on Arbitrary Substrates by Chemical Vapor Deposition.* Nano Letters, 2009. **9**(1): p. 30-35.
251. Amara, H., C. Bichara, and F. Ducastelle, *Understanding the Nucleation Mechanisms of Carbon Nanotubes in Catalytic Chemical Vapor Deposition.* Physical Review Letters, 2008. **100**(5): p. 056105.
252. Amara, H., et al., *Tight-binding potential for atomistic simulations of carbon interacting with transition metals: Application to the Ni-C system.* Physical Review B, 2009. **79**(1): p. 014109.
253. Oznuluer, T., et al., *Synthesis of graphene on gold.* Applied Physics Letters, 2011. **98**(18): p. 183101.
254. Li, X., et al., *Evolution of Graphene Growth on Ni and Cu by Carbon Isotope Labeling.* Nano Letters, 2009. **9**(12): p. 4268-4272.
255. Klink, C., et al., *An STM study of carbon-induced structures on Ni(111): evidence for a carbidic-phase clock reconstruction.* Surface Science, 1995. **342**(1–3): p. 250-260.
256. McCarroll, J.J., T. Edmonds, and R.C. Pitkethly, *Interpretation of a Complex Low Energy Electron Diffraction Pattern: Carbonaceous and Sulphur-containing Structures on Ni(111).* Nature, 1969. **223**(5212): p. 1260-1262.
257. Lee, J.-H., et al., *Dynamic mechanical behavior of multilayer graphene via supersonic projectile penetration.* Science, 2014. **346**(6213): p. 1092-1096.
258. Silva-Pinto, E. and B.R.A. Neves, *Charge Injection on Insulators via Scanning Probe Microscopy Techniques: Towards Data Storage Devices.* Journal of Nanoscience and Nanotechnology, 2010. **10**(7): p. 4204-4212.
259. Panchal, V., et al., *Standardization of surface potential measurements of graphene domains.* Scientific Reports, 2013. **3**: p. 2597.

260. Zhang, Y., et al., *Charge Percolation Pathways Guided by Defects in Quantum Dot Solids.* Nano Letters, 2015. **15**(5): p. 3249-3253.
261. Gross, L., et al., *Measuring the Charge State of an Adatom with Noncontact Atomic Force Microscopy.* Science, 2009. **324**(5933): p. 1428-1431.
262. Leoni, T., et al., *Controlling the Charge State of a Single Redox Molecular Switch.* Physical Review Letters, 2011. **106**(21): p. 216103.
263. Ziegler, D., et al., *Variations in the work function of doped single- and few-layer graphene assessed by Kelvin probe force microscopy and density functional theory.* Physical Review B, 2011. **83**(23): p. 235434.
264. Kulkarni, D.D., et al., *Chemical Reduction of Individual Graphene Oxide Sheets as Revealed by Electrostatic Force Microscopy.* Journal of the American Chemical Society, 2014. **136**(18): p. 6546-6549.
265. Esteban-Ferrer, D., et al., *Electric Polarization Properties of Single Bacteria Measured with Electrostatic Force Microscopy.* ACS Nano, 2014. **8**(10): p. 9843-9849.
266. Venugopal, G., et al., *An investigation of the electrical transport properties of graphene-oxide thin films.* Materials Chemistry and Physics, 2012. **132**(1): p. 29-33.
267. Kurra, N., R.G. Reifenberger, and G.U. Kulkarni, *Nanocarbon-Scanning Probe Microscopy Synergy: Fundamental Aspects to Nanoscale Devices.* ACS Applied Materials & Interfaces, 2014. **6**(9): p. 6147-6163.
268. Malvankar, N.S., et al., *Visualization of charge propagation along individual pili proteins using ambient electrostatic force microscopy.* Nat Nano, 2014. **9**(12): p. 1012-1017.
269. Mélin, T., et al., *Probing Nanoscale Dipole-Dipole Interactions by Electric Force Microscopy.* Physical Review Letters, 2004. **92**(16): p. 166101.
270. Mélin, T., M. Zdrojek, and D. Brunel, *Electrostatic Force Microscopy and Kelvin Force Microscopy as a Probe of the Electrostatic and Electronic Properties of Carbon Nanotubes*, in *Scanning Probe Microscopy in Nanoscience and Nanotechnology*, B. Bhushan, Editor. 2010, Springer Berlin Heidelberg. p. 89-128.
271. Mativetsky, J.M., et al., *Local Current Mapping and Patterning of Reduced Graphene Oxide.* Journal of the American Chemical Society, 2010. **132**(40): p. 14130-14136.
272. Plumere, N., *Single molecules: A protein in the spotlight.* Nat Nano, 2012. **7**(10): p. 616-617.
273. Yalcin, S.E., et al., *Direct Imaging of Charge Transport in Progressively Reduced Graphene Oxide Using Electrostatic Force Microscopy.* ACS Nano, 2015. **9**(3): p. 2981-2988.
274. Ma, Y., et al., *Graphene-diamond interface: Gap opening and electronic spin injection.* Physical Review B, 2012. **85**(23): p. 235448.
275. Liao, L., et al., *High-speed graphene transistors with a self-aligned nanowire gate.* Nature, 2010. **467**(7313): p. 305-308.
276. Lahiri, J., et al., *An extended defect in graphene as a metallic wire.* Nat Nano, 2010. **5**(5): p. 326-329.
277. Santos, E.J.G. and E. Kaxiras, *Electric-Field Dependence of the Effective Dielectric Constant in Graphene.* Nano Letters, 2013. **13**(3): p. 898-902.
278. Kliem, H., *Kohlrausch relaxations: new aspects about the everlasting story.* Dielectrics and Electrical Insulation, IEEE Transactions on, 2005. **12**(4): p. 709-718.
279. Rani, A., et al., *Electrical Conductivity of Chemically Reduced Graphene Powders under Compression.* Carbon letters, 2010. **11**(2): p. 90-95.
280. Crisci, A., et al., *Surface-potential decay due to surface conduction.* Eur. Phys. J. AP, 1998. **4**(1): p. 107-116.
281. Knorr, N., S. Rosselli, and G. Nelles, *Surface-potential decay of biased-probe contact-charged amorphous polymer films.* Journal of Applied Physics, 2010. **107**(5): p. 054106.

282. Guenther, R.B. and J.W. Lee, *Partial differential equations of mathematical physics and integral equations*. 1988: Courier Corporation.
283. Zhou, Y.S., et al., *In Situ Quantitative Study of Nanoscale Triboelectrification and Patterning.* Nano Letters, 2013. **13**(6): p. 2771-2776.
284. Datta, S.S., et al., *Surface Potentials and Layer Charge Distributions in Few-Layer Graphene Films.* Nano Letters, 2009. **9**(1): p. 7-11.
285. Kalinin, S.V. and D.A. Bonnell, *Imaging mechanism of piezoresponse force microscopy of ferroelectric surfaces.* Physical Review B, 2002. **65**(12): p. 125408.
286. Mele, E.J., *Screening of a point charge by an anisotropic medium: Anamorphoses in the method of images.* American Journal of Physics, 2001. **69**(5): p. 557-562.
287. Bodepudi, S.C., A.P. Singh, and S. Pramanik, *Giant Current-Perpendicular-to-Plane Magnetoresistance in Multilayer Graphene as Grown on Nickel.* Nano Letters, 2014. **14**(5): p. 2233-2241.
288. Yoon, D., Y.-W. Son, and H. Cheong, *Negative Thermal Expansion Coefficient of Graphene Measured by Raman Spectroscopy.* Nano Letters, 2011. **11**(8): p. 3227-3231.
289. Gunho, J., et al., *The application of graphene as electrodes in electrical and optical devices.* Nanotechnology, 2012. **23**(11): p. 112001.
290. Kyas, A., et al., *Investigations concerning the work function of doped graphite.* Plasma Chemistry and Plasma Processing, 1993. **13**(2): p. 223-235.
291. Kwon, K.C., K.S. Choi, and S.Y. Kim, *Increased Work Function in Few-Layer Graphene Sheets via Metal Chloride Doping.* Advanced Functional Materials, 2012. **22**(22): p. 4724-4731.
292. Park, J., et al., *Work-Function Engineering of Graphene Electrodes by Self-Assembled Monolayers for High-Performance Organic Field-Effect Transistors.* The Journal of Physical Chemistry Letters, 2011. **2**(8): p. 841-845.
293. Giovannetti, G., et al., *Doping Graphene with Metal Contacts.* Physical Review Letters, 2008. **101**(2): p. 026803.
294. Reina, A., et al., *Transferring and Identification of Single- and Few-Layer Graphene on Arbitrary Substrates.* The Journal of Physical Chemistry C, 2008. **112**(46): p. 17741-17744.
295. Regan, W., et al., *A direct transfer of layer-area graphene.* Applied Physics Letters, 2010. **96**(11): p. -.
296. Lee, W.H., et al., *Simultaneous Transfer and Doping of CVD-Grown Graphene by Fluoropolymer for Transparent Conductive Films on Plastic.* ACS Nano, 2012. **6**(2): p. 1284-1290.
297. Chang, J.-K., et al., *Graphene Anodes and Cathodes: Tuning the Work Function of Graphene by Nearly 2 eV with an Aqueous Intercalation Process.* ACS Applied Materials & Interfaces, 2015. **7**(31): p. 17155-17161.
298. Chan, J., et al., *Reducing Extrinsic Performance-Limiting Factors in Graphene Grown by Chemical Vapor Deposition.* ACS Nano, 2012. **6**(4): p. 3224-3229.
299. Kim, S., et al., *Dynamic modulation of electronic properties of graphene by localized carbon doping using focused electron beam induced deposition.* Nanoscale, 2015. **7**(36): p. 14946-14952.
300. Yang, G., et al., *Flexible graphene-based chemical sensors on paper substrates.* Physical Chemistry Chemical Physics, 2013. **15**(6): p. 1798-1801.
301. Jung, D.H., et al., *Anisotropic behavior of hydrogen in the formation of pentagonal graphene domains.* Carbon, 2015. **89**: p. 242-248.
302. Zhigao, D., et al., *Monolayer graphene on nanostructured Ag for enhancement of surface-enhanced Raman scattering stable platform.* Nanotechnology, 2015. **26**(12): p. 125603.

303. Kim, R.-H., et al., *Stretchable, Transparent Graphene Interconnects for Arrays of Microscale Inorganic Light Emitting Diodes on Rubber Substrates.* Nano Letters, 2011. **11**(9): p. 3881-3886.
304. Li, X., et al., *Transfer of Large-Area Graphene Films for High-Performance Transparent Conductive Electrodes.* Nano Letters, 2009. **9**(12): p. 4359-4363.
305. Liang, X., et al., *Toward Clean and Crackless Transfer of Graphene.* ACS Nano, 2011. **5**(11): p. 9144-9153.
306. Park, D.-W., et al., *Graphene-based carbon-layered electrode array technology for neural imaging and optogenetic applications.* Nature Communications, 2014. **5**: p. 5258.
307. Ahn, Y., et al., *Procedure of removing polymer residues and its influences on electronic and structural characteristics of graphene.* Applied Physics Letters, 2013. **102**(9): p. 091602.
308. Liu, L., et al., *A systematic study of atmospheric pressure chemical vapor deposition growth of large-area monolayer graphene.* Journal of Materials Chemistry, 2012. **22**(4): p. 1498-1503.
309. Huang, P.Y., et al., *Grains and grain boundaries in single-layer graphene atomic patchwork quilts.* Nature, 2011. **469**(7330): p. 389-392.
310. Park, H., et al., *Graphene As Transparent Conducting Electrodes in Organic Photovoltaics: Studies in Graphene Morphology, Hole Transporting Layers, and Counter Electrodes.* Nano Letters, 2012. **12**(1): p. 133-140.
311. *Simple, green, and clean removal of a poly(methyl methacrylate) film on chemical vapor deposited graphene.* Applied Physics Letters, 2013. **103**(17): p. 171609.
312. Zheng, M., et al., *Metal-catalyzed crystallization of amorphous carbon to graphene.* Applied Physics Letters, 2010. **96**(6): p. 063110.
313. Arco, L.G.D., et al., *Synthesis, Transfer, and Devices of Single- and Few-Layer Graphene by Chemical Vapor Deposition.* IEEE Transactions on Nanotechnology, 2009. **8**(2): p. 135-138.
314. Robertson, A.W., et al., *Dynamics of Single Fe Atoms in Graphene Vacancies.* Nano Letters, 2013. **13**(4): p. 1468-1475.
315. Cretu, O., et al., *Migration and Localization of Metal Atoms on Strained Graphene.* Physical Review Letters, 2010. **105**(19): p. 196102.
316. Krasheninnikov, A.V., et al., *Embedding Transition-Metal Atoms in Graphene: Structure, Bonding, and Magnetism.* Physical Review Letters, 2009. **102**(12): p. 126807.
317. Chhowalla, M., et al., *The chemistry of two-dimensional layered transition metal dichalcogenide nanosheets.* Nat Chem, 2013. **5**(4): p. 263-275.
318. Ding, S., et al., *Facile synthesis of hierarchical MoS2 microspheres composed of few-layered nanosheets and their lithium storage properties.* Nanoscale, 2012. **4**(1): p. 95-98.
319. Li, Y., et al., *MoS2 nanoparticles grown on graphene: an advanced catalyst for the hydrogen evolution reaction.* J Am Chem Soc, 2011. **133**(19): p. 7296-9.
320. Wu, W., et al., *Piezoelectricity of single-atomic-layer MoS2 for energy conversion and piezotronics.* Nature, 2014. **514**(7523): p. 470-474.
321. van der Zande, A.M., et al., *Grains and grain boundaries in highly crystalline monolayer molybdenum disulphide.* Nat Mater, 2013. **12**(6): p. 554-61.
322. Lin, Y.-C., et al., *Wafer-scale MoS2 thin layers prepared by MoO3 sulfurization.* Nanoscale, 2012. **4**(20): p. 6637-6641.
323. Ataca, C., et al., *A Comparative Study of Lattice Dynamics of Three- and Two-Dimensional MoS2.* The Journal of Physical Chemistry C, 2011. **115**(33): p. 16354-16361.
324. Zhao, Y., et al., *Interlayer Breathing and Shear Modes in Few-Trilayer MoS2 and WSe2.* Nano Letters, 2013. **13**(3): p. 1007-1015.
325. Molina-Sánchez, A. and L. Wirtz, *Phonons in single-layer and few-layer MoS${}_{2}$ and WS${}_{2}$.* Physical Review B, 2011. **84**(15): p. 155413.

326. Sahoo, S., et al., *Temperature-Dependent Raman Studies and Thermal Conductivity of Few-Layer MoS2.* The Journal of Physical Chemistry C, 2013. **117**(17): p. 9042-9047.
327. Lee, C., et al., *Anomalous Lattice Vibrations of Single- and Few-Layer MoS2.* ACS Nano, 2010. **4**(5): p. 2695-2700.
328. Li, H., et al., *From Bulk to Monolayer MoS2: Evolution of Raman Scattering.* Advanced Functional Materials, 2012. **22**(7): p. 1385-1390.
329. Chakraborty, B., et al., *Layer-dependent resonant Raman scattering of a few layer MoS2.* Journal of Raman Spectroscopy, 2013. **44**(1): p. 92-96.
330. Zhang, W., et al., *High-Gain Phototransistors Based on a CVD MoS2 Monolayer.* Advanced Materials, 2013. **25**(25): p. 3456-3461.
331. Chakraborty, B., et al., *Symmetry-dependent phonon renormalization in monolayer MoS${}_{2}$ transistor.* Physical Review B, 2012. **85**(16): p. 161403.
332. Zeng, H., et al., *Low-frequency Raman modes and electronic excitations in atomically thin MoS${}_{2}$ films.* Physical Review B, 2012. **86**(24): p. 241301.
333. Plechinger, G., et al., *Raman spectroscopy of the interlayer shear mode in few-layer MoS2 flakes.* Applied Physics Letters, 2012. **101**(10): p. 101906.
334. Zhan, Y., et al., *Large-Area Vapor-Phase Growth and Characterization of MoS2 Atomic Layers on a SiO2 Substrate.* Small, 2012. **8**(7): p. 966-971.
335. Wang, X., et al., *Controlled Synthesis of Highly Crystalline MoS2 Flakes by Chemical Vapor Deposition.* Journal of the American Chemical Society, 2013. **135**(14): p. 5304-5307.
336. Najmaei, S., et al., *Vapour phase growth and grain boundary structure of molybdenum disulphide atomic layers.* Nat Mater, 2013. **12**(8): p. 754-759.
337. Sekine, T., et al., *Dispersive Raman Mode of Layered Compound 2h-Mos2 under the Resonant Condition.* Journal of the Physical Society of Japan, 1984. **53**(2): p. 811-818.
338. Li, F., et al., *Pressure confinement effect in MoS2 monolayers.* Nanoscale, 2015. **7**(19): p. 9075-9082.
339. Ho, Y.-T., et al., *Layered MoS2 grown on c -sapphire by pulsed laser deposition.* physica status solidi (RRL) – Rapid Research Letters, 2015. **9**(3): p. 187-191.
340. Hussain, S., et al., *Large-area, continuous and high electrical performances of bilayer to few layers MoS2 fabricated by RF sputtering via post-deposition annealing method.* Scientific Reports, 2016. **6**: p. 30791.
341. Eda, G., et al., *Photoluminescence from Chemically Exfoliated MoS2.* Nano Letters, 2011. **11**(12): p. 5111-5116.
342. Mann, J., et al., *Facile growth of monolayer MoS2 film areas on SiO2.* The European Physical Journal B, 2013. **86**(5): p. 226.
343. Liu, K.-K., et al., *Growth of Large-Area and Highly Crystalline MoS2 Thin Layers on Insulating Substrates.* Nano Letters, 2012. **12**(3): p. 1538-1544.
344. Laskar, M.R., et al., *Large area single crystal (0001) oriented MoS2.* Applied Physics Letters, 2013. **102**(25): p. 252108.
345. Kadantsev, E.S. and P. Hawrylak, *Electronic structure of a single MoS2 monolayer.* Solid State Communications, 2012. **152**(10): p. 909-913.
346. Schuller, J.A., et al., *Orientation of luminescent excitons in layered nanomaterials.* Nat Nano, 2013. **8**(4): p. 271-276.
347. Ramana, E.V., et al., *Ferroelectric and magnetic properties of magnetoelectric (Na0.5Bi0.5)TiO3–BiFeO3 synthesized by acetic acid assisted sol–gel method.* Journal of the European Ceramic Society, 2014. **34**(16): p. 4201-4211.
348. Ryou, J., et al., *Monolayer MoS2 Bandgap Modulation by Dielectric Environments and Tunable Bandgap Transistors.* Scientific Reports, 2016. **6**: p. 29184.
349. Roxlo, C.B., et al., *Bulk and Surface Optical-Absorption in Molybdenum-Disulfide.* Journal of Vacuum Science & Technology a-Vacuum Surfaces and Films, 1987. **5**(4): p. 555-557.

350. Li, T. and G. Galli, *Electronic Properties of MoS2 Nanoparticles.* The Journal of Physical Chemistry C, 2007. **111**(44): p. 16192-16196.
351. Li, W., et al., *Broadband optical properties of large-area monolayer CVD molybdenum disulfide.* Physical Review B, 2014. **90**(19): p. 195434.
352. Zou, X., Y. Liu, and B.I. Yakobson, *Predicting Dislocations and Grain Boundaries in Two-Dimensional Metal-Disulfides from the First Principles.* Nano Letters, 2013. **13**(1): p. 253-258.